University of Windsor
Scholarship at UWindsor

Electronic Theses and Dissertations | Theses, Dissertations, and Major Papers

2007

Surface-enhanced Raman scattering for trace chemical detection

Nicholas Paul William Pieczonka
University of Windsor

Follow this and additional works at: https://scholar.uwindsor.ca/etd

Recommended Citation

Pieczonka, Nicholas Paul William, "Surface-enhanced Raman scattering for trace chemical detection" (2007). *Electronic Theses and Dissertations*. 4698.
https://scholar.uwindsor.ca/etd/4698

This online database contains the full-text of PhD dissertations and Masters' theses of University of Windsor students from 1954 forward. These documents are made available for personal study and research purposes only, in accordance with the Canadian Copyright Act and the Creative Commons license—CC BY-NC-ND (Attribution, Non-Commercial, No Derivative Works). Under this license, works must always be attributed to the copyright holder (original author), cannot be used for any commercial purposes, and may not be altered. Any other use would require the permission of the copyright holder. Students may inquire about withdrawing their dissertation and/or thesis from this database. For additional inquiries, please contact the repository administrator via email (scholarship@uwindsor.ca) or by telephone at 519-253-3000ext. 3208.

Surface-Enhanced Raman Scattering For Trace Chemical Detection

By

Nicholas Paul William Pieczonka

A Dissertation
Submitted to the Faculty of Graduate Studies
through Chemistry & Biochemistry
in Partial Fulfillment of the Requirements for the
Degree of Doctor of Philosophy at the
University of Windsor

Windsor, Ontario, Canada
2007

© 2007 Nicholas P.W. Pieczonka

Reproduced with permission of the copyright owner. Further reproduction prohibited without permission.

Library and Archives Canada

Published Heritage Branch

395 Wellington Street
Ottawa ON K1A 0N4
Canada

Bibliothèque et Archives Canada

Direction du Patrimoine de l'édition

395, rue Wellington
Ottawa ON K1A 0N4
Canada

Your file Votre référence
ISBN: 978-0-494-35088-1
Our file Notre référence
ISBN: 978-0-494-35088-1

NOTICE:
The author has granted a non-exclusive license allowing Library and Archives Canada to reproduce, publish, archive, preserve, conserve, communicate to the public by telecommunication or on the Internet, loan, distribute and sell theses worldwide, for commercial or non-commercial purposes, in microform, paper, electronic and/or any other formats.

The author retains copyright ownership and moral rights in this thesis. Neither the thesis nor substantial extracts from it may be printed or otherwise reproduced without the author's permission.

AVIS:
L'auteur a accordé une licence non exclusive permettant à la Bibliothèque et Archives Canada de reproduire, publier, archiver, sauvegarder, conserver, transmettre au public par télécommunication ou par l'Internet, prêter, distribuer et vendre des thèses partout dans le monde, à des fins commerciales ou autres, sur support microforme, papier, électronique et/ou autres formats.

L'auteur conserve la propriété du droit d'auteur et des droits moraux qui protège cette thèse. Ni la thèse ni des extraits substantiels de celle-ci ne doivent être imprimés ou autrement reproduits sans son autorisation.

In compliance with the Canadian Privacy Act some supporting forms may have been removed from this thesis.

While these forms may be included in the document page count, their removal does not represent any loss of content from the thesis.

Conformément à la loi canadienne sur la protection de la vie privée, quelques formulaires secondaires ont été enlevés de cette thèse.

Bien que ces formulaires aient inclus dans la pagination, il n'y aura aucun contenu manquant.

Canada

Reproduced with permission of the copyright owner. Further reproduction prohibited without permission.

ABSTRACT

In this work, the possibilities and the peculiar properties of trace chemical detection by the phenomena of surface-enhanced Raman scattering (SERS) and surface-enhanced resonance Raman scattering (SERRS) are examined.

Detection of single-molecule SERRS of three-dye molecules from Langmuir-Blodgett monolayers on nanostructured metal films is presented. Here the observation of overtones and combinations in the single-molecule spectra of several perylene derivatives is shown for the first time. Characteristic differences in the behavior of the SERRS signal arising from a few molecules to that of the ensemble are described. In addition, the particular experimental challenges encountered in the use of SERRS for single molecule detection are presented and discussed.

The unique complexities of enhanced Raman spectroscopy are highlighted through the study of several systems. First, an extensive study into the SERS signal of the small molecule 1,8-naphthalimide is presented. An attempt is made to explain the many perturbations to the characteristic Raman spectrum that are a result of SERS. In particular, the dispersion relations of field polarization at a metal surface, which give rise to surface selection rules, and non-uniform enhancement factors, are detailed. This is shown to be one of the clearest examples of surface selection rules in SERS to date. Second, the photodynamic behavior of the SERRS signal for several dyes is presented. This is one of the first systematic studies of the temporal behavior of the SERRS signal, and it explores important questions to both single molecule detection and SERRS in general.

Finally, the fabrication, characterization, and application of several new substrates for SERS/SERRS are demonstrated. These substrates include the following: mixed

Reproduced with permission of the copyright owner. Further reproduction prohibited without permission.

Ag/Au evaporated metal films; self-sustained, Au nanoparticle embedded chitosan films; and Layer-by-Layer, avidin/Ag nanoparticle films.

Reproduced with permission of the copyright owner. Further reproduction prohibited without permission.

For Leisa

Reproduced with permission of the copyright owner. Further reproduction prohibited without permission.

ACKNOWLEDGEMENTS

First, I would like to thank my supervisor, Dr Ricardo Aroca. There is no way for me to express the gratitude that I have for all the opportunities he has given me. His laboratory is a playground for ideas. I thank him for letting me "run amuck" in his space for a while.

"A child who does not play is not a child, but the man who doesn't play has lost forever the child who lived in him and who he will miss terribly."

Pablo Neruda

I also must give a thanks and big hugs to all the past and present members of the Materials and Surface science group, including the Old guard: Paul, Alicia, Case, Tibebe, Daniel, Mat, and Ben. The Second Wave: Lalo, David, Igor, Teodosio, Ramon, Suze Q, Chico, Dr. Job and the newbie's Salwan, Grace and Golam, as well as all the others that have passed through the doors of B77 Essex Hall. You have all enriched my life and made the time spent here quite the adventure.

To the Grad house, you will be missed old friend.

To my family and friends, whose love and support, if not always understanding, has made this possible.

To my mother who always said "I could do it" even though she never really understood what "it" was.

To my Dad, I hope one day to show you that all this can put food on the table.

To Rai and Sally, your support got me through the darkest nights.

To Leisa, who has been everything to me, I have no excuse now not to do the dishes.

Muchas gracias, Obrigado, Merci Beaucoup, Thank You

Reproduced with permission of the copyright owner. Further reproduction prohibited without permission.

TABLE OF CONTENTS

ABSTRACT iii
DEDICATIONS v
ACKNOWLEDGEMENTS vi
LIST OF TABLES x
LIST OF FIGURES xi
LIST OF ABBREVATIONS xvi
CHAPTER 1 1
1. INTRODUCTION 1
1.1 Introduction 2
References 5
CHAPTER 2 9
2. BACKGROUND 9
2.1 Introduction 10
2.2 Theory of Molecular Vibrations 10
2.2.1 Infrared Absorption 12
2.2.2 Raman Scattering 13
2.2.2.1 Classical Treatment 14
2.2.2.2 Quantum Mechanical Treatment 16
2.2.2.3 Resonance Raman Scattering 18
2.2.2.4 The Observed Raman Intensities 20
2.3 Theoretical foundations for SERS 22
2.3.1 Introduction 22
2.3.2 Single Particle Model 24
2.3.3 Advanced SERS Theories 27
References 29
CHAPTER 3 33
3. INSTRUMENTATION 33
3.1 Introduction 34
3.2 Raman Instrumentation 34
3.2.1.1 Spectrometers 36
3.2.1.2 Excitation Lasers 38
3.2.1.3 Rayleigh Blocking Filters 38
3.2.1.4 Slits and Gratings 41
3.2.1.5 Detector 41
3.2.2 UV Raman Spectrometer 42
3.2.3 Microscopy 43
3.2.3.1 Objectives 44
3.2.3.2 Energy Density 45

Reproduced with permission of the copyright owner. Further reproduction prohibited without permission.

3.2.4 Calibration and Instrument Correction 45
3.2.4.1 Calibration 46
3.2.4.2 System Response & Instrument Correction 47
3.3 Thin Film Fabrication by Vacuum deposition *52*
3.4 Atomic Force Microscopy *54*
3.4.1 Contact AFM 55
3.4.2 Tapping Mode 56
3.4.3 Phase Imaging 57
3.4.4 SPM System 58
3.5 Infrared Absorption *58*
3.6 UV-visible Absorption *59*
3.7 Langmuir- Blodgett Deposition system *60*
3.8 Computational Resources *61*
References 61

CHAPTER 4 ..... **64**

4. SINGLE MOLECULE SERRS USING LANGMUIR-BLODGETT FILMS **64**

4.1 Introduction *65*
4.2 Counting Photons *66*
4.3 An alternative approach to SM-SERRS *67*
4.4 Langmuir-Blodgett films *68*
4.5 Experimental *70*
4.6 Results and Discussion *75*
4.6.1 Absorption and Fluorescence 75
4.6.2 Surface Enhanced Resonance Raman Scattering of the Ensemble 78
4.6.3 SM-SERRS and the evidence for overtones and combinations 84
4.7 Conclusions *97*
References 98

CHAPTER 5 ..... **101**

5. DISPERSIONS RELATIONS IN SERS **101**

5.1 Introduction *102*
5.2 Background *102*
5.2.1 Surface Selection Rules 104
5.2.2 Dispersion of the Enhancement factor 105
5.3 Experimental *108*
5.4 Computational Method *109*
5.5 Results and discussion *109*
5.5.1 Raman and Resonance Raman Scattering of NPIMH 109
5.5.2 Surface Enhanced Raman Scattering of NPIMH 111
5.5.3 Selection Rules and Spectral modeling 118
5.5.4 Dispersion of Surface Enhancement 121
5.6 Conclusion *125*
References 125

CHAPTER 6 ..... **128**

Reproduced with permission of the copyright owner. Further reproduction prohibited without permission.

6. PHOTODYNAMICS OF SURFACE-ENHANCED RESONANCE RAMAN SCATTERING 128

6.1 Introduction 129
6.2 Background 129
6.3 Experimental 132
6.4 Results 133
6.4.1 SERRS/ SERS of TiOPc and BNPTCD 133
6.4.2 Time Studies of R6G on Ag island films 140
6.5 Conclusion 150
References 150

CHAPTER 7 153

7. SUBSTRATE DEVELOPMENT 153

7.1 Introduction 154
7.2 Island Films of Mixed Silver and Gold 155
7.2.1 Introduction 155
7.2.2 Experimental 156
7.2.3 Results and Discussion 157
7.2.4 Conclusion 161
7.3 Gold nanoparticle Embedded Chitosan Self-Sustained thin films 162
7.3.1 Introduction 162
7.3.2 Experimental 162
7.3.3 Results and Discussion 163
7.3.4 Characterization of Films 167
7.3.4.1 S1 Films 169
7.3.4.2 S3 Films 172
7.3.5 Conclusions 175
7.4 Avidin and Ag Layer-by-Layer Films 176
7.4.1 Introduction 176
7.4.2 Experimental 179
7.4.3 Results and Discussion 181
7.4.4 Conclusions 190
References 191

8. CONCLUSIONS 194

8.1 Conclusions 195
8.2 Future Work 197

VITA AUCTORIS 199

Reproduced with permission of the copyright owner. Further reproduction prohibited without permission.

LIST OF TABLES

Table 2.1: Cross Section for various Optical Processes.....13

Table 2.2: Real and imaginary parts of the dielectric function for silver and gold 25

Table 3.1: Excitation Lasers.....38

Table 3.2: Spectral Resolution for Grating – Laser combinations.....41

Table 3.3: List of Objectives.....44

Table 3.4: Laser powers and energy density in equivalent units of measurement.....45

Table 4.1: Probe Molecule to Fatty Acid Ratio 72

Table 4.2: Peak Positions for fundamentals, overtones and combinations.....81

Table 5.1: Observed and Calculated Raman frequencies and intensities 114

Reproduced with permission of the copyright owner. Further reproduction prohibited without permission.

LIST OF FIGURES

Figure 2.1: Potential energy diagram for a molecular vibration 12

Figure 2.2: Illustration of the scattering processes. 16

Figure 2.3: Energy level diagram for the scattering processes. 17

Figure 2.4: Energy Diagram of the ground and excited state. 19

Figure 2.5: Illustration of the Single Sphere model. 24

Figure 2.6: Illustration of the surface plasmon behaviour as an amplifier and emitter 25

Figure 2.7: Illustration of typical nanoparticle interactions encountered in SERS 28

Figure 3.1: Illustration of the key components of a Raman spectrometer. 35

Figure 3.2: Photographs of Raman instruments. 37

Figure 3.3: Inside a Raman Spectrometer. 37

Figure 3.4: Holographic Notch Filter 40

Figure 3.5: Characteristic Profiles of HNF and edge filter. 40

Figure 3.6: Response curve for a CCD detector. 42

Figure 3.7: Micro and Macro Sampling Configurations 44

Figure 3.8: Raman Calibration References. 47

Figure 3.9: Uncorrected Raman Spectra of Cyclohexane 50

Figure 3.10: Intensity Correction for 785 nm using NIST SRM 2182. 51

Figure 3.11: Metal Evaporation System 53

Figure 3.12: Illustration of the principles behind scanning probe microscopy. 55

Figure 3.13: Illustration showing the ideas behind phase imaging. 57

Figure 3.14: SPM Microscope 58

Figure 3.15: Bruker 55 Equinox FT-IR spectrometer 59

Figure 3.16: Cary 50 UV-Visible spectrometer 60

Reproduced with permission of the copyright owner. Further reproduction prohibited without permission.

Figure 3.17: Lauda Langmuir film balance 61

Figure 4.1: Illustration of the Z-type deposition of a Langmuir-Blodgett Film 69

Figure 4.2: AFM image of a 6 nm Ag island film. 71

Figure 4.3: Schematic of the LB approach to SM-SERS 74

Figure 4.4: Solution absorption spectra for the 3 PTCD molecules 76

Figure 4.5: Plasmon absorption of a 6 nm Ag island film. 77

Figure 4.6: Fluorescence spectra of the Bbip-PTCD solution. 78

Figure 4.7: RR and SERRS spectrum of a 1:1 azo-PTCD film. 79

Figure 4.8: SERRS spectrum of a 1:1 pentyl-PTCD film on 6 nm Ag island film 80

Figure 4.9: RR and SERRS of 1:1 film of Bbip-PTCD on Ag. 81

Figure 4.10: Time study of the photobleaching of a 1:1 Bbip-PTCD 83

Figure 4.11: SERRS spectra of pentyl-PTCD at decreasing concentrations 84

Figure 4.12: Single molecule SERRS spectrum of azo-PTCD 85

Figure 4.13: Single molecule SERRS spectrum of pentyl-PTCD 86

Figure 4.14: Single molecule SERRS spectrum of Bbip-PTCD 87

Figure 4.15: Spectra of the background carbon background. 89

Figure 4.16: Difficulties in collecting SM Spectra. 90

Figure 4.17: Demonstration of the disappearance of SM signal for azo-PTCD. 92

Figure 4.18: Illustration of the SM experiment 94

Figure 4.19: Illustration of the distribution of hotspot in an island film 96

Figure 4.20: Graphical representation of the contributions to enhancement. 97

Figure 5.1: Ratio of normal to tangential field components. 105

Figure 5.2: Calculated Enhancement Factor for a silver ellipsoid. 107

Figure 5.3: Comparison of the wavelength span of a Raman spectrum 108

Reproduced with permission of the copyright owner. Further reproduction prohibited without permission.

Figure 5.4: UV-Vis absorption spectrum of 1,8-naphthalimide in ethanol. 110

Figure 5.5: Comparison of calculated and experimental Raman spectra.....111

Figure 5.6: Plasmon absorption spectra of Ag colloids with and without NPIMH 112

Figure 5.7: Comparison of the SERS and Raman spectrum of 1,8-naphthalimide 112

Figure 5.8: Comparison of Calculated and SERS spectra. 115

Figure 5.9: SERS spectra of NPIMH for several excitation lines.....116

Figure 5.10: Comparison of SERS of NPIMH for several excitation wavelengths.....117

Figure 5.11: Comparison of SERS and UV-RR of NPIMH. 118

Figure 5.12. SERS at 442 nm and 785 nm.....119

Figure 5.13: Comparison of measured spectrum and simulated with $E^2_t / E^2_n = 5$.....120

Figure 5.14: Comparison of measured spectrum and simulated with $E^2_n / E^2_t = 25$.....121

Figure 5.15: Comparison of the reduced spectra. 123

Figure 5.16: Illustration for the possible cases of dispersion of the enhancement factor 124

Figure 6.1:. Simplified energy level diagram indicating three possible pathways. 130

Figure 6.2: UV-Visible absorption spectra of BNPTCD and TiOPc.....133

Figure 6.3: SERS and SERRS spectra of neat monolayers on glass of the two dyes. 134

Figure 6.4: SERS/SERRS signal from a TiOPc / BNPTCD 1:1 mixed monolayer.....135

Figure 6.5: Time-Dependent photobleaching of the SERS/SERRS 136

Figure 6.6: SERS/SERRS signal from a TiOPc / BNPTCD 1:1 mixed monolayer.....137

Figure 6.7: Signal decay in SERS and SERRS.....138

Figure 6.8: Comparison of the signal decay for BNPTCD.....139

Figure 6.9: Intensity decay of SERRS of TiOPc 140

Figure 6.10: UV-Visible absorption spectra of 10^{-7} R6G Solution 141

Figure 6.11: SERRS of a 10 μl casting of a 10^{-7} M R6G solution on a Ag island film..142

Reproduced with permission of the copyright owner. Further reproduction prohibited without permission.

Figure 6.12: Time Study of the SERRS signal of 10^{-7} R6G. 143

Figure 6.13: Intensity decay for SERRS R6G. 144

Figure 6.14: Signal decay for the SERRS signal of R6G for several ED. 145

Figure 6.15: Signal decay for the SERRS signal of R6G for 3 ED's 146

Figure 6.16: Integrated SERRS intensity of R6G for one dose for three different ED's. 147

Figure 6.17: Illustration of the possible mechanism for signal decay seen in SERRS 149

Figure 7.1: Gallery of SERS substrates 154

Figure 7.2: Plasmon absorption and AFM for Ag/Au island films 158

Figure 7.3: SERRS and SERS of BBip. 159

Figure 7.4: Several SM spectra of Bbip compared to the ensemble SERRS spectrum .. 160

Figure 7.5: Growth of surface plasmon with reaction time. 165

Figure 7.6: Plasmon absorption of films made from gold and chitosan 166

Figure 7.7: Comparison of FT-IR absorption spectra chitosan films 168

Figure 7.8: Comparison in AFM images between ofvchitosan films 169

Figure 7.9: Characterization of the S1 films.. 171

Figure 7.10: Characterization of the S3 films. 173

Figure 7.11: AFM of the SERS active films (S3) 174

Figure 7.12: SERS obtained with a Au-chitosan film 175

Figure 7.13: Illustration of the layer-by-layer method 177

Figure 7.14: Illustration of construction of LbL avidin/Ag film 179

Figure 7.15: Surface plasmon absorption from films with 2 to 10 bilayers 182

Figure 7.16: Optical images of the avidin/Ag nanoparticle LbL films. 183

Figure 7.17: AFM topography images showing the progression from 2,to 14 bilayers.. 184

Figure 7.18: AFM for 14 bilayers film 185

Reproduced with permission of the copyright owner. Further reproduction prohibited without permission.

Figure 7.19: UV-Visible absorption spectrum of a B4F Solution. 186

Figure 7.20: SERRS signal of B4F from 14 bilayer avidin/Ag films 187

Figure 7.21: 10 x 10 μm SERRS Intensity map for the B4F 188

Figure 7.22: SERRS signal of 5-AF after in situ biotinylation 190

Reproduced with permission of the copyright owner. Further reproduction prohibited without permission.

LIST OF ABBREVATIONS

5-AF	5-(aminomethyl)fluorescein
AA	Arachidic Acid
AFM	Atomic Force Microscopy
azo-PTCD	Bis (benzimidazo) perylene
B4F	Biotin-4-fluorescein
Bbip-PTCD	Bis–(benzylimido) perylene
BNPTCD	Bis(neopentylimido)perylene
CCD	Charge Coupled Device
DFT	Density Functional Theory
ED	Energy Density
EM	Electromagnetic
FT-IR	Fourier Transform Infrared Absorption
HNF	Holographic Notch Filters
IR	Infrared
IRC	Instrument Response Correction
LB	Langmuir-Blodgett
LbL	Layer-by-Layer
NA	Numerical Aperture
NIST	National Institute of Standards
NPIMH	1,8-naphthalimide
PB	Photobleaching
PBS	Phosphate buffered saline

Reproduced with permission of the copyright owner. Further reproduction prohibited without permission.

Pc	Phthalocyanine
PD	Photodegradation
pentyl-PTCD	n-pentylimido-benzimidazo perylene
PTCD	Perylene tetracarboxylic derivative
R6G	Rhodamine 6 G
RRS	Resonance Raman Scattering
RS	Raman Scattering
SERRS	Surface Enhanced Resonance Raman Scattering
SERS	Surface Enhanced Raman Scattering
SMD	Single Molecule Detection
SMS	Single Molecule Spectroscopy
SM-SERS	Single Molecule Surface Enhanced Raman Scattering
SPM	Scanning Probe Microscopy
SPR	Surface Plasmon Resonance
TEM	Transmission Electron Microscopy
TiOPc	Titanyl (IV) phthalocyanine
TM	Target Molecule
UV-Vis	Ultraviolet - Visible
XPS	X-ray Photoelectron Spectroscopy

Reproduced with permission of the copyright owner. Further reproduction prohibited without permission.

CHAPTER 1

INTRODUCTION

Reproduced with permission of the copyright owner. Further reproduction prohibited without permission.

1.1 Introduction

Surface-enhanced Raman scattering (SERS) has been the subject of vast theoretical and practical developments.[1,2] In particular, it is recognized as an ultrasensitive analytical technique, and it has been proven to be a viable single molecule spectroscopy.[2-7] In addition, it has the potential to be a very powerful spectroscopic tool for emerging fields in nanoscience.[8-10]

SERS is based on the fact that a metallic nanostructure with the right optical properties, proper size and morphology can enhance optical fields by orders of magnitude. These "optical amps" can augment the photo-processes of molecules located near their surface when excited with the appropriate frequency of radiation. In the case of Raman scattering, the total enhancement has been suggested to reach upwards towards 10^{10} and possible larger.[11] Theoretically, there is no implicit molecular specificity to the process, in practice however this is often not the case. SERS, a technique now over 30 years old, continues to draw a great deal of interest due to its unique ability to provide vibrational fingerprint at trace levels with unparalleled potential in many areas of analytical chemistry. A sampling of the current scientific literature finds SERS being applied in all branches of science. The life sciences have shown extensive interest in the possibilities offered by trace chemical detection through remote, non-evasive means. SERS has been used in a vast range of applications, from immunoassays to bio-recognition sensors.[12-14] Promising developments such as real time recording of glucose levels for diabetes,[15,16] the rapid detection and identification of pathogens,[17] early cancer detection,[18] and even potential use for the rapid sequencing of DNA[19] have only added to

Reproduced with permission of the copyright owner. Further reproduction prohibited without permission.

the growing interest in SERS. Material science, particularly the area of fullerene chemistry, has found SERS to be extremely useful for characterization.[20-22]

Those investigating the fringes of nanoscience look anxiously towards developments in SERS for the potential to monitor the bond formation in single molecule chemistry. SERS, as a direct application of metallic nanostructures, is part of an area of frantic research in nanoscience. It is now at the point that a demonstration of SERS activity, is part of the tool chest for characterization, along with plasmon absorption and transmission electron microscopy, for every new metallic nanoparticle synthesized.[23-29]

The field of SERS has also contributed to fundamental science, particularly the expanding fields of nanomaterials and plasmonics.[30,31] Much of the current knowledge of the optical properties of metallic nanoparticles has been fuelled, in part, as an attempt to explain the SERS phenomenon. Since the demonstration of single molecule detection by SERS, this area of research has exploded in the subsequent attempts to explain the large electromagnetic fields necessary for related observations.[32-36]

Of course all this great promise comes with a caveat. Aside from a set of well behaved average SERS measurements, SERS spectroscopy can be extremely challenging. Perturbations to the experiment are numerous and the interpretation of the results can be extremely perplexing.[37] This is especially evident at the trace and single molecule regime.[38-42]

To maximize SERS as a viable analytical tool, a deeper understanding of all the variables that impact the experiment is necessary. The limitations and the possibilities should be understood. The SERS practitioner will face many challenging questions, such as: How do the parameters of the experiment affect the measurements? What is the

Reproduced with permission of the copyright owner. Further reproduction prohibited without permission.

impact of nanostructures and substrates on the recorded spectrum? At what level do the ensemble statistics break down? What are the signatures of single molecule detection?

The work presented in this thesis is an attempt to provide insight into some of these questions. The title of this thesis, "Surface-enhanced Raman Scattering for Trace Chemical Detection," was chosen because all the work presented here deals, in one way or another, with various aspects of trace detection by enhanced Raman scattering. After this introduction, Chapter 2 sets the stage for the discussions to follow. The foundations of Raman scattering are discussed, followed by an overview of the underpinnings of the electromagnetic mechanism responsible for the augmented signal seen in SERS and SERRS experiments.

In Chapter 3, the instrumental methods used for this thesis are discussed, with particular emphasis on the role of instrumentation in Raman and SERS studies. Included in the third chapter is an overview of the methods used for the fabrication of nanoparticle films and the tools used for their characterization.

The results presented for the thesis can be divided into three sections. The first covers single molecule studies. The middle section is an examination of important peculiarities of enhanced Raman experiments, and the last encompasses work done on SERS substrate development.

Chapter 4 presents the use of monomolecular Langmuir-Blodgett for the SERRS studies of overtone and combination in the spectra of single molecules. The success and the challenges of SM-SERRS are highlighted.

In Chapters 5 and 6, several of the most relevant challenges to enhanced Raman experiments are examined and discussed. What at first may be seen as complications in SERS, may actually open doors to new ways to extract information from the SERS

Reproduced with permission of the copyright owner. Further reproduction prohibited without permission.

experiments. In particular, Chapter 5 looks at the many dispersion relations that are present in the SERS experiment through the case study of a small molecule. While in Chapter 6, the photodynamic studies of several systems investigated under resonance Raman conditions are presented and discussed.

In Chapter 7, the fabrication, characterization and application of several new substrates for SERS are presented. And finally Chapter 8 reiterates the main conclusions of this thesis, and possible future directions of study are discussed.

References

(1) Aroca, R. *Surface - Enhanced Vibrational Spectroscopy*; John Wiley & Sons, 2006.

(2) Pieczonka, N. P. W.; Goulet, P.; Aroca, R. In *Surface Enhanced Raman Scattering: Physics and Applications*; Kneipp, K., Moskovits, M., Kneipp, H., Eds.; Springer-Verlag: Berlin, 2006; Vol. 103.

(3) Goulet, P. J. G.; Pieczonka, N. P. W.; Aroca, R. F. *Journal of Raman Spectroscopy* **2005**, *36*, 574-580.

(4) Goulet, P. J. G.; Pieczonka, N. P. W.; Aroca, R. F. *Canadian Journal of Analytical Sciences and Spectroscopy* **2003**, *48*, 146-152.

(5) Moskovits, M.; Tay, L.-L.; Yang, J.; Haslett, T. *Topics in Applied Physics* **2002**, *82*, 215-226.

(6) Lemma, T.; Aroca, R. F. *Journal of Raman Spectroscopy* **2002**, *33*, 197-201.

(7) Nie, S.; Emory, S. R. *Science* **1997**, *275*, 1102-1106.

(8) Kneipp, K.; Wang, Y.; Kneipp, H.; Perelman, L. T.; Itzkan, I.; Dasari, R. R.; Feld, M. S. *Physical Review Letters* **1997**, *78*, 1667-1670.

Reproduced with permission of the copyright owner. Further reproduction prohibited without permission.

(9) Tian, Z. Q. *Journal of Raman Spectroscopy* **2005**, *36*, 466-470.

(10) Kincade, K. *Laser Focus World* **2006**, *42*, 109-111.

(11) Corni, S.; Tomasi, J. *Journal of Chemical Physics* **2002**, *116*, 1156-1164.

(12) Grubisha, D. S.; Lipert, R. J.; Park, H.-Y.; Driskell, J.; Porter, M. D. *Analytical Chemistry* **2003**, *75*, 5936-5943.

(13) Pieczonka, N. P. W.; Goulet, P. J. G.; Aroca, R. F. *Journal of the American Chemical Society* **2006**, *128*, 12626-12627.

(14) Farquharson, S.; Shende, C.; Inscore, F. E.; Maksymiuk, P.; Gift, A. *Journal of Raman Spectroscopy* **2005**, *36*, 208-212.

(15) Zhang, X. Y.; Shah, N. C.; Van Duyne, R. P. *Vibrational Spectroscopy* **2006**, *42*, 2-8.

(16) Stuart, D. A.; Yuen, J. M.; Lyandres, N. S. O.; Yonzon, C. R.; Glucksberg, M. R.; Walsh, J. T.; Van Duyne, R. P. *Analytical Chemistry* **2006**, *78*, 7211-7215.

(17) Driskell, J. D.; Kwarta, K. M.; Lipert, R. J.; Porter, M. D.; Neill, J. D.; Ridpath, J. F. *Analytical Chemistry* **2005**, *77*, 6147-6154.

(18) Vo-Dinh, T.; Stokes, D. L. *Biomedical Photonics Handbook* **2003**, 64/1-64/39.

(19) Kneipp, K.; Kneipp, H.; Dasari, R. R.; Feld, M. S. *Indian Journal of Physics, B* **2003**, *77B*, 39-47.

(20) Kneipp, K.; Kneipp, H.; Dresselhaus, M. S.; Lefrant, S. *Philosophical Transactions of the Royal Society of London, Series A: Mathematical, Physical and Engineering Sciences* **2004**, *362*, 2361-2373.

(21) Lefrant, S.; Baltog, I.; Baibarac, M.; Mevellec, J. Y.; Chauvet, O. *Carbon* **2002**, *40*, 2201-2211.

Reproduced with permission of the copyright owner. Further reproduction prohibited without permission.

(22) Aroca, R. F.; Pieczonka, N. P. W.; Nazri, M. *Óptica Pura y Aplicada* **2007**, *40*, 195-202.

(23) Lu, Y.; Liu, G. L.; Kim, J.; Mejia, Y. X.; Lee, L. P. *Nano Letters* **2005**, *5*, 119-124.

(24) Tao, A.; Kim, F.; Hess, C.; Goldberger, J.; He, R.; Sun, Y.; Xia, Y.; Yang, P. *Nano Letters* **2003**, *3*, 1229-1233.

(25) Aizpurua, J.; Hanarp, P.; Sutherland, D. S.; Kall, M.; Bryant Garnett, W.; Garcia de Abajo, F. J. *Physical Review letters* **2003**, *90*, 057401.

(26) Genson, K. L.; Holzmueller, J.; Jiang, C. Y.; Xu, J.; Gibson, J. D.; Zubarev, E. R.; Tsukruk, V. V. *Langmuir* **2006**, *22*, 7011-7015.

(27) Li, J. F.; Yang, Z. L.; Ren, B.; Liu, G. K.; Fang, P. P.; Jiang, Y. X.; Wu, D. Y.; Tian, Z. Q. *Langmuir* **2006**, *22*, 10372-10379.

(28) Li, Y.; Lu, G. W.; Wu, X. F.; Shi, G. Q. *Journal of Physical Chemistry B* **2006**, *110*, 24585-24592.

(29) Aroca, R. F.; Alvarez-Puebla, R. A.; Pieczonka, N. P. W.; Sanchez-Cortez, S.; Garcia-Ramos, J. V. *Advances in Colloid and Interface Science* **2005**, *116* 45-61.

(30) Imura, K.; Okamoto, H.; Hossain, M. K.; Kitajima, M. *Nano Letters* **2006**, *6*, 2173-2176.

(31) Maier, S. A. *Optics Express* **2006**, *14*, 1957-1964.

(32) Bergman, D. J.; Stockman, M. I. *Physical Review Letters* **2003**, *90*, 027402/1-027402/4.

(33) Brandl, D. W.; Mirin, N. A.; Nordlander, P. *Journal of Physical Chemistry B* **2006**, *110*, 12302-12310.

Reproduced with permission of the copyright owner. Further reproduction prohibited without permission.

(34) Kelly, K. L.; Coronado, E.; Zhao, L. L.; Schatz, G. C. *Journal of Physical Chemistry B* **2003**, *107*, 668-677.

(35) Andersen, P. C.; Rowlen, K. L. *Applied Spectroscopy* **2002**, *56*, 124A-135A.

(36) Stockman, M. I.; Faleev, S. V.; Bergman, D. J. *Physical Review Letters* **2001**, *87*, 167401/1-167401/4.

(37) Pieczonka, N. P. W.; Aroca, R. F. *ChemPhysChem* **2005**, *6*, 2473-2484.

(38) Goulet, P. J. G.; Pieczonka, N. P. W.; Aroca, R. F. *Analytical Chemistry* **2003**, *75*, 1918-1923.

(39) Otto, A. *Journal of Raman Spectroscopy* **2002**, *33*, 593-598.

(40) Maher, R. C.; Dalley, M.; Le Ru, E. C.; Cohen, L. F.; Etchegoin, P. G.; Hartigan, H.; Brown, R. J. C.; Milton, M. J. T. *Journal of Chemical Physics* **2004**, *121*, 8901-8910.

(41) Suh, Y. D.; Schenter, G. K.; Zhu, L.; Lu, P. H. *Ultramicroscopy* **2003**, *97*, 89-102.

(42) Bosnick, K. A.; Jiang, J.; Brus, L. E. *Journal of Physical Chemistry B* **2002**, *106*, 8096-8099.

Reproduced with permission of the copyright owner. Further reproduction prohibited without permission.

CHAPTER 2

BACKGROUND

Reproduced with permission of the copyright owner. Further reproduction prohibited without permission.

2.1 Introduction

SERS is a meeting ground between vibrational spectroscopy and the plasmonics of metal nanoparticles and nanostructures. In this chapter, both these aspects of SERS are discussed. Ultimately, SERS is a branch of vibrational spectroscopy, and as such, it is necessary for any proper interpretation of SERS results to have a robust understanding of the underpinning theoretical foundations of the vibrational theory of molecules and in particular of the vibrational spectrum observed using the inelastic scattering of light or Raman effect. In this section the theory of molecular vibrations will be discussed. The physics behind Raman scattering, both classical and semi-classical, are highlighted and the section ends with a look at Raman intensities

In the second part of this chapter the optical properties of nanoparticles and their role in the theoretical framework of surface enhanced Raman scattering are discussed.

2.2 Theory of Molecular Vibrations

The theoretical modeling of molecular vibrations can begin with the classical picture of a molecule as a collection of N objects connected through a set of massless springs. This assembly has a total of 3N degrees of freedom to describe the ability of each atom to move in the 3 Cartesian directions (x,y,z). The molecular system is treated as a whole, and so the translational movement accounts for 3 of these degrees of freedom, and 3 more (2 for a linear arrangement) have to be assigned to describe the rotational movement. This leaves 3N-6 (or 3N-5 for a linear molecule) vibrational degrees of freedom to describe the vibrational motion. Within the harmonic approximation, each degree of freedom is set in correspondence with the so called "normal modes of

Reproduced with permission of the copyright owner. Further reproduction prohibited without permission.

vibration", and they correspond to motions where all the nuclei undergo harmonic motion, move in phase and have the same frequency of oscillation.[1]

A very simple approximation for a molecular vibration is a classical harmonic oscillator that obeys Hooke's law:

$$F = -k(R - R_{eq}) \tag{2.2.1}$$

Here, R_{eq} is the equilibrium position for the vibration between two atoms and k is the force constant. Like the classical oscillator, the frequency v is given by the equation:

$$\nu = \frac{1}{2\pi}\sqrt{\frac{k}{\mu}} \tag{2.2.2}$$

where μ is the reduced mass.

Though this is a rough estimate, it does give a rationale for the frequencies measured in vibrational spectroscopy. This approximation fails to account for the presence of any anharmonicity, be it electrical or mechanical. As such, a better description is attained with the Morse potential, which can be seen in Figure 2.1. The presence of an anharmonicity relaxes the $\Delta v = \pm 1$ selection rule, explaining the observation of vibrational overtones and combination in the Raman spectrum. This is a spectral feature that will play an important role in the single molecule spectroscopy experiments discussed later.

A molecular system can reveal its vibrational information through the interaction with light. This can be either through the absorption or the scattering of photons. Two spectroscopies that arise from these two physical phenomena are: Infrared Absorption (IR) and Raman Scattering (RS). Although both techniques probe the same set of vibrations, each has a different physical origin. IR occurs with a change in a dipole

Reproduced with permission of the copyright owner. Further reproduction prohibited without permission.

moment, whereas RS requires a net change in the polarizability with the corresponding normal coordinate. As such, these methods are complementary tools for the characterization of the vibrational modes in a molecular system.

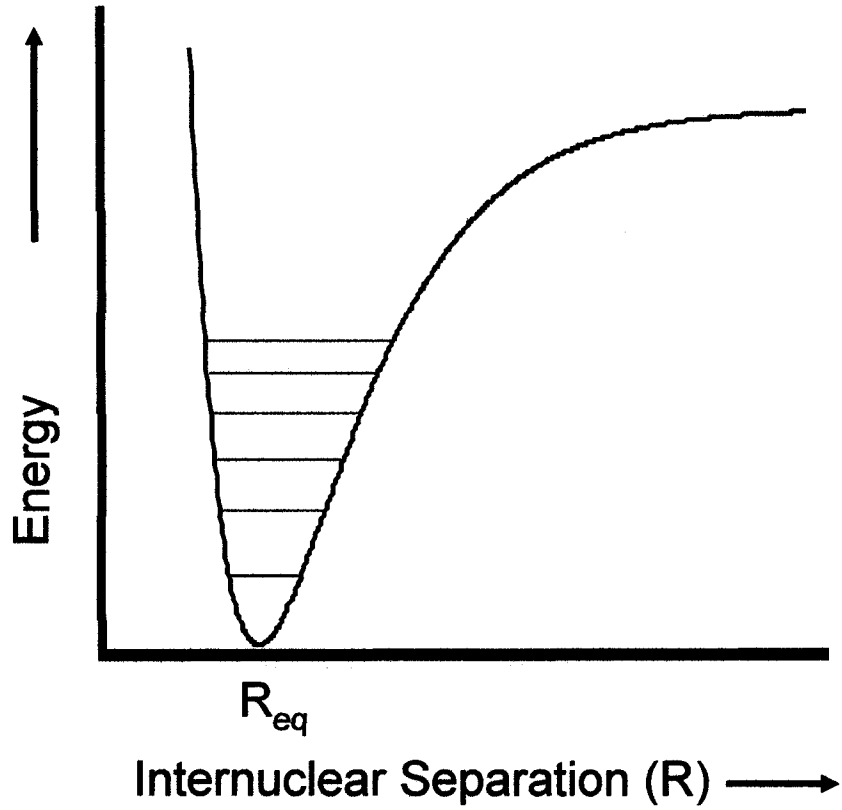

Figure 2.1: Potential energy diagram for a molecular vibration

2.2.1 Infrared Absorption

For the absorption of a photon by a molecule for a vibrational mode to occur the dipole moment must change during the motion of vibration, i.e. a change in the equilibrium geometry produces a net change in the dipole moment. When this condition is met a quantum of light of the same frequency as the vibration can be absorbed. The energy levels associated with molecular vibrations are in the infrared region of the electromagnetic spectrum thus forming the basis for infrared absorption spectroscopy.

Reproduced with permission of the copyright owner. Further reproduction prohibited without permission.

One measure of the efficiency of an optical process is the cross section, which gives a measure of the probability for an event to occur. The cross section for IR absorption is on the order of 10^{-20} cm^2 per molecules. For comparison, typical cross section values for the most common optical processes are shown in Table 2.1.[2]

Table 2.1: Cross Section for various Optical Processes

Process		σ (cm^2)
Absorption	UV	10^{-18}
	IR	10^{-21}
Fluorescence		10^{-19}
Raman Scattering		10^{-28}
Resonance Raman Scattering		10^{-24}

2.2.2 Raman Scattering

The interaction between a molecular system and monochromatic source of light can result in several types of scattering. The impinging photons can be scattered either elastically or inelastically. When there is no loss in energy, this elastic scattering is called Rayleigh scattering. In addition, there are a very small number of photons that experience an energy change that is equal to a vibrational quantum transition. These are the Raman scattered photons and provide the basis for Raman scattering spectroscopy. It is named in honour of Dr. C.V. Raman and his experimental discovery in 1928.[3] Raman scattering is very inefficient compared to other optical processes as can be seen in Table 2.1. The probability for the generation of a Raman scattered is about 1 for every ten million photons scattered by a molecule. In comparison, the top chromophores have a fluorescence quantum yield approaching 1, i.e. almost all the photons that are absorbed are emitted as fluorescence.

Reproduced with permission of the copyright owner. Further reproduction prohibited without permission.

The Raman effect can be described both classically and quantum mechanically. Both treatments are based upon the molecular response property of polarizability (α). More precisely, the property of interest is the induced polarization (P) that is the result of an interaction of the molecule with an electromagnetic field (E):

$$P = \alpha E \tag{2.2.3}$$

2.2.2.1 Classical Treatment

The response function is the polarizability, which is a description of the electron cloud that surrounds a molecule and essentially describes it's deformability in the presence of an electric field. Just as an oscillating dipole will radiate, so too will an induced dipole that arises due to an interaction with electromagnetic radiation. If the electric field of frequency v_o is given by $E = E_o \cos 2\pi v_o t$ or $E = E_o \cos \omega_o t$, then the induced dipole will be:

$$\mu = \alpha \cdot E_o \cdot \cos \omega_o t \tag{2.2.4}$$

At any one time the molecule is in a complex motion of vibrations which is approximated as the summation of normal vibrations. Of course the polarizability is a function dependent upon the normal coordinates $Q = Q_o \cos \omega_i t$, where ω_j is the frequency of the jth vibration. The polarizability can be expanded out as a Taylor series about the equilibrium:

$$\begin{aligned} \alpha &= \alpha_o + \left(\frac{\partial \alpha}{\partial Q}\right)_o \cdot Q + \ldots \\ \alpha &= \alpha_o + \left(\frac{\partial \alpha}{\partial Q}\right)_o \cdot Q_o \cos \omega_j t \end{aligned} \tag{2.2.5}$$

and the induced dipole moment becomes:

Reproduced with permission of the copyright owner. Further reproduction prohibited without permission.

$$\mu = \alpha_o \cdot E_o Q_o \cos\omega_o t + \left(\frac{\partial \alpha}{\partial Q}\right)_o \cdot Q_o \cdot E_o \cdot \cos\omega_j t \cdot \cos\omega_o t \qquad (2.2.6)$$

which can be expressed as:

$$\mu = \alpha_o E_o \cos\omega_o t + \frac{1}{2}\left(\frac{\partial \alpha}{\partial Q}\right)_o Q_o E_o \left[\cos(\omega_o + \omega_j)t + \cos(\omega_o - \omega_j)t\right] \qquad (2.2.7)$$

Thus the induced dipole oscillation is comprised of three frequencies which correspond to elastic scattering (Rayleigh), and inelastic scattering (Raman) with a lower frequency (Stokes) and higher frequency component (anti-Stokes) as illustrated in Figure 2.2. The main selection rule for Raman scattering results from the change in the polarizability during the motion of the vibration: $\left(\frac{\partial \alpha}{\partial Q}\right)_o \neq 0$

While this formalism explains the basic mechanisms of Raman scattering, there are several properties that are missing. Among these is any gauge of relative intensity as well as any inclusion of electronic resonance effects. For that we must turn to quantum mechanics.

Reproduced with permission of the copyright owner. Further reproduction prohibited without permission.

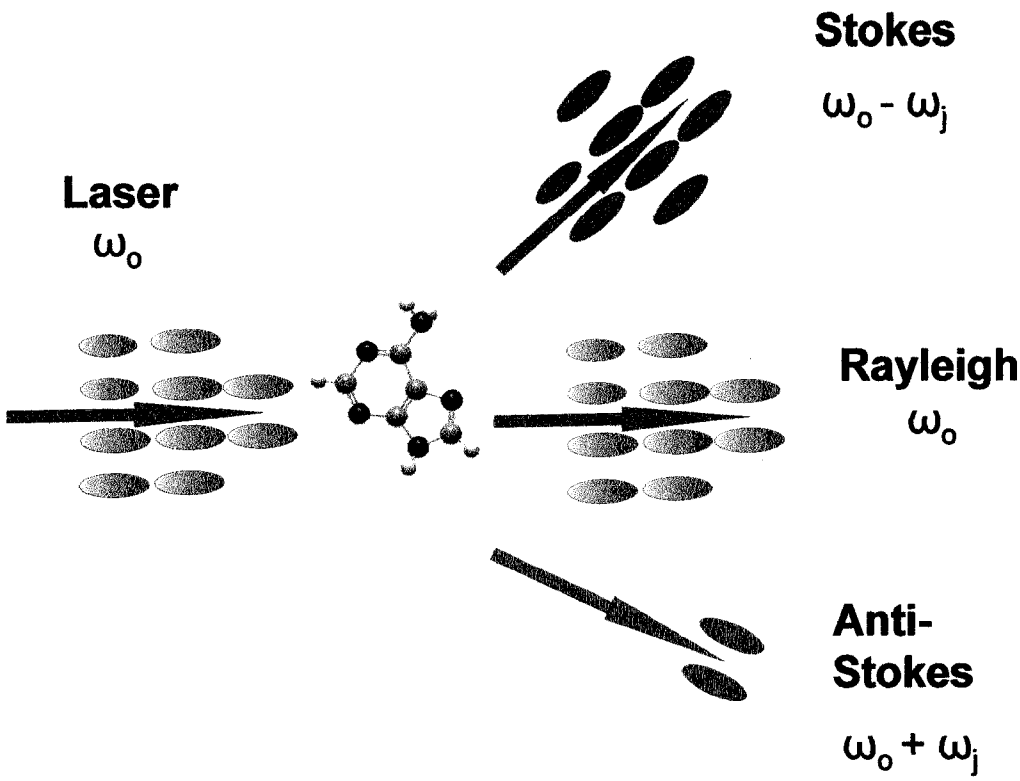

Figure 2.2: Illustration of the scattering processes.

2.2.2.2 Quantum Mechanical Treatment

In the QM formalism, the molecule is treated as a quantum object while the interacting electromagnetic field is treated classically. Here, the scattering events are seen as a result of an impinging photon initiating a transition between energy states. When the excitation is far from an electronic absorption the transition involves an intermediate state often referred to as a "virtual" state. When the excitation is coincident with an electronic excitation of the molecule, the transition involves a true eigenstate of the system and is known as resonance Raman scattering. The different possibilities are illustrated in Figure 2.3.

Reproduced with permission of the copyright owner. Further reproduction prohibited without permission.

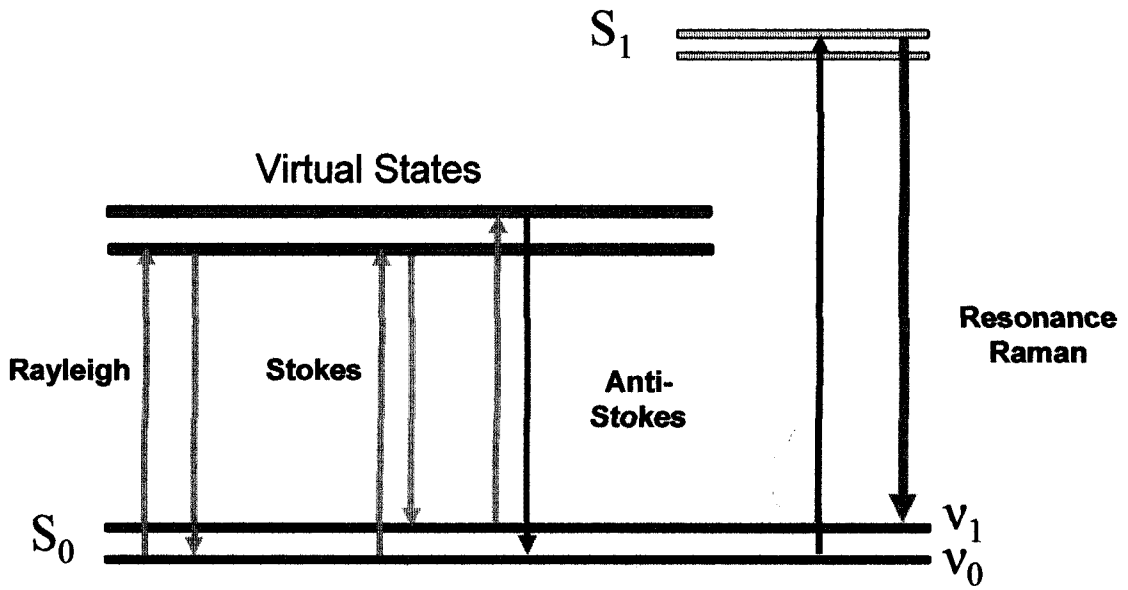

Figure 2.3: Energy level diagram for the scattering processes.

The classical polarizability tensor is replaced by a transition polarizability tensor $P_{m,n} = E \cdot (\alpha)_{m,n}$ which can be calculated from second-order perturbation theory.[4] This leads to the Kramers-Heisenberg-Dirac (KHD) equation:[4]

$$(\alpha_{\rho\sigma})_{m,n} = \frac{1}{h}\left(\sum_e \frac{\langle m|D_\sigma|e\rangle\langle e|D_\rho|n\rangle}{\nu_{em} - \nu_L - i\Gamma_e} + \frac{\langle m|D_\rho|e\rangle\langle e|D_\sigma|n\rangle}{\nu_{en} + \nu_L - i\Gamma_e} \right) \qquad (2.2.8)$$

Here, ν_L is the frequency of the excitation, ν_{em} is the frequency between two states, D is the electronic dipole moment operator, $|e\rangle$ corresponds to the intermediate state, and $i\Gamma$ is the damping term and is related to the lifetime of the state.

Reproduced with permission of the copyright owner. Further reproduction prohibited without permission.

2.2.2.3 Resonance Raman Scattering

There can be several changes in the Raman scattering of a molecule if the wavelength of the exciting line falls under the envelope of absorption. Looking at the KHD equation, one can see that as the excitation energy approaches an electronic resonance, the denominator tends to zero. This is manifested as a significant amplification of Raman intensity. Experimentally, increases on the order of 10^4 to 10^6 have been measured.[5] This intensity increase does not apply equally to all vibrations. Enhancement for a particular vibrational mode is strongly correlated to the bands symmetry. As well, modes that are involved in the electronic transition are those that are seen with the highest intensity in the RRS spectrum. It has been shown that there are several different mechanisms that can account for resonance enhancement. These can be expressed when the KHD is written as a Herzberg-Teller expansion of the electronic wavefunctions. The resulting expressions are grouped into what are known as the Albrecht terms: $\left(\alpha_{\rho\sigma}\right)_{mn} = A + B + C$.[4] The RR for the molecular systems studied in this thesis is predominantly described by the *A*-term.

The Albrecht *A*-term is comprised of calculations that measure vibrational overlap factors and the squares of which are called the Franck-Condon factors, hence RR scattering where this term is dominant is said to undergo a "Frank-Condon Enhancement". This term describes situations in which a component of the normal coordinate of the vibration is in a direction in which the molecule expands during an electronic excitation. The more the molecule expands along this axis when it absorbs light, the larger the enhancement factor. The magnitude of the intensity increase for a vibrational mode can be related to the quantity ΔQ, which is the measure of change in the

Reproduced with permission of the copyright owner. Further reproduction prohibited without permission.

equilibrium position of the normal coordinate of the ground state to that in excited state. This is pictorially presented in Figure 2.4. The *A*-term is applicable only to totally symmetric vibrations. Hence resonance Raman scattering under conditions where the *A*-term is active have spectra dominated by these modes.

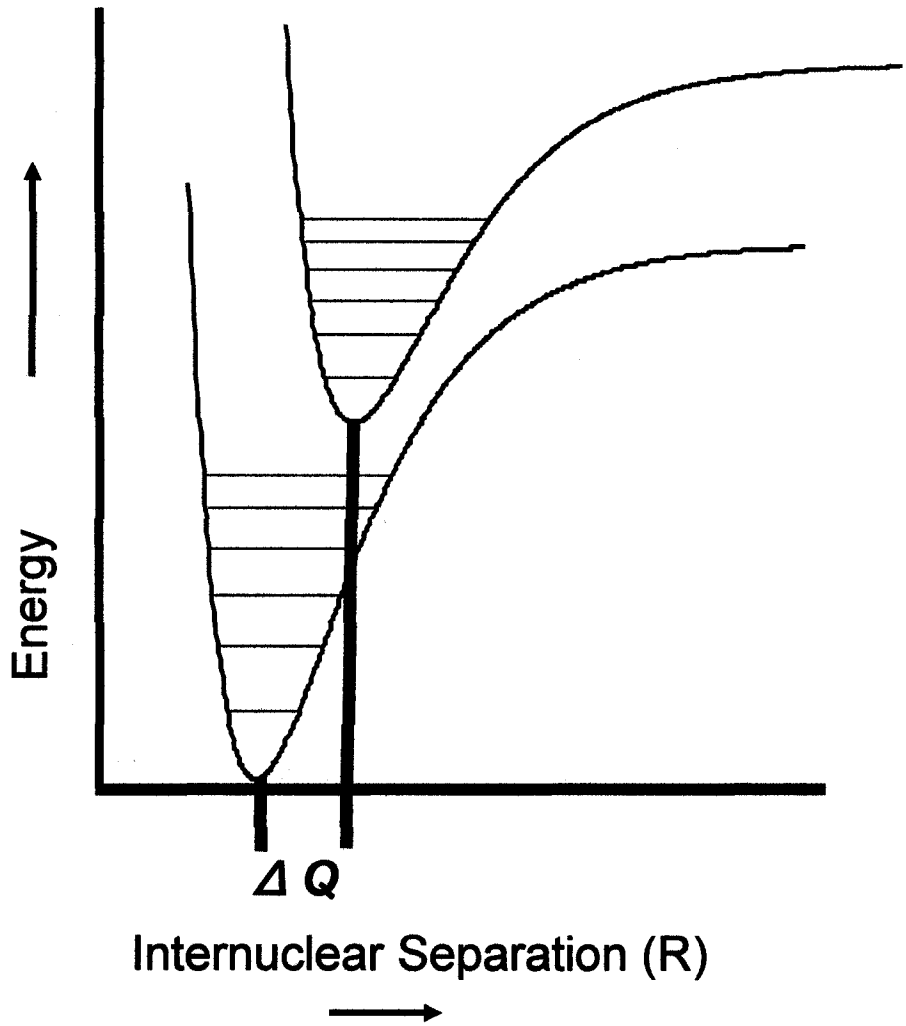

Figure 2.4: Energy Diagram of the ground and excited state. The potential energy of the ground and excited state is shown and the change in normal co-ordinate between the two, ΔQ

Reproduced with permission of the copyright owner. Further reproduction prohibited without permission.

An additional consequence of *A*-term scattering is that overtones and combinations are often observed. Their intensity and the extent of their progressions can be used as an indicator of the ΔQ factor. Their magnitude can give insight into possible differences between the ground and the excited state equilibrium geometries, as well as changes in the lifetimes of excited states.[6]

2.2.2.4 The observed Raman intensities

The best place to begin in the analysis of Raman intensities is to look at the power output for a classical dipole oscillator:

$$I \propto \nu^4 \bullet \mu^2 \tag{2.2.9}$$

where μ is the dipole moment and ν is the frequency of oscillation. The Raman intensity can be similarly expressed with the induced dipole moment expressed in terms of the elements of the polarizability derivative:

$$I \propto N(\nu_\circ \pm \nu_j)^4 \sum_{i,j} \left| \alpha_i \bullet E_j \right|^2 \tag{2.2.10}$$

As is evident, the intensity of a Raman band is a function of a molecule's polarizability derivative.

Experimentally, the transition probability and polarizability derivative tensor are related to a quantity more familiar in optical spectroscopies, the cross section, σ (cm^2):

$$\sigma \propto \left(\frac{\partial \alpha}{\partial Q_j} \right)^2 \tag{2.2.11}$$

Experimentally measured Raman intensity for the *j*th band can then be written in the simplest terms as:

$$I_{RS} = \sigma I_\circ N \tag{2.2.12}$$

Reproduced with permission of the copyright owner. Further reproduction prohibited without permission.

where I_{RS} is the measured intensity for a given volume element, I_o is the exciting intensity, and N is the number density of scatterers.

This describes the scattering of a collection of non-interacting molecules, in a vacuum, off resonance, with signal collection assumed to be over a complete integrated sphere. Neither temperature nor wavelength effects are included. To better predict what is measured in experiment, this intensity relation can be built up to account for additional terms as needed.

For instance, a common expression is the differential cross- section, which gives a measure of the rate of the removal of energy from a light source per unit of solid angle, $d\Omega$. Following the formalism of McCreery[7], this is given as:

$$\beta_j^o = \frac{d\sigma}{d\Omega} \tag{2.2.13}$$

Recall that the power output of an oscillating dipole has ν^4 dependence. This can be incorporated into the differential cross section so as to give a frequency-dependent cross section:

$$\beta_j = \beta_j^o(\tilde{\nu}_\circ - \tilde{\nu}_j)^4 \tag{2.2.14}$$

Present-day spectrometers use photon counting detectors, so an adjustment is made to have the cross section containing units of photons•s^{-1}, instead of Power (W):

$$\beta_j = \beta_j^o \tilde{\nu}_\circ(\tilde{\nu}_\circ - \tilde{\nu}_j)^3 \tag{2.2.15}$$

In addition, the intensity for anti-Stokes (AS) scattering can be related to that of the Stokes. Since AS arise from molecules in excited vibrational energy states, one needs to look at the energy distribution of molecules as governed by the Boltzman distribution. The ratio of anti-Stokes to Stokes intensity is described by the following:

Reproduced with permission of the copyright owner. Further reproduction prohibited without permission.

$$\frac{I_{AS}}{I_S} = \frac{\left(\omega_o + \omega_j\right)^4}{\left(\omega_o - \omega_j\right)^4} \exp(-\Delta E_j / kT) \qquad (2.2.16)$$

In summary the intrinsic intensity of Raman band is related to the properties of polarizability derivative tensor and the wavelength of light used for excitation. Later in the instrumental section, it will be shown how the Raman intensity that is measured is further modified by the experimental condition when recorded, and how ultimately what is measured can be related back to the original inherent molecular cross section.

2.3 Theoretical foundations for SERS

2.3.1 Introduction

The first measurement of "surface enhanced" Raman scattering was in the laboratory of Fleischmann. It was recorded from samples measured on the surface of a roughened electrode and was reported in 1974.[8] The enhancement was prescribed to the rough surface and the increase in surface area compared to a flat electrode. In 1977, two groups independently confirmed the results but refuted the explanation.[9,10] In the wake of these discoveries and the mountain of work that has followed, it is now generally accepted that the SERS effect predominantly is the result of enhanced electromagnetic local fields,[2,11,12] A second type of contribution, that can be provided by charge transfer resonances and other surface effects, are collected under the general term of "chemical effects" or chemical enhancement.

From the beginning SERS was used with the caveat that, "the surface is a rough surface", where rough was envisioned as protrusions that were modeled as semi-

Reproduced with permission of the copyright owner. Further reproduction prohibited without permission.

spheroids.[13-15] This has lead to the somewhat misleading moniker of SERS. The experimental results accumulated over the years have made it clear that SERS is observed on nanostructures. More importantly, it is the localised surface plasmons that are supported by these nanostructures that are the source for the optical enhancements measured.[16-21]

The intrinsic properties of the SERS experiment then can be explained in terms of an electromagnetic enhancing mechanism (EM enhancement). These include; distance dependence, metal selectivity, shape and size dependence, and the role of cavities and interstitial spaces. The SERS signal that is generated from the EM mechanism is proportional to the fourth power of the excitation field. The physical meaning of this mechanism can be appreciated using the most basic and simplest of formalisms, that of "the spherical model" with a single dipolar resonance as illustrated by the cartoon in Figure 2.5. It describes SERS at the surface of a spherical particle with dielectric function $\varepsilon(\omega)$ excited with incident laser line represented by a plane electromagnetic wave $E_i(r,\omega_o)$. Though the sphere is rarely what is encountered in experiment, the beauty of the spherical physical model is that it helps to rationalize many SERS features, and as such, is a useful guide for the experimentalist. The theory was put forth by several researchers in the immediate years following the discovery of SERS.[11,22,23]

Reproduced with permission of the copyright owner. Further reproduction prohibited without permission.

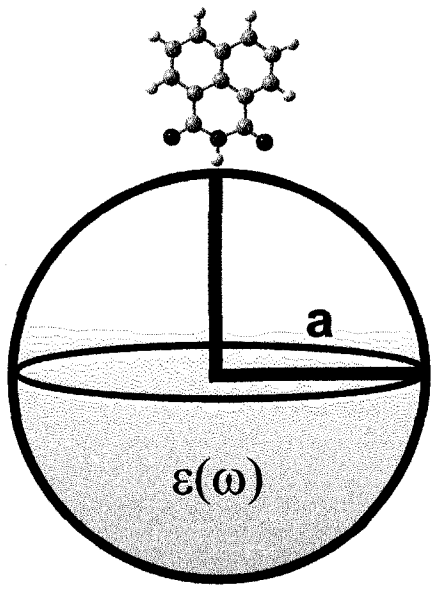

Figure 2.5: Illustration of the Single Sphere model.

2.3.2 Single Particle Model

For a singular spherical particle of radius R, composed of a material characterized by a complex wavelength-dependent dielectric function $\varepsilon(\lambda) = \varepsilon'(\lambda) + i\varepsilon''(\lambda)$. The electric field strength is dependent on the complex dielectric function of the metal, as well as that of the surrounding medium, shown in the following relation:

$$E \propto \frac{\varepsilon(\lambda) - \varepsilon_o(\lambda)}{\varepsilon(\lambda) + 2\varepsilon_o(\lambda)} \tag{2.3.1}$$

where ε and ε_o are the dielectric functions for the metal and the surrounding medium respectively.

From this, a key resonance condition becomes apparent. The large electric fields will occur when the following condition is met (provided that ε'' is negligible):

$$\mathrm{Re}\{\varepsilon(\lambda)\} = -2\varepsilon_o(\lambda) \tag{2.3.2}$$

Reproduced with permission of the copyright owner. Further reproduction prohibited without permission.

This relation determines not only the wavelength dependence of the surface plasmon but also gives an indication as to what metals are of use. The values for the real and imaginary parts of the dielectric function at the peak plasmon resonance for silver and gold, the two most common materials used for SERS substrates, are given in Table 2.2.

Table 2.2: Real and imaginary parts of the dielectric function for silver and gold

Metal	ε'	ε''	Plasmon Resonance (nm)
Silver	-2.029919	0.60192	350
Gold	-2.546544	3.37088	496

The dipole surface plasmon behaves as an emitter, so not only will the molecule experience the enhanced field of the laser, but whatever Raman scattered photon interact with the plasmon will be radiated with a greater intensity. This concept is illustrated in Figure 2.6.

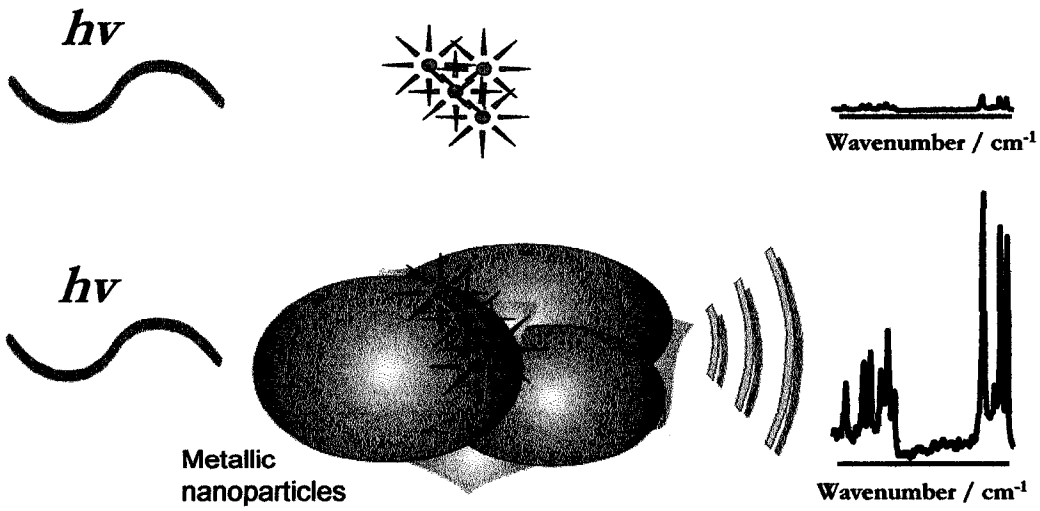

Figure 2.6: Illustration of the surface plasmon behaviour as an amplifier and emitter

Reproduced with permission of the copyright owner. Further reproduction prohibited without permission.

The enhancement factor is as follows:

$$G = \left| \frac{\varepsilon(laser) - \varepsilon_\circ}{\varepsilon(laser) + 2\varepsilon_\circ} \right|^2 \bullet \left| \frac{\varepsilon(Raman) - \varepsilon_\circ}{\varepsilon(Raman) + 2\varepsilon_\circ} \right|^2 \tag{2.3.3}$$

This is often simplified to:

$$EF = G_L^2 G_{RS}^2 \tag{2.3.4}$$

Or neglecting the Raman shift:

$$EF = G^4 \tag{2.3.5}$$

This is the basis for the SERS effect. The key points to illustrate is that regardless of the nanostructure used for the substrate, the enhanced Raman signal is predominately a factor of the local enhanced fields, and as such, any factor that tends to increase these fields will in turn increase the enhanced Raman scattering (or any other optical process for that matter).

These variables include a structure's composition, shape and morphology, as well as, contributions from field interactions (such as dipole-dipole interactions). These field's in-between nanostructures have been uncovered to be a significant factor for the extreme enhancements encountered in many single molecule studies.

There are several general features directly resulting from the EM enhancement that are worth mentioning.

1. It is dependent on nanostructures that can sustain dipolar plasmon resonances.
2. The average enhancements predicted are on the order of 10^3-10^7
3. The strength of the EM enhancement is dependent on the exciting frequency being in tune to a dipolar plasmon resonance of the nanostructure. This could

Reproduced with permission of the copyright owner. Further reproduction prohibited without permission.

be the dipolar mode of an isolated particle or a multimode present in aggregates.

4. Any substrate evoking an EM mechanism will demonstrate a distant dependence. For spheres, this is given by a $\frac{a}{(a+d)^{12}}$ relation where a is the radius of the sphere, and d is the distance from the enhancing surface. When covered with a monolayer at a distance d, the dependence has been found to be $\frac{a}{(a+d)^{10}}$.[24]

2.3.3 Advanced SERS Theories

While the spherical model is usefully for a rudimentary understanding of the phenomena, it is not a realistic description of what is encountered in the laboratory. Experimentally, the highest enhancements are realized with disordered, aggregated substrates such as evaporated metal island films and cast colloids.[25-27] Models have subsequently been developed in an attempt to account for these much more complex systems. Much theoretical work in this regard has been put forth by Stockman[28-30], as well as Shalaev[31,32], and Pendry[33]. From these works a more complex picture of the EM mechanism emerged, one where interparticle interactions become much more important. An example of this would be the extensively used fractal aggregates, or any similar collections of particles close enough to interact strongly as illustrated in Figure 2.7.

Reproduced with permission of the copyright owner. Further reproduction prohibited without permission.

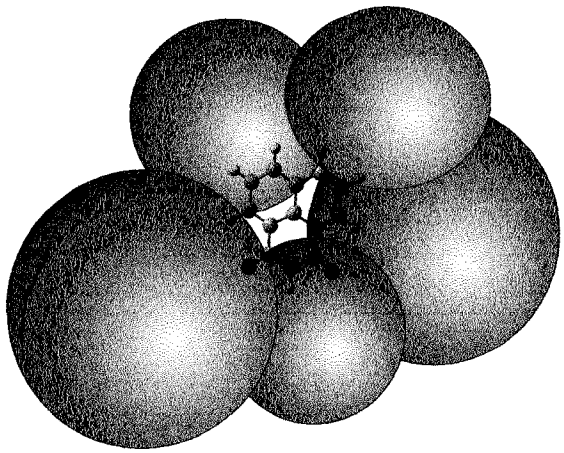

Figure 2.7: Illustration of typical nanoparticle interactions encountered in SERS experiments

Here the dipolar eigenmodes are complex electromagnetic modes of which some can be highly localized. There is a useful analogy between the theory of molecular vibrations and the present development of EM SERS. In the theory of molecular vibrations, the simplest case is the vibration of a diatomic molecule: one harmonic oscillator, one fundamental frequency. Similarly, the spherical nanoparticle sustains one dipolar resonance, a single mode. In polyatomic molecules one has 3N-6 (3N-5 for a linear molecule) normal modes or fundamental vibrational frequencies, some of which are highly localized. These are the characteristic vibrational modes, such as a C-H stretching vibration, that are easily identified in a spectrum. Others modes are highly delocalized and cannot be assigned to any specific functional group within the cluster of atoms. Similarly, a cluster of nanoparticles or small-particle composites and fractal aggregates, can sustain many eigenmodes or normal modes, and some of these dipolar eigenmodes can be highly localized. These highly localized modes are believed to be the origin of the

Reproduced with permission of the copyright owner. Further reproduction prohibited without permission.

areas of extreme enhancement known as "hotspots". Therefore, SERS as we know it seems to arise from highly localized, optically active surface plasmon resonances, which are sustained in metallic nanostructures with complex topologies. Hence, the incredible enhanced fields needed for single molecule detection can be the result of a purely electromagnetic phenomenon (apart from any chemically related resonance). This distribution of dipolar eigenmodes can impact the SERS experiment, as has been demonstrated by Etchegoin *et al.* in a series of papers.[34-38] As well, this influence can be seen in the results obtained from single molecules experiments to be presented here.

References

(1) Wilson, E. B. J.; Decius, J. C.; Cross, P. C. *Molecular Vibrations*; McGraw-Hill 1955.

(2) Aroca, R. *Surface - Enhanced Vibrational Spectroscopy*; John Wiley & Sons, 2006.

(3) Raman, C. V.; Krishnan, R. K. *Nature (London)* **1928**, *121*, 501-502.

(4) Tang, J.; Albrecht, A. C. In *Raman Spectroscopy*; Szymanski, H. A., Ed.; Plenum Press: New York, 1970; Vol. 2.

(5) Shorygin, P. P.; Krushinskij, L. L. *Journal of Raman Spectroscopy* **1997**, *28*, 383-388.

(6) Morris, D. E.; Woodruff, W. H. *Journal of Physical Chemistry*. **1985**, *89*, 5795-8.

(7) McCreery, R. L. *Raman Spectroscopy for Chemical Analysis*; John Wiley & Sons Inc: New York, 2000.

(8) Fleischmann, M.; Hendra, P. J.; McQuillan, A. J. *Chemical Physics Letters* **1974**, *26*, 163-6.

Reproduced with permission of the copyright owner. Further reproduction prohibited without permission.

(9) Jeanmaire, D. L.; Van Duyne, R. P. *Journal of Electroanalytical Chemistry and Interfacial Electrochemistry* **1977**, *84*, 1-20.

(10) Albrecht, M. G.; Creighton, J. A. *Journal of the American Chemical Society* **1977**, *99*, 5215-17.

(11) Moskovits, M. *Reviews in Modern Physics* **1985**, *57*, 783.

(12) Campion, A.; Kambhampati, P. *Chemical Society Reviews* **1998**, *27*, 241.

(13) Moskovits, M. *Journal of Chemical Physics* **1978**, *69*, 4159-61.

(14) Albrecht, M. G.; Evans, J. F.; Creighton, J. A. *Surface Science* **1978**, *75*, L777-L780.

(15) Hexter, R. M. *Solid State Communications* **1979**, *32*, 55-7.

(16) Kim, K.; Lee, H. S.; Kim, N. H. *Analytical and Bioanalytical Chemistry* **2007**, *388*, 81-88.

(17) Lu, Y.; Liu, G. L.; Kim, J.; Mejia, Y. X.; Lee, L. P. *Nano Letters* **2005**, *5*, 119-124.

(18) Kneipp, K.; Kneipp, H.; Dasari, R. R.; Feld, M. S. *Indian Journal of Physics, B* **2003**, *77B*, 39-47.

(19) Hildebrandt, P.; Stockburger, M. *Journal of Physical Chemistry* **1984**, *88*, 5935-44.

(20) Kelly, K. L.; Coronado, E.; Zhao, L. L.; Schatz, G. C. *Journal of Physical Chemistry B* **2003**, *107*, 668-677.

(21) Addison, C. J.; Brolo, A. G. *Langmuir* **2006**, *22*, 8696-8702.

(22) Wang, D. S.; Chew, H.; Kerker, M. *Applied Optics* **1980**, *19*, 2256-2257.

Reproduced with permission of the copyright owner. Further reproduction prohibited without permission.

(23) Schatz, G. C.; Van Duyne, R. P. In *Handbook of Vibrational Spectroscopy*; Chalmers, J. M., Griffiths, P. R., Eds.; John Wiley & Sons, Ltd, 2002; Vol. Volume 1.

(24) Kovacs, G. J.; Loutfy, R. O.; Vincett, P. S.; Jennings, C.; Aroca, R. *Langmuir* **1986**, *2*, 689-694.

(25) Corni, S.; Tomasi, J. *Journal of Chemical Physics* **2002**, *116*, 1156-1164.

(26) Lemma, T.; Aroca, R. F. *Journal of Raman Spectroscopy* **2002**, *33*, 197-201.

(27) Moskovits, M.; Tay, L.-L.; Yang, J.; Haslett, T. *Topics in Applied Physics* **2002**, *82*, 215-226.

(28) Stockman, M. I. *Physical Review E: Statistical Physics, Plasmas, Fluids, and Related Interdisciplinary Topics* **1997**, *56*, 6494-6507.

(29) Stockman, M. I. *Physical Review Letters* **1997**, *79*, 4562-4565.

(30) Stockman, M. I.; Pandey, L. N.; Muratov, L. S.; George, T. F. *Physical Review B: Condensed Matter* **1995**, *51*, 185-95.

(31) Markel, V. A.; Shalaev, V. M.; Stechel, E. B.; Kim, W.; Armstrong, R. L. *Physical Review B: Condensed Matter* **1996**, *53*, 2425-2436.

(32) Markel, V. A.; Shalaev, V. M.; Zhang, P.; Huynh, W.; Tay, L.; Haslett, T. L.; Moskovits, M. *Physical Review B: Condensed Matter and Materials Physics* **1999**, *59*, 10903-10909.

(33) Pendry, J. B.; Garcia-Vidal, F. J. *Physical Review Letters* **1996**, *77*, 1163-1166.

(34) Le Ru, E. C.; Etchegoin, P. G. *Chemical Physics Letters* **2006**, *423*, 63-66.

(35) Maher, R. C.; Etchegoin, P. G.; Le Ru, E. C.; Cohen, L. F. *Journal of Physical Chemistry B* **2006**, *110*, 11757-11760.

Reproduced with permission of the copyright owner. Further reproduction prohibited without permission.

(36) Maher, R. C.; Cohen, L. F.; Le Ru, E. C.; Etchegoin, P. G. *Journal of Physical Chemistry B* **2006**, *110*, 19469-19478.

(37) Le Rue, E. C.; Etchegoin, P. G.; Meyer, M. *Journal of Chemical Physics* **2006**, *125*, 204701-1 204701-13.

(38) Etchegoin, P.; Cohen, L. F.; Hartigan, H.; Brown, R. G. C.; Milton, M. J. T.; Gallop, J. C. *Journal of Chemical Physics* **2003**, *119*, 5281-5289.

Reproduced with permission of the copyright owner. Further reproduction prohibited without permission.

CHAPTER 3

INSTRUMENTATION

Reproduced with permission of the copyright owner. Further reproduction prohibited without permission.

3.1 Introduction

In this chapter, the various tools of characterization used for the work presented in this thesis will be discussed. As the focus of this thesis was SERS spectroscopy, Raman instrumentation is covered in depth. That is followed with briefer overviews of the other instrumental and experimental methods utilized.

3.2 Raman Instrumentation

In 1928, the "spectrometer" used for the first recording of the inelastic scattering of photons by a molecule, used filtered sunlight as the excitation source, a telescopic lens for the focusing optics, a coloured filter to block all light but the inelastically scattered photons (the dispersive element) and Sir Raman's eyes as the detector.[1]

Instrumentation has made amazing advancements since these humble beginnings.[1-5] The old, massive, room-filling equipment of double and triple monochromometers, diffraction gratings and photomultipliers has been superseded by compact, desktop-sized manufactured instruments. In the past decade, advancements in optical components and detector technology have greatly increased the sensitivity of Raman spectrometers. In addition, the coupling of spectrometers to microscopes has given the experimenter the ability to achieve high spatial resolution of the probed sample. These developments have led to an explosion in the field of Raman Microscopy, or Micro-Raman. In particular, Micro-Raman has been extremely instrumental in the development and understanding of the SERS phenomena and as will be shown, been crucial in the application of SERS to the detection of a single molecule.[6-8]

Essential to every Raman experiment is the performance of the spectrometer and the optical components that comprise that system. This is even more so in the case of

Reproduced with permission of the copyright owner. Further reproduction prohibited without permission.

enhanced Raman experiments where the signals dependence on the nature of the light delivery and collection is closely intertwined. It is necessary then, to outline the system used for my studies of SERS, and to highlight those aspects that are of key importance. Contained in Figure 3.1, is an illustration for a typical dispersive Raman spectrometer. The optical components of the system can be divided into those that belong to the following areas; optics for light delivery, light dispersion and finally detection.

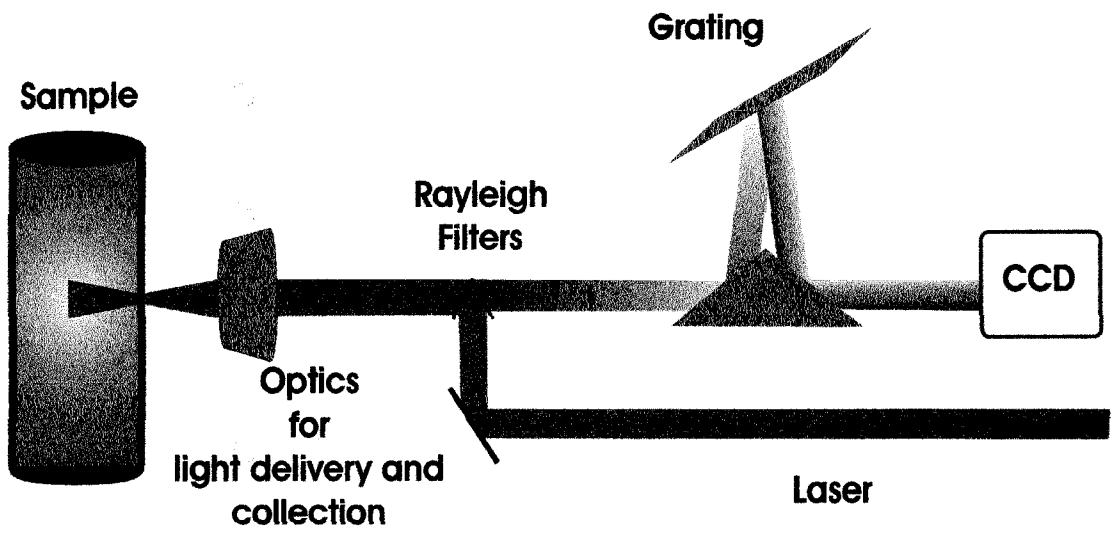

Figure 3.1: Illustration of the key components of a Raman spectrometer.

Raman spectroscopy is extremely flexible in terms of instrumentation. There are many possible configurations allowing one to tailor the instrumentation to a host of different applications. For example, systems that use a triple monochromometer for the separation of the Raman scattering from that of the Rayleigh, allow for the measurement of very low frequency Raman bands, but the throughput is extremely low, requiring the use of large laser powers. Enhanced Raman experiments, in contrast, require the use of relatively low energy densities for excitation due to the extreme conditions experienced in

Reproduced with permission of the copyright owner. Further reproduction prohibited without permission.

SERS (high local fields, reactive surfaces) which may lead to photodegradation of the molecular system under investigation. In particular, studies of single molecules under resonant conditions require an extremely small photon flux to avoid damage, presenting an additional challenge considering the already marginal signal to noise levels involved. This necessitates that the systems used for SERS studies incorporate optics and detectors that maximize both sensitivity and throughput.

3.2.1.1 Spectrometers

The spectrometers used for the work contained within this thesis were bench top systems manufactured by Renishaw (Renishaw, UK.). These are the "InVia" and the "System 2000", shown in Figure 3.2. A photograph of the interior is shown in Figure 3.3.

There are several key features that make these systems ideal for SERS studies. Primarily, they are Micro-Raman systems, which, with the proper choice of objectives, allows for high spatial resolution and control of probe volumes, both essential for single molecule studies. Secondly, these systems have optical configurations that maximize throughput and are equipped with high sensitivity detectors.

A proper interoperation of a recorded spectrum is impingent on a thorough, detailed understanding of all the optical elements. These key components will be discussed in the next section.

Reproduced with permission of the copyright owner. Further reproduction prohibited without permission.

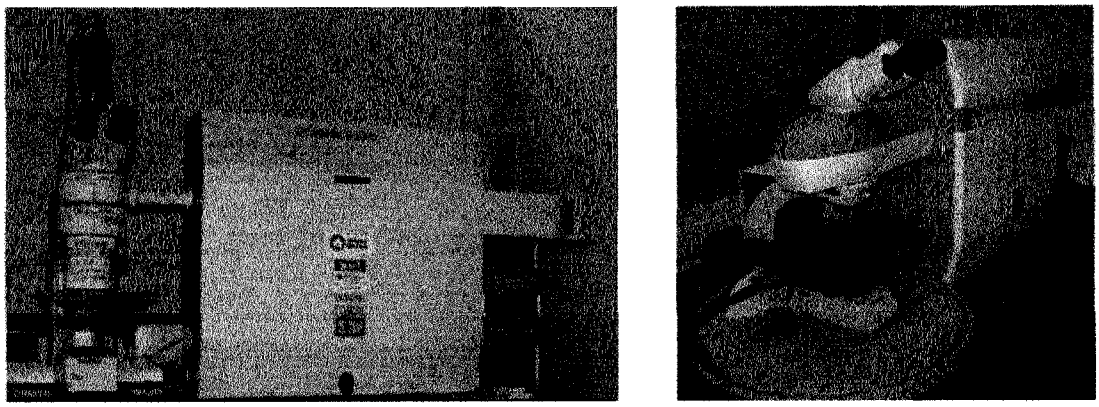

Figure 3.2: Photographs of Raman instruments. Ramanscope 2000 (Left) and the InVia (right) (Renishaw, UK)

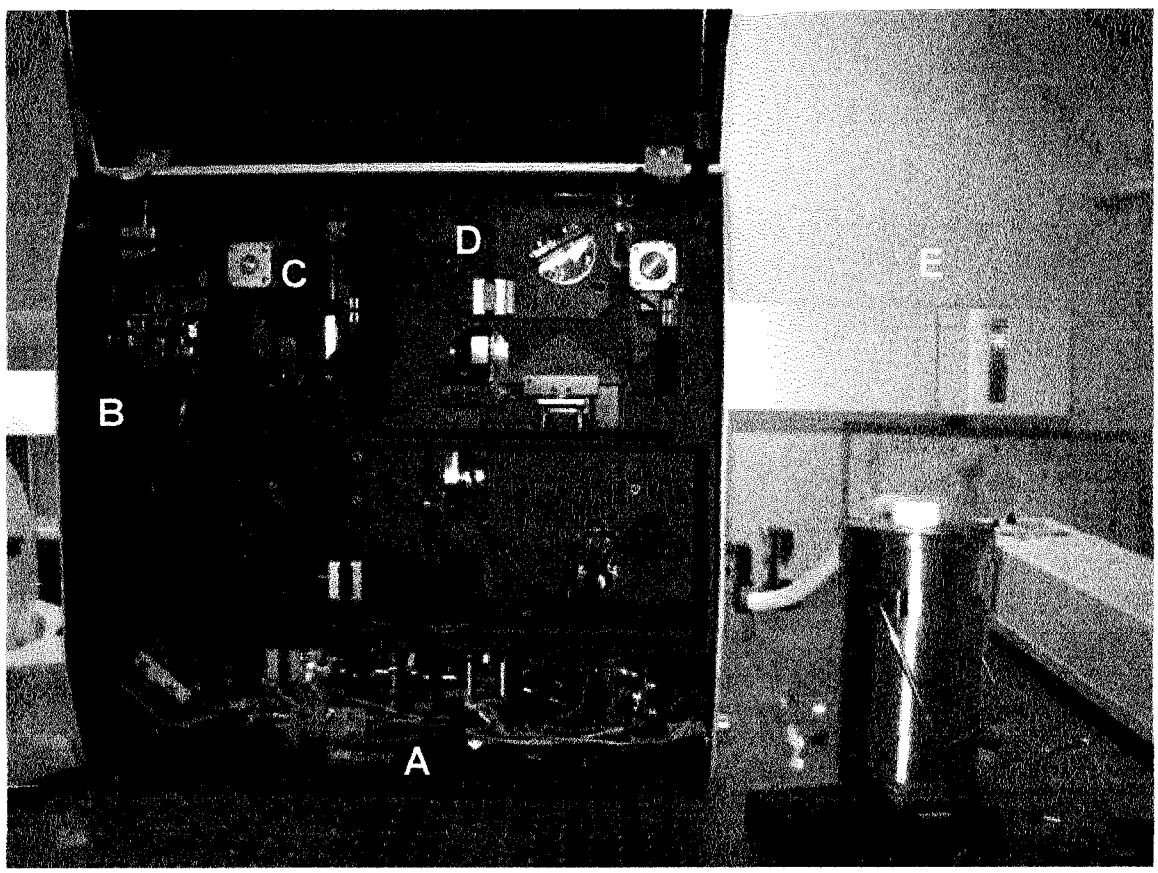

Figure 3.3: Inside a Raman Spectrometer.

A) Laser entrance and beam expanding optics. B) Location of the Rayleigh rejection filters. C) Pre-Slit lens and slits. D) Grating. E) CCD detector

Reproduced with permission of the copyright owner. Further reproduction prohibited without permission.

3.2.1.2 Excitation Lasers

The excitation lines used in this thesis are collected in Table 3.1.

Table 3.1: Excitation Lasers

Laser Type	Wavelength (nm)	Output Power (mW)
HeCd (Coherent)	442/325	20
Tunable Ar^+ (Lexar)	488 , 514	10 - 100
HeNe	633	18
Solid State Diode	785	19

Each line had at the time of use, an appropriate plasma-rejection line filter in place. The system's entrance beam path allows the laser light to pass through a set of neutral density (ND) filters which allow a degree of control over the laser light intensity at the sample used for the Raman experiment. The available attenuations begin with 50%, 10%, 5% and 1 % with a value down to 0.00025% possible. The light path is directed through beam expander optics which aids in keeping uniformity of the beam profile (Figure 3.3(A))

3.2.1.3 Rayleigh Blocking Filters

The laser beam is directed towards the microscope by the use of a special filter combination positioned at position B in Figure 3.3, and are shown in Figure 3.4. These filters provide two functions. First, in their capacity as beam splitter, they direct the light onto the optics for the coupled microscope. Secondly, and most importantly, they are filters for the Rayleigh scattered light that returns to the spectrometer in addition to the Raman scattered photons. Rayleigh scattering is much more intense than that of Raman, hence it is crucial to remove this light from the beam path so as not to obscure the much

Reproduced with permission of the copyright owner. Further reproduction prohibited without permission.

weaker Raman signal. This is accomplished in these instruments through the use of filters that block the unwanted light but allow the Raman photons to pass with minimal attenuation. There are two types of filters used in these experiments that accomplish this. They are edge filters and holographic notch filters (HNF). Edge filters are dielectric films and essentially block all light below a certain wavelength. HNF's are multilayered films that have the ability to block a small region of the spectrum by reflecting a narrow band of wavelengths, while all other wavelengths are transmitted with high efficiency.

There are two main advantages to the use of HNF. Both stokes and anti-stokes can be measured and HNF's have a much smoother transmission profile as evidenced by the characteristic transmission profiles in Figure 3.5. In either case, each filter has a cut-off that limits the instruments ability to measure low wavenumber frequencies. Two filters are used to remove as much Rayleigh scattering as possible. Each filter has an Optical Density of ~ 5, with a transmission greater than 80%. Because of the nature of these filters, each laser line requires its own set and hence will have a different cut-off. The InVia system is equipped with a motorized turret that can rotate to the needed filters to match the excitation line being used. This allows Raman measurements to be taken from the same spot with excitation from different laser lines without any optical realignment.

Reproduced with permission of the copyright owner. Further reproduction prohibited without permission.

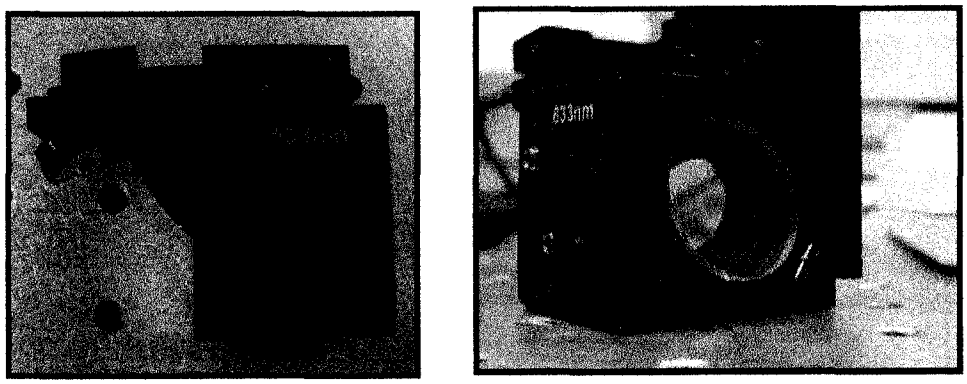

Figure 3.4: Holographic Notch Filter

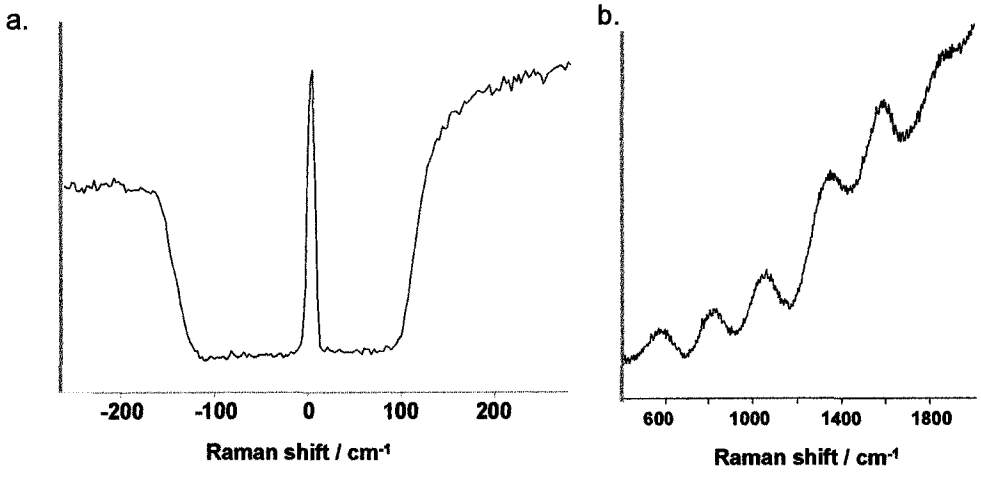

Figure 3.5: Characteristic Profiles of HNF and edge filter. The spectrum to the left (a) shows the typical cut-off for a HNF. The spectrum to the right illustrates the ripple background encountered with edge filters.

In the studies presented here HNF's were used for Raman spectra collected with 488, 514, 633, 785 nm excitations, while edge filters were used for 325 and 442 nm excitation, unless otherwise noted.

Reproduced with permission of the copyright owner. Further reproduction prohibited without permission.

3.2.1.4 Slits and Gratings

The scattered light is focused through a set of slits set to 50 μm for all measurements unless otherwise noted. The light is then focused onto a dispersive grating. The gratings used in these systems are holographic-ruled. There are several different gratings employed here depending on the excitation line used; these are collected in Table 3.2. The main feature of concern is the groove density, which in turn determines the effective spectral resolution. The approximate resolution for each laser/grating (determined from the measurement of the isotopic splitting in CCl_4) is also shown in Table 3.2.

Table 3.2: Spectral Resolution for Grating – Laser combinations

Laser Line *nm*	**Grating** *grooves/mm*	**Resolution** cm^{-1} **(50 µm silt)**
325	3600	3
442	2400	2
488	1800	2
514	1800	3
633	1800	2
785	1200	3

3.2.1.5 Detector

Finally, the spatially-dispersed light is focused onto a detector, in this case a CCD (Charge Coupled Device). The type of CCD used in these instruments is a UV sensitized, deep depleted, detector. Deep depletion is used for additional sensitivity in the near IR region; while the special coating for UV, allows its use at 325 nm. The CCD is in an array format with 578 X 385 pixels, and each pixel having dimensions of 22 µm x 22 µm. The peak Q.E. of the CCD is ~ 45%, but is wavelength dependent, as seen in Figure 3.5.

Reproduced with permission of the copyright owner. Further reproduction prohibited without permission.

The CCD used in these systems are thermo-electrically cooled (Peltier) to -70°C. The low operating temperature ensures very low thermal dark current counts with a recorded dark current rate of ~ 0.01 e^- $pixel^{-1}sec^{-1}$. This combination of sensitivity and low background is very important for SM experiments, as the measured S/N is so low.

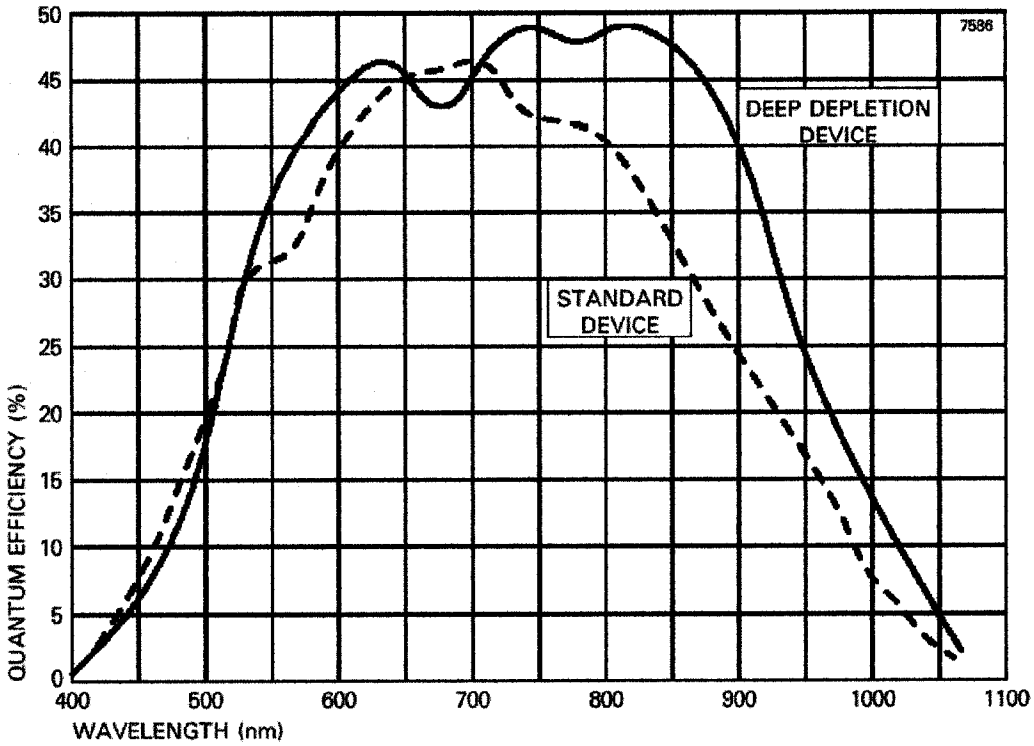

Figure 3.6: Response curve for a CCD detector. The CCD used in the both Raman spectrometers are deep depleted. Reprinted courtesy of Renishaw U.K.

3.2.2 UV Raman Spectrometer

Because of the nature of UV light, when using the 325 nm excitation for Raman spectroscopy, additional modifications to the optical configuration must be made.

Reproduced with permission of the copyright owner. Further reproduction prohibited without permission.

Primarily, the three focusing lenses must be exchanged for those that work in the UV, (a change of glass lenses to those made of quartz). As well, objectives that are optimized for UV light must be used.

3.2.3 Microscopy

The most crucial components for a Raman system are the optics for light delivery and collection. In micro-Raman systems this is accomplished through the coupling of the spectrometer to a microscope. In the 180° backscattering collection geometry used in micro-Raman, the objective is the important element as it defines both the excitation and probe volumes. The defining features of an objective are its Numerical Aperture (NA) value and its magnification. These in turn determine the spot size (diameter) of the exciting laser as given by the following relation:

$$spotsize = \frac{.61 * \lambda}{NA} \tag{3.6}$$

The laser spot size is a crucial parameter for single molecule SERS studies since the experimental procedure is based on this spatial resolution. The NA is also an important value as it is a measure of an objective's light collecting efficiency, where the higher the NA the better. In the micro-Raman there are two configurations that were used. Almost all measurements were taken in arrangement shown in Figure 3.7a. When a longer working distance was needed or a larger probe volume was desired, the configuration in Figure 3.7b was used.

Reproduced with permission of the copyright owner. Further reproduction prohibited without permission.

a.

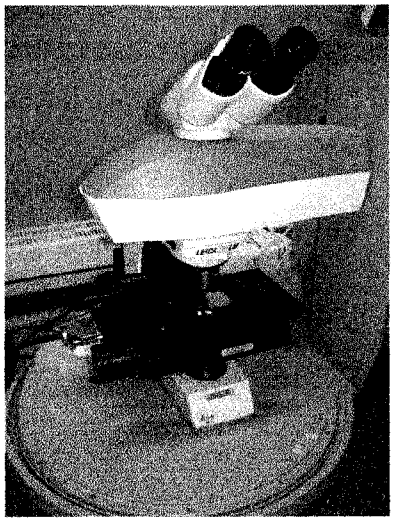

b.

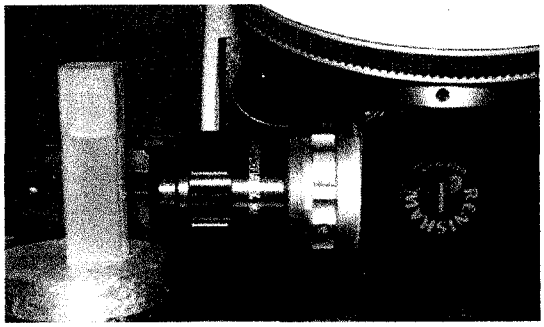

Figure 3.7: Micro and Macro Sampling Configurations

3.2.3.1 Objectives

In Table 3.3 the various objectives used in this study are given with their approximate measured laser spot size and NA. The NA is a key parameter which gives a measure of the light gathering ability for an objective.

Table 3.3: List of Objectives

Objective	NA	Spot Size μm^2
5 X	0.12	50
20 X	0.40	20
50 X	0.75	1
50 X L	0.55	1
100 X	0.90	< 1
f/15	0.34	30
40 X UV	0.32	5

Reproduced with permission of the copyright owner. Further reproduction prohibited without permission.

3.2.3.2 Energy Density

As has been mentioned before, laser power and energy density are always a concern. Generally, a laser's power is measured in [W] and its energy density (ED), is reported as [W/cm^2] The CCD though, measures photons/sec (electrons/s which is related to photons/s by a proportionality factor). In Table 3.4, the energy density and laser powers for a few lines are given in several equivalent units of measurement.

Table 3.4: Laser powers and energy density in equivalent units of measurement.

	Spot size		Energy Density		
λ	**Diameter**	**Power**			
nm	*μm*	*mW*	W/cm^2	W/m^2	$Photon\ s^{-1}\ \mu m^{-1}$
442	1	2	**2.55E+05**	**2.55E+09**	**4.45E+15**
514	1	1	**1.27E+05**	**1.27E+09**	**2.58E+15**
514	1	0.1	**1.27E+04**	**1.27E+08**	**2.58E+14**
514	1	0.0001	**1.27E+01**	**1.27E+05**	**2.58E+11**
633	1	3	**3.82E+05**	**3.82E+09**	**9.55E+15**
785	1	2	**2.55E+05**	**2.55E+09**	**7.90E+15**

3.2.4 Calibration and Instrument Correction

Though it may not be the most tantalizing of subjects, calibration and instrument response are essential elements. This part will be divided into two sections. The first will deal with the calibration of the instrument for frequency accuracy and range and the second will deal with steps taken for relative intensity corrections, which were needed for a several SERS experiments to be presented in Chapter 5.

Reproduced with permission of the copyright owner. Further reproduction prohibited without permission.

3.2.4.1 Calibration

Initial calibration of each instrument is performed by measurement comparisons to the emission spectrum of a calibrated neon light source. Once this is done, only small adjustments are needed on a day to day basis. Frequency accuracy is accomplished by comparison to a standard material whose Raman spectrum is well known, usually the 520 cm^{-1} band of silicon. Occasionally, other calibration checks are required; in this case materials with well resolved bands in the low and high wavenumber region are used. There are many materials that meet these requirements. In accordance with the National Institute of Standards & Technology (NIST), several materials were used to regularly confirm the spectrometers accuracy. These include the before-mentioned Si wafer (for frequency), Diamond (for frequency), Cyclohexane (for system response and frequency), and elemental Sulfur (S_8) (for calibration and system response for the low wavenumber region), as well as CCl_4 to test for polarization dependences.

Reproduced with permission of the copyright owner. Further reproduction prohibited without permission.

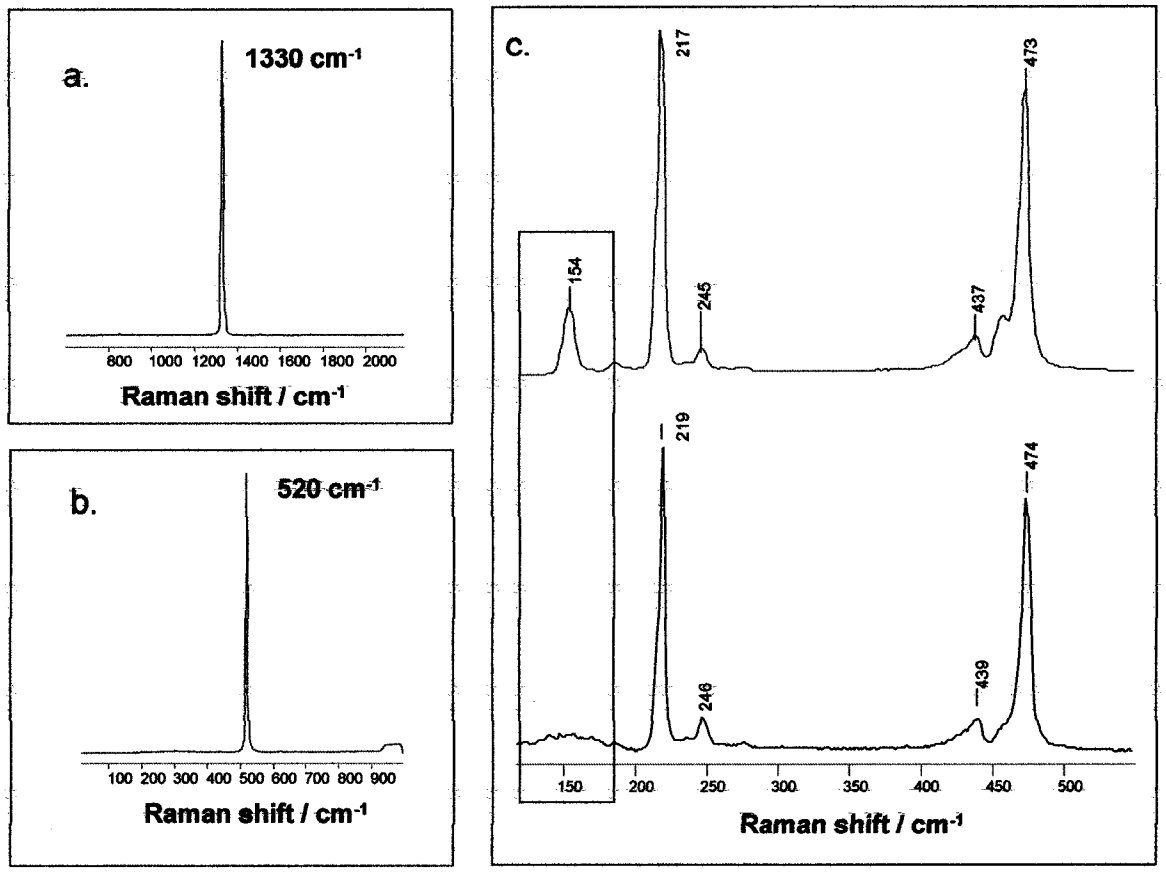

Figure 3.8: Raman Calibration References. a. Diamond. b. Si wafer. c. Elemental sulphur (S_8). The highlighted region shows the low wave number cut-off for 785 nm (top) and 514.5 nm (bottom) with due to their respective HNF.

3.2.4.2 System Response & Instrument Correction

Typically, the main goal in a Raman measurement is to attain the characteristic spectrum and one is generally concerned only with peak frequencies, with little regard for the relative intensities of the bands within a spectrum. When knowledge of the relative intensities is needed, the Raman experiment takes on an additional level of difficulty. There are many reasons to look at relative intensities, particularly for SERS studies as will be shown in later chapters. One possibility is to see how the molecular system

Reproduced with permission of the copyright owner. Further reproduction prohibited without permission.

responds to different excitation energies, by comparing spectra taken at various excitation lines. Here, the main challenges will be outlined for when relative intensity information is required.

The main difficulty is that the optical elements each have a different response function to the wavelength of light. The CCD has a frequency dependence that has a higher efficiency for the blue/green part of the spectrum over that of red with a steep drop off at ~ 1000 nm, corresponding to the CH region for a spectrum taken with the 785 nm excitation. As well, each grating has an efficiency that is wavelength dependent. To correct for these factors, the response of the instrument for a given configuration can be recorded. A general approach is to use a white light source (blackbody radiator) with a known intensity vs. wavelength relation. A spectrum is recorded and compared to the expected. A correction term can then be generated to be applied to the measured spectra.

White light sources have a disadvantage in that they can be difficult and cumbersome to use. Recently another type of standard source has emerged, that of luminescent standards. These materials have known luminescent intensity vs. wavelength curves for a given excitation and can be either a solution of fluorescent chromophores or solids such as doped glass.[9] The latter is the form that has found favour from NIST and is from what their issued standards for Raman intensity calibrations are constructed. These materials are glass, doped with rare earth elements. They have extremely reproducible and well-behaved luminescence outputs. As well they offer several advantages over that of the white light sources. For instance, they can be treated just as the samples would with the same optical configuration without any additional modifications. The standard then can be measured with the same optical geometry as would a sample.

Reproduced with permission of the copyright owner. Further reproduction prohibited without permission.

For some of the experiments to be presented here, it was necessary to have an accurate understanding of how the relative intensities of a SERS spectrum changed as a function of the excitation line used (see Chapter 5). The reference materials used to calibrate for relative intensity were the NIST Standard Reference Material® 2242 for 488/514.5 nm excitations and NIST Standard Reference Material® 2241 for 785 nm excitation.[9-12]

The reference material was placed in the same optical geometry as the sample, under the same systems configuration (grating, filters, objective) and its luminescence curve was recorded. The instrument response correction (IRC) was then generated with the following:

$$IRC = \frac{Certified}{Measured} \tag{3.7}$$

This generates an IRC term specific to that configuration by which all subsequent measured spectra are multiplied by for correction.

The need for such a correction can be seen in Figure 3.9, where the uncorrected Raman spectrum is presented for several different excitation lines for the liquid Cyclohexane.

Reproduced with permission of the copyright owner. Further reproduction prohibited without permission.

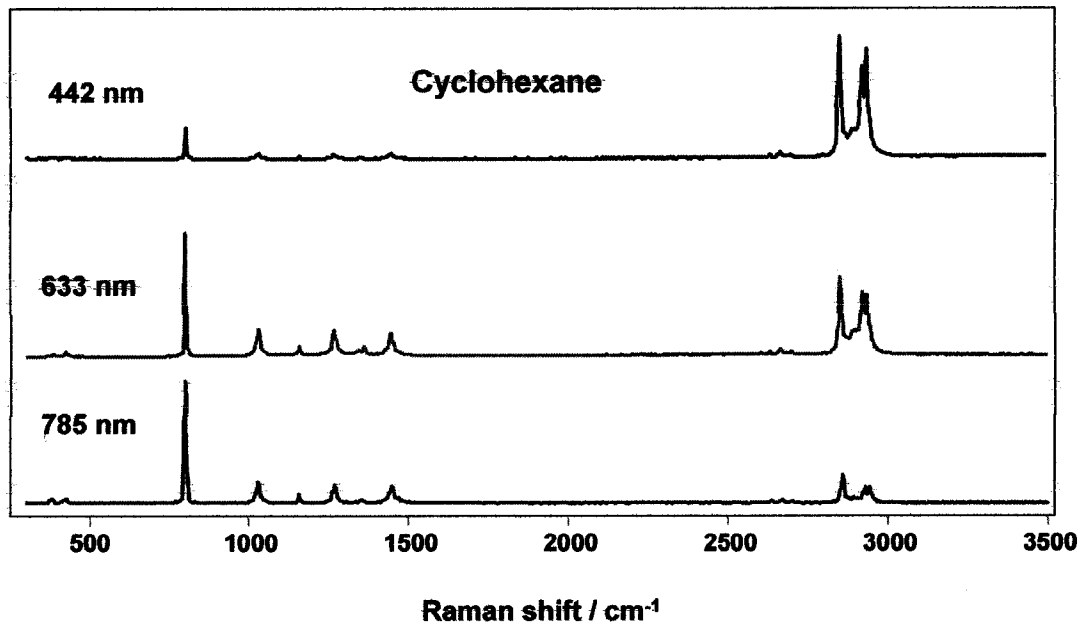

Figure 3.9: Uncorrected Raman Spectra of Cyclohexane

As can be seen going from blue to red excitation, the relative intensity of the CH region to the lower region is dramatic. This is primarily the result of the CCD response function as well as that of the grating. In Figure 10, the known luminescence profile (generated from a certified polynomial provided by NIST), the measured luminescence and the resulting correction file for SRM® 2241 785 are presented. In addition, the cyclohexane spectrum is shown with the instrument response correction applied. With the IRC, a direct comparison between different excitation lines can be made.

Reproduced with permission of the copyright owner. Further reproduction prohibited without permission.

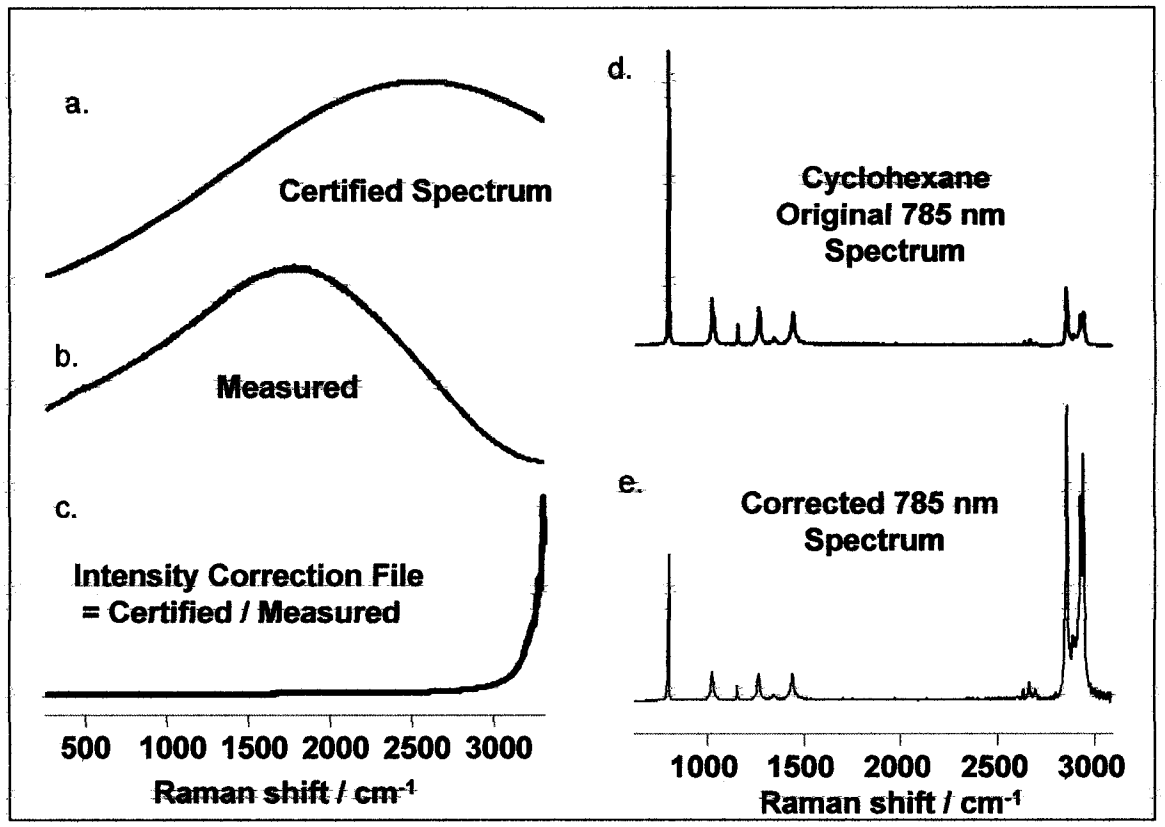

Figure 3.10 : Intensity Correction for 785 nm using NIST SRM 2182.

Reproduced with permission of the copyright owner. Further reproduction prohibited without permission.

3.3 Thin Film Fabrication by Vacuum deposition

Metal nanostructures can be created by evaporating a metal under vacuum conditions. This method is known as physical vapour deposition or thermal evaporation. The key point is that a solid is vaporized and passed onto a substrate. In the set up used for this thesis this was accomplished by the passing of a high current through a tungsten boat that held the metal, with the resulting high temperatures causesing the vaporization of the metal. The metal vapour condenses onto a substrate which is suspended above and under the proper conditions, can coalesce to form nanostructures. The evaporation must be done under high vacuum conditions so to remove contaminates as well as to reduce collision rates between the source atom and impurities, resulting in uniform arrival rates to the sample. The shape and morphology of the resulting nanoparticles can be controlled by changing the parameters of the evaporation. These include: rate of deposition, amount of material deposited (mass thickness) and the temperature of substrate both during the evaporation and after. Each is discussed in turn below. [13-16]

Rate of deposition: The rate of deposition is a measure of the metal atom flux. In the system used here this is controlled by the amount of current passed through the boat. Generally for the island films created in these studies, the rate of evaporation was held between 0.3 and 0.6 Å/s.

Mass Thickness: This is a measure of the amount of metal deposited. The mass thickness is measured as if all the metal was deposited as a solid block. It is monitored during the deposition with a quartz crystal oscillator. The mass thicknesses used for the island films used in the work were between 5-10 nm. At these deposition amounts, particles with features between 20 and 100 nm are formed.

Reproduced with permission of the copyright owner. Further reproduction prohibited without permission.

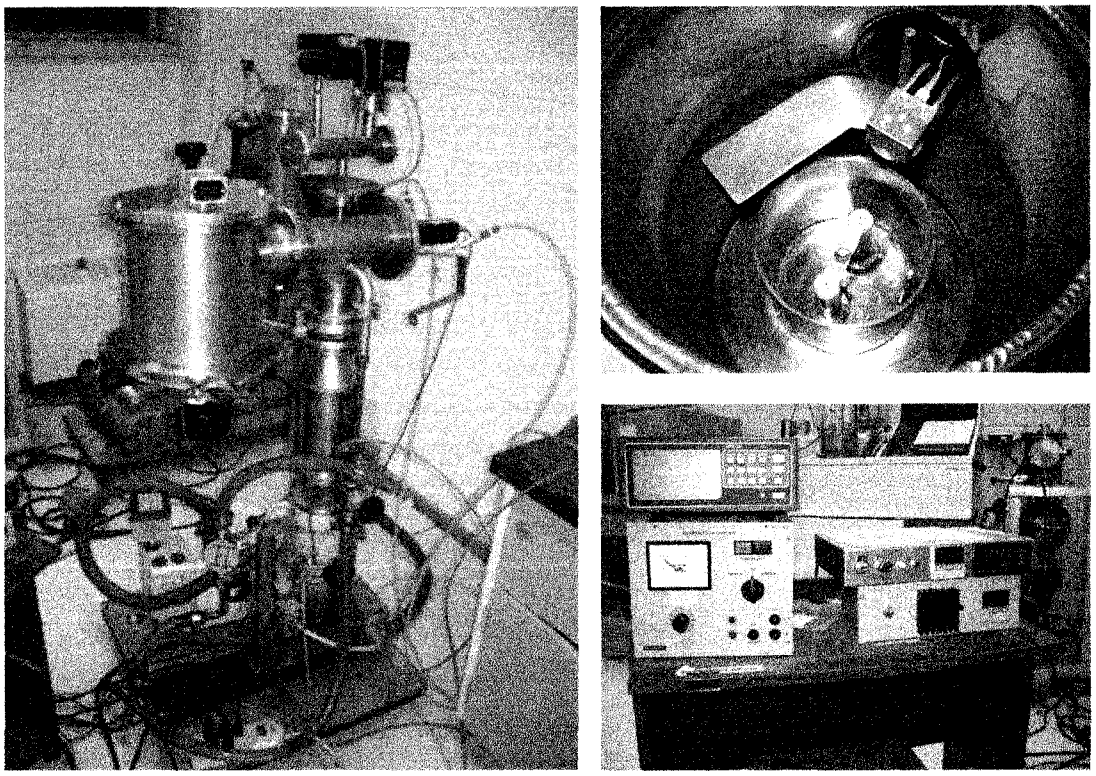

Figure 3.11: Metal Evaporation System. Photographs of the evaporation system used for this thesis. The full system is shown in the left image. The sample chamber with source and detector (top Right) and the controls and monitors (bottom right) are also shown

The evaporation system used in this work is shown in Figure 3.11, with the components of the system as described below.

1) Vacuum System

The entire evaporation system must be held under vacuum, with a pressure below 10^{-6} Torr. This is accomplished with a two-stage vacuum system. Initial vacuum conditions are achieved with a BOC-Edwards rotary vacuum pump, which lowers the pressure to ~ 10^{-2} Torr. After this pressure is achieved, an oil diffusion pump is used to lower the pressure to the needed sub 10^{-6} Torr levels.

Reproduced with permission of the copyright owner. Further reproduction prohibited without permission.

2) Deposition Chamber

The deposition chamber contains the evaporation source, the substrate holder/heating element and the mass thickness/ rate sensor. As well, the chamber contains the shield that either blocks or allows deposition on the substrate.

3) Evaporation Source

The holder of the metal solid is referred to as the "boat". These boats are made of tungsten and the particular design of the ones used here is known as "dimpled" boat. The evaporation control is through the use of a Balzers BSV 080 glow discharge evaporation system.

4) Substrate holder and Heater

The substrates (glass slides) are affixed to a heating element whose temperature can be controlled. The substrate is positioned to be a set distance above the source.

5) Sensors for pressure and mass thickness.

There are 2 pressure sensors used in this system, a Pirani gauge to monitor pressures between atmosphere and 10^{-2} Torr, and a Penning ionization gauge to monitor the vacuum pressure below 10^{-2} Torr.

Mass thickness and deposition rates were monitored with an XTC Inficon quartz crystal oscillator.

3.4 Atomic Force Microscopy

Atomic Force Microscopy (AFM) is part of a larger family of surface characterization techniques collectively known as Scanning Probe Microscopy (SPM). SPM is a collection of methods for mapping forces on the nanometric scale. All SPM methods work upon a similar basic principle. A probe is scanned across the surface of the

Reproduced with permission of the copyright owner. Further reproduction prohibited without permission.

sample, (or as is the case for this system, the tip is stationary and the sample is moved) and the resulting interaction forces are recorded to create a data correlation between response and position. These forces include, but are certainly not limited to, friction, magnetism, and chemical. In almost all cases, a flexible cantilever extends from a rigid substrate to which a tip or probe, which will respond to the force to be measured, is attached. Small perturbations as a result of interactions between the sample and probe are monitored by recorded the change in deflection of a laser that is reflected off the tip.

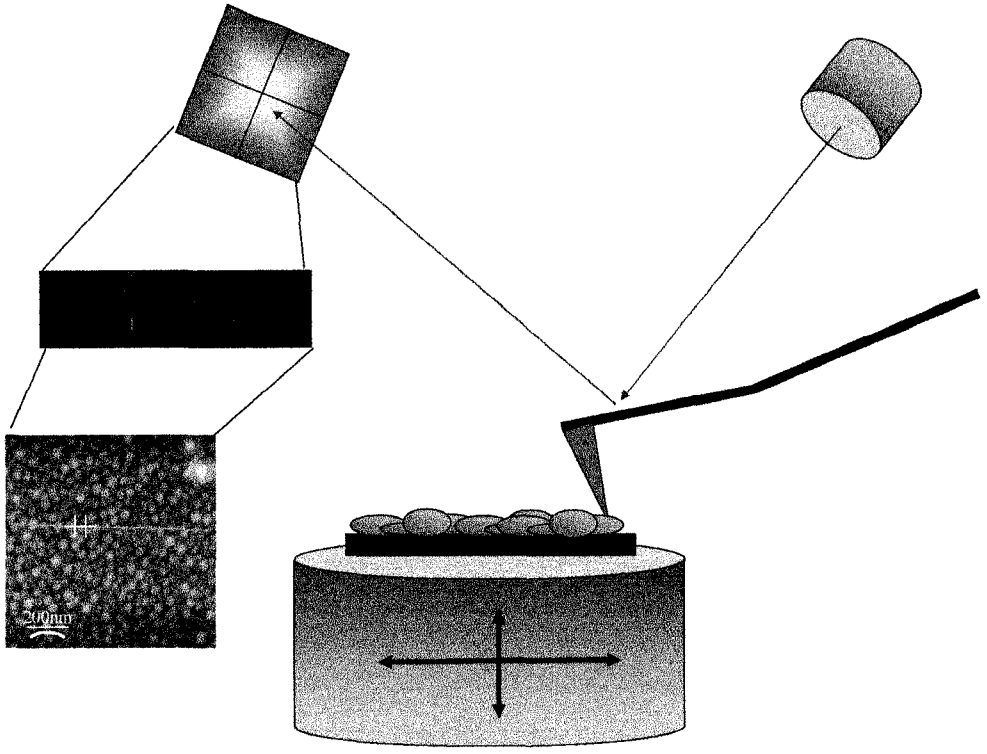

Figure 3.12: Illustration of the principles behind scanning probe microscopy.

Two methods of Atomic Force microscopy were used for the work presented in this thesis, Contact mode and the non-contact method of "TappingMode"

3.4.1 Contact AFM

Reproduced with permission of the copyright owner. Further reproduction prohibited without permission.

In contact mode AFM, the cantilever acts as a spring, allowing the tip to react to surface forces. The tip used is a v-shaped cantilever made of a silicon nitride. The typical spring constant for the tips used was 0.38 N/m. Because the tip is dragged across the surface, high lateral forces can result, which can damage "soft" samples. For this reason it is often necessary to use the less damaging non-contact mode for imaging.

3.4.2 Tapping Mode

By measuring the effect of surface interactions of an oscillating tip, a less damaging sampling of the surface can be accomplished. This is known as non-contact mode or "TappingMode." (a proprietary mode of Digital Instruments). This method is used in an attempt to minimize contact AFM forces, and is achieved by oscillating a tip and measuring the resultant damping on the tip's amplitude as well as any change in the phase of the vibration upon interaction with a surface. The oscillation occurs at or near the resonant frequency of the cantilever. The cantilevers are rigid silicon crystals with a typical resonant frequency ca. 300 kHz. The main advantage is a much gentler method for surface imaging that can by used for easily deformed or damaged samples such as biopolymer films. The tips used for tapping mode were, n+-silicon tips (NSC 14 model, Ultrasharp) with a reported tip radius of ~12 nm. There are three types of information recorded during a typical scan: height, the amplitude difference, and the phase change. The amplitude difference (or amplitude), is a measure of the change in the tip's amplitude, though there is no height information contained in these images they tend to have much better contrast then the height images. The phase image are described in the next section.

Reproduced with permission of the copyright owner. Further reproduction prohibited without permission.

3.4.3 Phase Imaging

An extremely useful method for characterizing a surface is Phase Imaging. In this type of imaging, the oscillation of the cantilever is monitored for changes in the phase. The technique can be used to differentiate between hard and soft materials, as well as compositional differences, for example the imaging of metal nanoparticles embedded in a polymer matrix. This type of application is illustrated in Figure 3.13. The additional requirement for phase imaging is that to achieve a good contrast it is necessary to increase the driving force (hit the sample "harder") than what is used in normal tapping mode.

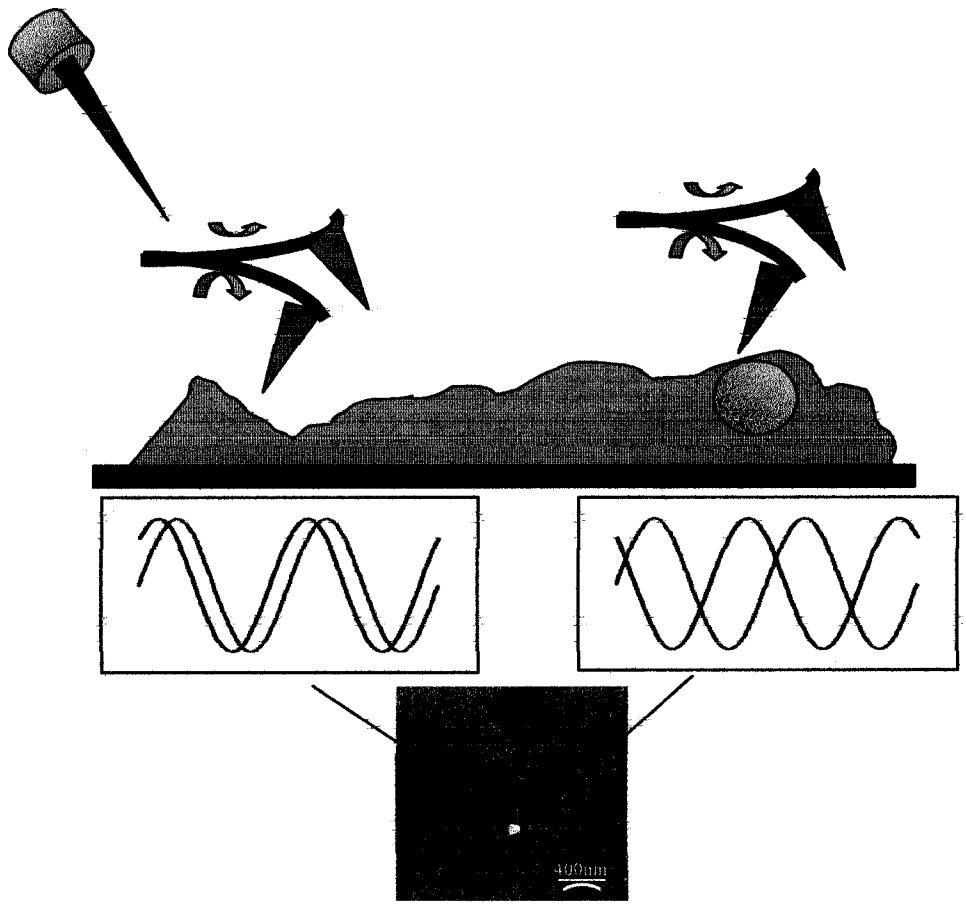

Figure 3.13: Illustration showing the ideas behind phase imaging. The blob material is a soft matrix while the sphere represents a metallic nanoparticle. In the phase image the contrast between "hard "and "soft" can be seen.

Reproduced with permission of the copyright owner. Further reproduction prohibited without permission.

3.4.4 SPM System

The SPM used for the AFM images presented in this work was the Veeco Digital Instruments Multi Mode SPM with Nano IV control hardware. The scanner consists of a piezoelectric scanner (the E scanner) with a xy range of 10 μm and maximum z displacement of 3.64 μm. Scan rate were typically between 0.5 and 1.0 Hz, with 512 sample lines per image. The software used for instrument control and data manipulation was the Veeco's Nanoware. Images were also generated with Nanotec WxSM 2.2.[17]

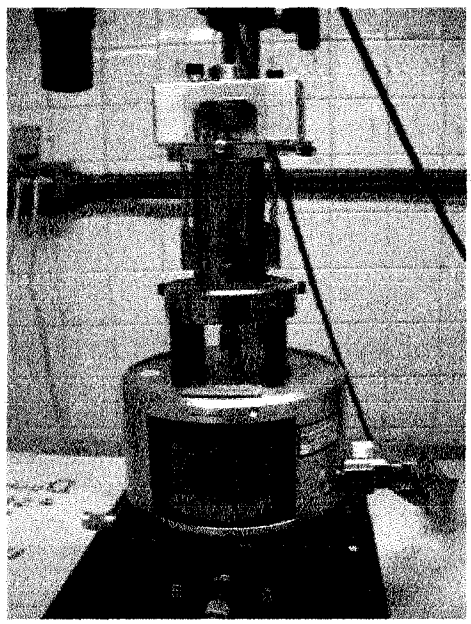

Figure 3.14: SPM Microscope

3.5 Infrared Absorption

The instrument used for all FT-IR measurements was the Bruker Equinox 55 FTIR equipped with a microscope shown in Figure 3.15. This system uses a nitrogen-

Reproduced with permission of the copyright owner. Further reproduction prohibited without permission.

cooled mercury cadmium telluride (MCT) detector. The spectral resolution used for the IR spectra recorded for this thesis was 4 cm^{-1}.

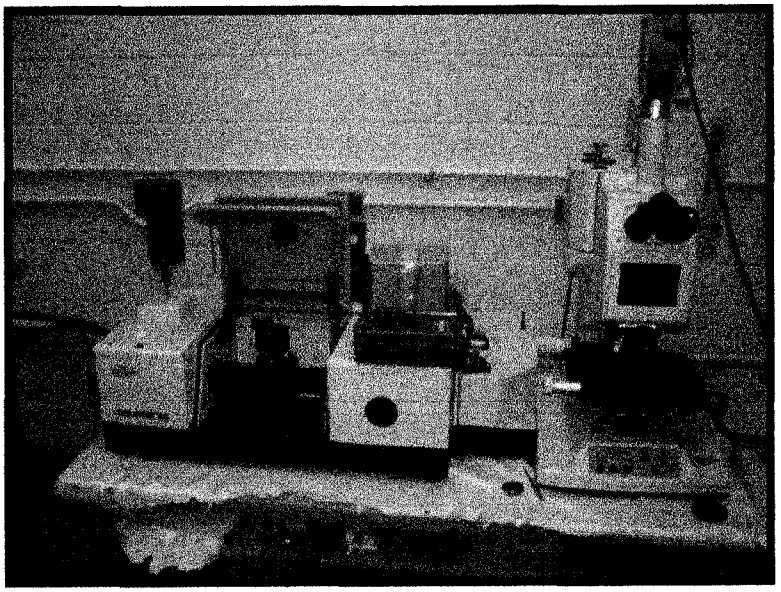

Figure 3.15: Bruker 55 Equinox FT-IR spectrometer

3.6 UV-visible Absorption

All molecular and plasmon absorptions were measured with the Cary 50 UV-Vis single beam spectrometer. It has a spectral range of 190 -1100 nm and is pictured in Figure 3.16.

Reproduced with permission of the copyright owner. Further reproduction prohibited without permission.

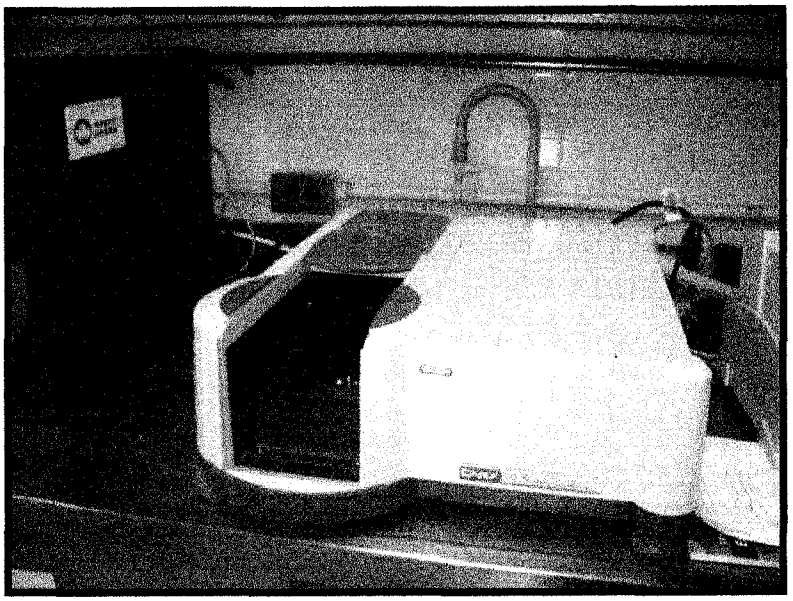

Figure 3.16: Cary 50 UV-Visible spectrometer

3.7 Langmuir- Blodgett Deposition system

The Lauda Langmuir film balance, shown in Figure 3.17, was used for the fabrication of the Langmuir-Blodgett films discussed in this thesis. Deionized water acquired from a Millipore system (measured resistivity of 18.2 MΩ cm) containing $CdCl_2$ (2.5×10^{-4} M) was used as the subphase, and maintained at a constant temperature of 15 °C. A Lauda Film Lift FL-1 electronically controlled dipping device was used for film depositions. Film compression was done with a constant surface pressure setting of 25 mN/m. The Langmuir films were transferred to glass slides, with and without metal island films, in the z-deposition style

Reproduced with permission of the copyright owner. Further reproduction prohibited without permission.

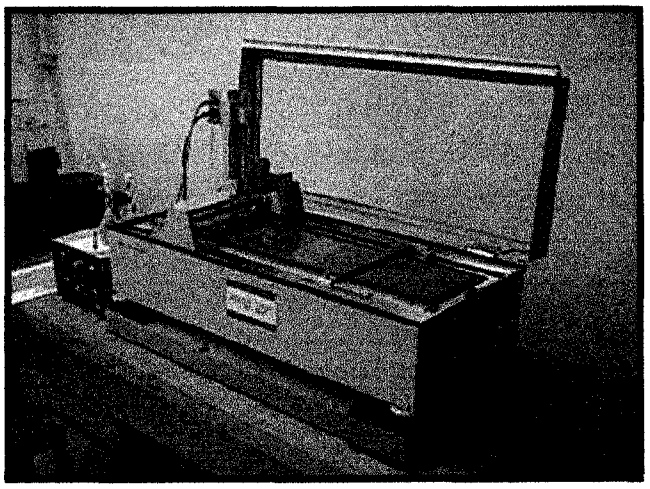

Figure 3.17: Lauda Langmuir film balance

3.8 Computational Resources

Spectral analysis was executed using Grams/AI (7.0) from ThermoGalactic.

All theoretical calculations presented in Chapter 4 were carried out using the Gaussion 03 computational package.[18] DFT calculations were performed using the density functional theory of Becke's three-parameter functional including the correlational functional of Lee, Yang, and Parr (B3LYP).[19,20] The 6-311G(d) , and Lanl2DZ basis set s were used.[21,22] No scaling factors were applied to calculated Raman frequencies.

GaussView 03 for Windows was used to view all calculated structures and to view molecular vibrations.[23]

Mie scattering calculations were performed using an in-lab Maple program.[24]

References

(1) Adar, F.; Delhaye, M.; DaSilva, E. *Journal of Chemical Education* **2007**, *84*, 50-60.

Reproduced with permission of the copyright owner. Further reproduction prohibited without permission.

(2) Owen, H. *Journal of Chemical Education* **2007**, *84*, 61-66.

(3) Krafft, C.; Sergo, V. *Spectroscopy-an International Journal* **2006**, *20*, 195-218.

(4) Zhang, P.; Smith, S.; Rumbles, G.; Himmel, M. E. *Langmuir* **2005**, *21*, 520-523.

(5) Le Ru, E. C.; Etchegoin, P. G. *Chemical Physics Letters* **2004**, *396*, 393-397.

(6) Goulet, P. J. G.; Pieczonka, N. P. W.; Aroca, R. F. *Analytical Chemistry* **2003**, *75*, 1918-1923.

(7) Constantino, C. J. L.; Lemma, T.; Antunes, P. A.; Aroca, R. *Analytical Chemistry* **2001**, *73*, 3674-3678.

(8) Weiss, A.; Haran, G. J. *Journal of Physical Chemistry B* **2001**, *105*, 12348-12345.

(9) Etz, E. S.; Choquette, S. J.; Hurst, W. S. *Microchimica Acta* **2005**, *149*, 175-184.

(10) McCreery, R. L. In *Handbook of Vibrational Spectroscopy*; Chalmers, J. M., Grifftiths, P. R., Eds.; John Wiley & Sons Ltd: Chichester, 2002.

(11) Choquette, S. J.; Etz, E. S.; Hurst, W. S.; Blackburn, D. H.; Leigh, S. D. *Applied Spectroscopy* **2007**, *61*, 117-129.

(12) Frost, K. J.; McCreery, R. L. *Applied Spectroscopy* **1998**, *52*, 1614-1618.

(13) Roark, S. E.; Rowlen, K. L. *Applied Spectroscopy* **1992**, *46*, 1759-61.

(14) Roark, S. E.; Rowlen, K. L. *Chemical Physics Letters* **1993**, *212*, 50-6.

(15) Roark, S. E.; Rowlen, K. L. *Analytical Chemistry* **1994**, *66*, 261-70.

(16) Roark, S. E.; Semin, D. J.; Rowlen, K. L. *Analytical Chemistry* **1996**, *68*, 473-80.

(17) Horcas, I.; Fernandez, R.; Gomez-Rodriguez, J. M.; Colchero, J.; Gomez-Herrero, J.; Baro, A. M. *Review of Scencetific Instruments* **2007**, *78*, 013705.

(18) Frisch, M. J.; Trucks, G. W.; Schlegel, H. B.; Scuseria, G. E.; Robb, M. A.; Cheeseman, J. R.; Montgomery, J., J. A.; Vreven, T.; Kudin, K. N.; Burant, J. C.; Millam, J. M.; Iyengar, S. S.; Tomasi, J.; Barone, V.; Mennucci, B.; Cossi, M.;

Reproduced with permission of the copyright owner. Further reproduction prohibited without permission.

Scalmani, G.; Rega, N.; Petersson, G. A.; Nakatsuji, H.; Hada, M.; Ehara, M.; Toyota, K.; Fukuda, R.; Hasegawa, J.; Ishida, M.; Nakajima, T.; Honda, Y.; Kitao, O.; Nakai, H.; Klene, M.; Li, X.; Knox, J. E.; Hratchian, H. P.; Cross, J. B.; Bakken, V.; Adamo, C.; Jaramillo, J.; Gomperts, R.; Stratmann, R. E.; Yazyev, O.; Austin, A. J.; Cammi, R.; Pomelli, C.; Ochterski, J. W.; Ayala, P. Y.; Morokuma, K.; Voth, G. A.; Salvador, P.; Dannenberg, J. J.; Zakrzewski, V. G.; Dapprich, S.; Daniels, A. D.; Strain, M. C.; Farkas, O.; Malick, D. K.; Rabuck, A. D.; Raghavachari, K.; Foresman, J. B.; Ortiz, J. V. C., Q. ; Baboul, A. G.; Clifford, S. C., J.; Stefanov, B. B.; Liu, G.; Liashenko, A.; Piskorz, P.; Komaromi, I.; Martin, R. L.; Fox, D. J.; Keith, T.; Al-Laham, M. A.; Peng, C. Y.; Nanayakkara, A.; Challacombe, M.; Gill, P. M. W.; Johnson, B.; Chen, W.; Wong, M. W.; Gonzalez, C.; Pople, J. A.; Gaussian, Inc: Wallingford CT,, 2004.

(19) Becke, A. D. *Physical Review A* **1988**, *38*, 3098-3100.

(20) Lee, C. T.; Yang, W. T.; Parr, R. G. *Physical Review B* **1988**, *37*, 785-789.

(21) Dunning, T. H.; Hay, P. J. In *Methods of Electronic Structure Theory*; Schafer, H., Ed.; Plenum Press: New York, 1977; Vol. 2.

(22) Hay, P. J.; Wadt, W. R. *Journal of Chemical Physics* **1985**, *82*, 299-310.

(23) Dennington II, R.; Keith, T.; Millam, J. E., Ken. ; Hovell, W. L.; Gilliland, R.; Version 3.09 ed.; Semichem, Inc: Shawnee Mission, KS, 2003.

(24) Ross, D., 2003.

Reproduced with permission of the copyright owner. Further reproduction prohibited without permission.

CHAPTER 4

SINGLE MOLECULE SERRS USING LANGMUIR-BLODGETT FILMS

Reproduced with permission of the copyright owner. Further reproduction prohibited without permission.

4.1 Introduction

The ultimate limit of detection for any analytical technique is the ability to identify and quantify the signal arising from a single molecule. SERS has joined a small handful of optical spectroscopies with the capabilities to achieve this limit. Chemistry books are written with single molecule reactions and formulae. However, chemists and physicists only measured average quantities, not the single molecule reactions or the properties of single molecules. The detection of a single molecule was first achieved in fluorescence spectroscopy, however, its identification by its vibrational fingerprints had to wait for the powerful SERS.[1] Today, it is clear that by studying single molecules, new areas of research are developing (single molecule spectroscopy, SMS), revealing features that ensemble measurements average out. SMS could be used for instance to study molecular dynamics at surfaces or to follow the behaviour of a molecule during interactions with its surroundings, an important advance for understanding chemical and biochemical processes. In addition, developments in nanotechnology will soon require the ability to measure single molecular chemistry and SM-SERS would be a powerful tool in this regard. Ultimately, it is an attempt to push the limits, to see what is happening at the edges and uncover behaviour that differs from the collective.

The first optical spectroscopy reported to detect a single molecule was low temperature fluorescence. In subsequent years, fluoresce has been successfully used to detect SM's in a variety of environment with relative ease.[2] While this approach has proven to be very successful, fluorescence lacks chemical information when compared to Raman, which provides complete vibrational detail. Furthermore, fluorescence requires molecules with exceptional quantum efficiency, something that, at least in theory, SERS

Reproduced with permission of the copyright owner. Further reproduction prohibited without permission.

does not. Early work by Kneipp suggested single molecule detection by SERS was possible, in particularly SERRS.[3] In 1997, two groups made claims that this was indeed so. Papers by Kneipp and Nie marked the beginning of SM-SERS.[4,5] These seminal papers started a new found interest in SERS and opened a floodgate of research activity which continues to this day.[6-15]

4.2 Counting Photons

There is plenty of published work that has supported, and seems to attest to, the feasibility of SM detection using SERS and/or SERRS. However, for many the question naturally arises "Is it really possible?" A back of the envelope calculation will show that, indeed it is.

Recall, the Raman intensity for a given band can in simplest terms be written as:

$$I_{RS} = I_o \sigma_{RS} N \tag{4.2.1}$$

where. I_{RS} [photons/sec], I_o [photons/sec • cm^2], σ [cm^2] and N would be the number of scatterers. The following experimental parameters are assumed;

1) The measured "count" = 1 photon for an ideal detector.
2) The signal is collected over complete sphere with no loss due to optics.
3) A typical Raman cross section (non-resonant) is ca. 10^{-28} cm^2.
4) A detection level of at least 100 "counts" • s^{-1} is needed to be discernable above the background noise (a value typically encountered in SM-SERS).

Looking at the needed laser intensity for single molecule experiments ($N = 1$):

$$I_o = \frac{100}{\sigma_{RS}} N = \frac{100}{10^{-28} cm^2} = 10^{30} photons/s \tag{4.2.2}$$

Reproduced with permission of the copyright owner. Further reproduction prohibited without permission.

For 514.5 nm, the flux then would need to be ~ 3.86 x 10^{11} W/cm^2, an experimentally unreasonable value. For comparison, the 514.5 nm laser used in these experiments is generally measured at the sample to have an energy density of 1 mW/μm^2 (9.97 x 10^4 W/cm^2). Using an energy density of 1 mW/μm^2 with the same Raman scattering cross section, N would then need to be 10^7 to allow for the detection of a signal.

In the case of resonance Raman, the cross section can increase to 10^{-24} cm^2. Then for 1 mW at 514.5 nm, the number of molecules that can be detected would be ~10^3. If we assume that σ_{RRS} does not change when interacting with a metal nanoparticle substrate (not always the case) then for SM detection there needs to be an enhancement of at least 10^3. This is an idealized experiment where every photon is counted. A more realistic quantum efficiency for the detector would be in the range of 30 to 50 %, with only a fraction of the total scattering sphere collected. In addition, to prevent laser damage with SERS, it is necessary to use μW's of laser power. Of course, any decrease in the Raman cross section, or in instrument efficiency would require a larger enhancement by SERRS for SM detection. Even with these additional considerations, assuming a SERRS enhancement of 10^6, a value routinely realized both theoretically and experimentally, SM detection is indeed possible.

4.3 An alternative approach to SM-SERRS[a]

Most reports on SM detection by SERS have been attained with Ag or Au aggregated colloidal nanoparticles. The approach used, often relies on the ability to dilute the target analyte in solution to levels where it is believed to be at most, 1 molecule in the probe volume during the time of data collection. The drawback is that these arguments

[a] This work was a collaborative effort with P. J. G. Goulet. Langmuir-Blodgett film fabrication was mostly completed by P. J. G. Goulet

Reproduced with permission of the copyright owner. Further reproduction prohibited without permission.

are thermodynamically driven and there is no real control of the concentration of analyte.[16] There is an experimental technique that provides an alternative approach to SM-SERS. This was demonstrated by Aroca and collaborators when they extended their work of studying monomolecular Langmuir-Blodgett films by SERRS to show that the method can successfully be applied to SM studies.[13,15,17-24]

4.4 Langmuir- Blodgett films

The Langmuir-Blodgett (LB) technique is based on the fact that certain classes of molecules, such as amphiphilic molecules with hydrophilic "heads" and hydrophobic tails, will organize themselves on the surface of a subphase (typically water) in a single molecular layer.[25] This layer can be carefully transferred to a substrate through a controlled deposition as shown in the cartoon of Figure 4.1. An advantage of LB films is that they allow control of molecular architecture such as orientation and intermolecular distances. Additionally, the concentration of target analytes can be controlled with a great deal of certainty. This can be accomplished by systematically reducing the concentration of target analyte in a spectrally "inert" matrix (a molecule with a very low Raman and SERS cross section compared to the target analyte), typically a fatty acid such as Arachidic Acid. The use of monomolecular films reduces the probe volume to a probe area. The reduction from 3D to 2D greatly reduces the ambiguity of analyte concentration. When coupled with the spatial resolution and sensitivity of Raman microscopy, highly controlled experiments are possible.

Reproduced with permission of the copyright owner. Further reproduction prohibited without permission.

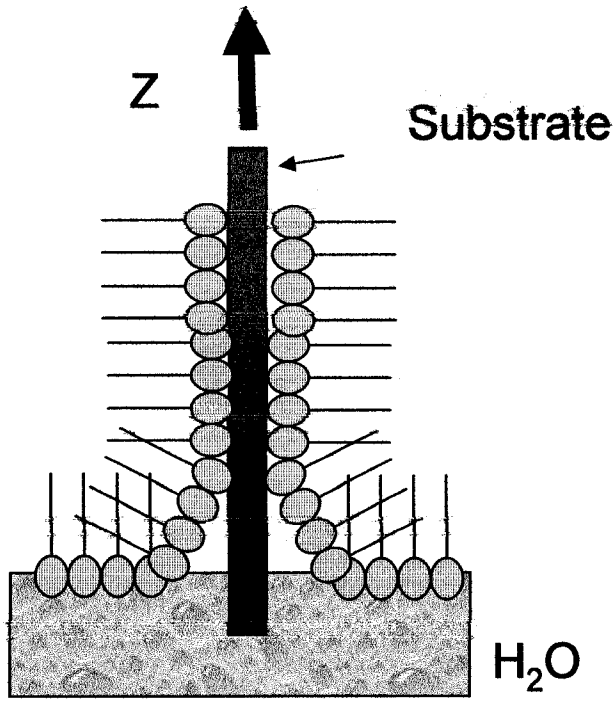

Figure 4.1: Illustration of the Z-type deposition of a Langmuir-Blodgett Film

The LB methodology was used in the study of three perylene dyes down to SM levels. The goal was to further the previous work done on SM-SERRS both to address experimental challenges in addition to attempting to see spectral features that had not been recorded in previous studies, such as overtones and combinations. These vibrations arise under resonance condition in Raman spectroscopy.[26] Since in RRS they are related to the excited state of a molecule, they could be used potentially as sensitive probes for perturbations to a molecule's electronic state as a result of interactions with either the metallic nanostructure or the extremely high local fields encountered in SERRS.

This work will demonstrate how the technique of LB monolayers was used for the successful detection of the SM-SERRS signal, containing overtones and combinations, for 3 different dyes.[13,18]

Reproduced with permission of the copyright owner. Further reproduction prohibited without permission.

4.5 Experimental

The materials used for SMD here are Bis-(benzylimido) perylene, $C_{40}H_{22}N_2O_4$, (Bbip-PTCD), n-pentylimido-benzimidazo perylene, $C_{35}H_{23}N_3O_3$ (pentyl-PTCD), and Bis (benzimidazo) perylene $C_{36}H_{16}N_4O_2$ (azo-PTCD). (Structures can be seen in Figure 4.4)

In this work, Langmuir-Blodgett films of these 3 different PTCD derivatives were deposited onto thin silver island films, in varying concentrations. The films used in this study were formed from evaporating Ag onto glass substrates (Corning 7059 glass slides). The 6 nm (mass thickness) Ag island films were prepared by vacuum evaporation at a pressure of 10^{-7} Torr, and a temperature of +200 °C with deposition rate of 0.5 Å/s. These films were then heated at the same temperature for 1 hour after evaporation, and then left to cool to room temperature under vacuum. An AFM image of a typical film is shown in Figure 4.2. The average particle diameter was measured to be ca. 50 nm.

Reproduced with permission of the copyright owner. Further reproduction prohibited without permission.

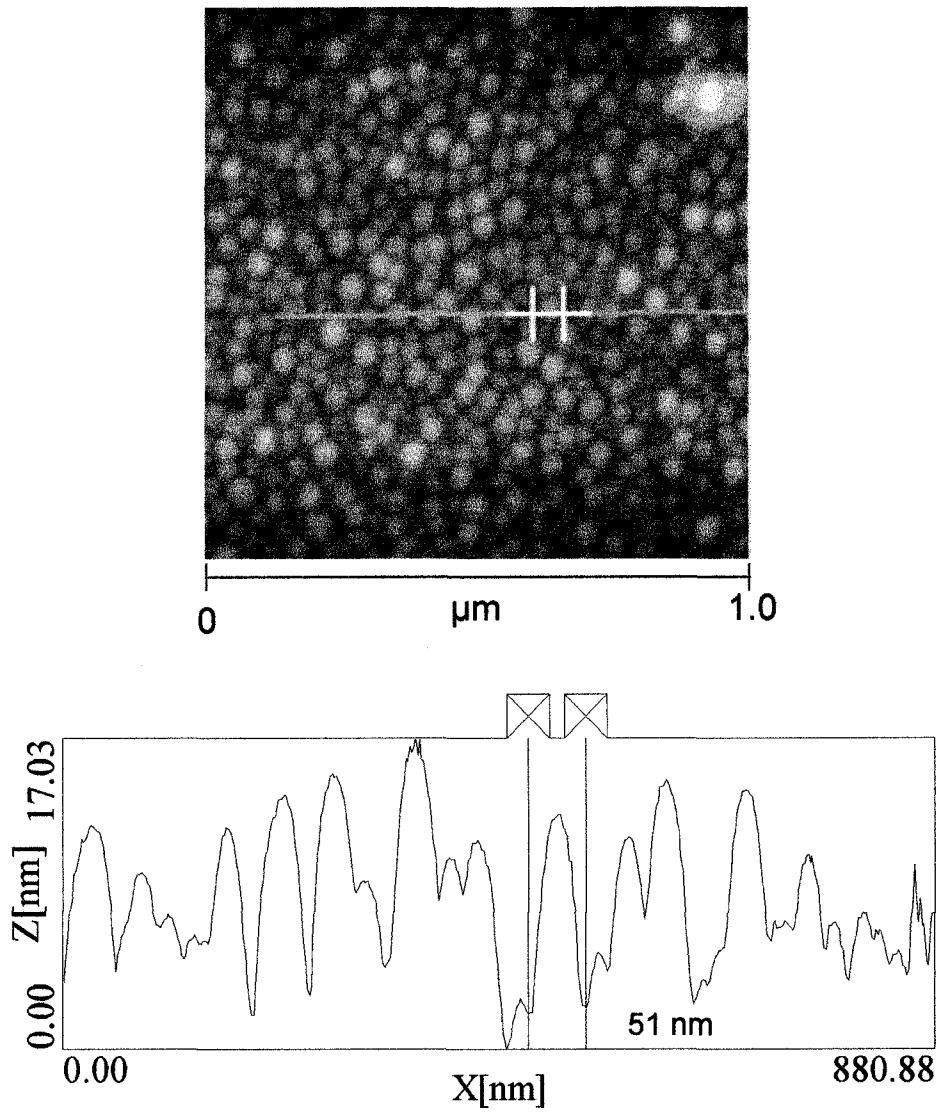

Figure 4.2: AFM image of a 6 nm Ag island film.

The spreading solutions used were composed of both a perylene derivative, and a fatty acid (arachidic acid (AA), $C_{19}H_{39}COOH$) that is known to form very well characterized, and stable Langmuir films that can be transferred to form LB films. These solutions were prepared in such a way as to achieve various concentrations from 10^6 to 1 dye molecule per square micron of trough area. The corresponding molar ratios of perylene to arachidic acid are shown in Table 4.1. The choice of 1 μm^2 is determined by

Reproduced with permission of the copyright owner. Further reproduction prohibited without permission.

the laser spot size for the 50X objective (NA =.75) used in these experiments.

Table 4.1: Probe Molecule to Fatty Acid Ratio with the approximate number of molecules in 1 μm^2

	Approximate Number of Molecules in 1 μm^2	
Ratio	Dye	AA
1:1	2,000,000	2,000,000
1:10	363,636	3,636,363
1:100	39,604	3,960,396
1:1000	3,996	3,996,004
1:40,000	100	3,999,900
1:400,000	10	3,999,990
1:4,000,000	1	3,999,999

The preparations of all perylene/fatty acid solutions were accomplished using the same procedures and calculations as outlined below for the case of a "single molecule" spreading solution.

To begin, the area of the matrix molecule, arachidic acid, must be considered. It has a well-established area per molecule of 25 Å^2.[27] Therefore, within 1 μm^2 of trough area, there will be 4 X 10^6 molecules. Of these, only *one* will be the probe molecule. This dye will comprise .000025 % of the total number of spread molecules, while arachidic acid will make up the remainder. For the Lauda Langmuir Film Balance used in this work the number of molecules set to be on the subphase is 8.640 X 10^{16}. In order to achieve a single probe molecule per micron squared, it then becomes necessary to spread a total of 2.16 X 10^{10} PTCD molecules, and 8.64 X 10^{16} fatty acid molecules on the trough. A convenient spreading volume (500 μL), is assumed and the concentrations of both the PTCD and AA in the spreading solution are calculated using the equation:

$$C = \frac{N_{molecules}}{N_A V_{spread}} \qquad (4.2.3)$$

Reproduced with permission of the copyright owner. Further reproduction prohibited without permission.

For a "single molecule" solution, using a 500 μL spreading volume, the calculated concentrations are 7.18 X 10^{-11}M and 2.87 X 10^{-4}M for PTCD and AA respectively.

All solutions were prepared using spectrophotometric grade dichloromethane as the solvent. However, due to the limited solubility of PTCD's, it was necessary to add spectrophotometric grade trifluoroacetic acid to initial stock solutions (10^{-4}M) in order to fully dissolve the powders. The TFA amounts are extremely low in the very dilute solutions, as they only make up 10% of the initial stock solution. It was not used in the preparation of any of the less concentrated solutions.

Mixed PTCD-AA Langmuir films were fabricated using a Lauda Langmuir film balance with a subphase of pure water (18.2 MΩ cm), containing small amounts of cadmium chloride (2.5 10^{-4} mol L^{1}), and maintained at a constant temperature of 15 °C. Corning 7059 glass slides, clean, or coated with 6 nm Ag island film, were immersed in the water subphase using a Lauda Film Lift FL-1 electronically controlled dipping device.

The mixed PTCD-AA solutions were then spread (500 μL), and 20 minutes was allowed for solvent evaporation. Film compression was then begun with a single barrier moving at 3.5cm/min. It was continued using a constant surface pressure setting of 25mN/m, corresponding with the condensed phase of the Langmuir film. After allowing the monolayer to completely stabilize on the subphase, it was transferred to a glass slide supporting a 6 nm Ag while maintaining constant surface pressure using the Film Lift with a speed of 3 mm/min. All transfers were performed by Z-deposition, and transfer ratios were calculated to be near unity. An outline to the LB approach to SM-SERRS is illustrated in Figure 4.3.

Reproduced with permission of the copyright owner. Further reproduction prohibited without permission.

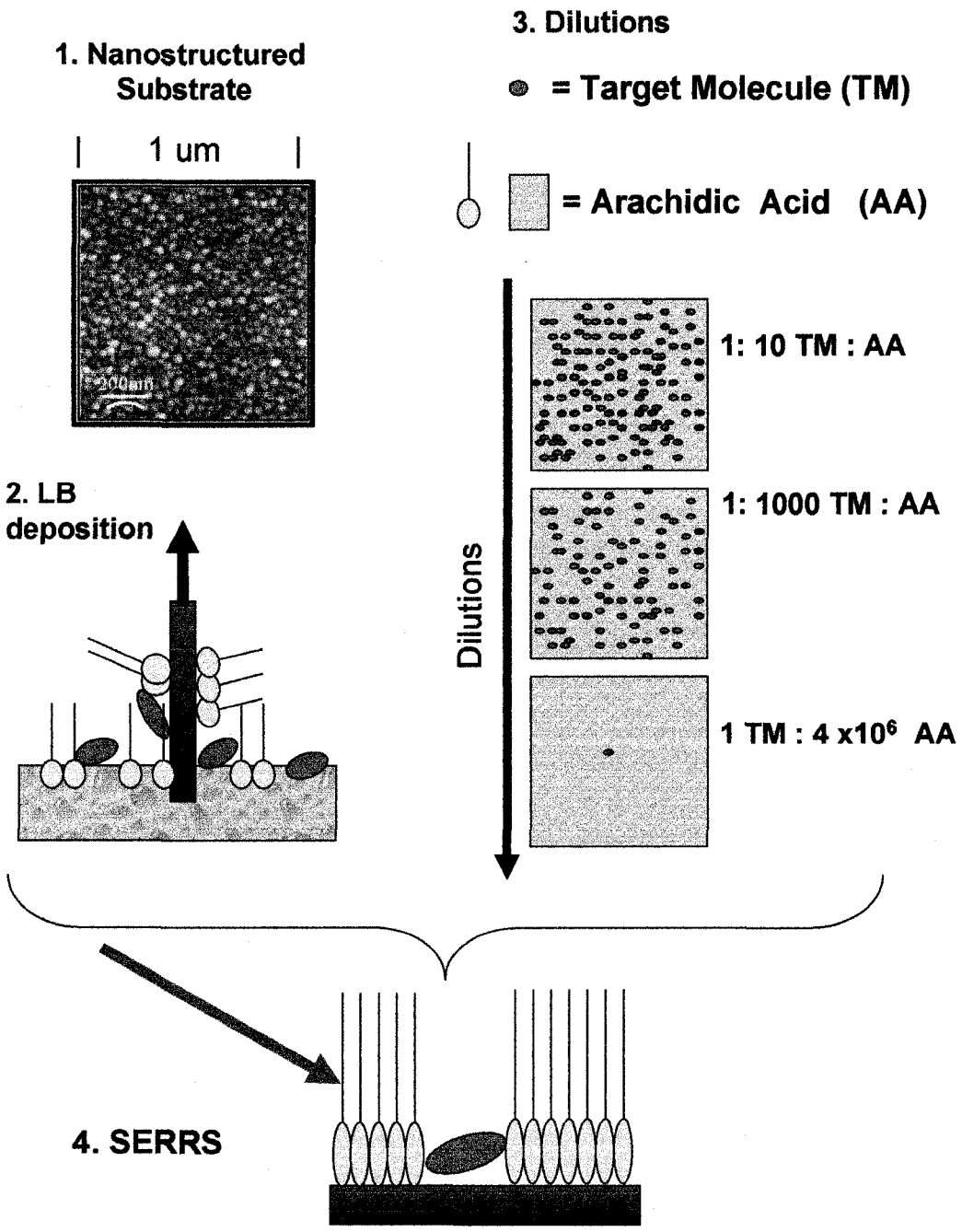

Figure 4.3: Schematic of the LB approach to SM-SERS

Reproduced with permission of the copyright owner. Further reproduction prohibited without permission.

The 514.5 nm excitation line was used in this investigation in order to take full advantage of the increased scattering efficiency of resonance Raman. In single molecule experiments, laser power was kept low (< 20 μW) to diminish the chance of photodegradation of the target molecule. Laser spot sizes were ca. 1 μm^2 using a 50X (NA .75) objective. Spectra collected over a large range (3500 to 200 cm^{-1}) were recorded in the continuous mode of the Renishaw system with accumulation times on the order of 10 seconds. Static spectra (fixed spectral window) were collected with a 1 second exposure time.

4.6 Results and Discussion

4.6.1 Absorption and Fluorescence

The absorption spectra of 10^{-6} M solutions of the three dyes are shown in Figure 4.4 The perylene moiety common to all of them, has characteristic absorption peaks (vibronic structure) associated with a π-π^* electronic transition.[28] For example, for Bbip-PTCD, the 0-0-transition band appears at 527 nm with additional vibronic structure at 490 and 458 nm. The absorption cross section calculated from a series of dilute solutions at 527 nm is ca. 10^{-17} cm^2/molecule. The plasmon absorption spectrum of a 6 nm silver island film is shown together with the solution absorption of Bbip-PTCD to demonstrate the double resonance conditions for these experiments in Figure 4.5.

Reproduced with permission of the copyright owner. Further reproduction prohibited without permission.

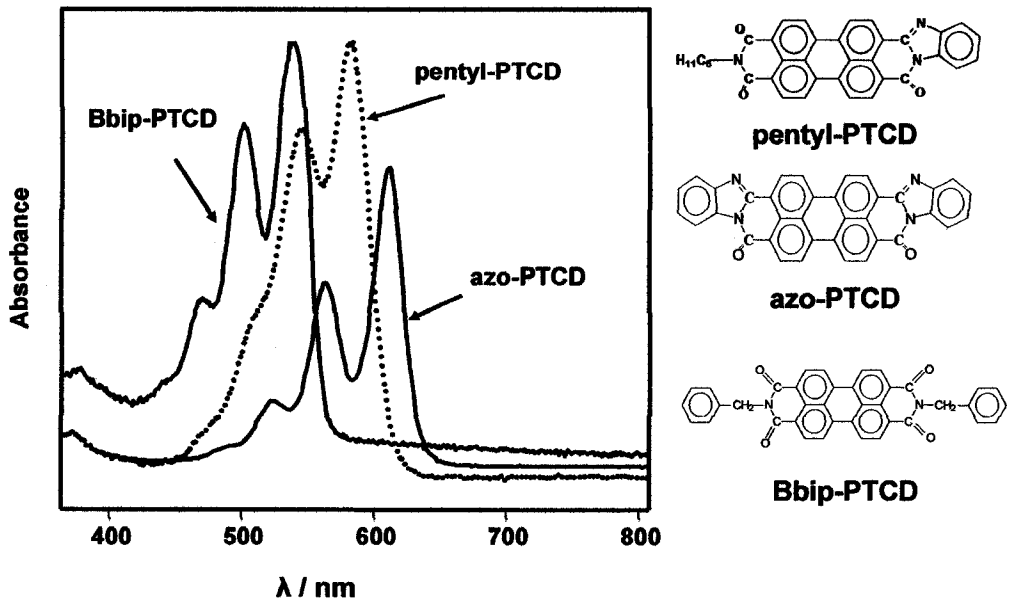

Figure 4.4: Solution absorption spectra for the 3 PTCD molecules in dichloromethane. Structure of each molecule is also shown

Reproduced with permission of the copyright owner. Further reproduction prohibited without permission.

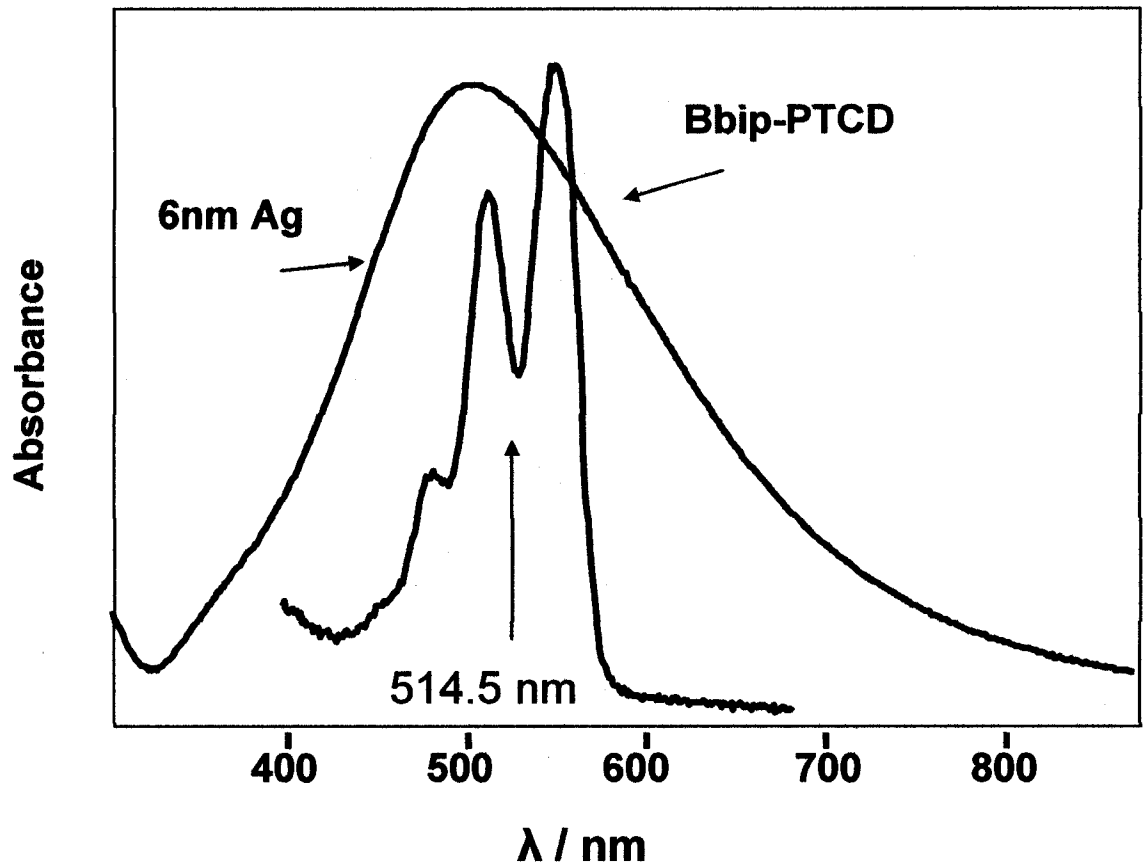

Figure 4.5: Plasmon absorption of a 6 nm Ag island film. Also shown is the solution absorption spectrum of Bbip-PTCD. The wavelength of the laser line is shown to demonstrate the double resonant condition of these experiments.

Typical fluorescence trends for these dyes are shown by the spectra of dilute Bbip-PTCD solutions in dichloromethane in Figure 4.6. The profile measured from the higher concentration of 10^{-4} has the red-shifted excimer emission characteristic of aggregated PTCD as the dominant feature. At the lower concentrations of 10^{-6} and 10^{-8} M, this feature is absent and the monomer fluorescence is clearly seen as the main absorption. This result indicates that the spreading solutions used for SM molecule samples contained no aggregates of the PTCD molecules.

Reproduced with permission of the copyright owner. Further reproduction prohibited without permission.

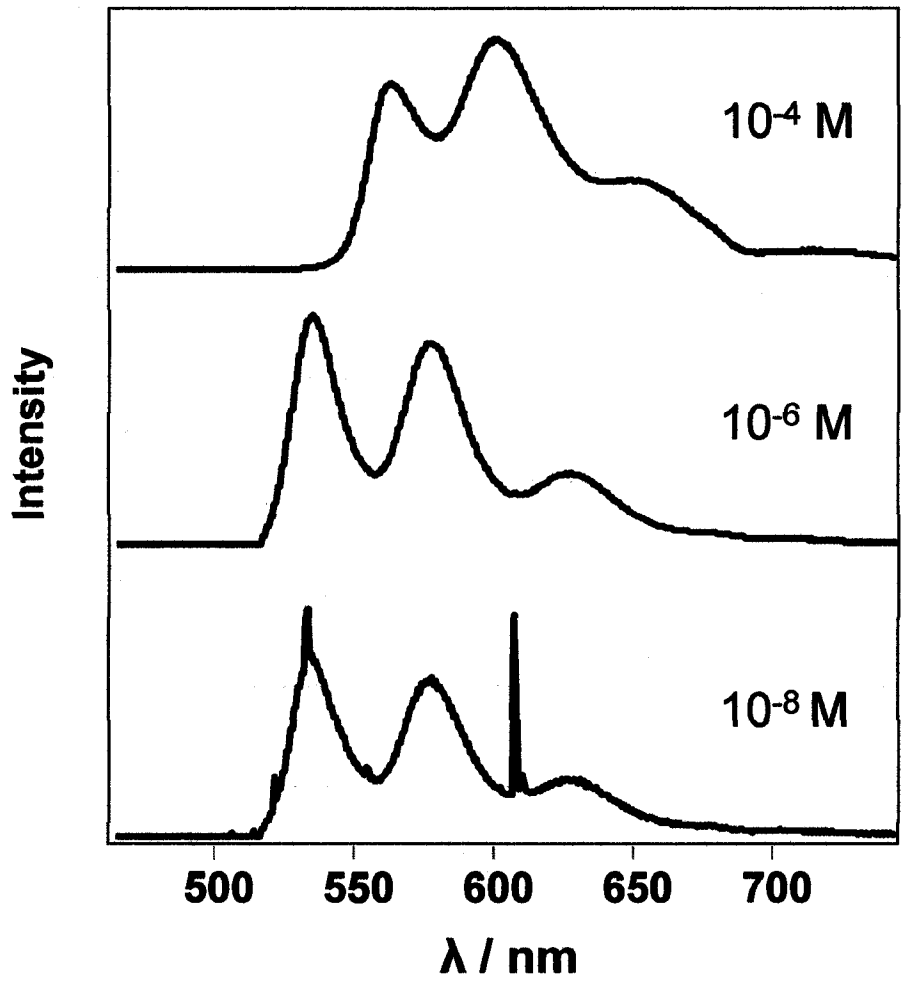

Figure 4.6: Fluorescence spectra of the Bbip-PTCD solution.

4.6.2 Surface Enhanced Resonance Raman Scattering of the Ensemble

To begin, the evidence that it is indeed SERRS that is being recorded in these experiments is provided by examining the Raman spectra recorded on Ag and on glass for a concentrated monolayer (1:1). These spectra, excited with the 514.5 nm laser line are shown in Figure 4.7.

Reproduced with permission of the copyright owner. Further reproduction prohibited without permission.

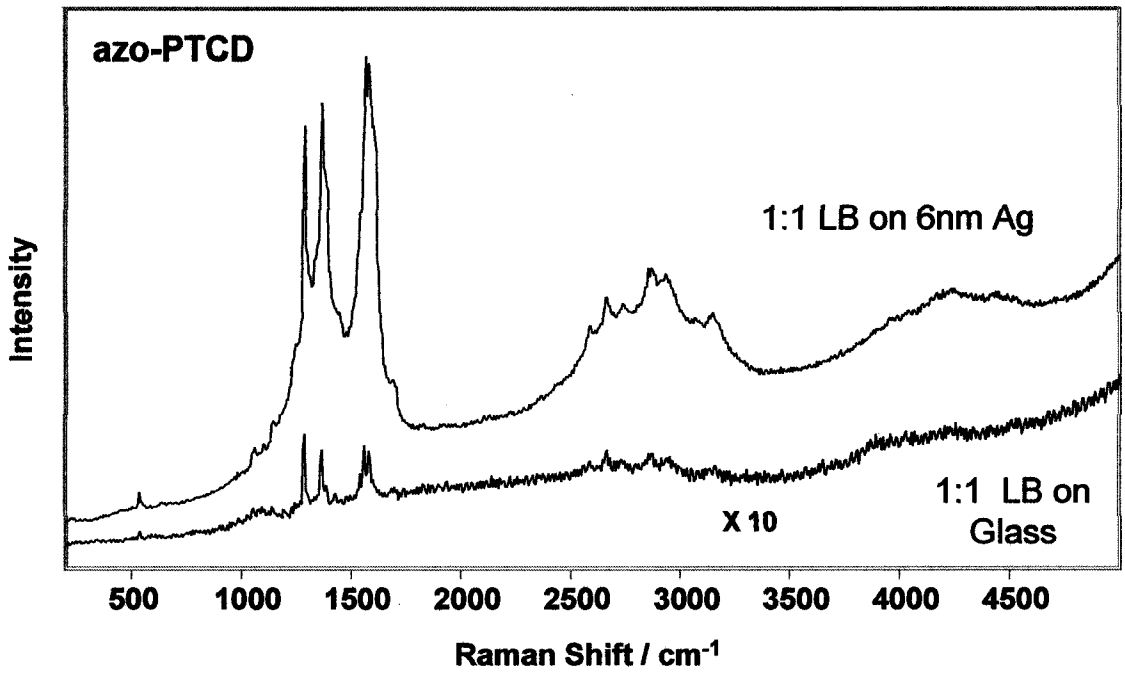

Figure 4.7: RR and SERRS spectrum of a 1:1 azo-PTCD film on 6 nm Ag island film. RRS of the same film on glass. Both spectra acquired with 514.5 nm.

The spectrum of the concentrated PTCD LB monolayers on silver contain the signature SERRS on a background of surface-enhanced excimer fluorescence and is approximately 100X greater than that recorded from glass under the same conditions. In Figure 4.8, the SERRS spectrum of pentyl-PTCD of the same concentration is shown. First, the raw spectrum and, secondly, the baselined SERRS spectrum is given to illustrate the overtone and combination regions that are present in the spectra of these systems. The approximate Raman shifts for the 3 strongest fundamentals and the location of their overtones and combinations are listed is Table 4.2.

Reproduced with permission of the copyright owner. Further reproduction prohibited without permission.

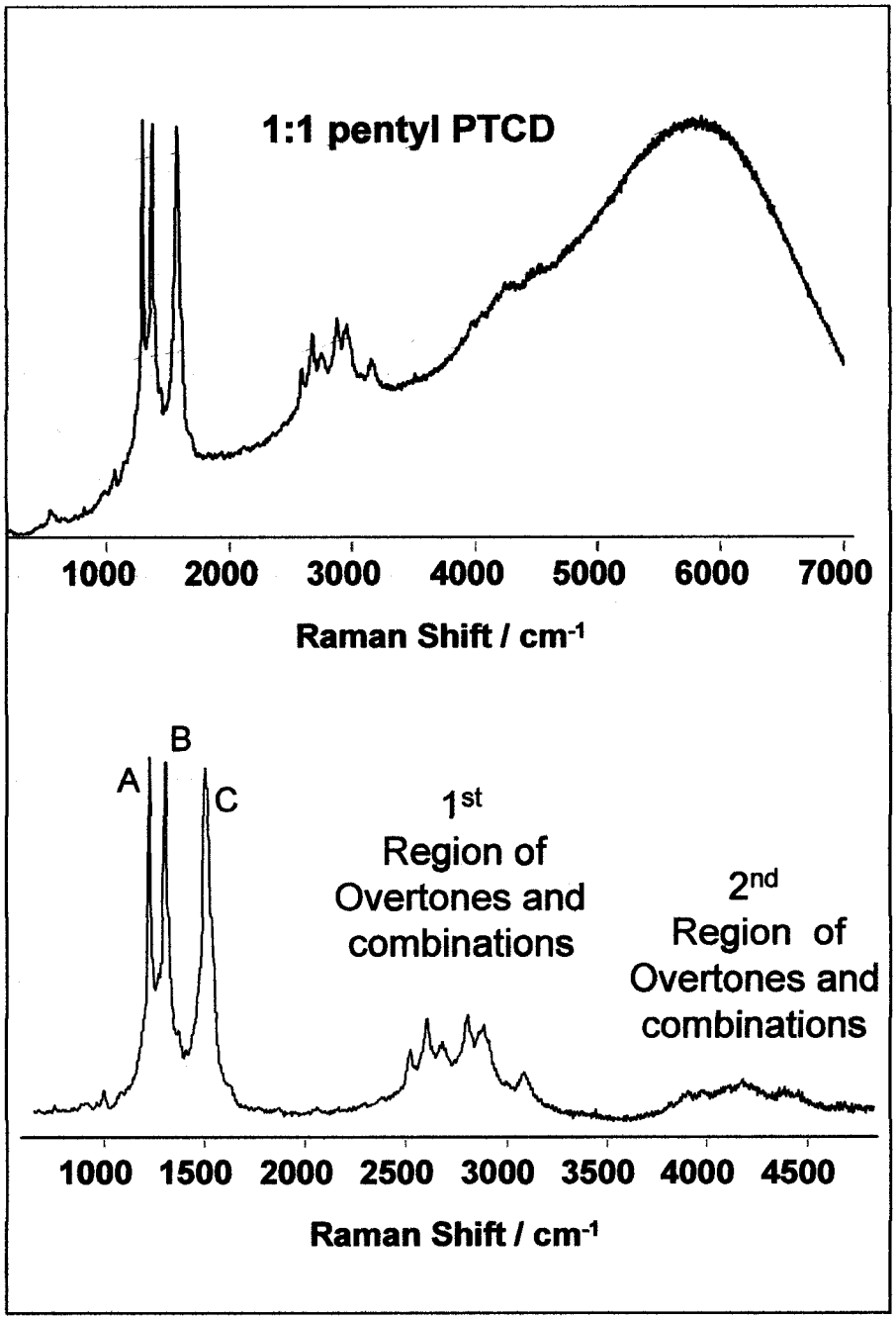

Figure 4.8: SERRS spectrum of a 1:1 pentyl-PTCD film on 6 nm Ag island film. Strong overtone and combination progression is seen as it the enhanced excimer emission (top). The same spectrum is baselined for comparison of the fundamental to the overtone regions

Reproduced with permission of the copyright owner. Further reproduction prohibited without permission.

Table 4.2: Peak Positions for fundamentals, overtones and combinations

cm^{-1}	Assignment	Overtones			Combinations	
		Fundamental	1st	2nd		
A	Ring Stretch	1299	2598	3897	A+B	2675
B	Ring Stretch	1376	2752	3158	A+C	2873
C	Ring Stretch	1574	3148	4722	B+C	2950
					A+B+C	4249
					2C+A	4457
					2C+B	4534

The progressions of overtones and combinations, which can be seen in the SERRS spectra shown in Figures 4.7 & 4.8, are unique due to their high relative intensity. This is evidenced by a comparison of the RRS obtained from the solid at 244 nm, which itself has a strong overtone progression, to the SERRS spectrum of Bbip-PTCD in Figure 4.9.

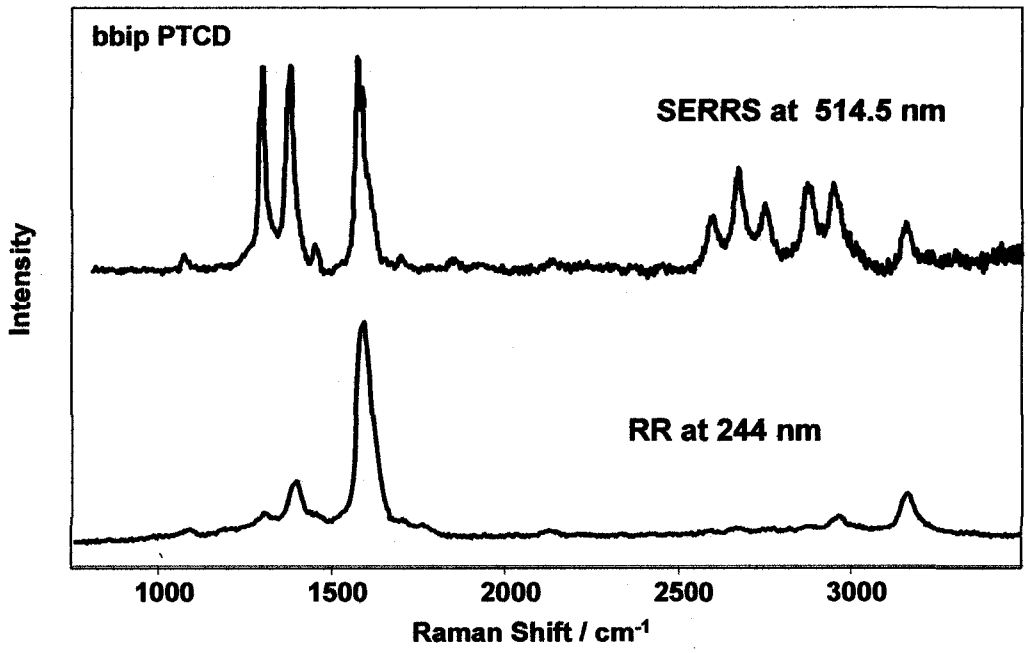

Figure 4.9: RR and SERRS of 1:1 film of Bbip-PTCD on Ag. Comparison between the overtone progressions seen in the SERRS spectrum of a 1:1 film of Bbip-PTCD on Ag, to the RR spectrum of the solid at 244 nm

Reproduced with permission of the copyright owner. Further reproduction prohibited without permission.

From these ensemble SERRS measurements there are two observations relevant to single molecule detection. First, the resonance Raman spectrum and the SERRS spectrum show vibrational frequencies with the same wavenumbers. The absence of evidence of frequency shifting indicates that the PTCD molecules do not strongly interact with the metal nanostructures, and that the metal-molecule interaction in all these cases can be treated as physical adsorption. The second important observation is that the SERRS signal decays with laser exposure. Figure 4.10 shows a series of 20 SERRS spectra taken from a concentrated 1:1 Bbip-PTCD LB film. Spectra were collected for a 10 second accumulation period with approximately 5 second lag between acquisitions. When plotted in 3D, the decrease in the SERRS signal is clearly evident. This experiment was performed with relatively low laser intensity at the sample (0.5 mW) and is evidence for the propensity of these systems to undergo photodegradation. This will be an important issue as the single molecule regime is approached.

Reproduced with permission of the copyright owner. Further reproduction prohibited without permission.

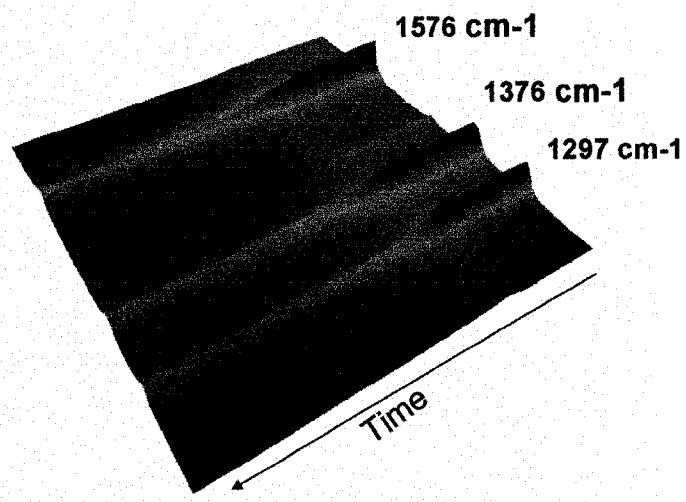

Figure 4.10: Time study of the photobleaching of a concentrated 1:1 Bbip-PTCD LB film on a Ag island film.

In Figure 4.11, the breakdown from ensemble to truly trace detection can be seen for the case of pentyl-PTCD, when the changes in the SERRS spectrum is followed as the molar ratio of PTCD to AA is diluted. The spectrum of the ensemble shows strong SERRS and can be seen from any location of the LB sample with little change in spectral profile. In addition, the overtone and combination region can be clearly observed and the excimer emission (Figure 4.9), characteristic of dye aggregates, is seen. As the concentration of analyte is reduced to approximately 100 molecules these spectral features change. First, excimer emission is no longer detected, indicating that the probe molecules are present as monomers. In addition the overall spectral intensity is much weaker. The weakly enhanced CH bands of the AA now appear in the spectrum. The characteristic spectrum of the probe molecule is also no longer uniformly detected. At the

Reproduced with permission of the copyright owner. Further reproduction prohibited without permission.

"10" molecule level, the detection of a measurable signal was a rare event requiring many measurement attempts of different areas of the sample.

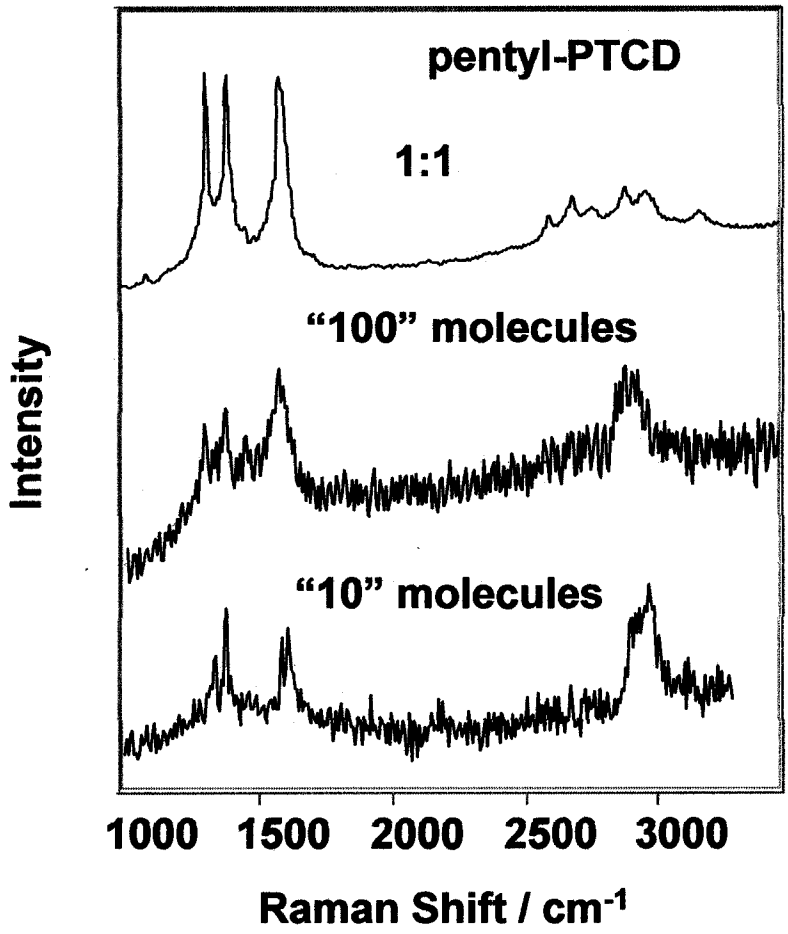

Figure 4.11: SERRS spectra of pentyl-PTCD at decreasing concentrations

4.6.3 Single Molecule SERRS and the evidence for overtones and combinations

All the SMD presented here were collected with 514.5 nm excitation so to take advantage of the increased intensity found with resonance Raman. Other excitation lines of 488 and 633 nm were attempted but failed to measure spectra from the SM samples.

Reproduced with permission of the copyright owner. Further reproduction prohibited without permission.

The high sensitivity of SERRS with the combination of the spatial resolution of Raman microscopy and the validity of the LB method, gives confidence to the fact that for the 1 molecule/μm^2 samples, if a characteristic Raman spectrum is detected, it is indeed arising from a single molecule. The challenge is to actually record a quality Raman spectrum. With proper care this was indeed possible as evidenced by the SM spectra in figures 4.12 and 4.13 for azo-PTCD and pentyl-PTCD.

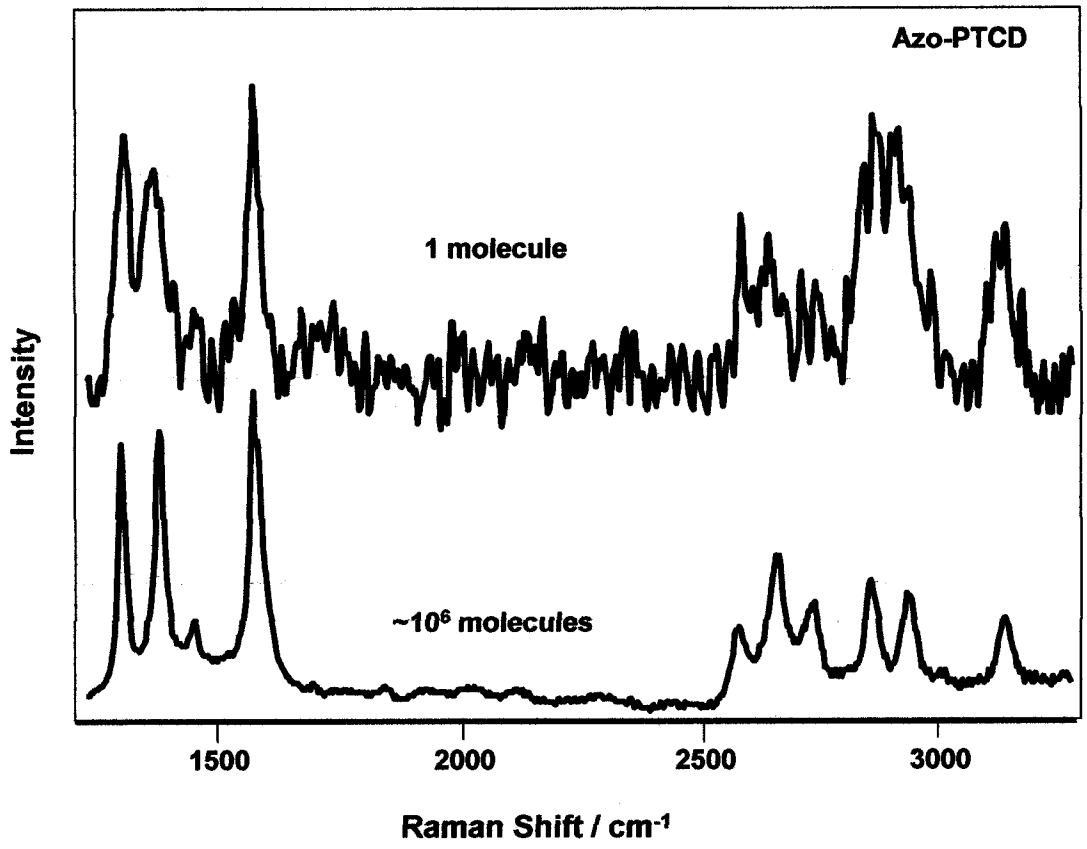

Figure 4.12: Single molecule SERRS spectrum of azo-PTCD as compared to the SERRS arising from 10^6 molecules

Reproduced with permission of the copyright owner. Further reproduction prohibited without permission.

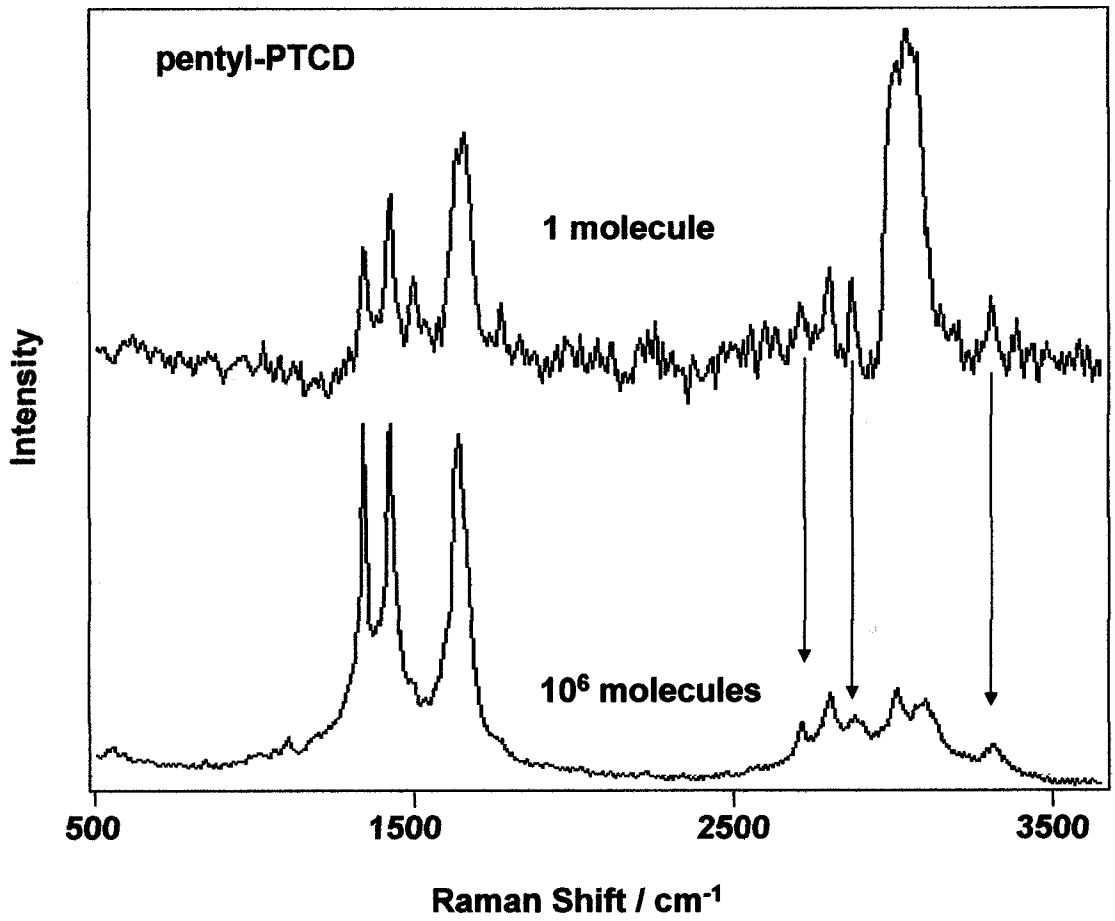

Figure 4.13: Single molecule SERRS spectrum of pentyl-PTCD as compared to the SERRS arising from 10^6 molecules.

In each figure, the single molecule spectrum is compared to that measured for the ensemble. In the SM spectra of each molecule, the fundamentals and the overtones and combinations, though weak, are recorded.

The measured SM spectra for Bbip-PTCD are shown in Figure 4.14, where again the average SERRS spectrum is included for comparison.

Reproduced with permission of the copyright owner. Further reproduction prohibited without permission.

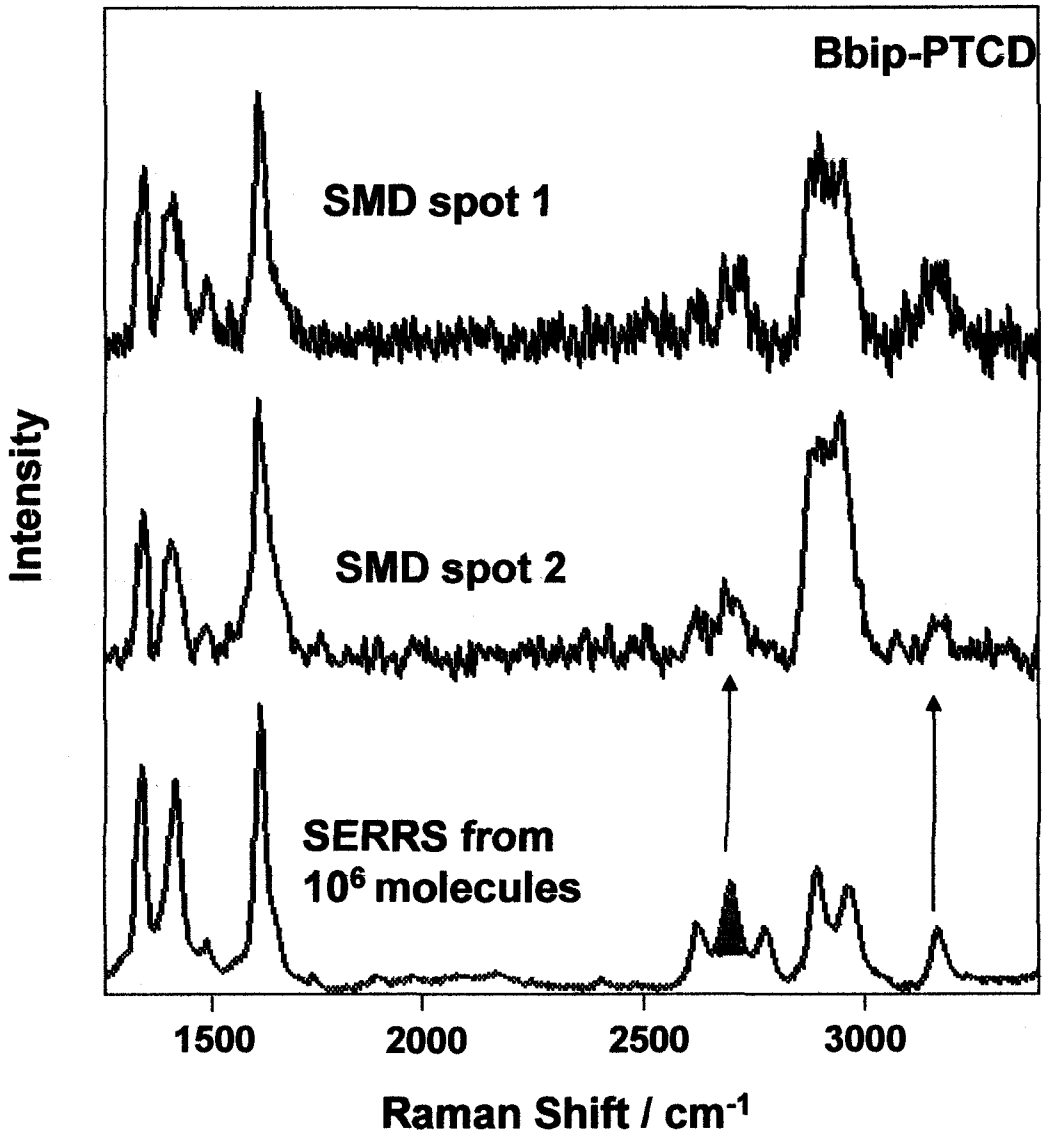

Figure 4.14: Single molecule SERRS spectrum of Bbip-PTCD. SM spectra are compared to the SERRS signal arising from 10^6 molecules. The variability seen in SM spectra is shown

Reproduced with permission of the copyright owner. Further reproduction prohibited without permission.

Single molecule spectra from two different spots on the LB surface are shown. Although weak, the presence of overtone and combination bands is unquestionable in both. These spectra illustrate a common feature of SM detection; there is much variation in the spectral parameters of the measured SM spectra. Changes in relative intensity, bandwidth and peak position can be seen. The reproducible spectrum encountered with the concentrated samples, is no longer measurable.

Measuring single molecule spectra is confounded in this work by at least two main factors. The first was the background contributions from photoproducts that can be generated on the silver surface. Above a certain power density, these can effectively bury any single molecule signal. An example of this is shown is Figure 4.15, where the ubiquitous carbon background that is seen is shown relative to a successful SM detection. This interference can be attributed to possible impurities on the metal surface and the high reactivity of the silver substrate with both the monolayers and molecules in the environment.

Reproduced with permission of the copyright owner. Further reproduction prohibited without permission.

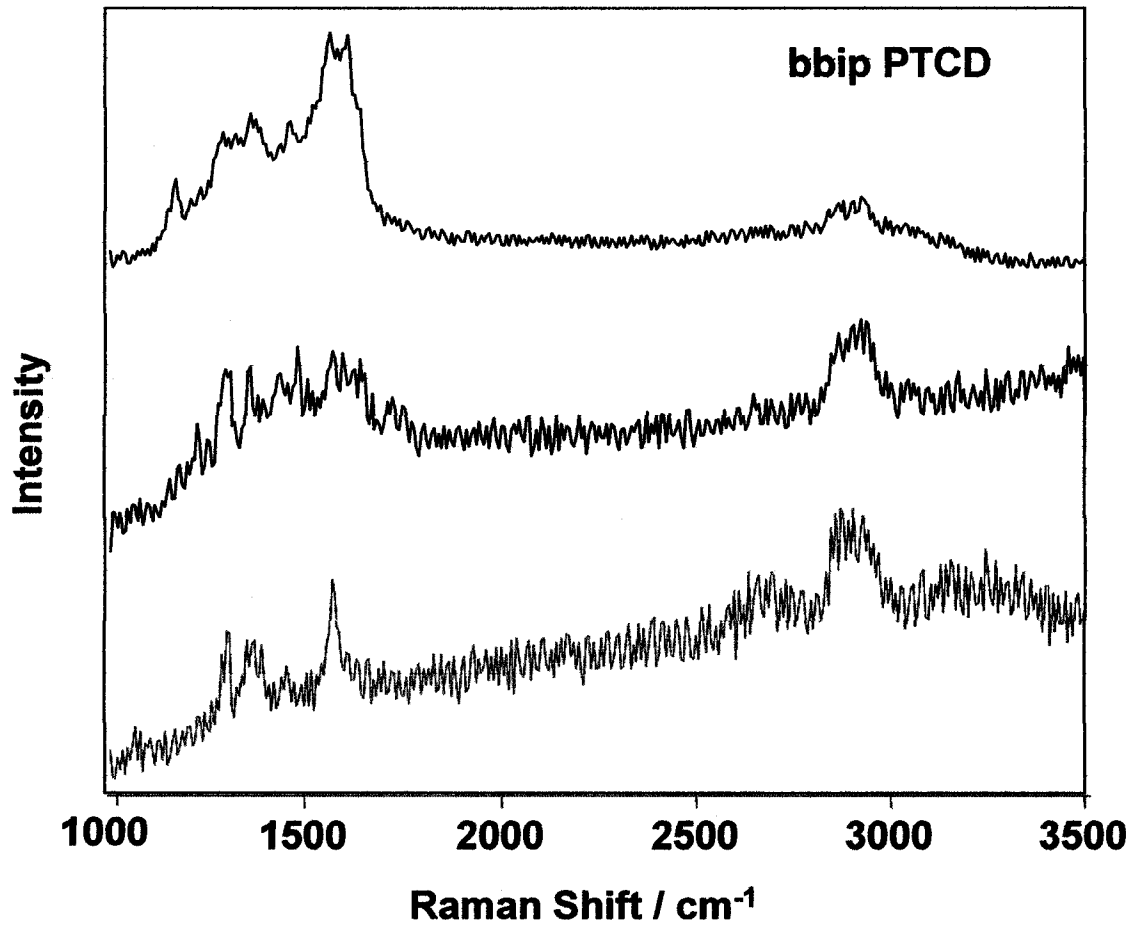

Figure 4.15: Spectra of the background carbon background. Comparison of the carbon background to successful single molecule detection (bottom)

The second major challenge to SMD, was the perylene signal diminishing with the molecule's increased exposure to laser light. This effect could be attributed to photodegradation, as observed for the concentrated LB SERRS, or could be the result of some other photoinduced process such as molecular movement driven by the laser. To minimize these problems, it was necessary to use very low laser power, generally < 20 μW at the sample. Even with these levels, large collection times still resulted in poor spectra that were dominated by the background. This was also true for all attempts at

Reproduced with permission of the copyright owner. Further reproduction prohibited without permission.

increasing the number of accumulations. Attempts at acquiring accumulated spectra resulted in a blurring and broadening of the signal caused by a changing spectrum with time. This is demonstrated in Figure 4.16, where two consecutive spectra from the same spot are shown.

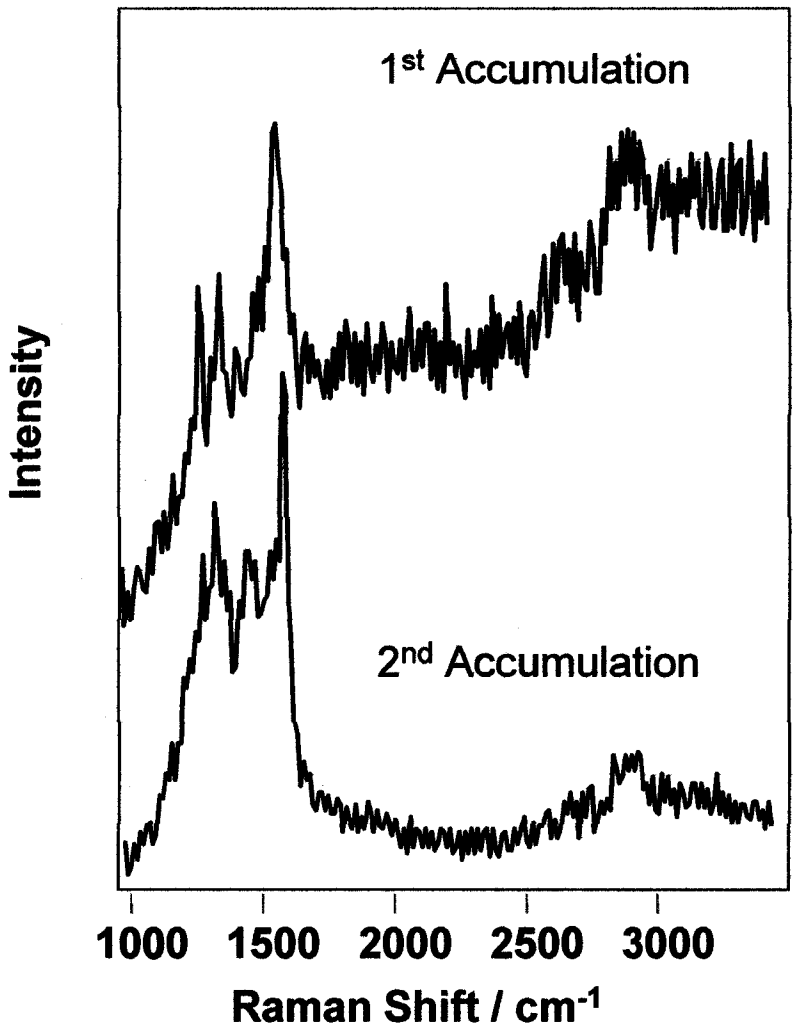

Figure 4.16: Difficulties in collecting SM Spectra. Illustrating the difficulty in attempting to accumulate signal from single molecule of azo-PTCD, the top spectrum is the initial signal recorded. The second was recorded 10 seconds later. The SM signal is gone and the carbon background is dominant.

Reproduced with permission of the copyright owner. Further reproduction prohibited without permission.

The disappearance of the single molecule spectrum is shown for the case azo-PTCD. To further investigate these signal losses, static spectra with a reduction in exposure times to 1 second were taken. These SERRS experiments were performed on an LB film containing 1 azo-PTCD molecule/μm^2 and using 514.5 nm excitation. Spectra were recorded upon the first illumination of the sample. On initial exposure, single molecule spectra were recorded from several spots of the LB film, with the characteristic fundamental peaks observed with relatively strong intensity. However, subsequent spectra, recorded 1 second later, showed no signal. Figure 4.17 shows one such occurrence of signal disappearance. Dynamical studies of the SM-SERRS signal proved elusive for there was no return of the signal at a given spot after the initial spectrum had been recorded. Again the origin of the signal loss is not clear but SM bleaching has been reported for the case of SM-SERRS of Rhodamine 6 G.[11] The more general problem of photodegradation is addressed in the Chapter 6.

Reproduced with permission of the copyright owner. Further reproduction prohibited without permission.

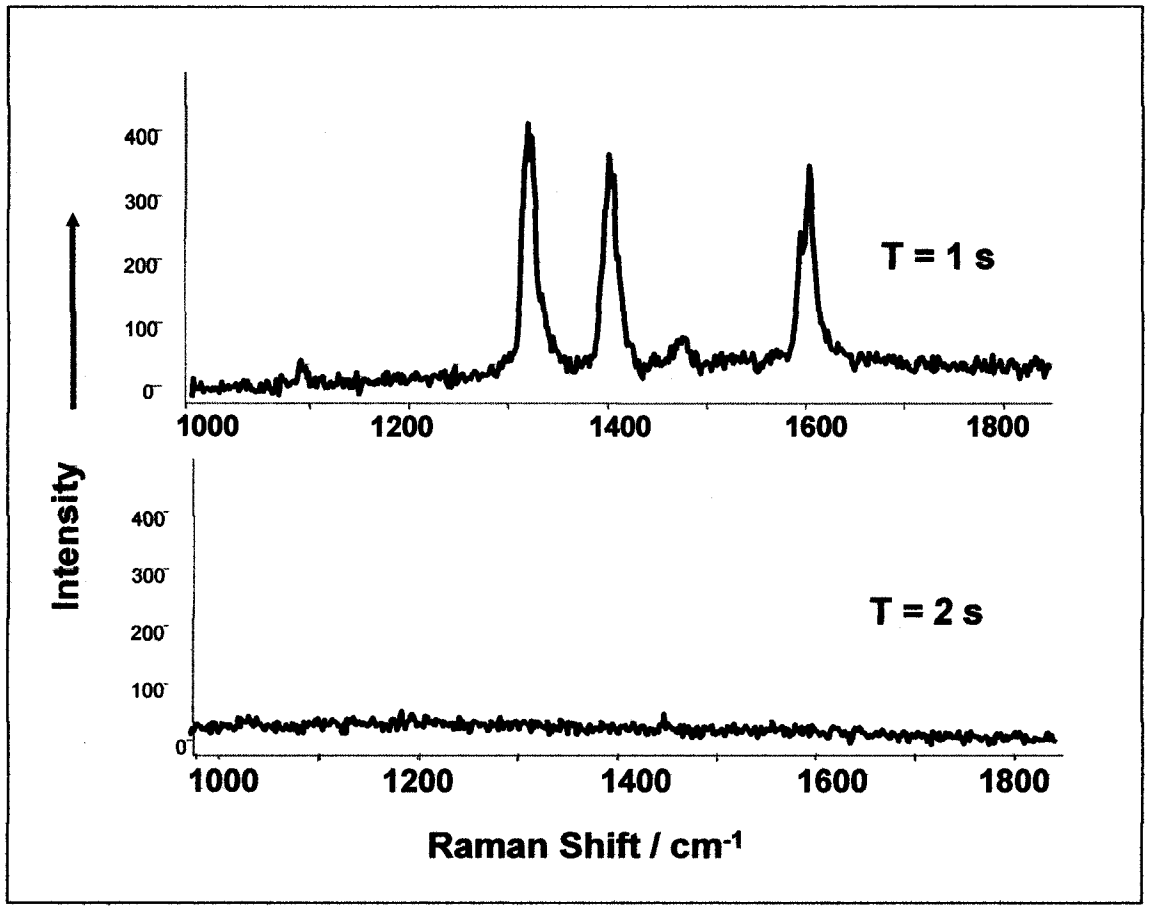

Figure 4.17: Demonstration of the disappearance of SM signal for azo-PTCD.

To summarize, only with low ED, small collection times ($\leq$ 10s) and a single accumulation, were SM signals detected. In addition, sampling had to be conducted on fresh spots upon first exposure to the laser excitation. Any exposure prior to accumulation resulted in a background dominated spectrum. By carefully following these steps, SM-SERRS could be measured with reasonable quality.

An important observation for these results is the fact that SM spectra are "rare events" in these experiments. When a single spectrum is recorded, it is the result of a very labour intensive search for SM's. (experiments were carried out by a random sampling of

Reproduced with permission of the copyright owner. Further reproduction prohibited without permission.

the surface). It generally took many attempts, probing many spots before a spectrum could be recorded. Consider the images in Figure 4.18. The top image shows the laser spot as observed through a mounted CCD camera on the microscope, giving the ~ $1\mu m^2$. The middle picture is a representative AFM image of the 6 nm mass thickness Ag island film used in this investigation. The dimension of the image is a 1 x 1 μm. Outlined is the approximate $1\mu m^2$ probe area sampled by the laser when using a 50X (NA .75) objective. The probe molecule is slightly exaggerated in size for ease of viewing, but the image is roughly to scale (1 probe molecule ~ 65 $Å^2$). The final image is that of 250 X 250 nm magnification of the same film, again with probe molecule approximately to scale. These are provided to give a clearer insight to the LB approach to SM detection. Within the probe area there are ~ 4,000,000 molecular sites for the target molecule to reside. As can be see in the AFM image, in the same area there are distributed ~ 400 particles. It is known that nanostructures such as this have very complex distribution of EM fields.[29,30] Figure 4.18 is an attempt to illustrate that fact. Only when a probe molecule resides in an area which has a significant enhancement at the excitation frequency will a SM signal be

Reproduced with permission of the copyright owner. Further reproduction prohibited without permission.

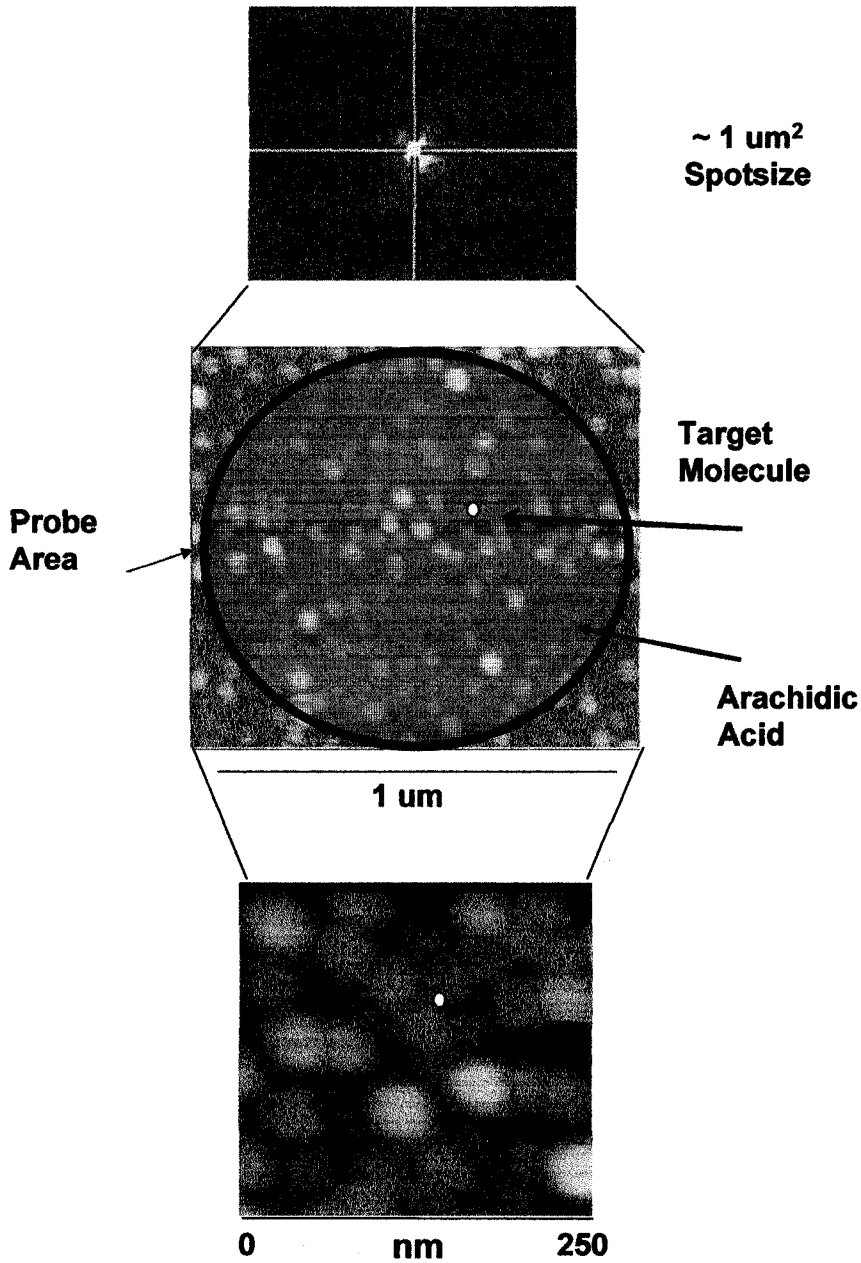

Figure 4.18: Illustration of the SM experiment.

Reproduced with permission of the copyright owner. Further reproduction prohibited without permission.

detected. The latter gives a possible explanation to the low probability of the SM events. The LB experiments on silver and gold island films for SM detection suggest that even at 100 and 10 molecules/μm^2 levels, what is detected are SM events. The plasmonics of these films as illustrated in Figure 4.19, may help to understand the arguments put forth at the beginning of this chapter. For SM detection, a minimum intensity is needed, in the case where resonance Raman is at play the required field enhancement is what is needed to put the signal above the detection limit as shown in Figure 4.20. This implies that the extreme field enhancement of "hotspots' are not required for SM detection in SERRS. If the excitation excludes any possibility of RR, then the needed enhancement is orders of magnitude higher and would require the intense fields associated with electromagnetic 'hotspots".

Reproduced with permission of the copyright owner. Further reproduction prohibited without permission.

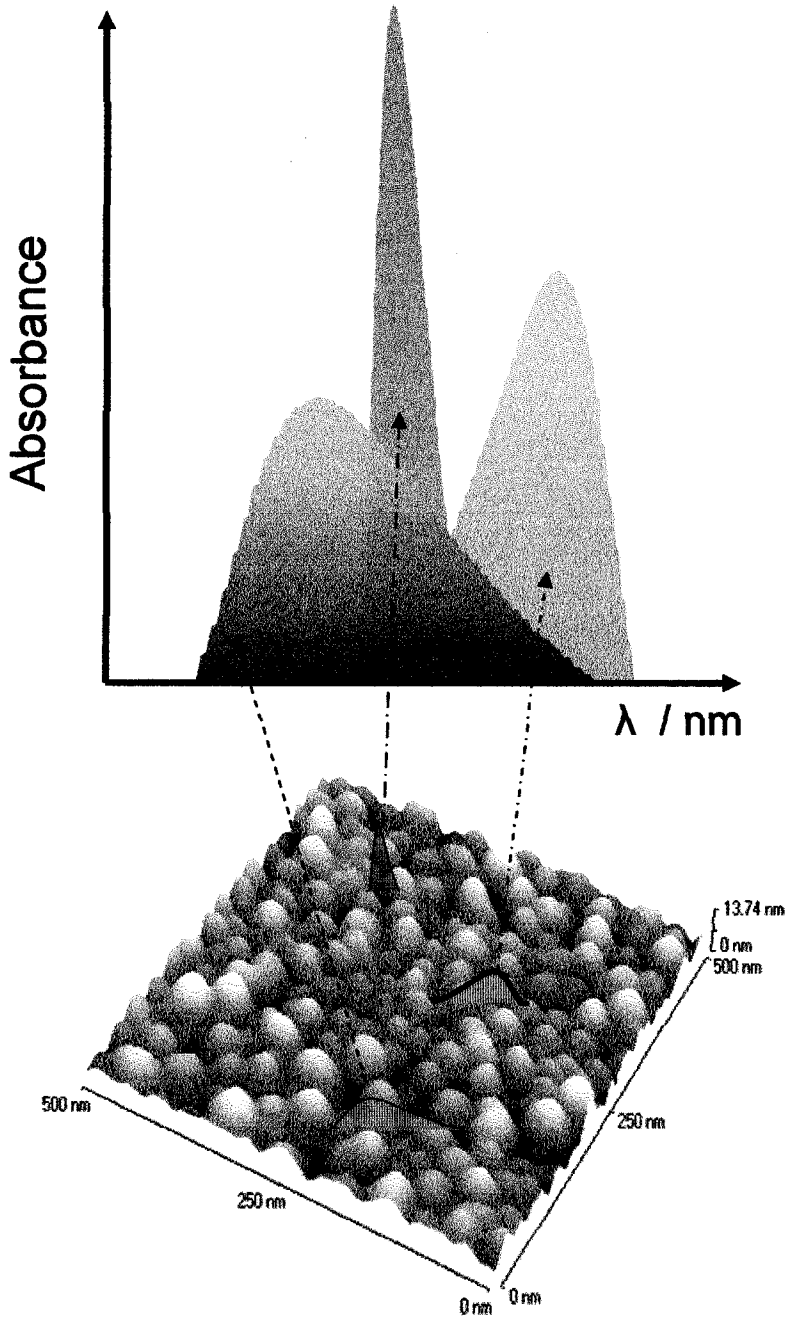

Figure 4.19: Illustration of the distribution of hotspot in an island film.

Reproduced with permission of the copyright owner. Further reproduction prohibited without permission.

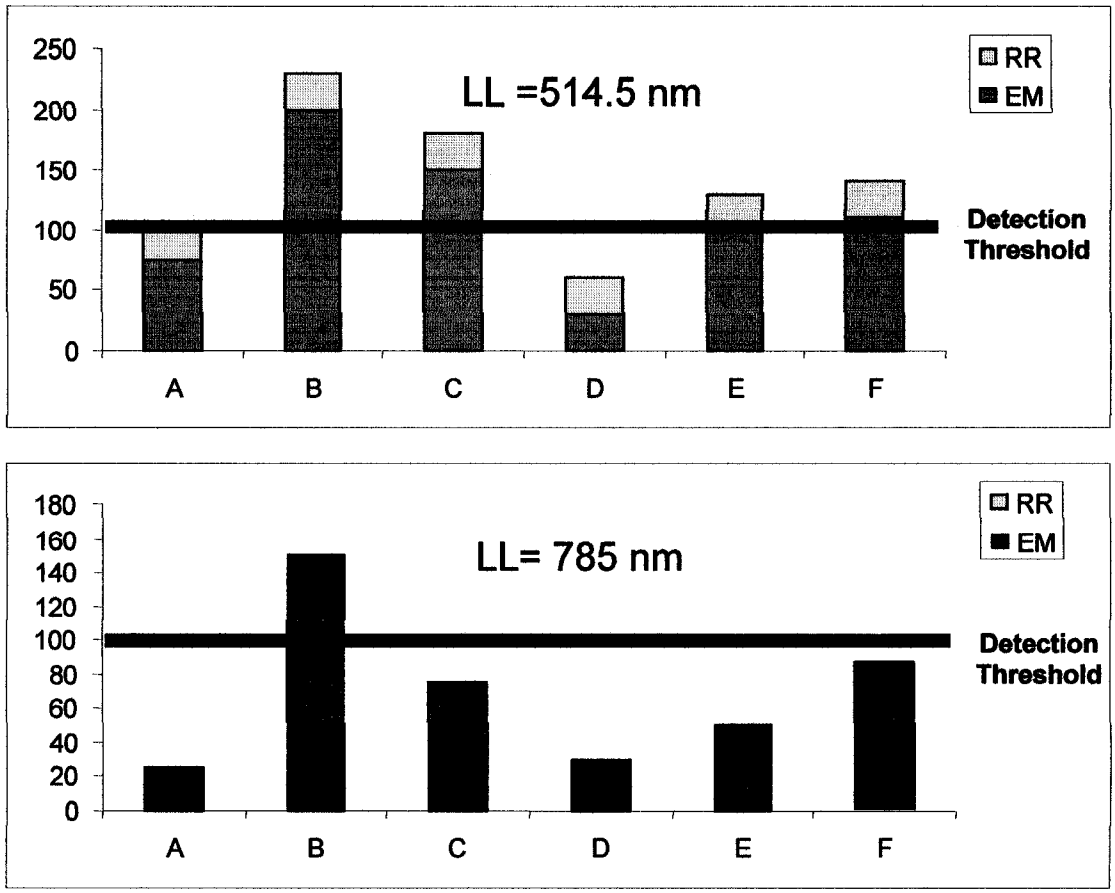

Figure 4.20: Graphical representation of the contributions to enhancement. The graph shows the relative contributions of the Electromagnetic enhancement and resonance Raman at two different laser lines for different hypothetical areas of a substrate, A-F.

4.7 Conclusions

Using the LB technique, and the spatial resolution of Raman microscopy, the SERRS of a single molecule, for three different PTCD derivatives, was collected. In each case, it was found that the single molecule SERRS allows for the observation of fundamentals and at least the first set of overtones and combinations. Evidence of possible single molecule photobleaching, as well as other peculiar features of SM spectra, has also been presented.

Reproduced with permission of the copyright owner. Further reproduction prohibited without permission.

References

(1) Fromm, D. P.; Sundaramurthy, A.; Kinkhabwala, A.; Schuck, P. J.; Kino, G. S.; Moerner, W. E. *Journal of Chemical Physics* **2006**, *124*.

(2) Moerner, W. E. *Journal of Physical Chemistry B* **2002**, *106*, 910-927.

(3) Kneipp, K.; Wang, Y.; Dasari, R. R.; Feld, M. S. *Applied Spectroscopy* **1995**, *49*, 780-4.

(4) Kneipp, K.; Wang, Y.; Kneipp, H.; Perelman, L. T.; Itzkan, I.; Dasari, R. R.; Feld, M. S. *Physical Review Letters* **1997**, *78*, 1667-1670.

(5) Nie, S.; Emory, S. R. *Science* **1997**, *275*, 1102-1106.

(6) Pettinger, B.; Picardi, G.; Schuster, R.; Ertl, G. *Electrochemistry (Tokyo)* **2000**, *68*, 942-949.

(7) Otto, A. *Physica Status Solidi A: Applied Research* **2001**, *188*, 1455-1470.

(8) Kneipp, K.; Kneipp, H.; Itzkan, I.; Dasari, R. R.; Feld, M. S. *Springer Series in Chemical Physics* **2001**, *67*, 144-160.

(9) Moskovits, M.; Tay, L. L.; Yang, J.; Haslett, T. L. In *Optical Properties of Nanostructured Random Media*; Shalaev, V. M., Ed.; Springer, 2001.

(10) Lemma, T.; Aroca, R. F. *Journal of Raman Spectroscopy* **2002**, *33*, 197-201.

(11) Maher, R. C.; Cohen, L. F.; Etchegoin, P. *Chemical Physics Letters* **2002**, *352*, 378-384.

(12) Corni, S.; Tomasi, J. *Journal of Chemical Physics* **2002**, *116*, 1156-1164.

(13) Goulet, P. J. G.; Pieczonka, N. P. W.; Aroca, R. F. *Canadian Journal of Analytical Sciences and Spectroscopy* **2003**, *48*, 146-152.

Reproduced with permission of the copyright owner. Further reproduction prohibited without permission.

(14) Le Rue, E. C.; Etchegoin, P. G. M., M. *Journal of Chemical Physics* **2006**, *125*, 204701-1 204701-13.

(15) Constantino, C. J. L.; Lemma, T.; Antunes, P. A.; Aroca, R. *Spectrochimica Acta, Part A: Molecular and Biomolecular Spectroscopy* **2002**, *58A*, 403-409.

(16) Goulet, P. J. G.; Aroca, R. F. *Analytical Chemistry* **2007**, *79*, 2728-2734.

(17) Constantino, C. J. L.; Lemma, T.; Antunes, P. A.; Aroca, R. *Analytical Chemistry* **2001**, *73*, 3674-3678.

(18) Goulet, P. J. G.; Pieczonka, N. P. W.; Aroca, R. F. *Analytical Chemistry* **2003**, *75*, 1918-1923.

(19) Shegai, T. O.; Haran, G. *Journal of Physical Chemistry B* **2006**, *110*, 2459-2461.

(20) Le Ru, E. C.; Meyer, M.; Etchegoin, P. G. *Journal of Physical Chemistry B* **2006**, *110*, 1944-1948.

(21) Kneipp, K.; Kneipp, H. *Applied Spectroscopy* **2006**, *60*, 322A-334A.

(22) Habuchi, S.; Hofkens, J. In *Surface-Enhanced Raman Scattering: Physics and Applications*, 2006; Vol. 103.

(23) Futamata, M. *Faraday Discussions* **2006**, *132*, 45-61.

(24) Bizzarri, A. R.; Cannistraro, S. In *Surface-Enhanced Raman Scattering: Physics and Applications*, 2006; Vol. 103.

(25) Petty, M. C. *Langmuir-Blodgett Films. An Introduction*; Cambridge University Press: Cambridge, 1996.

(26) Morris, D. E.; Woodruff, W. H. *Journal of Physical Chemistry.* **1985**, *89*, 5795-8.

(27) Constantino, C.; Duff, J.; Aroca, R. *Spectrochimica Acta, Part A: Molecular and Biomolecular Spectroscopy* **2001**, *57A*, 1249-1259.

Reproduced with permission of the copyright owner. Further reproduction prohibited without permission.

(28) Kam, A.; Aroca, R.; Duff, J.; Tripp, C. P. *Internet Journal of Vibrational Spectroscopy* **2000**, *4*.

(29) Markel, V. A.; Shalaev, V. M.; Zhang, P.; Huynh, W.; Tay, L.; Haslett, T. L.; Moskovits, M. *Physical Review B: Condensed Matter and Materials Physics* **1999**, *59*, 10903-10909.

(30) Otto, A. *Journal of Raman Spectroscopy* **2006**, *37*, 937-947.

Reproduced with permission of the copyright owner. Further reproduction prohibited without permission.

CHAPTER 5

DISPERSIONS RELATIONS IN SERS

Reproduced with permission of the copyright owner. Further reproduction prohibited without permission.

5.1 Introduction

In principle, there exists a dispersion of the Raman spectral bands even when the excitation is far from the energy required for a molecular electronic transition. In practice, excluding the v^4 dependence, for normal Raman scattering, the relative intensities of Raman bands, which follow the laser line used for excitation, and the Raman spectrum can be considered independent of exciting frequency. This approximation breaks down though when the excitation line is within the envelope of an electronic absorption of the molecular system, which is the case of the resonance Raman scattering (RRS) effect. The RRS creates a dispersion profile that is characteristic to a given molecular system. In the case of Surface-Enhanced Raman Scattering, there are additional dispersion relations present which can be advantageously used for chemical identification. In this section, it will be shown how the measured spectrum can be influenced by both the effect of molecular dispersion and the various consequences of the electromagnetic fields that give rise to the enhancement. As a demonstration the small organic molecule 1,8-naphthalamide on silver colloids is presented as a case study. Spectral interpretation is aided with computational calculations and spectral simulations. This example is also used as a guide to discuss what factors and variables must be considered in the interpretation of SERS spectra. As well, I will suggest how these relations may one day be used in the use of single molecule studies to probe the local electromagnetic field.

5.2 Background

To bring about the enhancement of signal seen with SERS; a target molecule must be brought into proximity to an enhancing "surface". In the interaction between the analyte and the surface, there are many variables that come into play.[1] The most

Reproduced with permission of the copyright owner. Further reproduction prohibited without permission.

important is what type of adsorption, chemical or physical, will occur. The additional complexities of the former are due to the fact that what is being analysed is no longer the original target molecule, but now a complex with different molecular properties. The complex may present a completely different Raman spectrum as well as new electronic states (new absorption spectrum). In the presence of new electronic states, additional resonances can exist which may result in resonance Raman contributions. These new electronic resonances (for instance, charge transfer states) carry a large intrinsic Raman cross section and correspondingly an intense Raman signal, a result that is generally termed a "chemical" enhancement and can account for a small part to the overall enhancement.[2] Even though the result of chemical adsorption is a complex (new species), it can be characterized for a given analyte-metal system. With cautious vibrational analysis of the SERS spectra, it can be linked directly to the original analyte.

This illustrates one of the primary difficulties of SERS spectroscopy, the proper interpretation of the recorded spectra. The classification of SERS spectra provides a unique challenge over that of traditional Raman by the presence of features that are dependent on the excitation line used. The various dispersions relations seen in SERS experiments are discussed in this section. The observed dispersions may be separated into two categories, those that are dependent on the excitation line used (λ), and those that are dependent on the particular frequency of the Raman scattered photons (cm^{-1}). The dispersions due to the excitation frequency include: resonance Raman enhancement[3], the magnitude of SERS enhancement[4], and, as will be shown, the so called surface selection rules[5]. The second dispersion effect is due to the fact that the SERS enhancement factor cannot necessarily be applied uniformly to the Raman scattering of all vibrations.[6]

Reproduced with permission of the copyright owner. Further reproduction prohibited without permission.

5.2.1 Surface Selection Rules

In addition to chemical perturbations, the SERS spectrum impacted by the fact that electric fields are polarized at metallic surfaces. As was pointed out by Moskovits, this polarization is responsible for what is called the surfaces selection rules or propensity rules of SERS.[5] This effect is briefly summarized here.

The metal surfaces that generate the necessary surface plasmons have a preferential treatment to the components of an electric field. Each metal nanostructure has a peak plasmon resonance frequency. To the red of this frequency, the metallic surface preferentially enhances the electric field component tangential to the surface, E_t. To the blue, it is the normal component of the electric field, E_n that is relatively enhanced. At the plasmon resonance frequency, the enhancement is approximately equal for both components. This can be better illustrated by looking at the special case of a silver nanosphere. At the surface of a sphere of radius R, Moskovits and Suh have shown that the relative enhancement of the averaged field components can be summarized by the following relationships:[5]

$$\begin{aligned} \overline{E_t^2} &\propto 2E_o^2\left|1-g\right|^2 \\ \overline{E_n^2} &\propto E_o^2\left|1+2g\right|^2 \\ g &= \frac{\varepsilon-\varepsilon_o}{\varepsilon+2\varepsilon_o} \end{aligned} \qquad (5.1.1)$$

In Figure 5.1, the ratio of these components were calculated for a single silver sphere in water (ε_o = 1.77) with a plasmon resonance at 390 nm, and are plotted as a function of wavelength.

Reproduced with permission of the copyright owner. Further reproduction prohibited without permission.

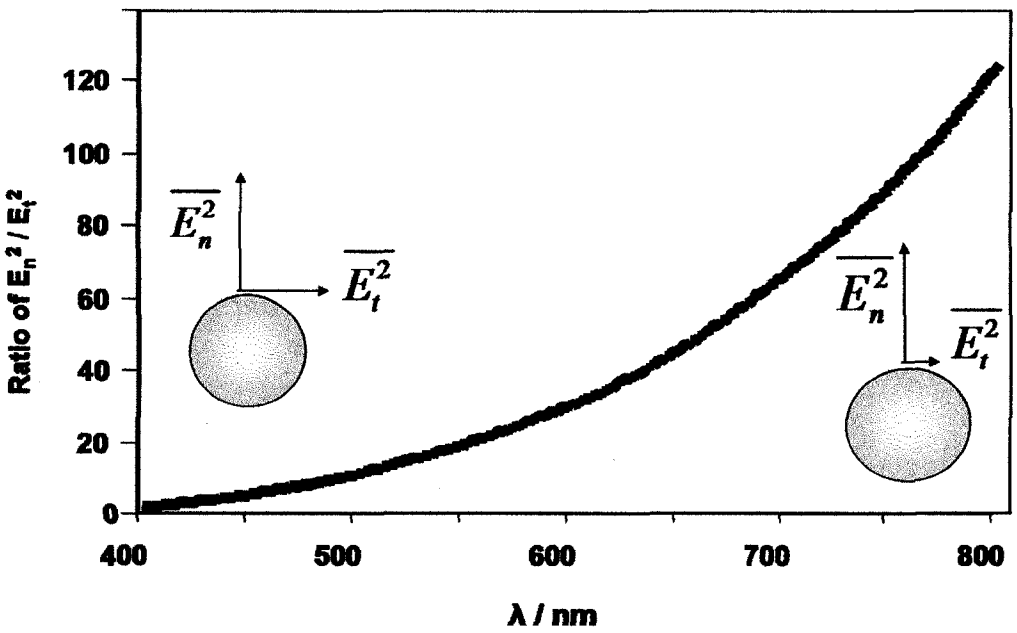

Figure 5.1: Ratio of normal to tangential field components. The field components are plotted as a function of wavelength for a silver sphere, peak plasmon resonance at 390 nm

For a molecule whose orientation is fixed to the surface, (such is the case of chemisorbed molecules) this will impact the fields a particular vibrational mode will experience. For instance, for an analyte fixed with its main axis (z) of symmetry aligned normal to the surface, the following predictions can be made. To the red of the plasmon resonance frequency, modes with polarizability components that have α_{zz} will be preferentially enhanced over those that have $\alpha_{xz,}$, α_{yz} , α_{xy} components. To the blue, the dominance of α_{zz} is significantly lessened and bands of all symmetries can be seen with measurable intensity.

5.2.2 Dispersion in the Enhancement factor

Recall that the magnitude for a particular Raman vibration is a factor of the field enhancement at frequency of excitation and the Raman scattered photon:

Reproduced with permission of the copyright owner. Further reproduction prohibited without permission.

$$G \approx E_{laser}^2 \bullet E_{Raman}^2 \tag{5.1.2}$$

More explicitly:

$$G \approx \left| \frac{\varepsilon(\omega_o) - \varepsilon_\circ}{\varepsilon(\omega_o) + 2\varepsilon_\circ} \right|^2 \bullet \left| \frac{\varepsilon(\omega_{RS}) - \varepsilon_\circ}{\varepsilon(\omega_{RS}) + 2\varepsilon_\circ} \right|^2 \tag{5.1.3}$$

This implies that for a well defined plasmon mode, not all vibrational modes are enhanced equally. Modes that are shifted farther away from the excitation line, and the center of the plasmon resonance, will be less enhanced than those that lie close. This is shown in Figure 5.2, for the case of a single ellipsoid.[7] The maximum enhancement occurs when the two factors are coincident, and sharply drops off from there.

In addition, though the Raman spectrum is assumed to be independent of the laser line used for excitation (outside resonance conditions), the spectral wavelength span that a Raman spectrum covers is not. This is shown in Figure 5.3, where the span for a Raman spectrum taken with 514 nm and 785 nm excitations, is compared, given 116 nm and 297 nm respectively.

Reproduced with permission of the copyright owner. Further reproduction prohibited without permission.

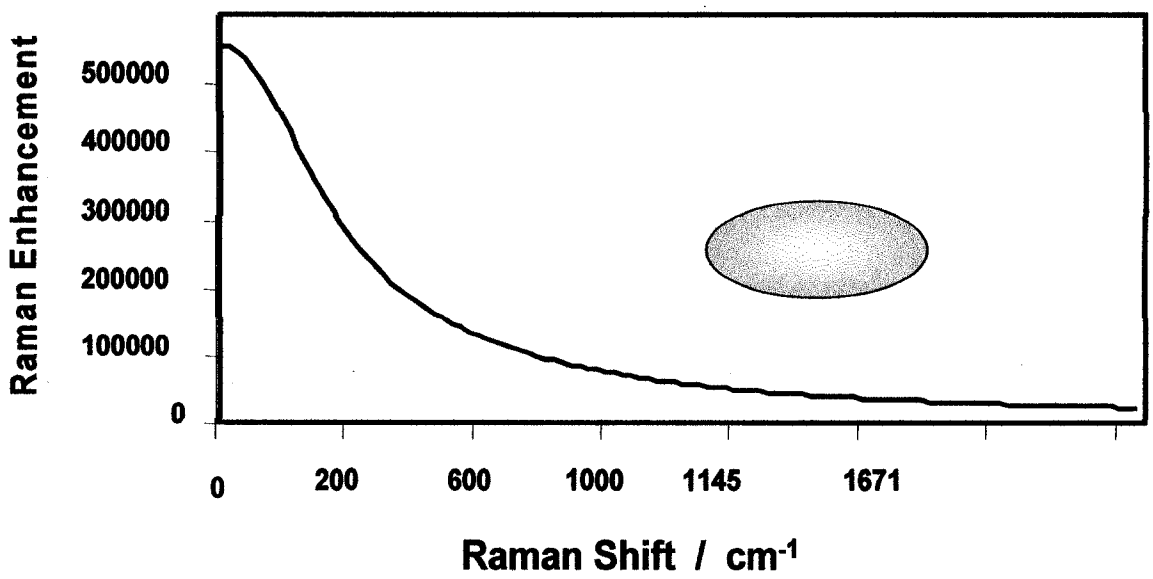

Figure 5.2: Calculated Enhancement Factor for a silver ellipsoid. The ellipsoid has an aspect ratio 3:1. The enhancement factor is plotted as function of Raman shift when excited at peak resonance (407 nm). Calculation of enhancement factor based on the formulism of Zeman and Schatz.[8]

Reproduced with permission of the copyright owner. Further reproduction prohibited without permission.

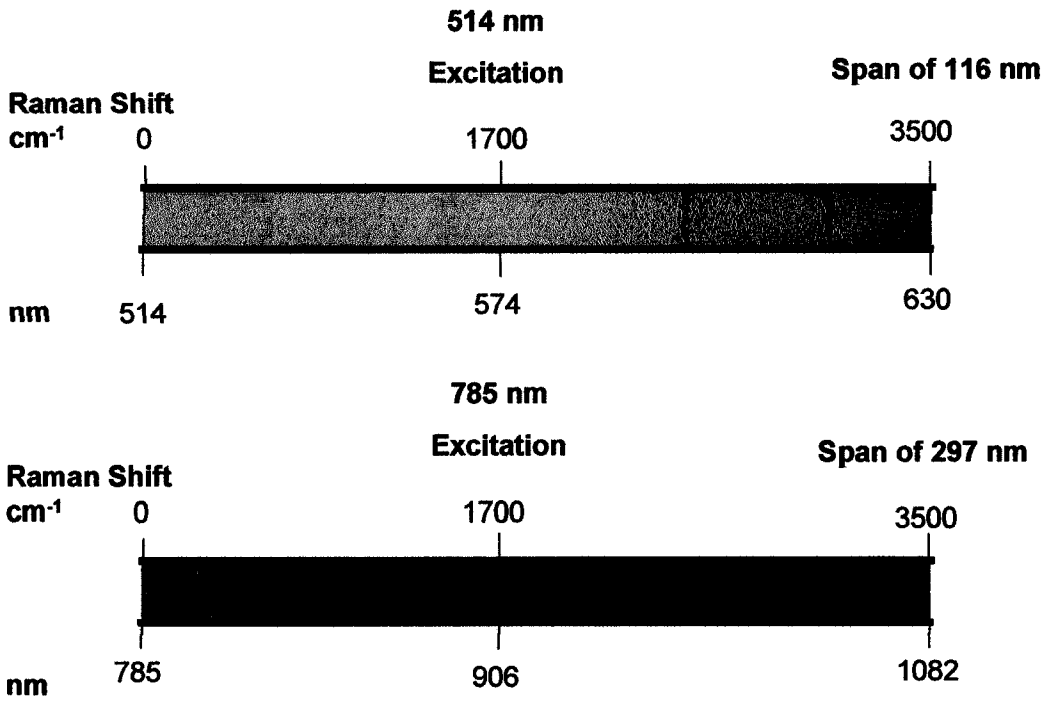

Figure 5.3: Comparison of the wavelength span of a Raman spectrum when taken at 514.5 and 785 nm

In the section to follow, the role of these dispersion relations are examined for the case study of the small molecule 1,8-naphthalimide and its SERS signal as measured with Ag colloids as the substrate.

5.3 Experimental

1,8-naphthalimide (NPIMH) (99% pure) was acquired from Aldrich. Raman spectra were acquired with < 1 mW of laser power. Solid spectra were recorded with 50X objectives, while solution spectra were recorded with the samples in a quartz cuvette and the f/15 objective. Silver colloids were prepared by the citrate reduction method outlined by Lee and Meisel.[9] The resulting nanoparticles in an aqueous solution showed a peak plasmon at 420 nm. Samples for SERS studies were prepared from a stock 10^{-3} M

Reproduced with permission of the copyright owner. Further reproduction prohibited without permission.

NPIMH ethanol solution with 10 μL added to 3 mL of silver colloids, giving a final concentration of NPIMH to be 10^{-5} M.

5.4 Computational Method

The vibrational analysis in this study was aided by quantum mechanical calculations for geometry optimization and computation of Raman frequencies and intensities. The Gaussian 03 computational suite with the density functional theory of Becke's three parameter functional, including the Lee et al. correlational functional, was used (B3LYP).[10,11] Calculations for the gas phase monomer were completed with the 6-311G(d) basis set, while for the gas phase Ag complex, the Lanl2DZ basis set was used.[12,13] No scaling factors were applied to calculated Raman frequencies. These structures were visualized with the aid of GaussView 03 for Windows.

5.5 Results and discussion

5.5.1 Raman and Resonance Raman Scattering of NPIMH

NPIMH is a molecule with C_{2v} symmetry with a total of 60 normal modes.[14] In previous vibrational and SERS studies of this molecule it was shown to form a surface complex with Ag.[14] The molecule shows two strong electronic absorptions, at 231 and 338 nm, when measured in an ethanol solution as shown in Figure 5.4.

Reproduced with permission of the copyright owner. Further reproduction prohibited without permission.

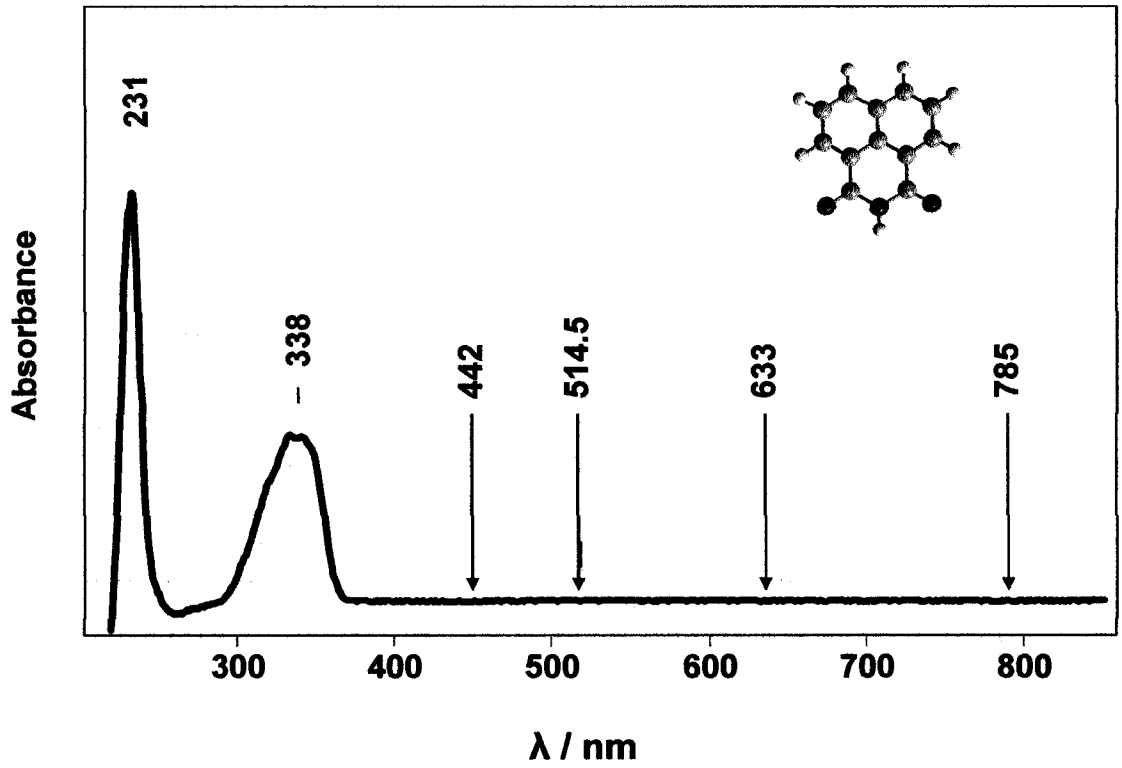

Figure 5.4: UV-Vis absorption spectrum of 1,8-naphthalimide in ethanol. The absorption spectrum is shown as well the wavelengths of the excitation lines used for SERS are indicated.

To ascertain the best vibrational assignment for the SERS spectra, a full and thorough investigation of the spontaneous non-enhanced Raman scattering was first conducted. Raman spectra of the powder were recorded with several excitations lines covering the UV to near-IR (325, 442, 514, 633, 785 nm). Looking at the UV-Vis absorption in Figure 5.4, the molecule has a strong band about 338 nm. This would indicate that Raman spectrum taken with the 325 nm laser would constitute a resonance Raman spectrum. The non-resonant Raman spectral profile of NPIMH shows little variation in the range of 800 cm^{-1} to 1700 cm^{-1}.

Reproduced with permission of the copyright owner. Further reproduction prohibited without permission.

To aid in vibrational assignment and to establish symmetry species of the normal modes, theoretical calculations were carried out. Geometry optimization and frequency calculation for the monomer were determined with DFT B3LYP level of theory with the 6-311g(d) basis set utilized. The C_{2v} symmetry was confirmed and the 60 normal modes were found to be distributed among the following symmetry species; $21a_1$, $8a_2$, 20 b_2 and $11b_1$. The calculated Raman spectrum shows excellent agreement when compared to that measured for the solid as seen in Figure 5.5 .

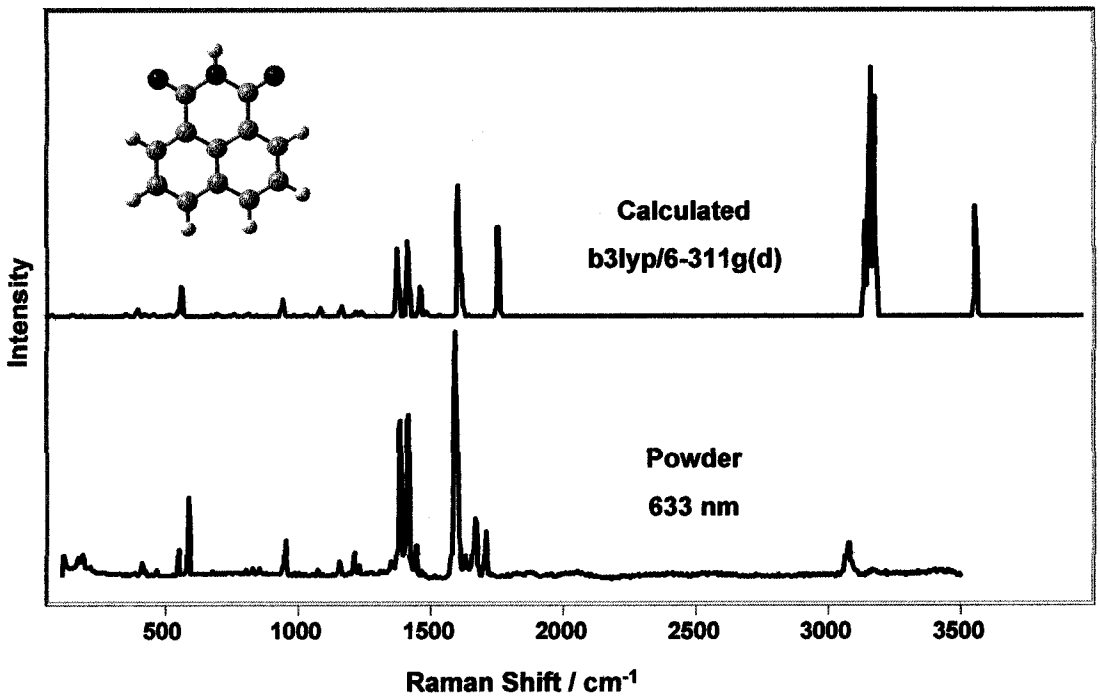

Figure 5.5: Comparison of calculated and experimental Raman spectra.

5.5.2 Surface Enhanced Raman Scattering of NPIMH

The SERS spectrum was attained from solutions of NPIMH and Ag citrate colloids. The plasmon absorption of the colloids before and after the addition of NPIMH is shown in Figure 5.6. The appearance of a broad band centered at 725 nm is indicative

Reproduced with permission of the copyright owner. Further reproduction prohibited without permission.

of aggregation of the colloid on addition of analyte. This results in a redshift of the surface plasmon for those aggregated particles.[15]

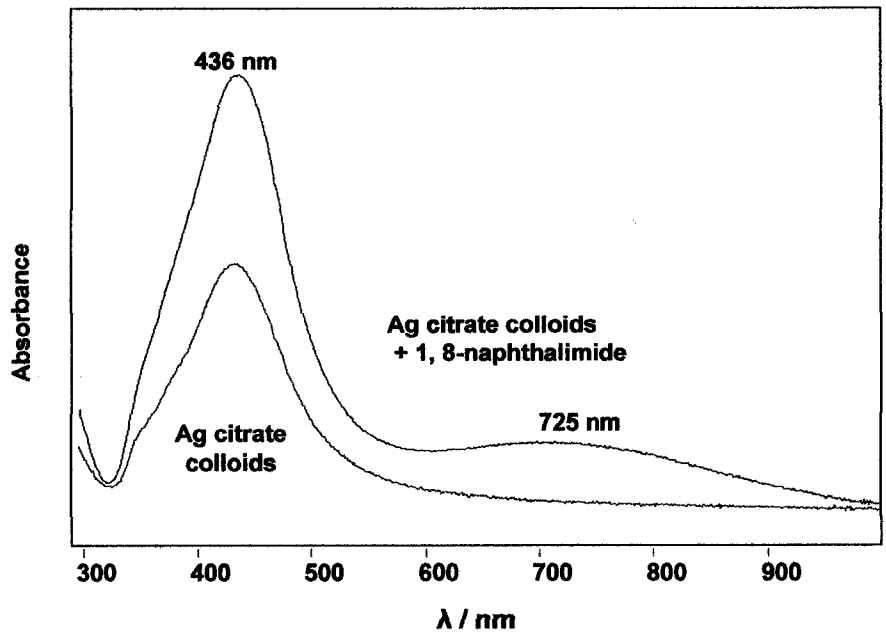

Figure 5.6: Plasmon absorption spectra of Ag colloids with and without NPIMH

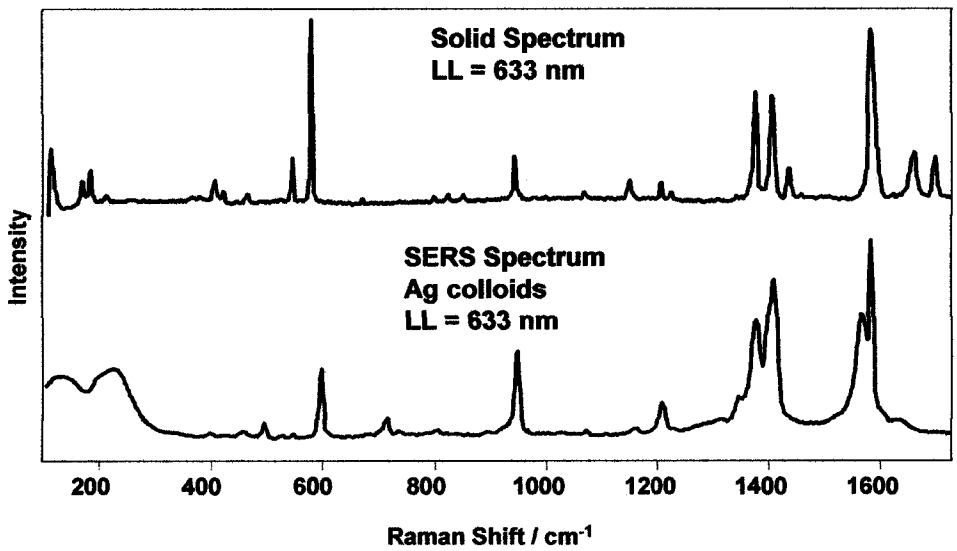

Figure 5.7: Comparison between the SERS and Raman spectrum of 1,8-naphthalimide powder

Reproduced with permission of the copyright owner. Further reproduction prohibited without permission.

A comparison between the spectrum measured for the solid and the measured SERS spectrum at 633 nm is shown in Figure 5.7.

There are several key differences that are seen between the two spectra. The appearance of new bands is indicative of the surface complex between silver and NPIMH. In particular is the presence of the low wavenumber bands around 200 cm^{-1} which have been assigned to the Ag-N stretching vibrations.[14] To help explain the other changes in the Raman profile a theoretical calculation of the silver salt of naphthalimide was carried out. To establish a clear comparison between the two calculations, a visualization program (GaussView 03) was used to assign corresponding vibrational modes. The complex showed the same C_{2v} symmetry and the results of this analysis are given in Table 5.1, in addition to band assignments. In the assessment of the vibrations of the NPIMH monomer and those of the vibrations of the NPIM-Ag complex there is one noticeable change, a down shift in the frequencies of the C=O bands. In the monomer, the symmetric CO stretch is found at 1775 cm^{-1}, while in the complex it is found at 1586 cm^{-1}. This trend is confirmed in the SERS spectrum where there is the appearance of a prominent new band at 1568 cm^{-1} not seen in the solid. This comparison between monomer, complex and the SERS spectrum are all shown in Figure 5.9

Reproduced with permission of the copyright owner. Further reproduction prohibited without permission.

Table 5.1: Observed and Calculated Raman frequencies and intensities

	Calculated				Measured SERS				
	Monomer		Ag-Complex		λ (nm)				Assignment
sym	cm^{-1}	Activity	cm^{-1}	Activity	442	514.5	633	785	
			177	9.9			223	226	N-Ag stretch
a_1	464	2.4	515	18.9	496	494	494	495	
a_1	570	39.5	577	49.6	598	594	595	595	Ring Breathing
a_1	703	1.8	738	31.0	715	711	713	713	
a_1	816	1.7	818	0.9	789	787	787	785	
a_1	954	24.2	951	48.0	949	945	946	948	Ring Stretch
a_1	1096	11.7	1096	20.9			1071	1075	
a_1	1188	0.1	1184	12.9	1160	1158	1160	1161	
a_1	1233	5.3	1234	21.1	1213	1206	1207	1209	
a_1	1378	4.3	1347	12.7	1352	1345	1346		Ring Stretch
a_1	1392	94.9	1449	274.6	1376	1375	1376	1379	C-N symm. stretch
a_1	1431	96.8	1411	0.5					
a_1	1477	40.2	1470	86.7	1400	1409	1409	1412	
a_1	1624	183.0	1627	121.2	1586	1583	1583	1587	Ring stretch
a_1	1636	41.0	1643	91.7					Ring stretch
a_1	1775	106.9	1586	44.7		1568	1567	1569	C=O symm. stretch
a_1	3171	130.4	3196	99.7			2979		C-H stretch
a_1	3189	202.0	3219	135.3	3153				C-H stretch
a_1	3207	309.6	3237	319.7					C-H stretch
a_1	3590	156.1							N-H stretch
a_2	432	3.5	443	3.6		455	454	452	
a_2	626	0.1	636	0.1	615	615			
b_1	708	1.9	758	1.0	740	735	733	734	
b_1	770	3.2			778				
b_1	800	0.3	812	0.9	805		804	805	
b_1	858	0.6	890	4.2		897	895		
b_1	960	1.3	1004	0.3	986				
b_1	999	1.6	1048	3.8	1012	1010	1003	1006	
b_2	402	9.7	407	7.6			396	393	
b_2	556	8.0	559	10.8	547	546	545	546	
b_2	679	0.7	697	0.5	655				
b_2	825	2.9	868	7.0	824	821			
b_2	1178	13.3	1201	10.2	1138				
b_2	1219	0.1	1244	0.8	1197	1194			
b_2	1253	5.5	1268	14.4	1297	1287			
b_2	1265	0.8	1350	0.8	1459				C-N anti-symm. stretch
b_2	1500	4.8	1497	3.7	1316	1314	1312		
b_2	1665	0.7	1675	7.4	1616	1614			
b_2	1773	20.0	1576	6.4					C=O anti-symm. stretch
b_2	3168	3.3	3194	6.5	2933	2930	2930		C-H stretch
b_2	3188	151.1	3218	123.7	3063	3061	3059		C-H stretch

Reproduced with permission of the copyright owner. Further reproduction prohibited without permission.

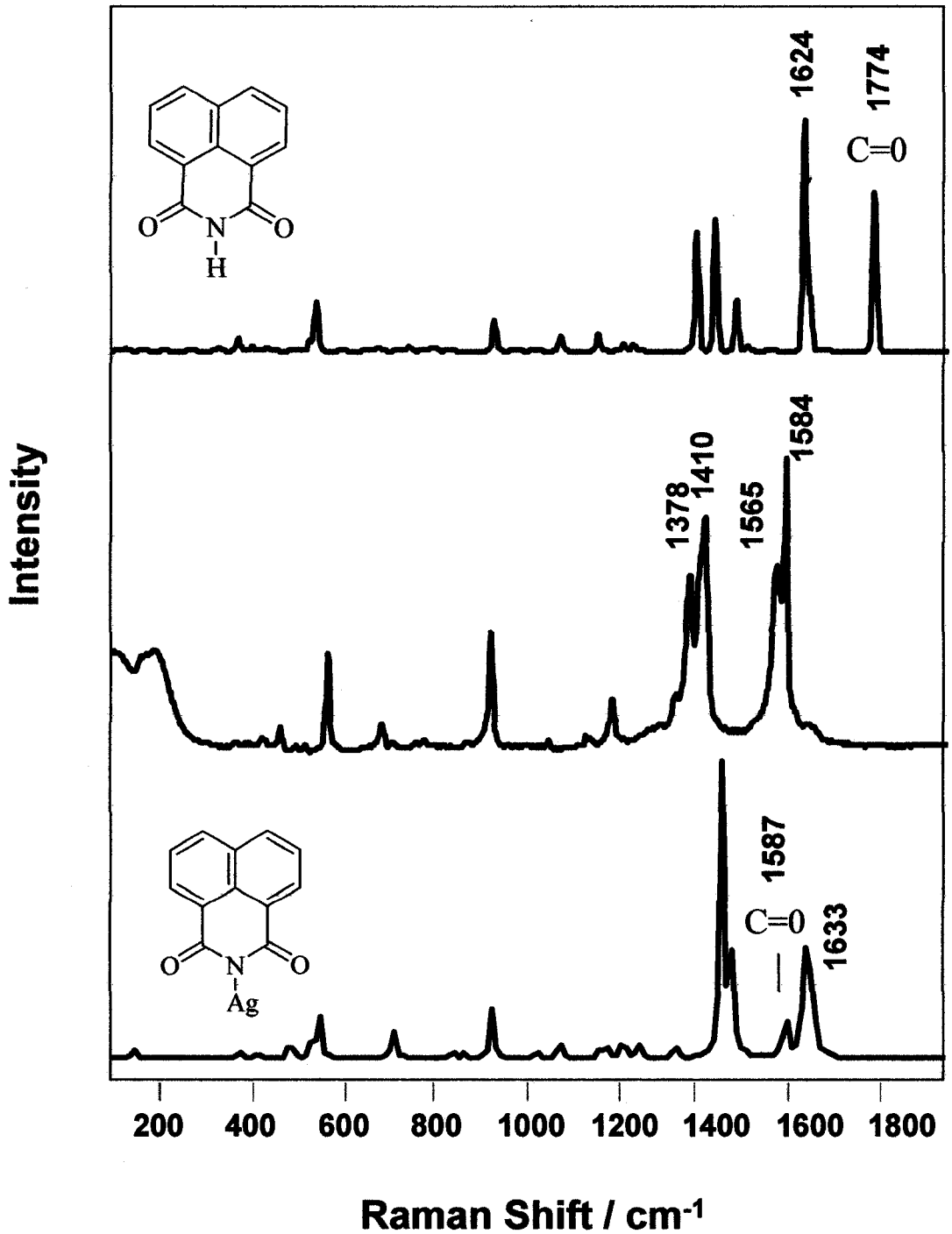

Figure 5.8: Comparison of Calculated and SERS spectra. The SERS spectrum (middle) is compared to the calculated monomer (top) and Ag complex (bottom). An artificial FWHM of 5 cm^{-1} is added to the calculated bands for comparison.

Reproduced with permission of the copyright owner. Further reproduction prohibited without permission.

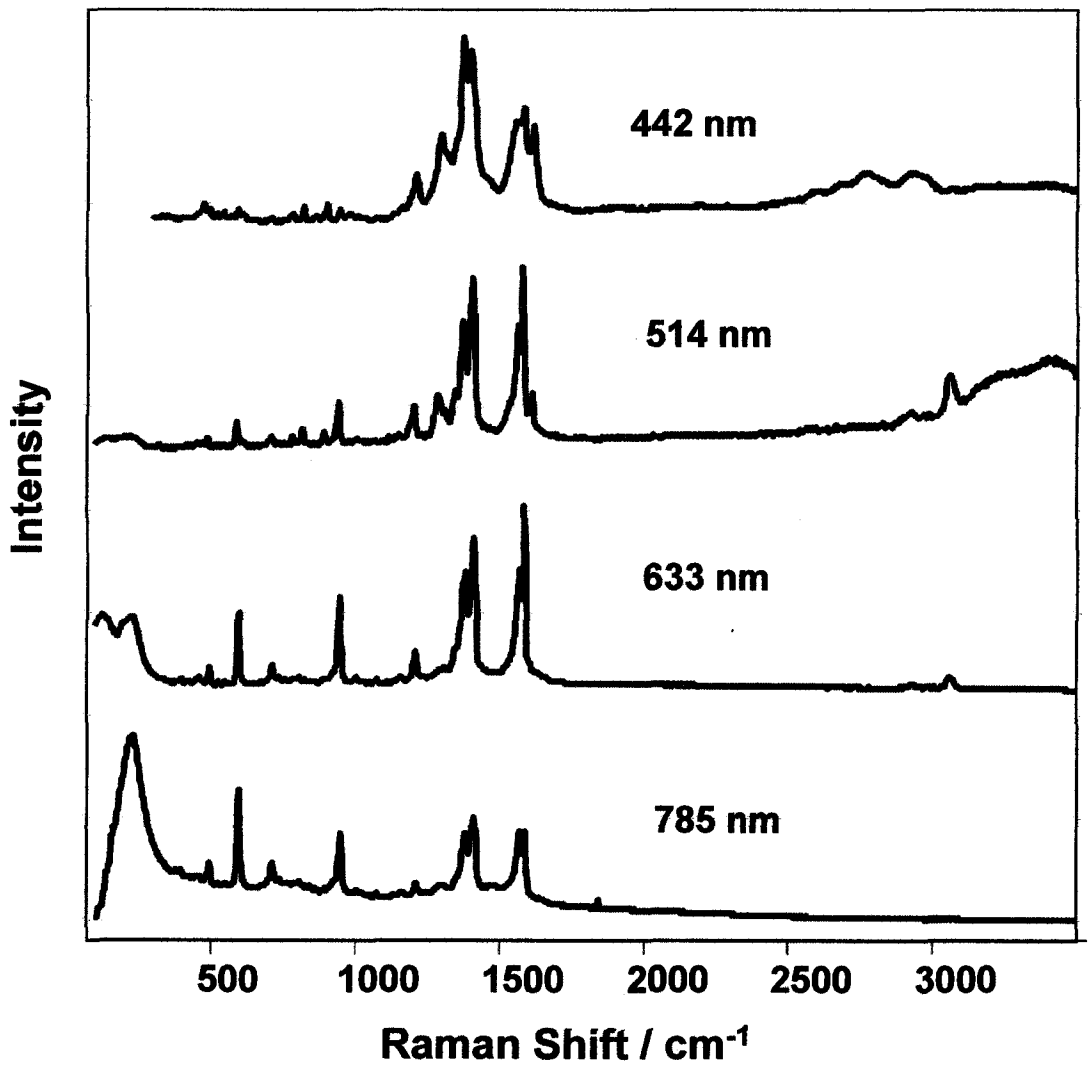

Figure 5.9: SERS spectra of NPIMH for several excitation lines.

Reproduced with permission of the copyright owner. Further reproduction prohibited without permission.

In Figure 5.9, the SERS spectra of NPIMH as recorded for excitation lines of 442, 514.5, 633, 785 nm, are shown. A quick glance can see the spectral profile is dependent on the excitation line. This is even clearer when the region of 400-1700 cm^{-1} is focused on as in Figure 5.10. In attempt to explain these changes, it is necessary to examine the extent of the contribution of the several dispersion relations discussed above.

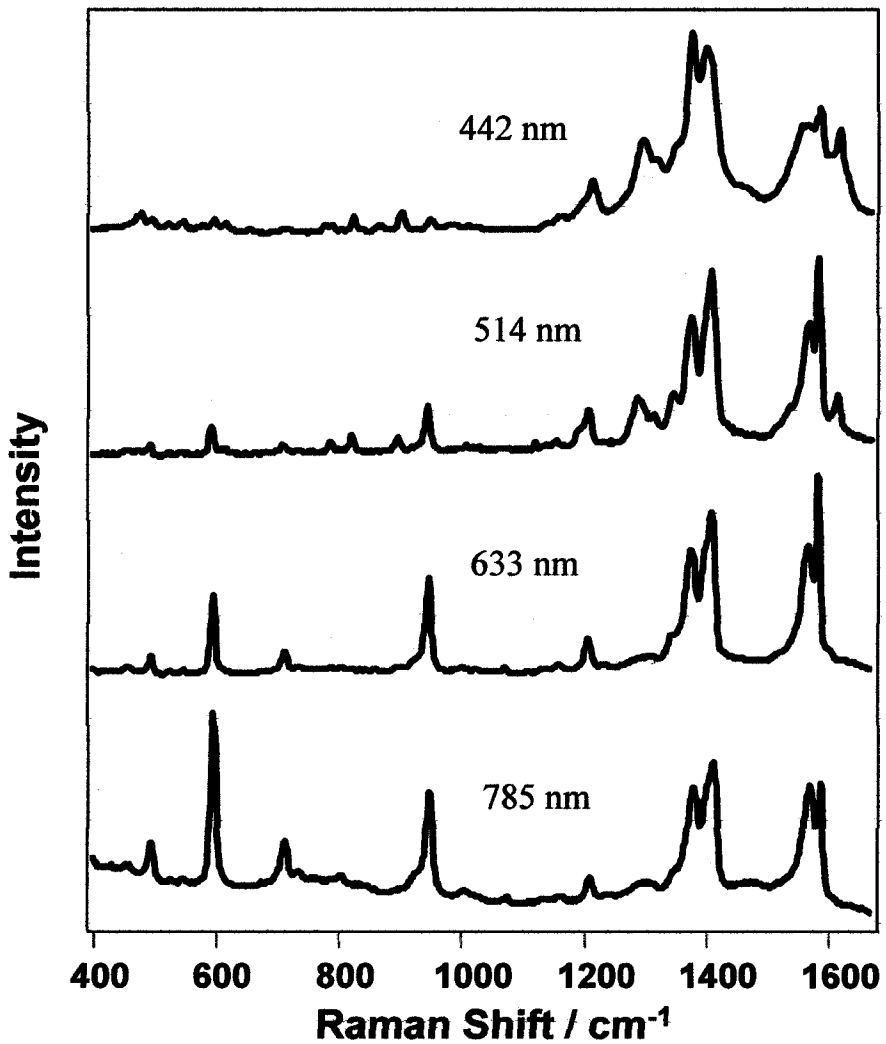

Figure 5.10: Comparison of SERS of NPIMH for several excitation wavelengths.

Reproduced with permission of the copyright owner. Further reproduction prohibited without permission.

5.5.3 Selection Rules and Spectral modeling

Beginning at the blue extreme, the SERS spectral profile at 442 nm can be, in part, explained by the contribution of a pre-resonant enhancement as evidenced by the dominance of the ring modes in the spectrum. This is supported by the similarities between the 442 spectrum and that taken of the solid NPIMH at 325 nm, seen in Figure 5.11.

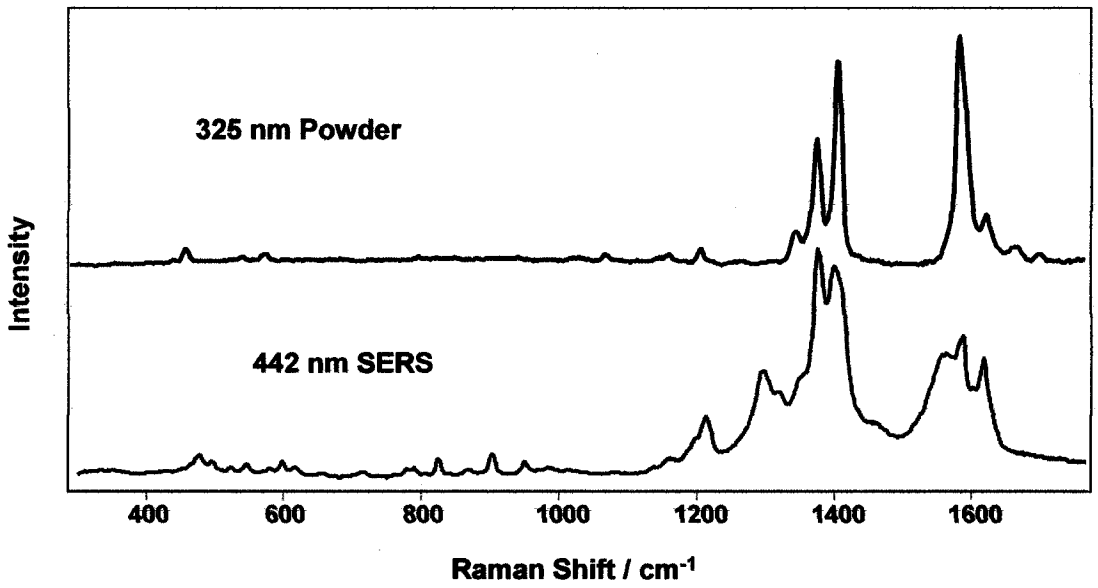

Figure 5.11: Comparison of SERS and UV-RR of NPIMH. The SERS spectrum from 442 nm is compared to the resonance Raman spectrum of the bulk at 325 nm. Evidence of pre-resonance is seen in the SERS spectrum.

This does not explain though the variation in the profile of the SERS spectra especially when compared to that measured at 785 nm, as seen in Figure 5.12. The 442 nm SERS spectrum clearly has many more modes contributing, while that at 785 nm is

Reproduced with permission of the copyright owner. Further reproduction prohibited without permission.

dominated by only a few. To explain this variation it necessary to look at the different symmetry species in conjunction with the surface selection rules for SERS.

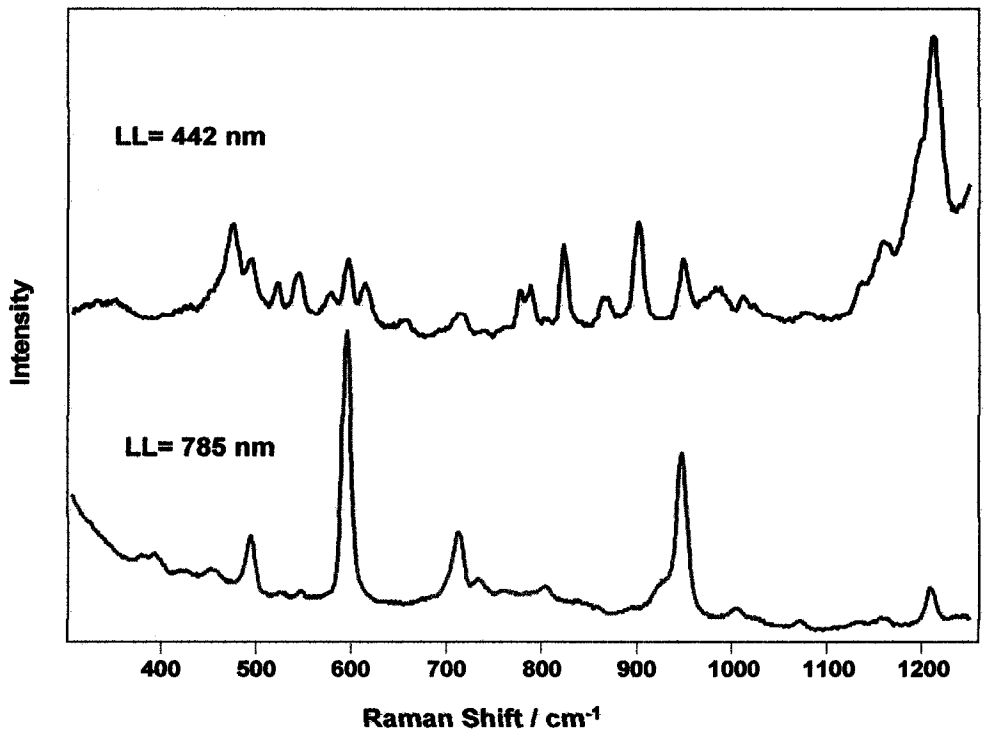

Figure 5.12. SERS at 442 nm and 785 nm.

The effect of the selection rules can be modeled by using as a basis set, the calculated vibrational modes of the NPIM-Ag complex. For a C_{2v} molecule oriented with axis of symmetry parallel to the surface normal, modes of a_1 symmetry will contain the α_{zz} polarizability tensor component, while a_2, b_1 and b_2 modes will have polarizability tensor components α_{xy}, α_{xz}, and α_{yz} respectively.[16] Using the model for a silver sphere as a reference, at 442 nm, E_t and E_n are approximately equal and so to should be the relative enhancements of a_1 modes to those of a_2, b_1 and b_2 symmetry. A simulated spectrum which includes all modes should find good agreement with the SERS profile measured at 442 nm. This was not the case; it was found that a better agreement occurred when E_t was

Reproduced with permission of the copyright owner. Further reproduction prohibited without permission.

considered to be slightly greater than E_n. By applying a factor of 5 (representing a E^2_t/E^2_n ratio of 5) to the calculated activities of a_2, b_1 and b_2 modes, a simulated spectrum was generated that shows good agreement with that of the SERS taken at 442 nm, as seen in Figure 5.13. This is not unreasonable result for the system studied here. Moskovits and Suh have shown that for aggregated systems of colloids, the main plasmon may be red-shifted; giving the possibility that 442 nm excitation is actually slightly to the red of the plasmon resonance, accounting for this obsevation.[5]

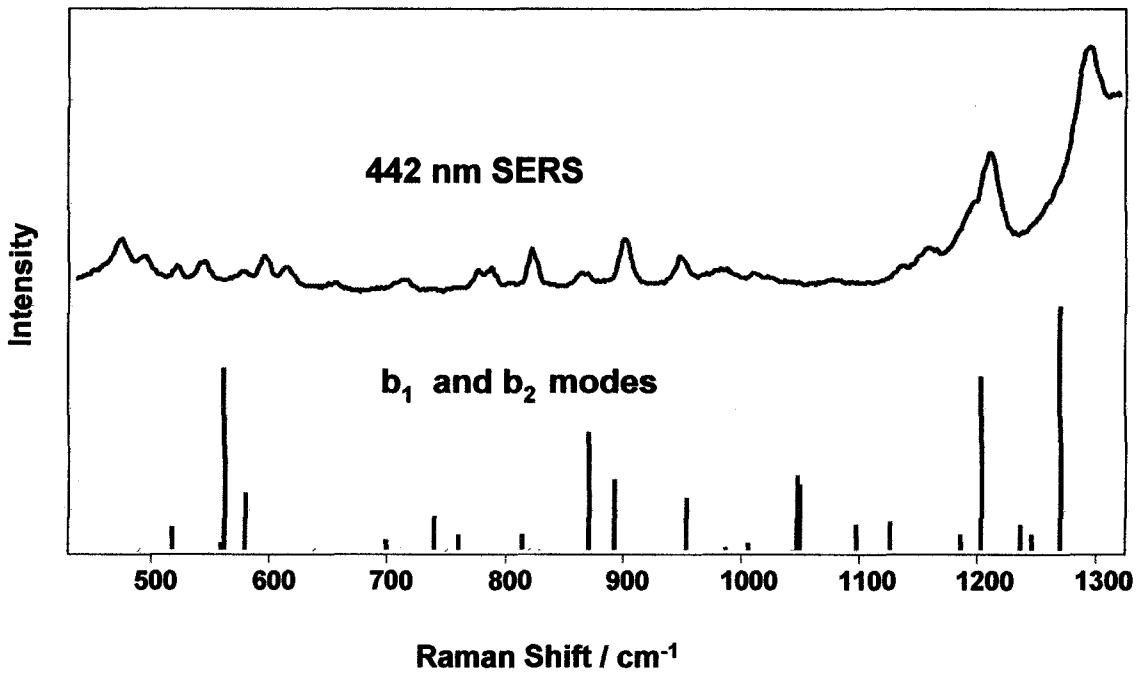

Figure 5.13: Comparison of measured spectrum and that been simulated with E^2_t / E^2_n = 5.

At 785 nm, which is far to the red of the main plasmon resonance of silver colloids, the rules predict that E_n is enhanced over E_t. In turn, a_1 modes should dominant the spectrum. The effects of the surface can again be modeled by applying an appropriate

Reproduced with permission of the copyright owner. Further reproduction prohibited without permission.

factor (here E^2_n/E^2_t = 25) to account for the relative field enhancements. The resulting theoretical spectrum is dominated by the a_1 modes, with a spectral profile that compares very favourably with the SERS spectrum recorded at 785 nm, as shown in Figure 5.14.

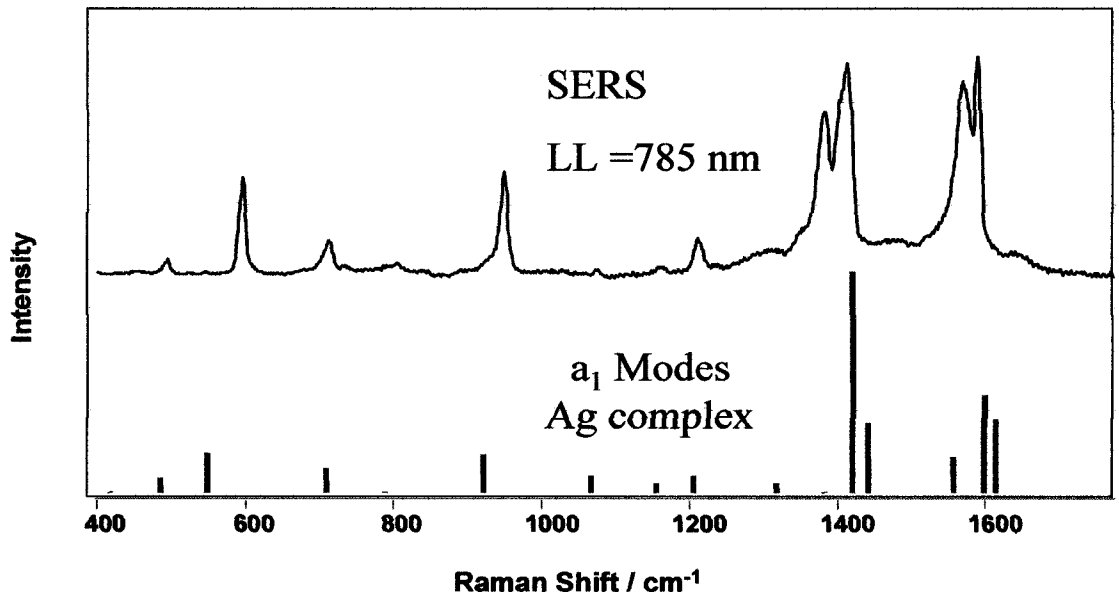

Figure 5.14: Comparison of measured spectrum and simulated with E^2_n/E^2_t =25.

The changes in the spectral profile of the measured SERS for NPIM-Ag at different laser lines can be satisfactorily explained by the inclusion of local field properties through the application of the surface selection rules of SERS as well as a consideration of molecular symmetry. What is still left to explain is the variation in relative intensities with changing excitation line. This will be addressed in the next section.

5.5.4 Dispersion of Surface Enhancement

To determine if the dispersion in relative intensities seen is real and not just an artefact of the experimental conditions, it is necessary to correct the measured spectrum

Reproduced with permission of the copyright owner. Further reproduction prohibited without permission.

for several factors. First the spectrum should be corrected for instrument response, as was outlined in chapter 2.2.3. At the time of these experiments only corrections for 785 and 514 nm laser lines were available. In addition, the concept of a "reduced Raman spectra" is useful and is outlined here briefly.[17]

The measured Raman intensity can be given by:

$$I(v) \propto C_{IRC} v_o (v_o - v_j)^3 \beta_j F^{-1} \tag{5.1.4}$$

where C_{IRC} is the correction for instrument response, v_o is the excitation frequency, v_j is the frequency difference in scattered radiation (Raman shift) and β_j is the scattering cross section of the j^{th} vibration. F is the approximation used to account for the effects of temperature:

$$F = 1 - \exp(-hv_j c / kT) \tag{5.1.5}$$

The temperature and frequency dependence can be factored out of the measured intensity to give a function that is directly proportional to the scattering cross section. This is the concept of the reduced Raman spectrum and is defined by:

$$R(v) \propto I(v) v_o^{-1} (v_o - v_j)^{-3} F \tag{5.1.6}$$

With the reduced Raman spectrum, the effect of excitation energy on relative intensities is more readily apparent.

These corrections were applied to the SERS spectra of NPIMH as taken at 785 and 514.5 nm. The result is shown in Figure 5.15.

Reproduced with permission of the copyright owner. Further reproduction prohibited without permission.

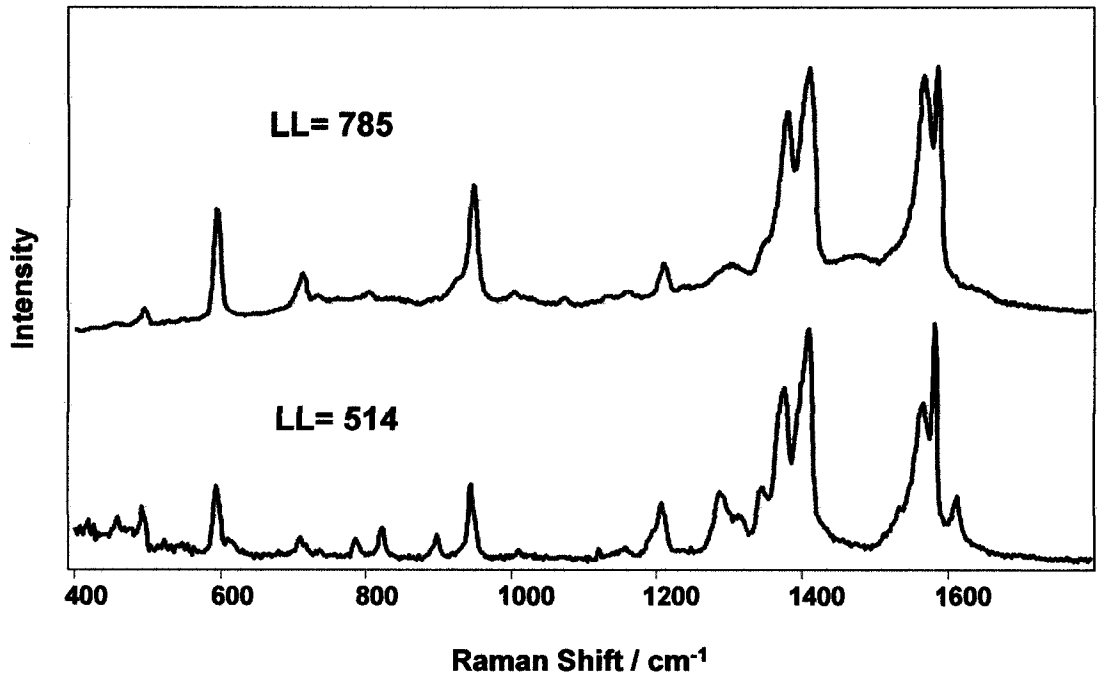

Figure 5.15: Comparison of the reduced spectra. SERS taken at 514.5 nm and 785 nm corrected for Instrument Response, Wavelength and Temperature.

Even upon correction, there is still a significant difference in relative intensities between 785 and 514.5 nm excitations for bands below 1000 and to those above 1200 cm^{-1}. This result could be rationalized by considering the fact that the SERS enhancement factor is not uniform across the spectral range. In addition, as the excitation is moved to the red, the distance a given vibrational mode is away from the driving frequency of the laser and the center of the plasmon resonance center is greater and the enhancement it will experience is less. This effect will be strongly dependent on the width of a plasmon and this is illustrated in Figure 5.16.

Reproduced with permission of the copyright owner. Further reproduction prohibited without permission.

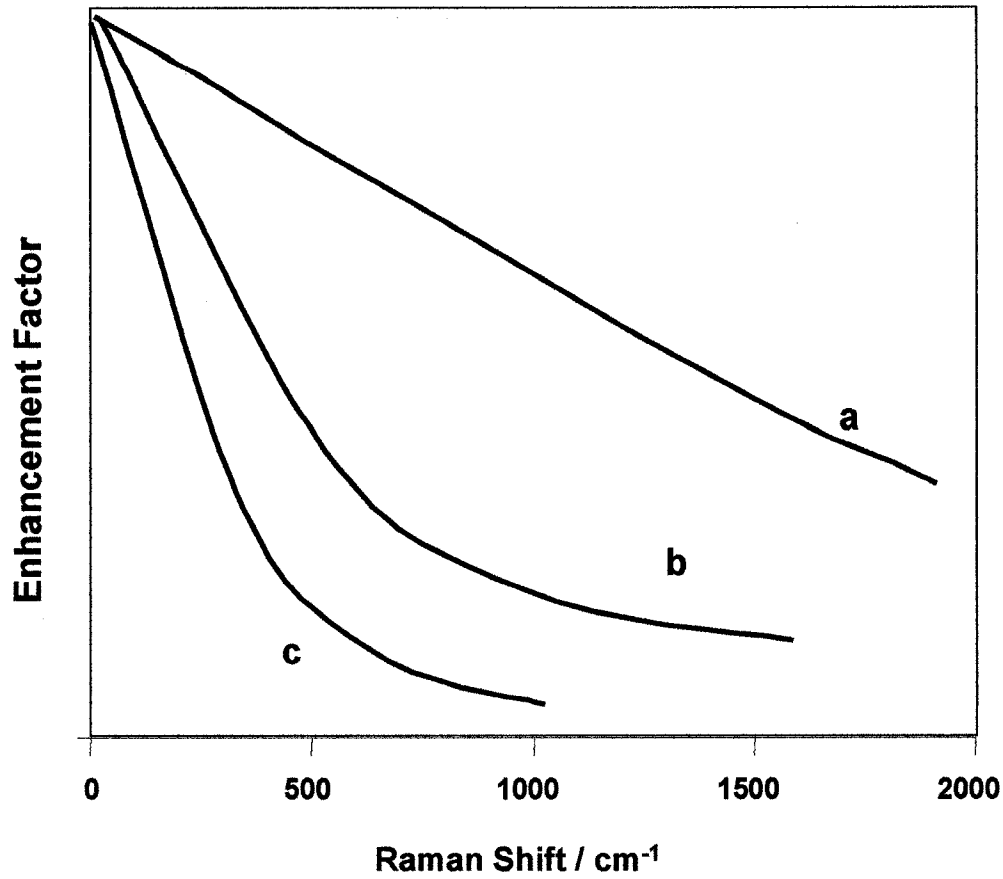

Figure 5.16: Illustration for the possible cases of dispersion of the enhancement factor. Line (a) represents the case of average enhancement with a wide surface plasmon envelope. Line (b) is for an intermediate case, while (c) is indicative of the case of a dispersion that might be seen in extreme field enhancement and a narrow SP that may be experienced with hotspots.

These results suggest new possibilities for a SERS experiment. Consider the following, the same dispersion relations seen in this case of average SERS should exist at the trace and single molecule regimes. In particular, the dispersion of the SERS enhancement may be even more pronounced. Based on the present theoretical understanding of "hotspots", the plasmon absorption of areas of high fields are narrower

Reproduced with permission of the copyright owner. Further reproduction prohibited without permission.

than that which gives rise to average enhancement.[18,19] This could result in a steeper drop in enhancement away from the driving frequency of the excitation line and extremely high enhancement for low wavenumber vibrations compared to the rest of the spectrum. The local plasmon absorption may be imprinted in the spectrum of a carefully considered probe molecule. With meticulous procedures and knowledge of true relative intensities of vibrational bands, this information could be extracted. In essence it may be possible to reverse the SERS experiment and use a probe molecule as a reporter to the complex local fields in nanostructures.

5.6 Conclusion

In this chapter the impact on the measured SERS spectra of several dispersive dependencies were examined. It was shown how, with careful consideration of molecular symmetry and the appropriate application of the surface selection rules, the SERS profile measured at different wavelength of excitation, can be satisfactorily simulated. The demonstration of these rules with the SERS of 1,8-naphthalimide is one of the strongest and clearest examples to date. In addition, the effect of non-uniform enhancement factors is discussed. Finally, possible future experiments based on these results are suggested

References

(1) Tully, J. C. *Annual Review of Physical Chemistry* **2000**, *51*, 153-178.

(2) Kambhampati, P.; Child, C. M.; Foster, M. C.; Campion, A. *Journal of Chemical Physics* **1998**, *108*, 5013-5026.

(3) Shorygin, P. P.; Krushinskij, L. L. *Journal of Raman Spectroscopy* **1997**, *28*, 383-388.

Reproduced with permission of the copyright owner. Further reproduction prohibited without permission.

(4) Moskovits, M. *Reviews in Modern Physics* **1985**, *57*, 783.

(5) Moskovits, M.; Suh, J. S. *Journal of Physical Chemistry* **1984**, *88*, 5526-5530.

(6) Aroca, R. *Surface - Enhanced Vibrational Spectroscopy*; John Wiley & Sons, 2006.

(7) Schatz, G. C.; Van Duyne, R. P. In *Handbook of Vibrational Spectroscopy*; Chalmers, J. M., Griffiths, P. R., Eds.; John Wiley & Sons, Ltd, 2002; Vol. Volume 1.

(8) Zeman, E. J.; Schatz, G. C. *Journal of Physical Chemistry* **1987**, *91*, 634.

(9) Lee, P. C.; Meisel, D. *Journal of Physical Chemistry* **1982**, *86*, 3391-5.

(10) Lee, C. T.; Yang, W. T.; Parr, R. G. *Physical Review B* **1988**, *37*, 785-789.

(11) Becke, A. D. *Physical Review A* **1988**, *38*, 3098-3100.

(12) Dunning, T. H.; Hay, P. J. In *Methods of Electronic Structure Theory*; Schafer, H., Ed.; Plenum Press: New York, 1977; Vol. 2.

(13) Hay, P. J.; Wadt, W. R. *Journal of Chemical Physics* **1985**, *82*, 299-310.

(14) Menendez, J. R.; Obuchowska, A.; Aroca, R. *Spectrochimica Acta, Part A: Molecular and Biomolecular Spectroscopy* **1996**, *52A*, 329-336.

(15) Munro, C. H.; Smith, W. E.; Garner, M.; Clarkson, J.; White, P. C. *Langmuir* **1995**, *11*, 3712-20.

(16) Aroca, R. F.; Clavijo, R. E.; Halls, M. D.; Schlegel, H. B. *Journal of Physical Chemistry A* **2000**, *104*, 9500-9505.

(17) Brooker, M. H.; Nielsen, O. F.; Praestgaard, E. *Journal of Raman Spectroscopy* **1988**, *19*, 71-76.

Reproduced with permission of the copyright owner. Further reproduction prohibited without permission.

(18) Markel, V. A.; Shalaev, V. M.; Zhang, P.; Huynh, W.; Tay, L.; Haslett, T. L.; Moskovits, M. *Physical Review B: Condensed Matter and Materials Physics* **1999**, *59*, 10903-10909.

(19) Futamata, M.; Maruyama, Y.; Ishikawa, M. *Journal of Physical Chemistry B* **2003**, *107*, 7607-7617.

Reproduced with permission of the copyright owner. Further reproduction prohibited without permission.

CHAPTER 6

PHOTODYNAMICS OF SURFACE-ENHANCED RESONANCE RAMAN SCATTERING

Reproduced with permission of the copyright owner. Further reproduction prohibited without permission.

6.1 Introduction

In this section, experimental results of signal decay of the surface enhanced resonance Raman scattering (SERRS) of several systems is presented. Many of the problems that plague SM fluorescence are present in SM-SERRS studies. The advantage gained by using an excitation energy that is in a region of a molecular absorption is the large increase of the Raman scattering cross section, up to a 10^6 enhancement, over that of normal Raman. While the strength of the absolute signal is greater, SERRS inherits all the unwanted side effects associated with molecular absorption and traditional resonance Raman, such as the propensity for photochemistry.[1]

In addition, the high fields present in SERRS experiments fosters conditions where the photobleaching process can be exasperated. There is a strong dependence between the rate of signal decay and the laser intensity used. The SERRS signal is dependent on a complex relationship between the excitation rate, the relaxation rate and the rate of photobleaching. It will be shown how the survival times of molecules are significantly lengthened by low flux excitation. As well, analysis of the signal decay reveals a multi-exponential fit which suggests the presence of both a fast and slow process. It is suggested that these trends may be a consequence of the contribution to the signal of molecules residing in areas of high enhancement ("hotspots") and those experiencing an average enhancement from the surface.

6.2 Background

In previous chapters it has been shown that when resonance Raman is coupled with plasmon enhancement, extremely high molecular cross sections can allow for the detection of single molecules to be achieved. The presence of the plasmon enhances both

Reproduced with permission of the copyright owner. Further reproduction prohibited without permission.

the local electric field, as well as that of the Raman scattered photons. In addition, the increase in field strength can also lead to enhanced absorption and fluorescence.[2] The proximity of a molecule to a nanostructure has been shown to effect the lifetimes as well.[3,4] These processes can compete with each other and, as will be shown, this competition creates collection regimes based upon the intensity used in the collection of the SERRS signal. The simplified state diagram in Figure 6.1, will help illustrate the discussion that follows.

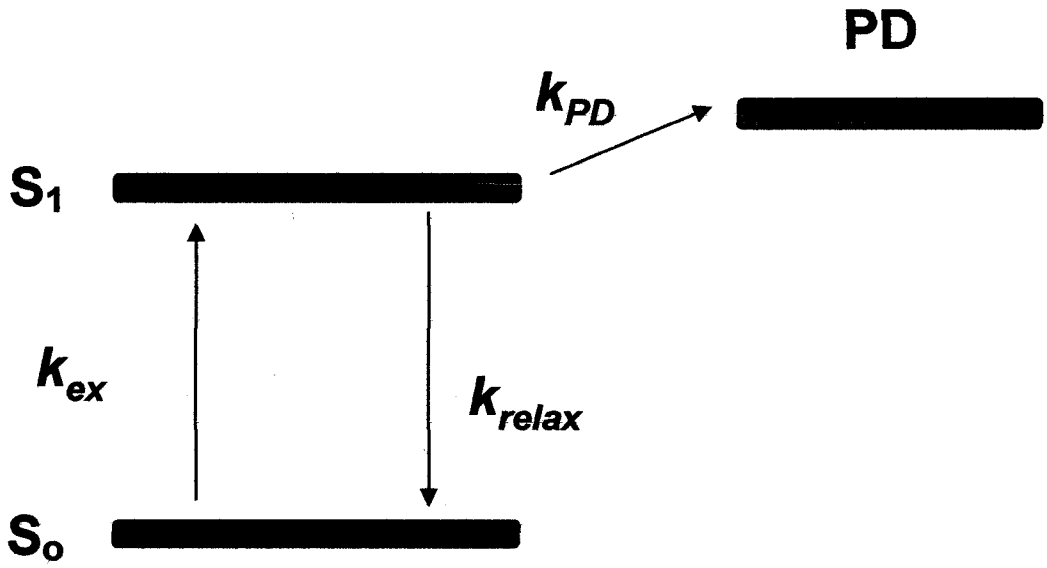

Figure 6.1:. Simplified energy level diagram indicating three possible pathways. The pathway to PD,(k_{PD}) represents all processes that lead to photodegradation

where k_{ex} is the excitation rate, k_{relax} is the relaxation rate and k_{PD} would give the rate as to which a photodegradation or photobleaching event would occur.

Photobleaching (Photodegradation) is a process where a molecule loses its ability to fluoresce due a chemical change or destruction upon exposure to excitation light.[5] The mechanism of photobleaching is very dependent on the molecular system under study, and in many cases not clearly known. Often, it is a triplet state which plays an important

Reproduced with permission of the copyright owner. Further reproduction prohibited without permission.

role, since these long lived states are the pathway for photochemical reactions.[6-8] The presence of a photobleaching mechanism effectively creates saturation thresholds that have a bearing on the energy density (ED) that can be used in the experiment. Consider the following system where, for low ED intensities, photobleaching (photodegradation) occurs through a long lived triplet state:[9]

$$S_0 \xrightarrow{h\nu} S_1 \rightarrow T_1 \rightarrow PB \tag{6.1}$$

At high intensities of photon flux, excited states, including reactive triplet states, are more likely to be occupied, which can lead to increased chance of photobleaching when the relaxation rate is long compared to the rate of incoming photons:

$$S_0 \xrightarrow{h\nu} S_1 \rightarrow T_1 \xrightarrow{h\nu} T_n \rightarrow PB \tag{6.2}$$

This population of these reactive states leads to a much higher rate of photobleaching.

In the presence of nanoparticles, the k_{ex} term can be modified due to the enhanced local field. Similarly, Weitz et al, have shown that there is an increase in the non-radiative decay rate for a molecule at a metal surface.[3,10] This would suggest that there is a competition between the excitation rate, the relaxation rate (including any effects due to the proximity of a nanoparticle) and the rate of photobleaching.

It is reasonable to assume that in the enhanced resonance Raman experiment there exists a similar dependence between photon flux and the rate of signal decay. Such that if $k_{ex} >> k_{relax}$ then k_{PD} would be extremely probable and would result in high photobleaching rates.

Supporting evidence for photobleaching as a source of the signal loss in SERRS, was the inability to fit the signal decay with a single exponential:

$$S(t) = e^{-t/k_t} \tag{6.3}$$

Reproduced with permission of the copyright owner. Further reproduction prohibited without permission.

A biexponential of the form below was found to fit the data extremely well:

$$S(t) = S_0 + A_1 e^{-t/k_1} + A_1 e^{-t/k_1} \quad (6.4)$$

In the fluorescence photobleaching studies found in the literature, this type of fit is often rationalized as inhomogeneous environments for the molecules under investigation.[6-8] It is not too much of a stretch to see the inhomogeneity of fields encountered in SERRS experiments with metal island films may lead to similar behaviour.

In the following section the results of time studies of the SERRS spectroscopic signal for two systems are presented. The first is a binary monolayer composed of two dyes: a perylene and a phthalocyanine. The second is series of studies on the signal loss of the SERRS of rhodamine 6G (R6G) when measured from a silver island film.

6.3 Experimental

The fabrication procedure for evaporated Au/Ag films (10 average thickness) is described in Chapter 7. Neat Langmuir-Blodgett films of titanyl (IV) phthalocyanine (TiOPc) and bis(neopentylimido)perylene (BNPTCD) LB as well as LB film with 1:1 TiOPc:BNPTCD ratio, were provided for these studies by T. DelCano. Full characterization of these films can be found in the following references.[11,12] The 1:1 LB film was created to have an equal number of TiOPc to BNPTCD molecules per unit area.

In the study of R6G, SERRS studies were of dilute solutions cast onto evaporated 6 nm silver island films. A 10^{-7} M solution of R6G was prepared with deionised water. A small drop of 10 μl was cast onto the Ag island film and left to dry before analysis.

UV-Vis and plasmon absorption were recorded. The excitation lines of 514.5 and 633 nm were used in this investigation to explore each molecules resonance and off

Reproduced with permission of the copyright owner. Further reproduction prohibited without permission.

resonance enhanced Raman All Raman spectra reported here were recorded under ambient condition.

6.4 Results

6.4.1 SERRS/ SERS of TiOPc and BNPTCD

In the study case presented here, the sample is that of a LB monolayer fabricated so as to have an equal number of a perylene derivative (BNPTCD) and phthalocyanine (TiOPc) molecules per unit area.[11] These molecules have very distinct electronic absorptions also shown by the absorption spectra for neat monolayers for the two materials in Figure 6.2.

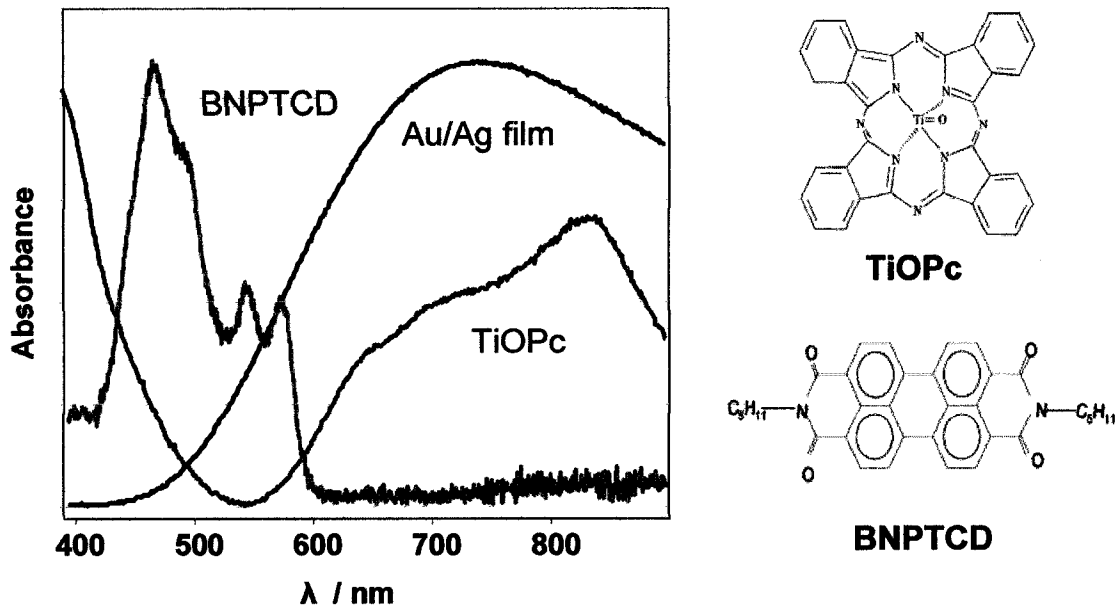

Figure 6.2: UV-Visible absorption spectra of BNPTCD and TiOPc neat monolayers on glass. Absorption spectra of the two dyes are overlaid with the plasmon of the Au/Ag island film. The structures for the two dyes are also shown.

Reproduced with permission of the copyright owner. Further reproduction prohibited without permission.

BNPTCD is in resonance with the 514.5 nm laser line while the TiOPc is in resonance with 633 nm excitation. The LB was deposited on an Ag/Au metal island film. The surface plasmon for this film is also shown in Figure 2. Notably, the 633 nm line is in full resonance with both the surface plasmon and the TiOPc electronic absorption, hence creating a double-resonance situation. The BNPTCD molecule meanwhile should only experience an enhancement from the resonance with the surface plasmon and not from any molecular resonances. In Figure 6.3, the SERRS of a neat LB of TiOPc and the SERS of a neat LB of BNPTCD, as taken with 633 nm excitation, is shown.

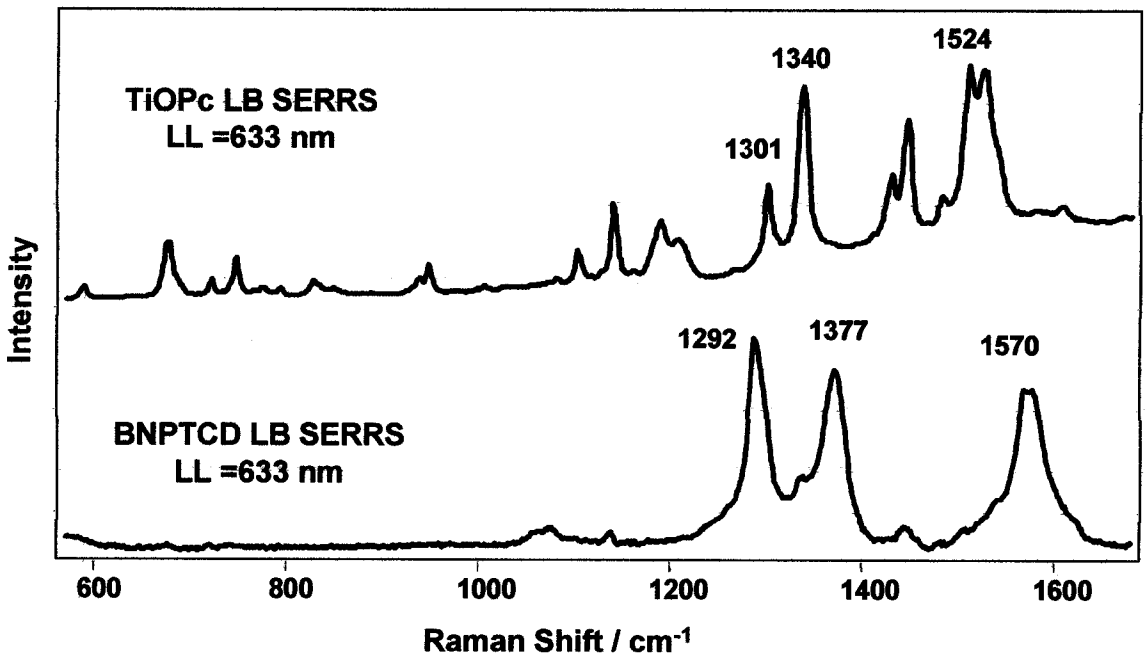

Figure 6.3: SERS and SERRS spectra of neat monolayers on glass of the two dyes.

The two-dimensional and well organized LB of the 1:1 mixed monolayer is ideal system to study SERS and SERRS under the same conditions. Of particular interest here is the effect of energy density on the intensity of the SERS/SERRS spectra. The spectra shown in Figure 6.4 were measured under identical conditions (illumination with a 633

Reproduced with permission of the copyright owner. Further reproduction prohibited without permission.

nm laser, through a 50X objective with an accumulation time of 10s) but for two different laser powers (different energy density at the sample of the same frequency).

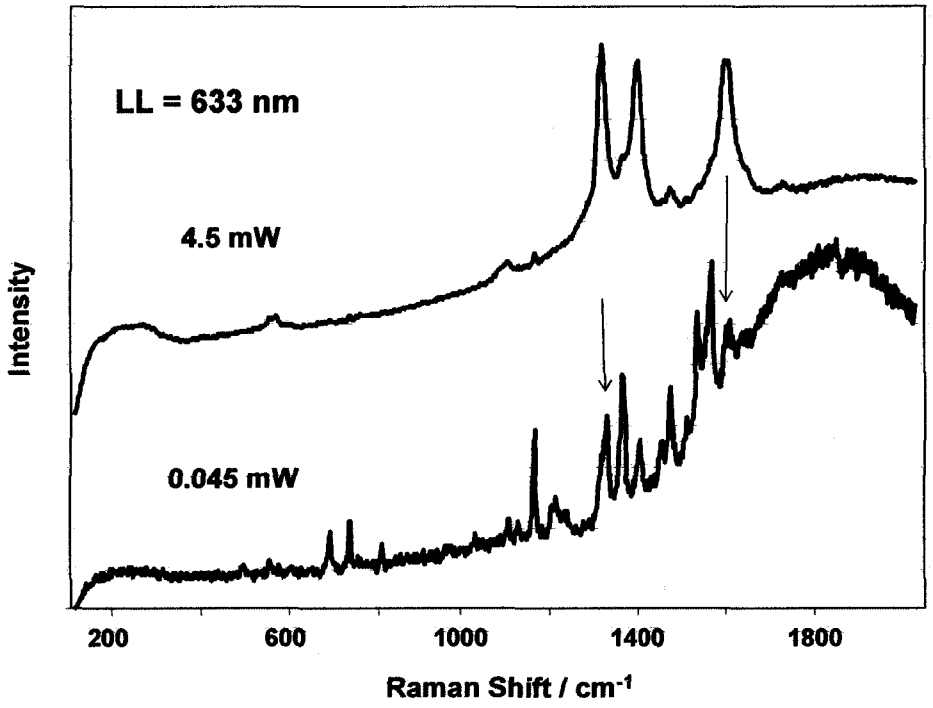

Figure 6.4: SERS/SERRS signal from a TiOPc / BNPTCD 1:1 mixed monolayer at two energy densities.

The top spectrum is one recorded with ~ 4.5 mW at the sample, while the bottom spectrum was recorded with the laser power lowered to 0.045 mW, or 1% of that initially used. The former contains only the fingerprint spectrum of BNPTCD while the latter shows the expected compliment of bands of both chemical species. When the experiment is conducted with higher laser powers, it is the vibrational fingerprint bands of BNPTCD that is seen with little or no evidence of TiOPc. To better understand the contrasting spectra, the laser power was further reduced to 0.0225 mW and the accumulation time was reduced to 1 second. Consecutive spectra were recorded every second for 40 seconds.

Reproduced with permission of the copyright owner. Further reproduction prohibited without permission.

This time evolution of signal is shown in Figure 6.5 and a sampling of spectra from the beginning, middle and end of the collection, is shown in Figure 6.6.

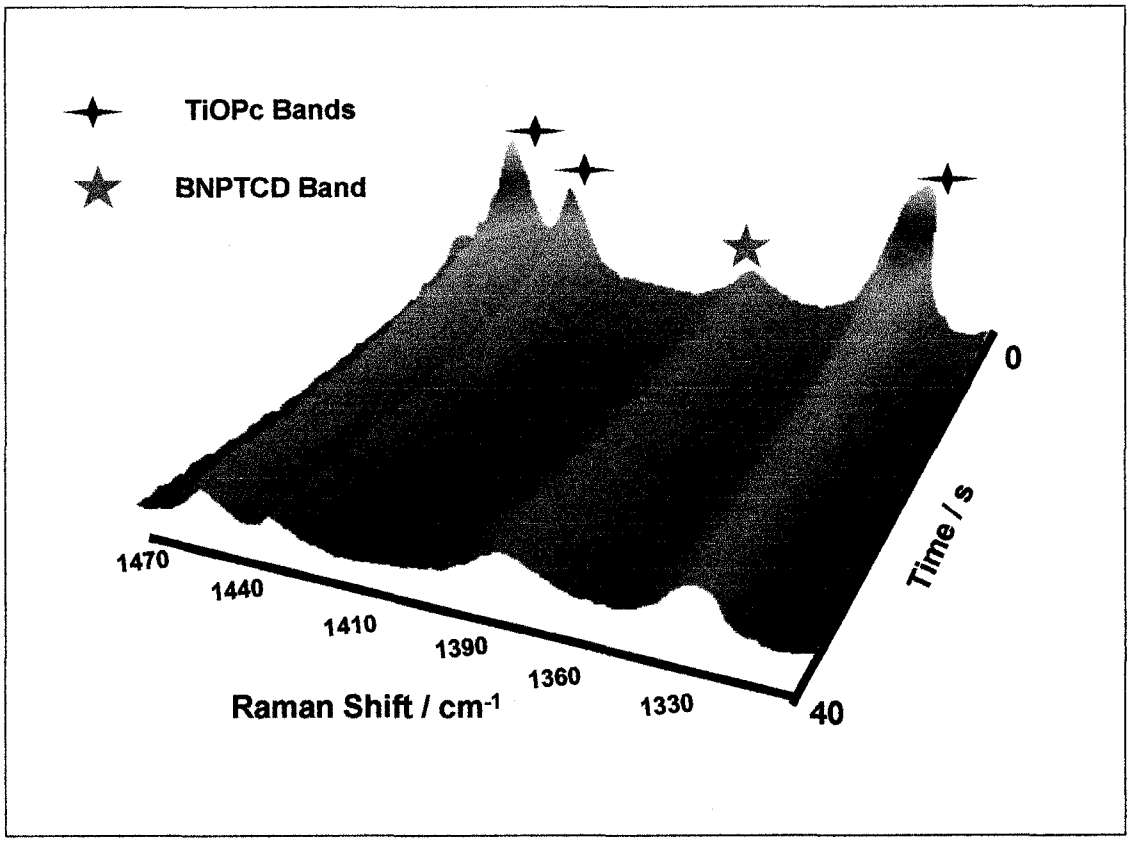

Figure 6.5: Time-Dependent photobleaching of the SERS/SERRS signal from a TiOPc / BNPTCD 1:1 mixed monolayer.

Reproduced with permission of the copyright owner. Further reproduction prohibited without permission.

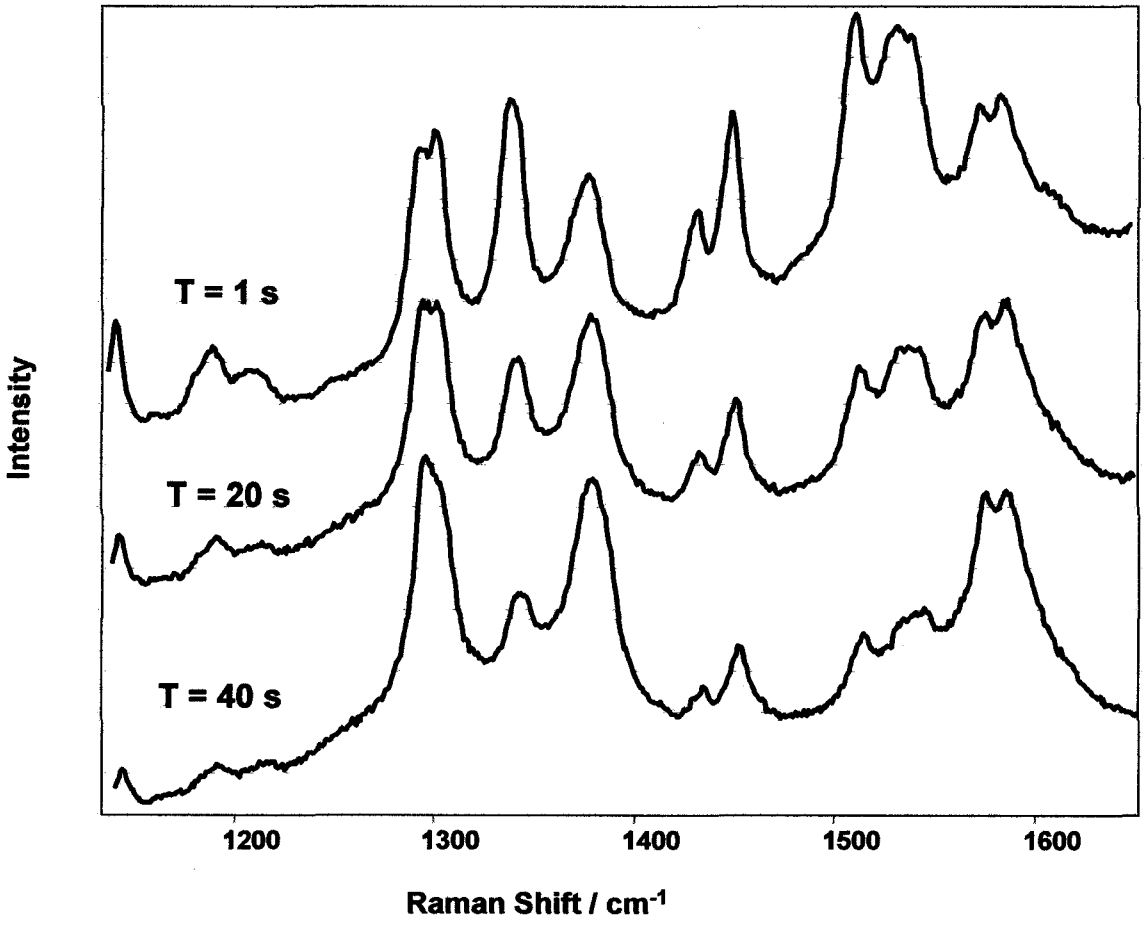

Figure 6.6: SERS/SERRS signal from a TiOPc / BNPTCD 1:1 mixed monolayer at T=1s, T=20s, T=40s for the time series shown in Figure 6.5.

It can be seen that the main peaks of both the BNPTCD (1292, 1377, 1570 cm^{-1}) and TiOPc (1301, 1340, 1524 cm^{-1}) are present in the initial spectrum. Within 20 seconds, the TiOPc signal is diminished, while that of BNPTCD remains relatively constant. After 40 seconds the BNPTCD bands are dominant. The normalized integrated intensity for a representative band for each molecule is plotted in Figure 6.7.

Reproduced with permission of the copyright owner. Further reproduction prohibited without permission.

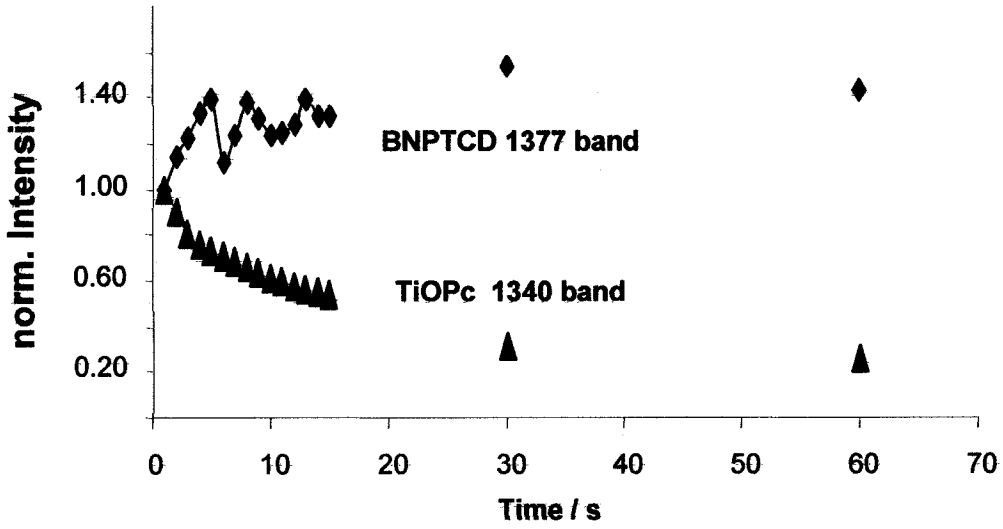

Figure 6.7: Signal decay in SERS and SERRS. Normalized integrated intensity for a representative band for each molecule is plotted.

It is clearly seen that while the TiOPc signal decays, the BNPTCD signal stays relatively constant. The fact that the SERS of the BNPTCD molecules is maintained, suggests that the underlying enhancing metallic nanostructure is not being modified and can be excluded as the reason for the intensity loss. The key difference between the two molecules is their molecular resonances. With 633 nm excitation, the TiOPc, is SERRS enhanced, and undergoes an expedited photodegradation, while the BNPTCD being SERS enhanced, is relatively unaffected. This changes when the wavelength of excitation is 514.5 nm, which is in resonance with BNPTCD, as evidenced by the plot in Figure 6.8.

Reproduced with permission of the copyright owner. Further reproduction prohibited without permission.

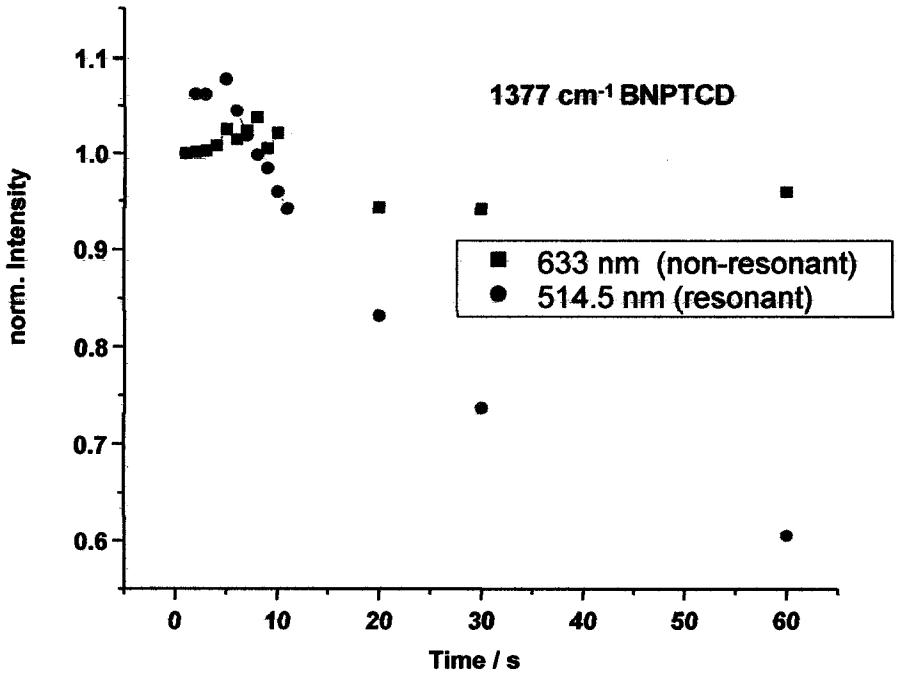

Figure 6.8: Comparison of the signal decay for BNPTCD when excited with resonance and non-resonant excitation.

The reason for the rapid decay of the TiOPc signal is not quite clear. The molecule is known to have a reactive triplet state.[13] It is possible that a situation similar to that described earlier in the chapter for a system with a reactive triple state may explain the behaviour encountered here.

An attempt was made to model the dynamics of the SERRS signal with a simple exponential decay; it was found that this curve fitting was inadequate. When a double exponential of the form shown in the introduction was used, excellent agreement could be found as shown in Figure 6.9.

Reproduced with permission of the copyright owner. Further reproduction prohibited without permission.

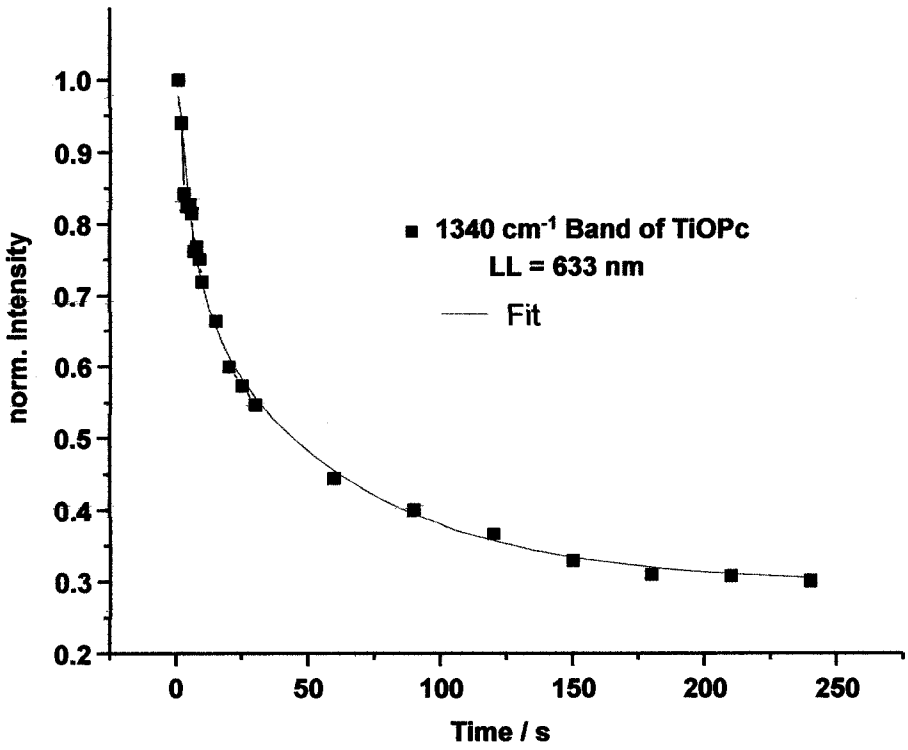

Figure 6.9: Intensity decay of SERRS of TiOPc. Spectra taken with 633 nm, at 45 μW, 1 second exposure and 1 second between scans for 100 scans. Fitted curve is a double exponential with the following parameters $S_o = 0.29$, $A_1 = 0.45$, $A_2 = 0.31$, $k_1 = 62\ s^{-1}$, $k_2 = 6.4\ s^{-1}$ ($R^2 = .99$)

As discussed earlier, the presence of a biexponential fit could be interpreted in terms of inhomogeneity in the environment for the analyte under study. This could be related to variation in the EM fields or morphology of the enhancing surface. To see if this is a more general property of SERRS, a dynamics study on the SERRS signal of the dye molecule, rhodamine 6G, were carried out.

6.4.2 Time Studies of R6G on Ag island films

Besides being the probe molecule of choice for SERS investigations,[14-17] R6G is also an extremely well researched molecule for photobleaching studies.[6-8,18] In Figure

Reproduced with permission of the copyright owner. Further reproduction prohibited without permission.

6.10, the electron absorption spectrum for R6G is shown along with the plasmon for a 6 nm silver island film. With 514.5 nm excitation, the double resonance condition for SERRS is achieved.

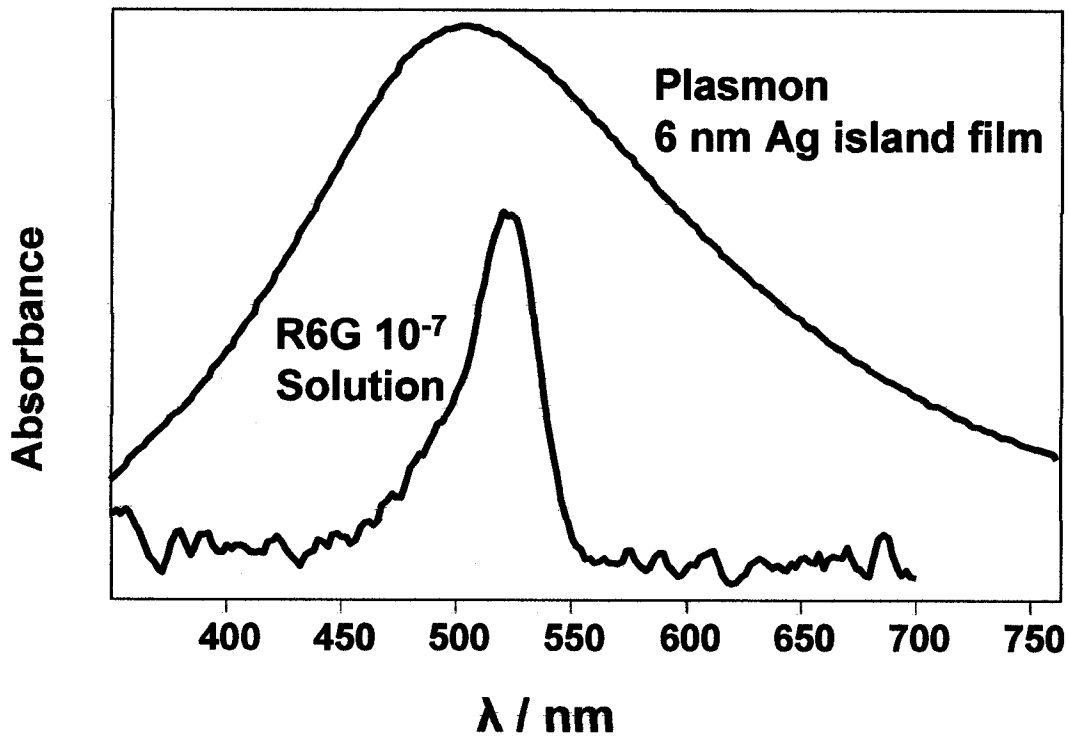

Figure 6.10: UV-Visible absorption spectra of 10^{-7} R6G Solution and the plasmon of the 6 nm Ag film.

In Figure 6.11, the SERRS spectrum for R6G is given; with the strongest band observed at 1650 cm^{-1}. It is the integrated intensity of this band that is used for all dynamic analysis presented in this section.

Reproduced with permission of the copyright owner. Further reproduction prohibited without permission.

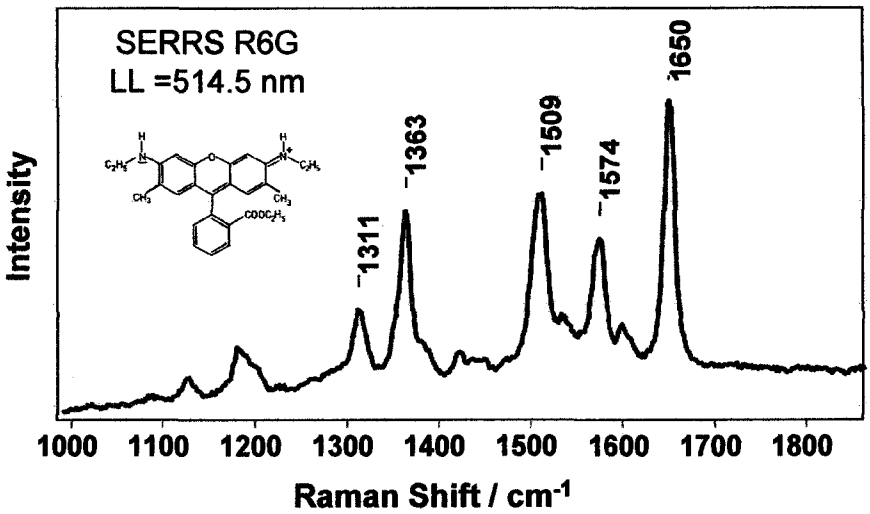

Figure 6.11: SERRS of a 10 µl casting of a 10^{-7} M R6G solution on a Ag island film.

In Figure 6.12, the signal decay of the R6G is plotted as a 2D map. This map demonstrates that even when there is loss of total intensity with time, the entire spectrum is still being recorded and the decay affects the entire fingerprint region.

Reproduced with permission of the copyright owner. Further reproduction prohibited without permission.

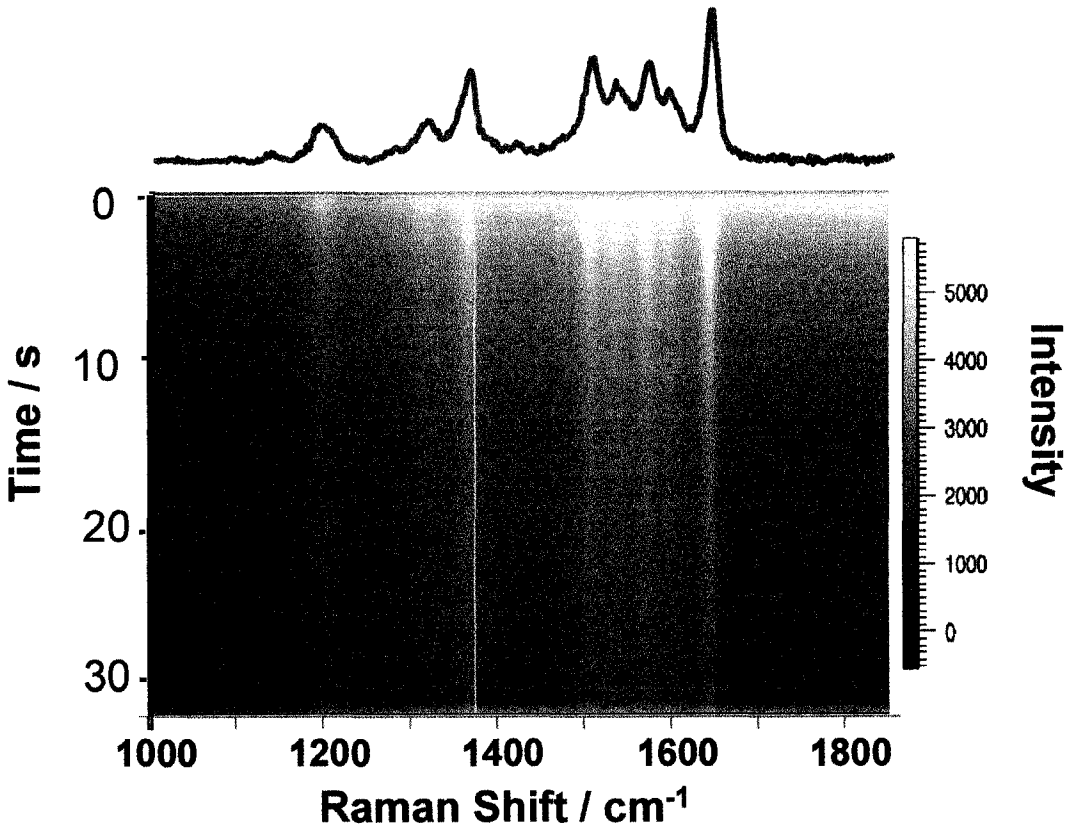

Figure 6.12: Time Study of the SERRS signal of 10^{-7} R6G. Spectra taken from a casting of R6G on a Ag island film with 514.5 nm, ED= 1mW, 1 second accumulation, 30 scans.

In Figure 6.13, the decay in signal is shown thorough the plot of the integrated intensity of one band (1650 cm^{-1}). Based on the intensity map shown in Figure 12, photobleaching is expected, and the shape of the curve reveals that something more than a simple exponential decay is occurring. Again the biexponential provides an excellent fit to the data suggesting this behaviour may be a general trend for SERRS-photobleaching on Ag island films.

Reproduced with permission of the copyright owner. Further reproduction prohibited without permission.

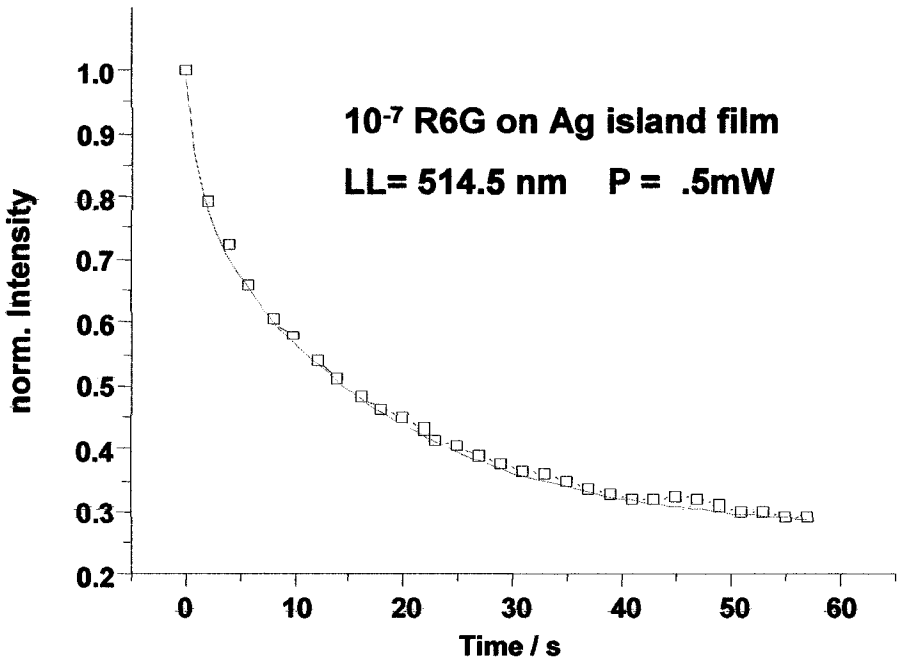

Figure 6.13: Intensity decay for SERRS R6G. Spectra were taken with 0.5 mW at 514.5 nm, 1 second exposure and 2 seconds between scans for 30 scans. Fitted curve is a double exponential with the following parameters $S_o = 0.27$, $A_1 = 0.19$, $A_2 = 0.53$, $k_1 = 1.47$ s^{-1}, $k_2 = 17.4$ s^{-1}, ($R^2 = 0.99$).

To see the effect of energy density of the rate of degradation a series of measurements where taken at different laser powers at the sample. The summary of these results are presented in Figure 6.14.

Reproduced with permission of the copyright owner. Further reproduction prohibited without permission.

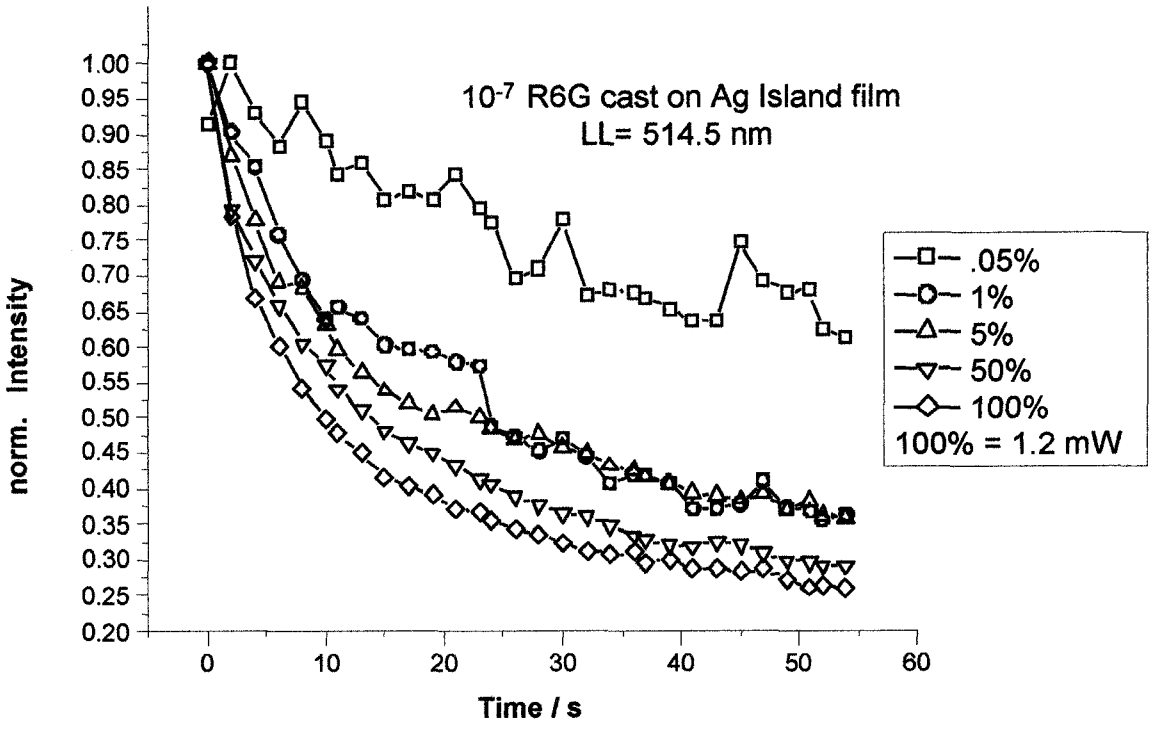

Figure 6.14: Signal decay for the SERRS signal of R6G for several ED. Condition for collected spectra are: accumulation time = 0.5 s for 30 scans, 2 s dead time between scans

At each laser power, 30 spectra were collected 2 seconds apart (dead time of instrument) with a time of accumulation of 0.5 s. Each set of data was normalized to what was measured on first exposure. As can be seen, for anything above 0.05% there is significant drop off in the first few seconds. This type of behaviour has an important impact when attempting any type of accumulation of signal, especially if moderately high powers are used. Take for instance the data for the full 1.2 mW, where within the first 5 seconds there is over a 30% loss of signal.

Reproduced with permission of the copyright owner. Further reproduction prohibited without permission.

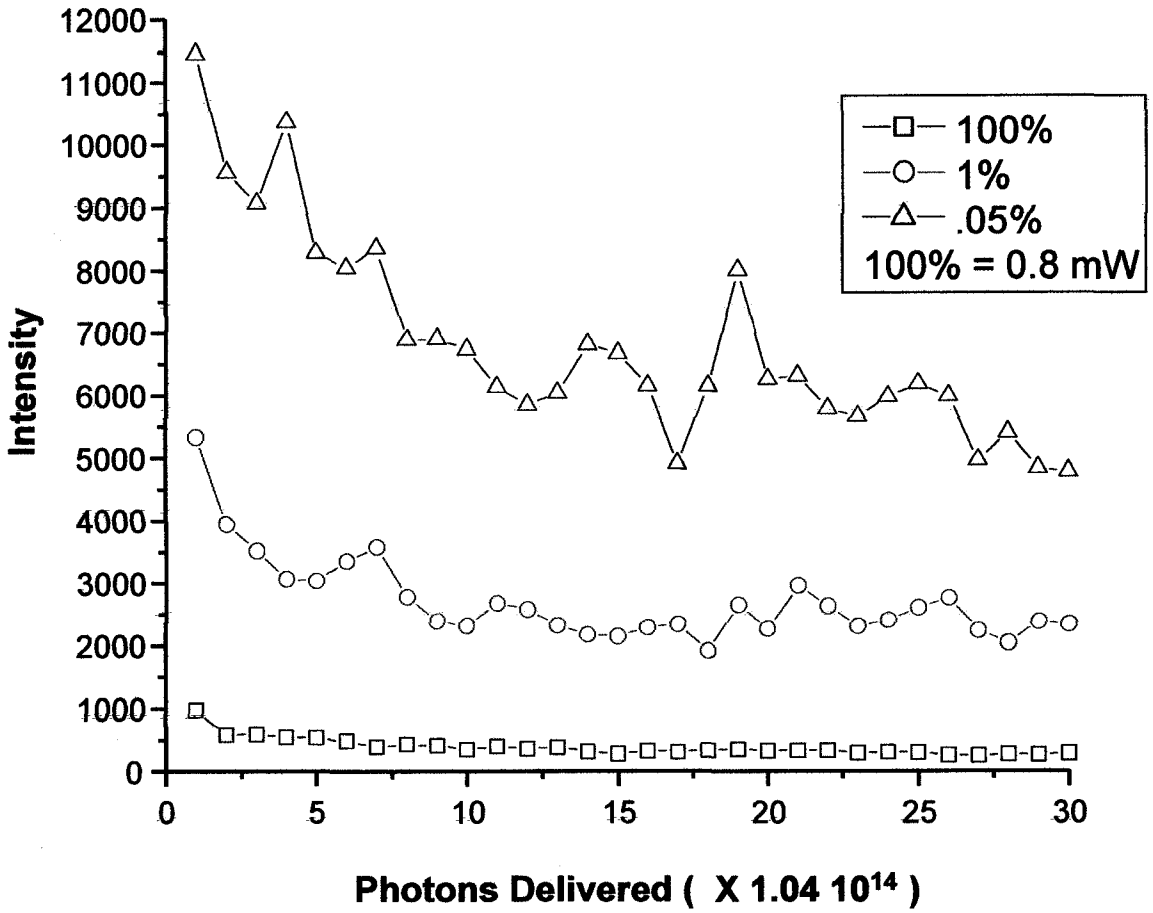

Figure 6.15: Signal decay for the SERRS signal of R6G for 3 ED's for equal number of striking photons.

To see that the effect of ED is beyond doubt, it is informative to look at the signal decay as a function of total photons delivered. SERRS signal of R6G was examined at different laser intensities, ranging from 800 to 0.4 μW. To ensure that the same numbers of photons were delivered, the exposure time was adjusted from 0.05s to 100s accordingly. By increasing exposure time with decreasing power, the same number of photons can be delivered to the sample. The result of this test is shown in Figure 6.15 and it can be clearly seen that ED has a huge impact in SERRS.

Reproduced with permission of the copyright owner. Further reproduction prohibited without permission.

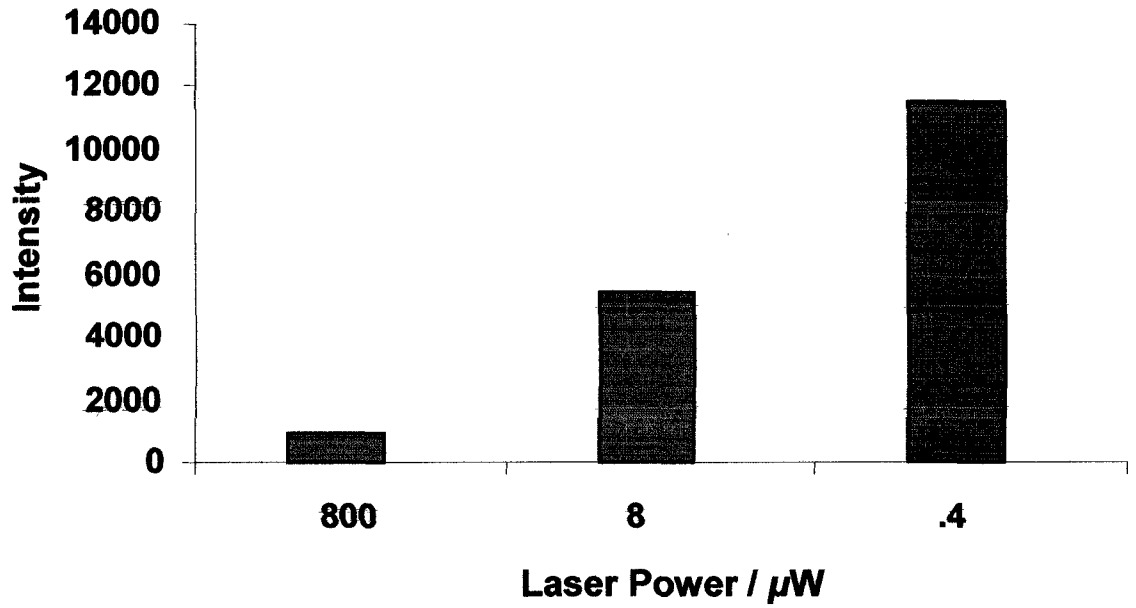

Figure 6.16: Integrated SERRS intensity for the 1650 cm^{-1} band of R6G for one dose for three different ED's.

Recall that Raman intensity should be linear with time and laser intensity. These results demonstrate that the linear relationship between Raman intensity and laser intensity is lost in SERRS due to the effects of photodegradation. The "survival" time of analyte is strongly tied to the photon flux that is used. This is starkly illustrated by the graph shown in Figure 6.16, were the initial intensity that is recorded for equal number of striking photons is given for each laser power. Approximately, 12 times more "counts" in the first "dose" can be attained with 0.4 μW compared to 800 μW.

The behaviour of R6G investigated here is consistent with results of Bout *et al.*,[7] In their study of single molecule fluorescence of the R6G molecule, they have shown that

Reproduced with permission of the copyright owner. Further reproduction prohibited without permission.

the rate of photobleaching is strongly dependent on the energy density used. They found that excitation with low ED resulted in unexpectedly high photon yields and a longer lifetime for the molecule. It stands to reason that a similar situation is occurring here, only amplified by the enhanced fields involved. Thus, photon flux, increased absorption, competing rates of excitation and relaxation times, the presence of nonradiative relaxation routes, and excited state photochemistry, all play a part in the photodegradation seen in SERRS experiments.

These results help the understanding and give a possible interpretation of the biexponential decay. There may be two types of molecular sites for analytes deposited onto Ag island films that contribute to the SERRS spectra. These could be attributed to those molecules that reside in hotspots and those situated in areas of average enhancement. It is known that the SERS/SERRS signal is dominated by those molecules residing in areas of highest enhancements.[19,20] At these hotspots, the fields can be orders of magnitude larger than the average enhancement. Molecules situated in hotspots experience a local field that would be considered extremely intense. This could create a situation where $k_{ex} >> k_{relax}$. For molecules in areas of average enhancement, $k_{ex} > k_{relax}$ then k_{PD} is small as the probability of photobleaching is less likely. When the conditions are such that $k_{ex} \sim k_{relax}$, the non-radiative decay can play a more dominate role. This may reduce k_{PD} and as such a molecule is less chance to be in a state where a photochemical process can occur. Under these conditions the effective scattering life time for a molecule is significantly increased. This is one possible explanation for the decay profiles recorded here, and this idea is illustrated in Figure 6.17.

Reproduced with permission of the copyright owner. Further reproduction prohibited without permission.

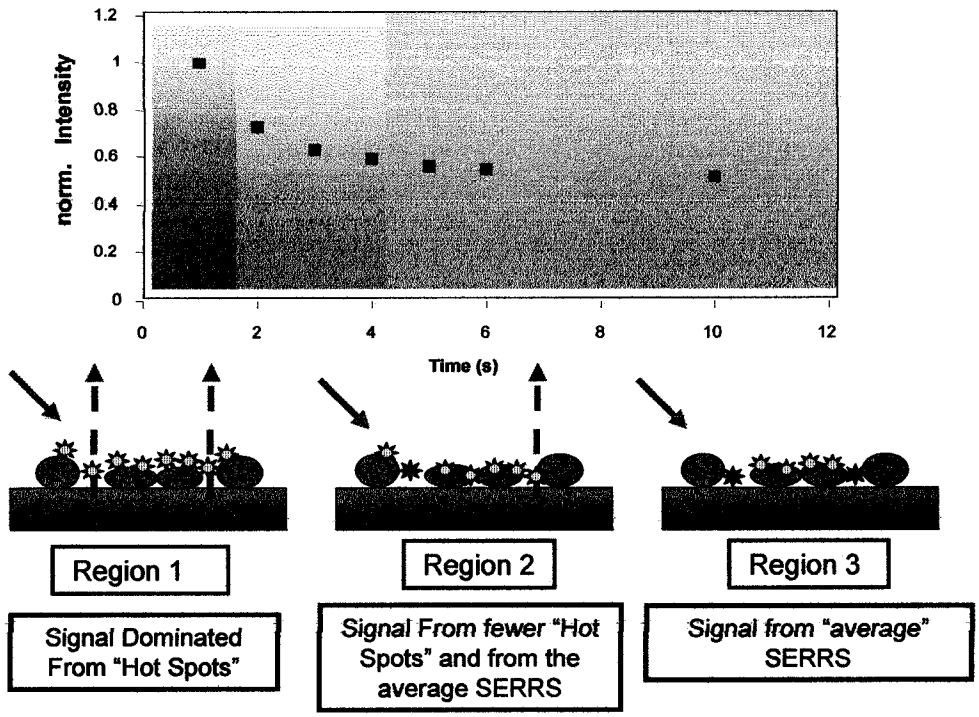

Figure 6.17: Illustration of the possible mechanism for the signal decay seen in SERRS experiments.

The excitation rate can be considered to be related to the enhanced local field

$$k_{ex} \propto GE_L^2 \tag{6.4}$$

where G is the enhancement factor. So to is the rate of photobleaching k_{PD}. This would manifest itself in the decay rates (Γ), for photobleaching. This has been suggested by Le Rue et al, with $\Gamma \sim G\, I_o$.[19] Hence, the photobleaching rate is dependent on both the local field enhancement and the incident excitation intensity. This actually gives as starting point to the possible use of photobleaching to measure the enhanced local fields and possibly their distribution.

Reproduced with permission of the copyright owner. Further reproduction prohibited without permission.

6.5 Conclusion

SERRS experiments in general are plagued by photodegradation of the analyte. By various processes, the target molecules stop scattering and the quality of signal degrades in time. This is especially evident at SM-SERRS regime as seen in Chapter 3 in the work of SM detection of several perylene derivatives. Here, I have presented experimental evidence of the photobleaching for three different dyes and for two types of samples. Photobleaching is observed in numerous cases and it is a common occurrence in experimental SERS/SERRS.[21] The biexponential behaviour is associated with the inhomogeneity in the electromagnetic enhancement, one coming from molecules in "hotspots" and the more common enhancement referred as "average enhancement". The experiment with varying energy density seems to support this interpretation and the use of low energy density becomes crucial when the experiment approaches the single molecule detection. The results may be important for future work of SM-SERRS, and SERRS in general, to fully understand the full impact of these enhanced fields.

References

(1) Myers, A. B. *Journal of Raman Spectroscopy* **1997**, *28*, 389-401.

(2) Weitz, D. A.; Garoff, S.; Gersten, J. I.; Nitzan, A. *Journal of Electron Spectroscopy and Related Phenomena* **1983**, *29*, 363-70.

(3) Weitz, D. A.; Garoff, S.; Hanson, C. D.; Gramila, T. J.; Gersten, J. I. *Optics Letters* **1982**, *7*, 89-91.

(4) Lakowicz, J. R.; Shen, Y.; D'Auria, S.; Malicka, J.; Fang, J.; Gryczynski, Z.; Gryczynski, I. *Analytical Biochemistry* **2002**, *301*, 261-277.

Reproduced with permission of the copyright owner. Further reproduction prohibited without permission.

(5) Song, L.; Hennink, E. J.; Young, T.; Tanke, H. *Biophysical Journal* **1995**, *68*, 2588-2600.

(6) Eggeling, C.; Widengren, J.; Rigler, R.; Seidel, C. A. M. *Analytical Chemistry* **1998**, *70*, 2651-2659.

(7) Deschenes, L. A.; Bout, D. A. V. *Chemical Physics Letters* **2002**, *365*, 387-395.

(8) Eggeling, C.; Volkmer, A.; Seidel, C. A. M. *ChemPhysChem* **2005**, 791-804.

(9) Molski, A. *Journal of Chemical Physics* **2001**, *114*, 1142-1147.

(10) Weitz, D. A.; Garoff, S.; Gersten, J. I.; Nitzan, A. *Journal of Chemical Physics* **1983**, *78*, 5324-5338.

(11) Del Caño, T.; Goulet, P. J. G.; Pieczonka, N. P. W.; Aroca, R. F.; De Saja, J. A. *Synthetic Metals* **2005**, *148*, 31-35.

(12) Del Cano, T.; Aroca, R.; De Saja, J. A.; Rodriguez-Mendez, M. L. *Langmuir* **2003**, *19*, 3747-3751.

(13) Gulbinas, V. *Chemical Physics* **2000**, *261*, 469-479.

(14) Hildebrandt, P.; Stockburger, M. *Journal of Physical Chemistry* **1984**, *88*, 5935-44.

(15) Bosnick, K. A.; Jiang, J.; Brus, L. E. *Journal of Physical Chemistry B* **2002**, *106*, 8096-8099.

(16) Jensen, L.; Schatz, G. C. *Journal of Physical Chemistry A* **2006**, *110*, 5973-5977.

(17) Futamata, M.; Maruyama, Y. *Analytical and Bioanalytical Chemistry* **2007**, *388*, 89-102.

(18) Maher, R. C.; Cohen, L. F.; Etchegoin, P. *Chemical Physics Letters* **2002**, *352*, 378-384.

Reproduced with permission of the copyright owner. Further reproduction prohibited without permission.

(19) Le Rue, E. C.; Etchegoin, P. G.; Meyer, M. *Journal of Chemical Physics* **2006**, *125*, 204701-1 204701-13.

(20) Le Ru, E. C.; Etchegoin, P. G. *Chemical Physics Letters* **2006**, *423*, 63-66.

(21) Pieczonka, N. P. W.; Aroca, R. F. *ChemPhysChem* **2005**, *6*, 2473-2484.

Reproduced with permission of the copyright owner. Further reproduction prohibited without permission.

CHAPTER 7

SUBSTRATE DEVELOPMENT

Reproduced with permission of the copyright owner. Further reproduction prohibited without permission.

7.1 Introduction

A major challenge in experimental SERS arises from the fact that the phenomenon is observed on nanostructured substrates of one form or another, with the required optical properties. Therefore the properties of that surface have an immense impact on the success or failure in the detection of a desired analyte, and correspondingly, there has been an explosion of reports on the fabrication of enhancing surfaces SERS substrates.[1] SERS substrates are, in general, metal nanostructures (nanoparticles and nanoparticle aggregates), and they come in all shapes and forms, from random distributions,[2] to well organized two-dimensional patterns.[3] To illustrate, the SERS substrate gallery, a sample of some of the substrates used in this work, is shown in Figure 7.1. It includes the commonly used metal colloids prepared by wet chemistry, (for which you can find hundreds of variations), metal island films prepared by physical methods, as well as some more sophisticated substrates that will be presented in this chapter.

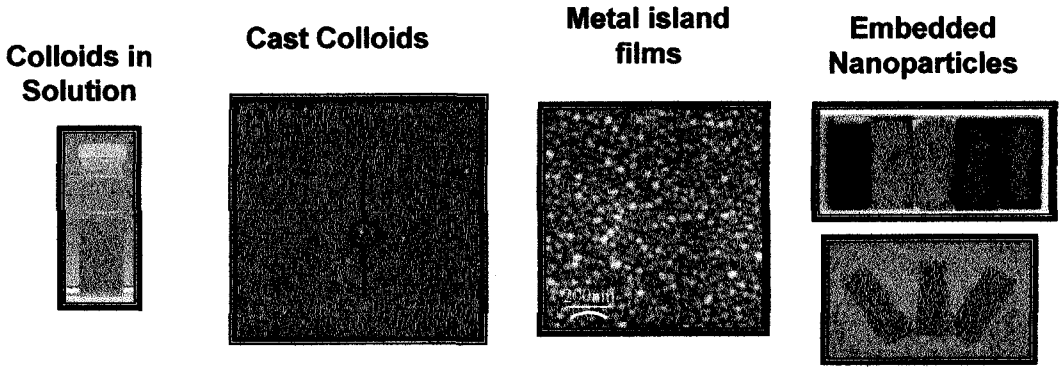

Figure 7.1: Gallery of SERS substrates

Reproduced with permission of the copyright owner. Further reproduction prohibited without permission.

As stated before, substrate development is in itself a rich and diverse area of research.[4-8] An analysis of the experimental results have made it clear that there is no point in searching for a "universal SERS substrate". It has become evident that each SERS substrate must be tailored to the type of analyte and application it is to be used for.

The substrates presented were designed to address specific issues that would improve the probability of attaining a good SERS/SERRS spectrum. The first substrate to be discussed is a mixed silver/ gold island which was created to overcome some of the limitations encountered when using pure Ag films. The second substrate development was an attempt to create SERS substrates that could find applications as possible biosensors by embedding the enhancing nanoparticles in a bio-friendly matrix. The final substrates development discussed here are the result of a desire to add functionality to the SERS substrates through the incorporation of a bio-recognition element.

7.2 Island Films of Mixed Silver and Gold[b]

7.2.1 Introduction

The motivation for the work presented here stemmed from the previous single molecule studies of LB using Ag island films as substrates. One of the chief problems, as was discussed in that chapter, was the large interference of impurities and a carbon background which is believed to be due to the reactivity of the silver surface. In attempt to suppress this, modification to the island film was sought. The next metal in relative strength of enhancement is gold. The gold plasmon resonance is to the red of that of silver

[b] This work was a collaborative effort with P. J. G. Goulet. Langmuir-Blodgett film fabrication was mostly completed by P. J. G. Goulet

Reproduced with permission of the copyright owner. Further reproduction prohibited without permission.

with peak plasmon absorption generally above 600 nm. Though its average enhancement factor is less than silver, it is known to provide a less reactive surface.

Here, a method was developed to combine gold and silver for the creation of a new substrate that demonstrated enhancement factors high enough for single molecule detection. In this section, this fabrication is described and characterized. The use of these films for SM studies is demonstrated with the SMD of a PTCD molecule in a LB monolayer. The novel substrate is characterized by its plasmon absorption, XPS of the metal surface and atomic force microscopy (AFM) topographical imaging. This work introduced a new substrate for trace detection as this was the first report of mixed Ag/Au film to be used for single molecule detection.

7.2.2 Experimental

Metal island films were prepared by vacuum evaporation at pressures of 10^{-7} Torr, and temperatures of +200 °C (maintained for 1 hour after evaporation), With total mass thicknesses of 10 nm, these substrates were prepared by two separate evaporation steps. First, 5 nm Ag films were deposited onto 7059 Corning glass slides, and, after allowing sufficient cooling times (1-2 hrs.), a second layer film of 5 nm Au was then deposited on top at the same +200 °C temperature. All depositions were carried out at evaporation rates of ca. 0.5 Å/s. The characterization of all mixed Ag/Au substrates was accomplished through the use of three complimentary techniques; UV-visible absorption spectroscopy, X-ray photoelectron spectroscopy (XPS)[c], and atomic force microscopy (AFM).).

[c] XPS samples were sent out for analysis to Surface Science Western, London, Ontario

Reproduced with permission of the copyright owner. Further reproduction prohibited without permission.

Mixed Langmuir-Blodgett films of bis-benzylimido perylene (Bbip) and arachidic acid were deposited onto mixed silver/gold island films at concentrations down to 1 molecule/μm^2. These mixed BBIP-AA Langmuir films were fabricated in the same manner as previously detailed in Chapter 3 with the exception that the substrate is now a glass slides coated with mixed Ag/Au (5 nm Ag + 5 nm Au) island films. All Raman spectra were collected with the Renishaw Ramanscope 2000. Excitation lines of 514.5, and 633 nm were used in this investigation to explore both resonance and off resonance Raman. In single molecule experiments, laser power was kept low (< 20 μW) to diminish the chance of photodegradation. Laser spot sizes were ca. 1 μm^2 using the 50X objective. Accumulation times were between 10 and 20 seconds.

7.2.3 Results and Discussion

The plasmon spectrum of a 10 nm mixed film (5 nm Ag + 5 nm Au) is shown in Figure 2. For reference, the plasmons for the more traditional substrates of the 6 nm Ag and 5 nm Au island films are also shown. The mixed substrate shows a much redder plasmon maximum (697 nm) due to the presence of gold as well as an overall broader absorption. The broader and shifted plasmon may be explained by slightly larger particles seen in the AFM (Figure 2). The particle size ranged between 20 and 120 nm, a larger size range than is typically measured for 6 nm Ag island films.

Reproduced with permission of the copyright owner. Further reproduction prohibited without permission.

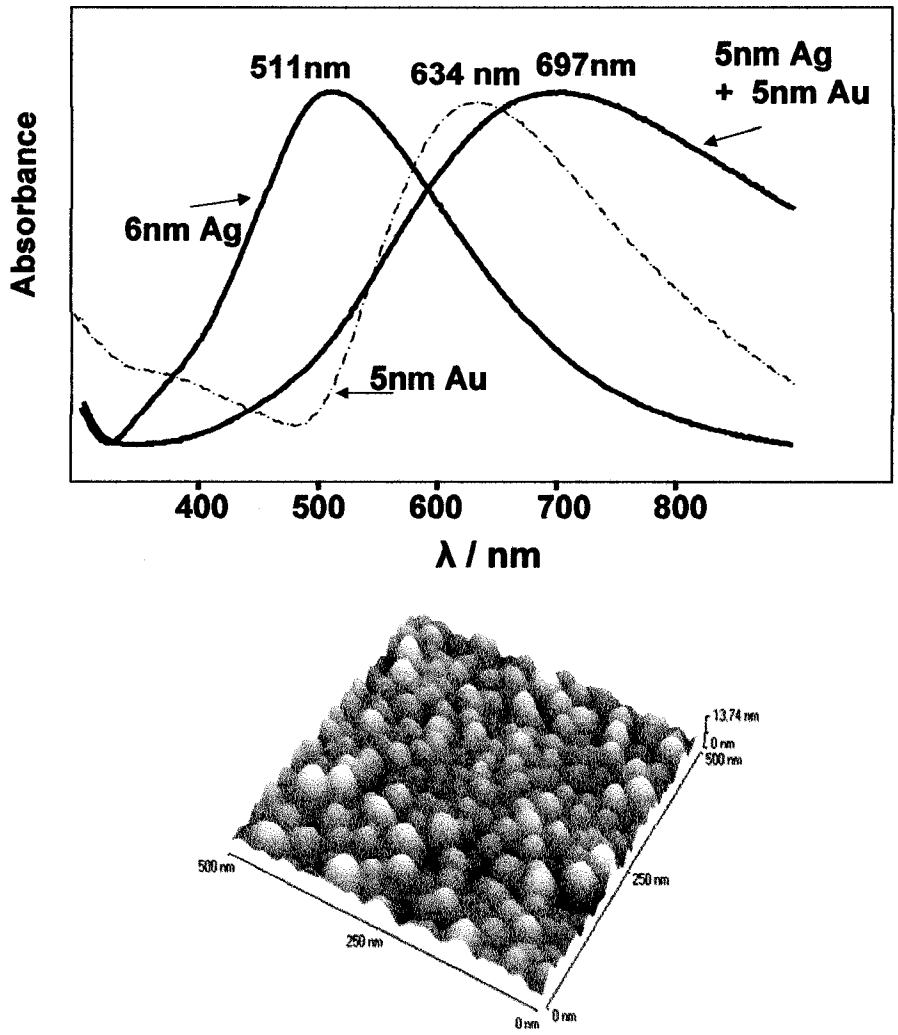

Figure 7.2: Plasmon absorption and AFM for Ag/Au island films. Plasmon absorption is shown for 6 nm Ag island film, 5 nm Au island film and a mixed Ag/Au (5 nm Ag + 5 nm Au) island film (top). AFM image of a 500 x 500 nm section of the Ag/Au film is also shown

The mixed Ag/Au character of these films were confirmed by XPS. Results indicated an equal amount of gold and silver on the surface of films made from this deposition process.

Reproduced with permission of the copyright owner. Further reproduction prohibited without permission.

Silver is very reactive surface in nanostructures and can be contaminated by interaction with the ambient environment . As the single molecule regime is approached this becomes even more of an issue, as has been shown in several independent reports.[9] The enhanced Raman scattering of these contaminations can compete and conceal the SERS signal of an analyte. By mixing the silver with gold, the high reactivity of the metal film with the environment is reduced while still maintaining the high Raman enhancement that is attained with the unique optical properties of silver island films.

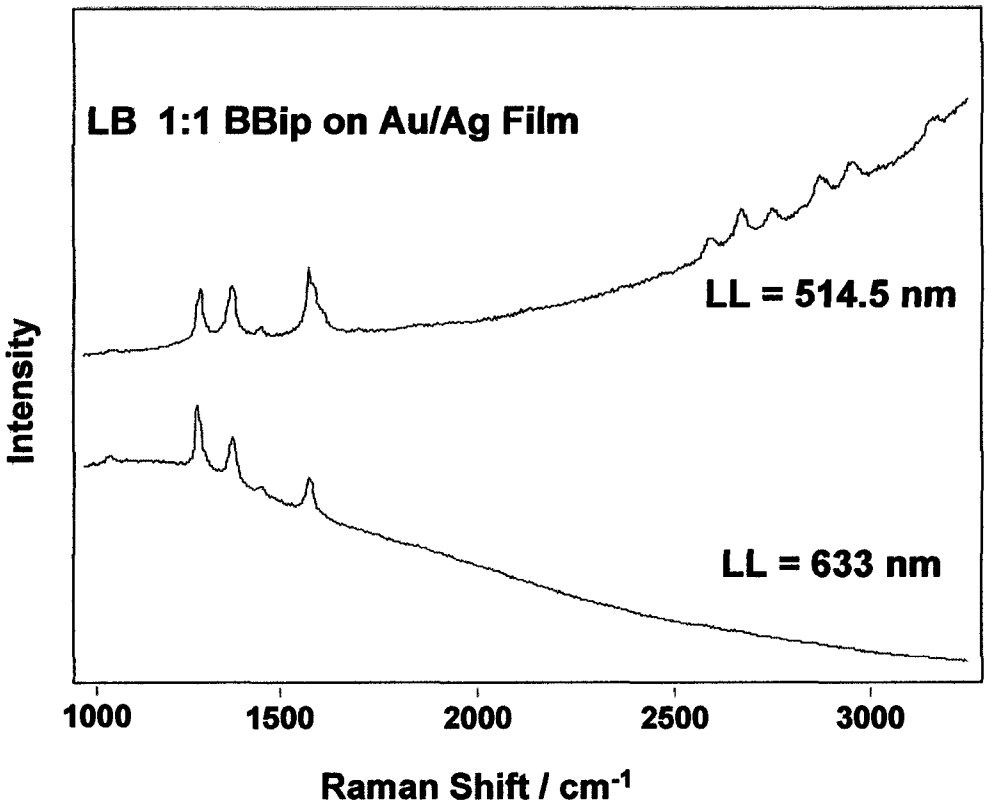

Figure 7.3: SERRS and SERS of BBip. SERRS (top) and SERS (bottom) spectra of a 1:1 Bbip film on mixed Ag/Au island film.

The effectiveness of these films as SERS and SERRS substrates is exemplified in Figure 7.3. The SERRS spectrum of a 1:1 Bbip monolayer on a Ag/Au film is shown

Reproduced with permission of the copyright owner. Further reproduction prohibited without permission.

along with the SERS spectrum attained at 633 nm. The latter also demonstrates that these mixed Ag/Au substrates are versatile and can be used with several laser lines. The average surface enhancement for Raman was estimated to be on the order of 10^3 from a comparison of the Raman signal recorded from the LB on glass to that of the SERRS measured from the LB on the island film. The use of these substrates for detection for a single Bbip molecule is shown in Figure 7.4. Here several of the SMD signals detected from these films are presented. The SERRS spectrum for the 1:1 concentrated film is also shown for reference.

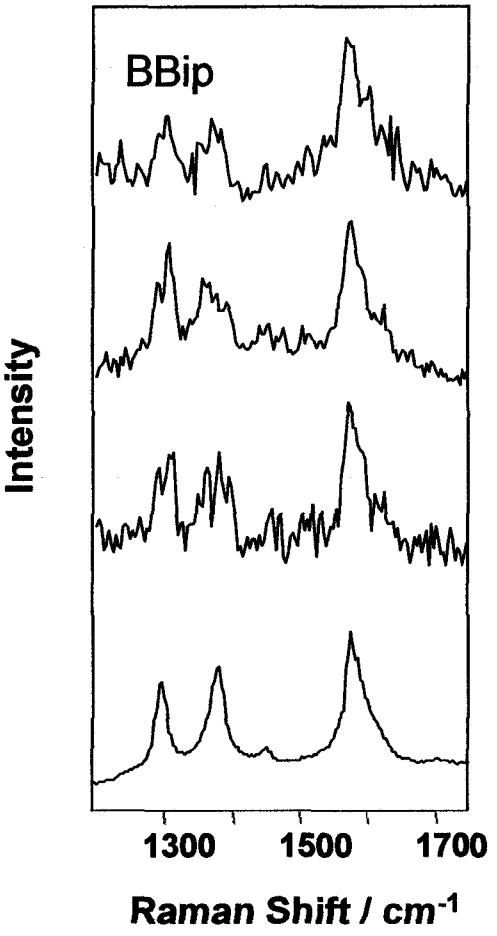

Figure 7.4: Several SM spectra of Bbip compared to the ensemble SERRS spectrum

Reproduced with permission of the copyright owner. Further reproduction prohibited without permission.

The SM character of the spectra is evident with changes in relative intensities and bandwidth seen in the detected signal. The use of Ag/Au mixed films did succeed in providing a large reduction in the interference of contaminations and carbon resulting in better quality SM spectra. Though the SM signal was still hard to pin down, the number of SMD events was on average higher then what was encountered with the 6 nm silver island films.

7.2.4 Conclusion

An interesting new substrate has been employed in this work, and has shown to be a very promising. The use of the high enhancing metal of Ag with the less reactive gold has resulted in a film that greatly reduces interferences as well as providing a high SERS enhancement. In addition the broad and red shifted surface plasmon allows the use of this substrate for wide range of excitation frequencies. The potential for single molecule SERRS studies was shown in the successful measurement of the SM signal of Bbip-PTCD.

Reproduced with permission of the copyright owner. Further reproduction prohibited without permission.

7.3 Gold nanoparticle Embedded Chitosan Self-Sustained thin films[d]

7.3.1 Introduction

The development of novel, environmentally friendly methods for the fabrication of nanoscale structures has now become an important challenge facing materials science. In this work, self-sustained, biocompatible, biodegradable films containing gold nanostructures were fabricated for potential applications in sensitive chemical and biochemical analysis. This was accomplished through a novel synthesis of gold nanoparticles mediated by the biopolymer chitosan. Self-supporting thin films were formed from the resultant gold-chitosan composite solutions, and characterized by UV-visible surface plasmon absorption, transmission electron microscopy, atomic force microscopy, infrared absorption, and Raman scattering measurements. Results demonstrated a degree of control over the size and distribution of the nanoparticles produced. The SERS activity of these films is demonstrated for the test molecule R6G

7.3.2 Experimental

Chitosan, obtained from shrimp chitin (an N-acetylglucosamine polymer), was provided by Cyrbe do Brasil Corporation. It has an average molecular weight of 500,000 g/mol, as determined by viscometry, and a 75% degree of deacetylation.[10] It was purified twice in 1% aqueous acetic acid solution, filtered with filter paper, precipitated with a 1% aqueous sodium hydroxide solution, and washed extensively with deionized water until neutral pH was reached. Hydrochloroauric acid was purchased from Aldrich, and used

[d] This work was done in collaboration with D. S. dos Santos Jr and P. J. G. Goulet. With film preparation carried out by D. S. dos Santos Jr with feed back and direction from N. P. W. Pieczonka and P. J. G. Goulet

Reproduced with permission of the copyright owner. Further reproduction prohibited without permission.

without further purification. All glassware was thoroughly cleaned by detergent, aqua regia, and copious rinsing with deionized water. Solutions were prepared using deionized water. Films were prepared by casting measured volumes of the solutions onto glass slides at room temperature, and allowing for evaporation of the solvent.

UV-visible absorption spectroscopy was used to monitor the plasmon absorption of the gold nanoparticles produced. AFM images were recorded in non-contact tapping mode with a n+-silicon tip. A scan rate of 1 Hz was used with 256 and 512 sample lines per image. Transmission electron microscopy (TEM) images were obtained with a Philips CM20 STEM operating with a 120 kV accelerating voltage.[e] Infrared absorption measurements were recorded with the Bruker Equinox 55 FTIR spectrometer. Each spectrum was measured in transmission mode with 256 scans, and 4 cm^{-1} resolution. All Raman spectra were acquired using a 633 nm excitation line directed through a 50X objective with < 1 mW of laser power at the sample.

7.3.3 Results and Discussion

Chitosan has been extensively studied for more then 30 years as an inexpensive, renewable material.[11] It has unique structures and physicochemical characteristics that differ considerably from typical synthetic polymers.[12,13] Chitosan's structure is similar to that of cellulose, but it has better processability due to the presence of amino groups. In fact, its chemistry is largely determined by its amino and hydroxyl groups. Chitosan is well known as a strong chelating agent for metals and proteins making it particularly

[e] All transmission electron microscopy (TEM) samples were sent for imaging to McMaster University, Hamilton ON

Reproduced with permission of the copyright owner. Further reproduction prohibited without permission.

useful in sensor development.[14,15] It has been shown to make biocompatible, biodegradable films; all these properties make the material a good candidate as a basis for new types of SERS substrate with potential application in biosensing.

The use of chitosan to facilitate the production of gold nanoparticles showed the capability to generate a vast range of films with a range of particle densities and sizes. The resulting optical properties of the fabricated films were found to be dependent on the relative ratio of gold to chitosan, as well as the temperature at which the reaction was carried out. The chitosan is believed here to be both a catalyst and stabilizing agents for the gold nanoparticles. In conjunction with the use of the mild reducing agent, acetic acid, this synthesis demonstrated a degree of control over the resulting size and density of gold nanoparticles in these films.

Each synthesis was monitored by plasmon absorption to track particle growth and particle density. A typical progression is shown in Figure 1 for the syntheses denoted S1. The reaction was monitored for 5 hours. Here the increase in the plasmon intensity indicates an increase in particle density. This particular syntheses was made by mixing equal volumes (15 mL) of a 1% chitosan solution in 1% aqueous acetic acid with a 0.01% aqueous tetrachloroauric(III) acid ($HAuCl_4$) solution at 85 °C. The observed increase in the extinction of the 528 nm surface plasmon band can be attributed to the formation and increasing population of gold nanoparticles.

Reproduced with permission of the copyright owner. Further reproduction prohibited without permission.

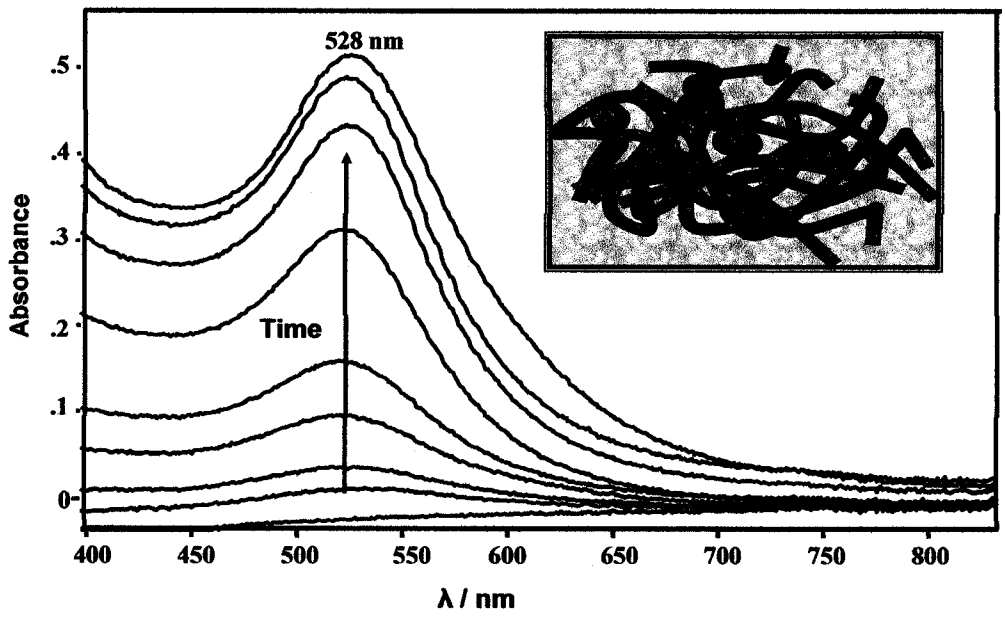

Figure 7.5: Growth of surface plasmon with reaction time. The growth in the plasmon indicates the production of Au nanoparticles. The inset is a cartoon of the proposed substrate.

For thin film fabrication, these solutions were allowed to cool under ambient conditions, and were cast onto glass substrates, where they were allowed to dry for 24 hours. The resulting films showed a wide range of colors from light pink to dark violet. This large range of films that could be produced is evidenced by the variety of colour films captured in the photograph shown in Figure 7.6. Plasmon absorptions of the dried films showed a range a λ_{max} ,also shown in Figure7.6.

Reproduced with permission of the copyright owner. Further reproduction prohibited without permission.

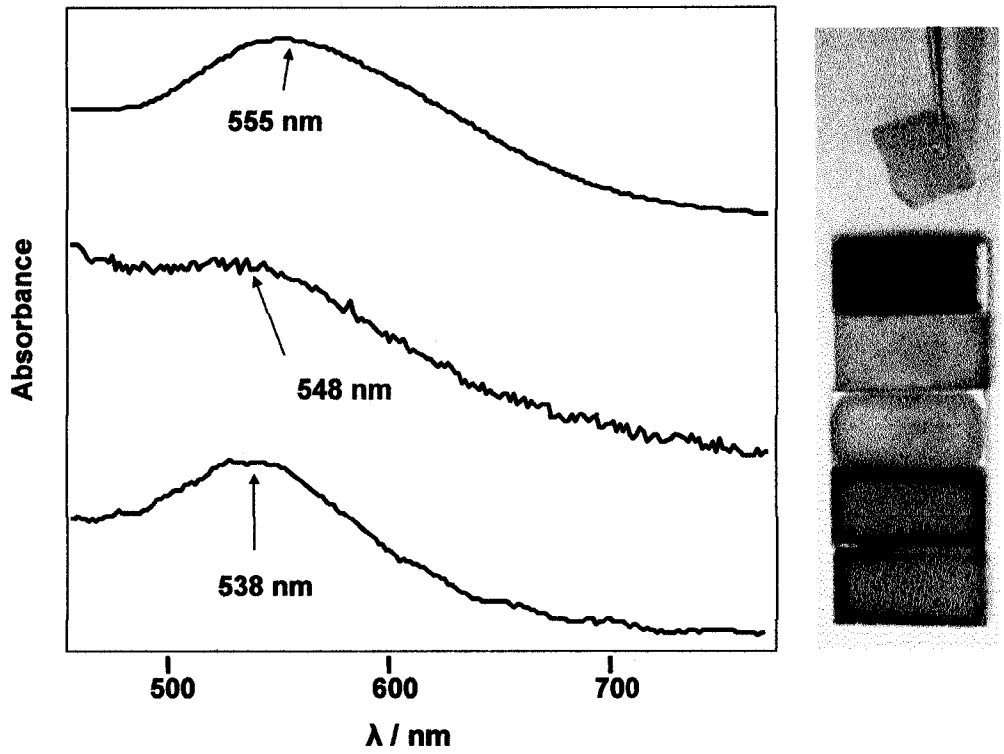

Figure 7.6: Plasmon absorption of several of the films made from gold/chitosan composite solutions. Plasmon absorption is shown along with a photograph of several different films. The top image is an example of a typical self-sustained nanocomposite film

One major advantage of working with chitosan is that is can form thin films, free of glass support. This is accomplished by a process of neutralization with a 1% aqueous solution of NaOH. Self-sustained, stable, and flexible nanocomposite films are the result, an example of one of them is shown in the top corner of Figure 7.6. Films such as these could be used in investigations where traditional SERS substrates, such as metal island films on glass, could not. As well, the biofriendly nature of the matrix material makes these films possible candidates for in vitro sensors.[16]

Reproduced with permission of the copyright owner. Further reproduction prohibited without permission.

While a large variety of films could be generated, only two syntheses were chosen for extensive characterization. The first films to be studied were produced by the above S1 reaction, which created a film embedded with small, well separated particles. The second were from syntheses (S3), where the amount of $HAuCl_4$ was increased to a 0.0625 % while keeping all other parameters the same. This produced films with a high degree of aggregated gold nanoparticles. Films fabricated from these two solutions provided an interesting contrast into what works for a SERS substrate as the former showed no SERS activity while the latter did. Full details of these syntheses can be found in reference 17.

7.3.4 Characterization of Films

Since one of the primary motivations for using chitosan are to take advantage of its many unique properties, it was hoped that there would be little modification to the biopolymer upon reaction with gold. FT-IR measurements of the free films seem to support this. Films with and without gold particles are shown in Figure 7.7. There were no noticeable changes in the spectra when compared.

Reproduced with permission of the copyright owner. Further reproduction prohibited without permission.

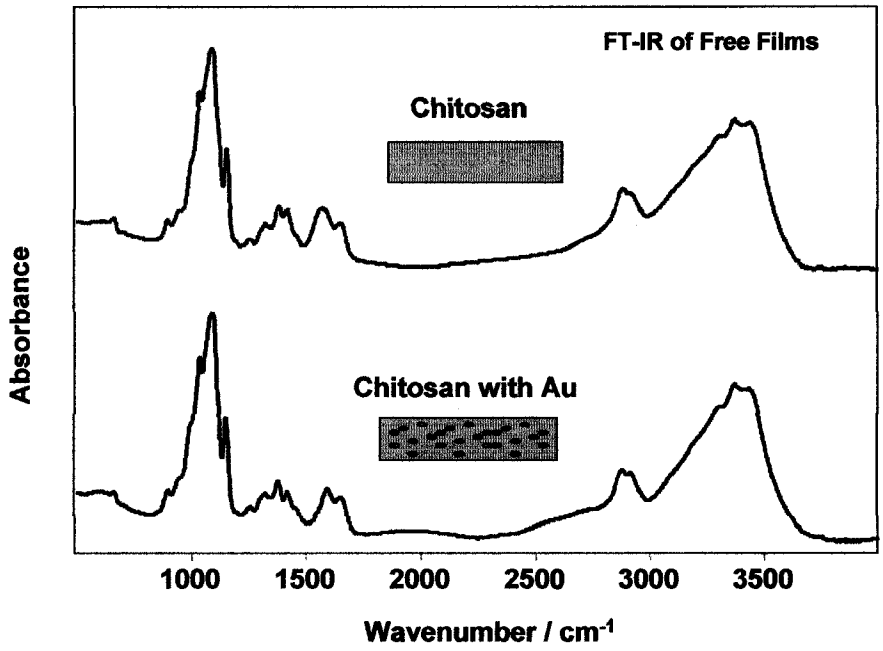

Figure 7.7: Comparison of FT-IR absorption spectra of pure chitosan film and chitosan film embedded with Au nanoparticles

Reproduced with permission of the copyright owner. Further reproduction prohibited without permission.

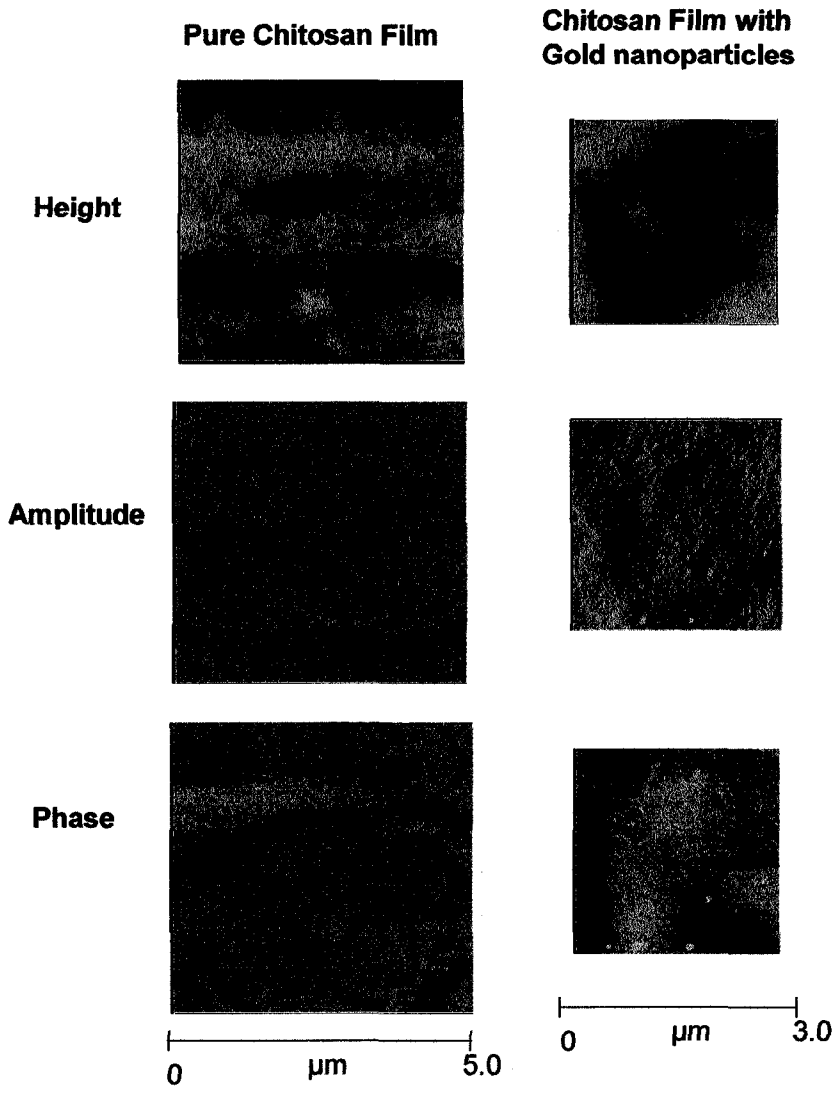

Figure 7.8: Comparison in AFM images between a pure chitosan film and a chitosan film embedded with Au nanoparticles

7.3.4.1 S1 Films

AFM of the surface of these films were done to see changes in morphology. Being a biopolymer, the surface is relatively soft and it was found contact mode was ineffective

Reproduced with permission of the copyright owner. Further reproduction prohibited without permission.

at producing quality images; tapping mode though caused little problems and produced all images presented here.

In Figure 7.8, height, amplitude and phase images were used for characterizing the surface. The AFM of samples of the pure chitosan film indicated the surfaces were relatively flat, with an average of surface roughness found to be 3.8 nm. In contrast, films with gold nanoparticles were very rough with values over 25 nm. Films with gold particles were also found to be very inhomogeneous making characterization of the topography of the surface difficult. However, the AFM did show that there were very few gold particles on the surface of these films. The Au nanoparticles seem to be truly embedded. TEM was required to determine the size and shape and distribution of the nanoparticles inside these films. Embedded Au nanostructures provide a rationale to forecast the analyte/substrate interactions, since the analyte would have to permeate into the film for SERS enhancement, a property that could be very advantageous with potentially built-in selectivity. In Figure 7.9, the characterization results for a chitosan gold particle embedded film created by S1 are shown. TEM at two magnifications (low and high) reveal well spaced small particles, with a size of ca. 20 nm. The AFM images again showed little gold on the surfaces. The usefulness of phase imaging is demonstrated here by being able to distinguish between the softer polymer and the harder nanoparticles. Though they are not distinguishable in the height image, the locations of the metallic particles are indicated by white dots in the phase image. The plasmon measured for these films was 538 nm. Mie extinction calculations for 20 nm Au sphere in a chitosan matrix (refractive index = 1.5),[18] showed great agreement with the measured plasmon. This supports the mono disperse nature of the particles in this particular film, which again showed negligible SERS activity

Reproduced with permission of the copyright owner. Further reproduction prohibited without permission.

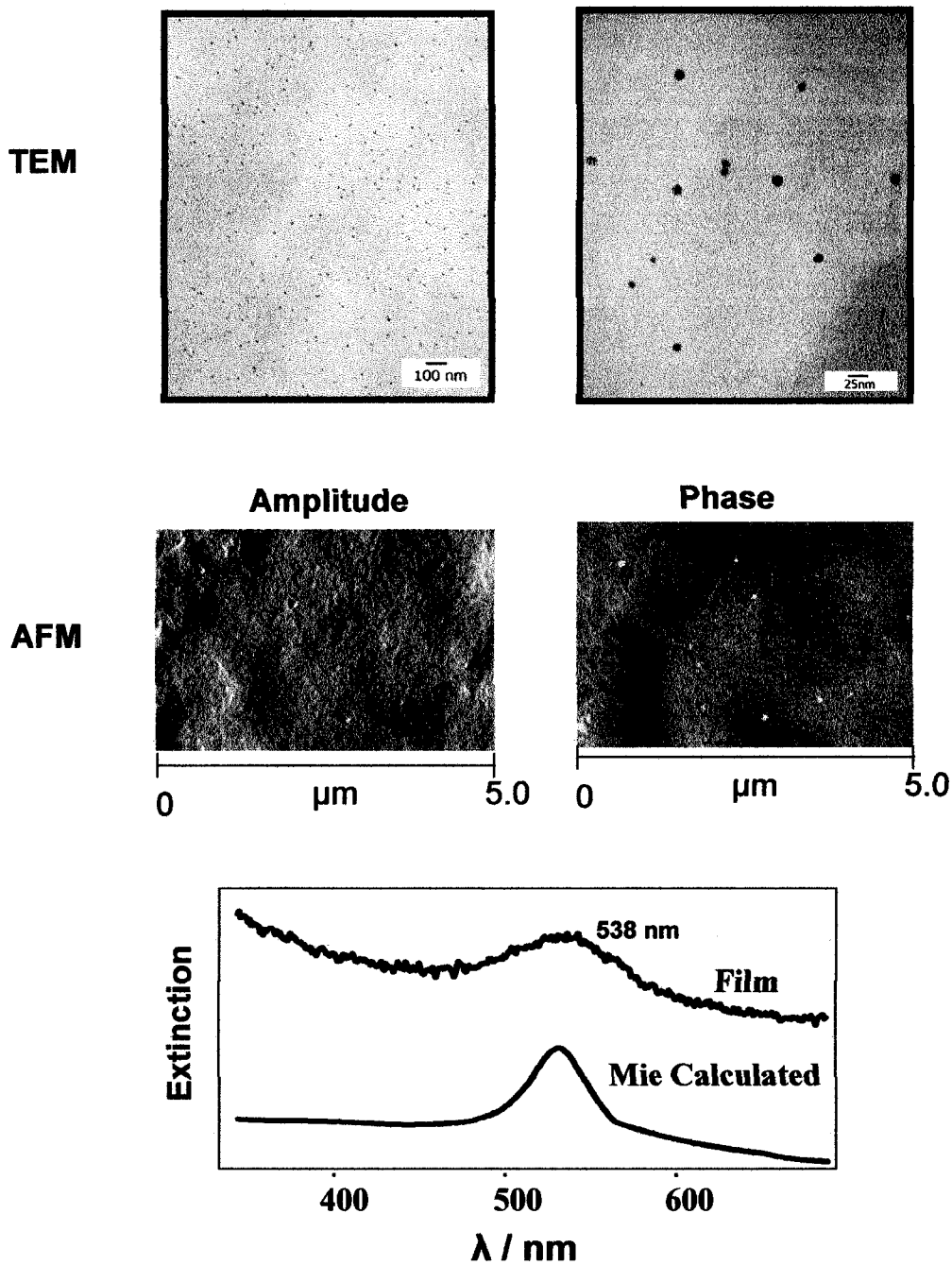

Figure 7.9: Characterization of the S1 films. TEM, AFM and plasmon absorption. The calculated extinction spectrum is shown for comparison.

Reproduced with permission of the copyright owner. Further reproduction prohibited without permission.

7.3.4.2 S3 Films

In contrast, excellent SERS activity was found with films produced with the S3 synthesis. In Figure 7.10, the characterization for this sample is presented. The plasmon absorption maximum at 555 nm is redshifted in comparison to S1. A photograph of the film is shown as an inset. TEM images clearly show the presence of Au aggregates, which is believed to be the source the SERS activity. In Figure 7.11, the AFM images of the samples are presented, with the rough topography again makes surface imaging difficult. The phase imaging shows once more very little gold on the surface. The higher magnification images show the few particles and aggregates that do peak through the surface.

Reproduced with permission of the copyright owner. Further reproduction prohibited without permission.

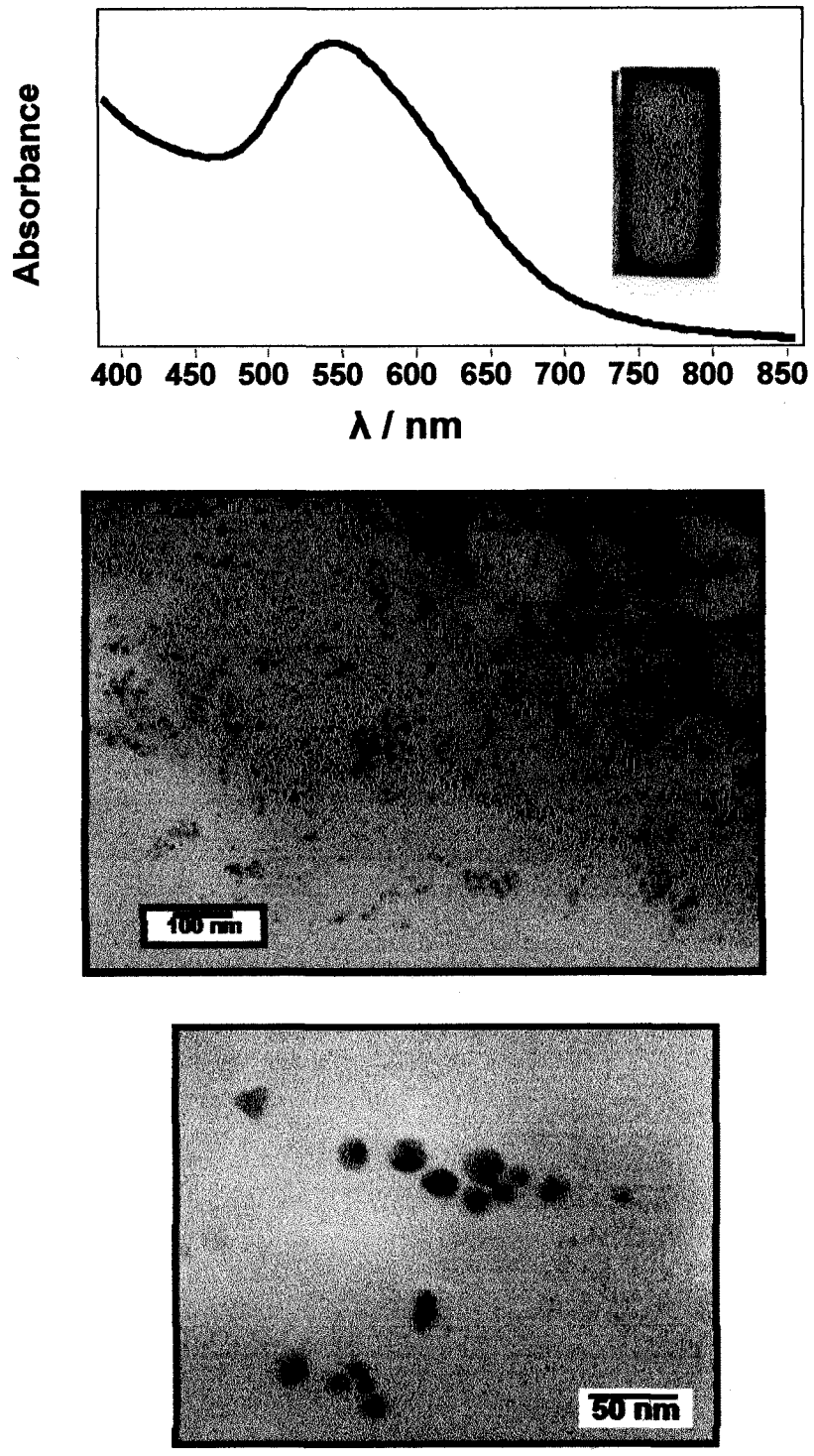

Figure 7.10: Characterization of the S3 films. TEM and plasmon absorption. A photograph of the film is shown as a inset.

Reproduced with permission of the copyright owner. Further reproduction prohibited without permission.

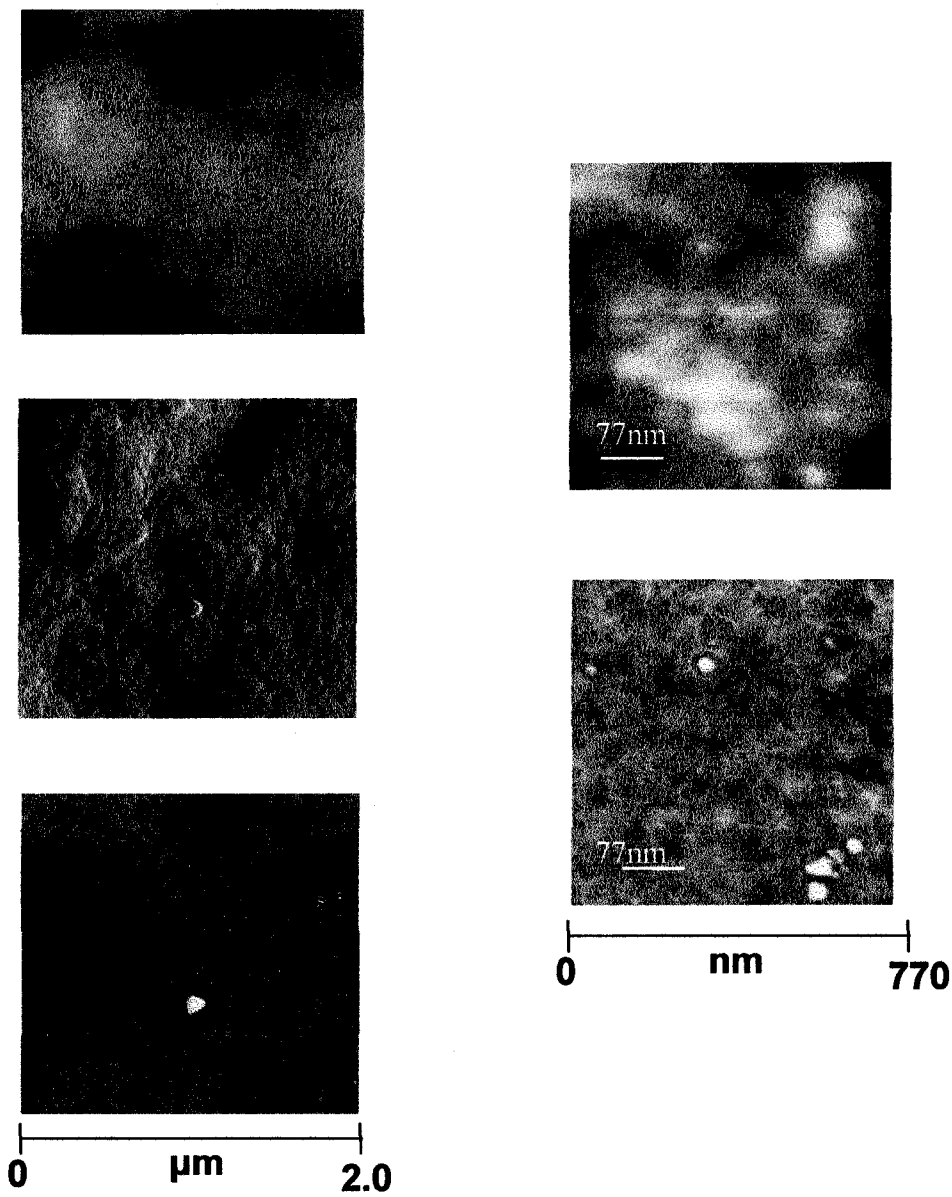

Figure 7.11: AFM of the SERS active films (S3).

Reproduced with permission of the copyright owner. Further reproduction prohibited without permission.

To test the SERS activity of this film, a film of the S3 variety was dipped in a solution of the analyte R6G at concentration range from 10^{-4} to 10^{-6} M. For comparison pure chitosan films (without gold)) were dipped in the same solutions. The SERRS signal of R6G was easily seen down to 10^{-6} M. In comparison, only the florescence of R6G could be seen from the pure chitosan film, even at 10^{-4}, as seen in Figure 7.12.

The role of aggregates for SERS is evident in the comparison of the two film types. The mono disperse particles registered no SERRS activity under these conditions, while the aggregated particles did. This supports a general property of SERS substrates, the highest enhancements arise from aggregated systems.

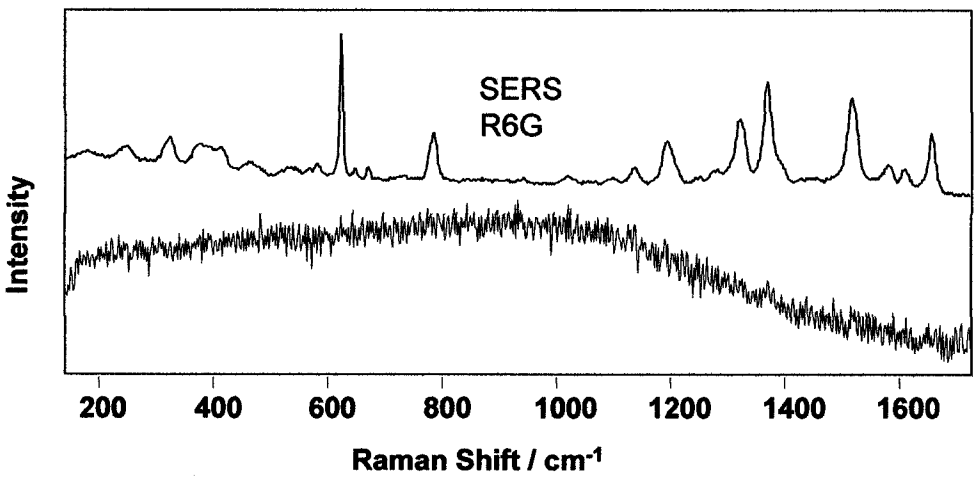

Figure 7.12: SERS obtained with a Au-chitosan film. SERRS spectrum recorded from a Au-chitosan film (S3) dipped in a 10^{-4} M R6G solution (Top). Spectrum recorded from a pure chitosan film dipped in the same solution (Bottom)

7.3.5 Conclusions

Reproduced with permission of the copyright owner. Further reproduction prohibited without permission.

The development of biocompatible analytical methods is now becoming increasingly important. In particular, the in situ detection of trace quantities in living systems, without disturbing them, is of utmost importance. This work shows the fabrication and testing of self-sustained, biocompatible, biodegradeable, and non-toxic thin films for the detection and chemical analysis of trace quantities. It is hoped that this work will provide new perspectives into the development of ecologically responsible analytical methods, and find application in new biological and medical technologies.

7.4 Avidin and Ag Layer-by-Layer Films [f]

7.4.1 Introduction

It has been wildly established that the plasmonics of metal nanoparticles is one of most interesting properties of any material in the nano regime. As a result of a dipole plasmon resonance that is dependent on the dielectric function and is sensitive to size, morphology and environment, metal nanostructures may be used in a wide range of applications. It is this versatility that makes their use in biosensors so appealing and also why their incorporation into bio-recognition systems is such a vibrant field of research. In this pursuit, nanoparticles have been functionalized with, antibodies,[4] ligands,[19] and DNA strands,[20] to mention but a few.

An alternative way of incorporating the unique optical properties of metal nanoparticles with chemically selective materials is provided by the Layer-by-Layer (LbL) method for thin film fabrication. Since its inception, this technique has been shown

[f] This work was a collaborative effort with P. J. G. Goulet.

Reproduced with permission of the copyright owner. Further reproduction prohibited without permission.

to be extremely successful in creating multi-component, structured films with tailored functionality and properties. Pioneered by Dresher[21] the method allows through consecutive adsorption steps, composite films to be constructed from a variety of materials, such as polymers and proteins. A cartoon of this wet chemistry procedure is shown in Figure 7.13

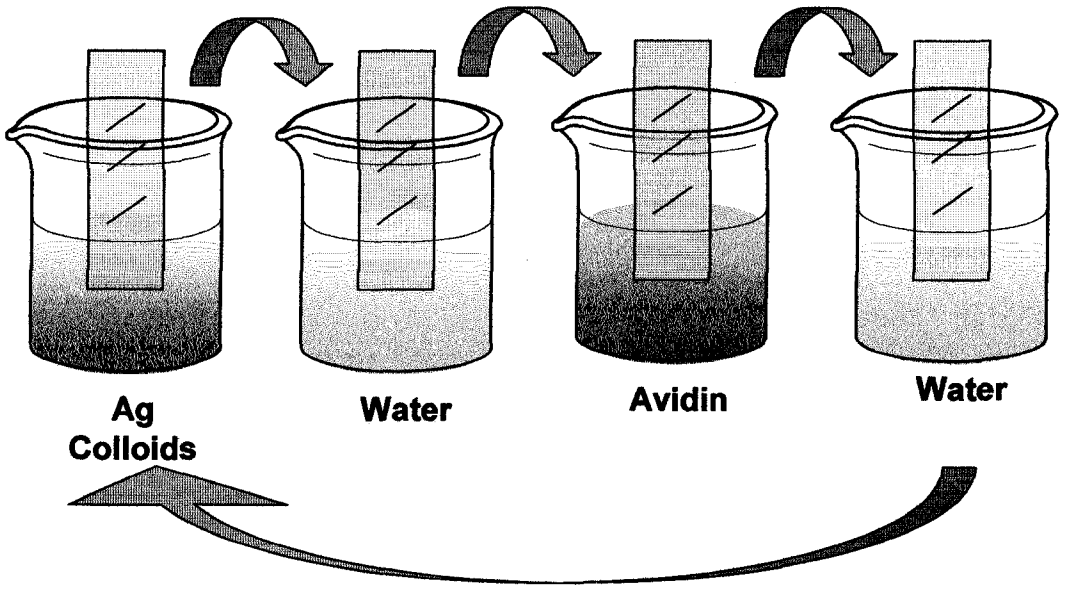

Figure 7.13: Illustration of the layer-by-layer method

Nanostructures, such as quantum dots,[22] and metal nanoparticles,[23] have been shown to be included in these layered films with no loss of their photonic ability. Here this is extended to chemical selective materials, particularly those that are active components of bio-recognition systems. The presence of optically active nanoparticles allows the resulting binding events to be reported by several methods. These include, localized surface plasmon resonance spectroscopy,[24] enhanced fluorescence,[25] and of particular interest here, SERRS.

Reproduced with permission of the copyright owner. Further reproduction prohibited without permission.

LbL is an easy and versatile method for combining the unique optical properties of metal nanoparticles with chemically selective materials for use in functional SERRS substrates. For example, films constructed with alternating layers of avidin and silver nanoparticles can be fabricated. These films are used as "smart" substrates that can significantly increase the SERRS signal for a target analyte through an effective concentration enhancement. The prototype system chosen to illustrate the possibilities of this approach is the avidin/biotin pair. Avidin is a glycoprotein (molecular weight, 68 000), found in egg whites and contains four identical binding sites for the biotin ligand. The affinity between avidin and biotin is one of the strongest known to exist, with a reported binding constant of 10^{15} M^{-1}.[26] This incredible affinity has been utilized in numerous applications where selectivity is desired. The Ag colloids used here are effectively negatively charged with a measured zeta potential to be approximately -50 mV at pH of 6.[27] Contrary, avidin is strongly cationic at neutral pH values due to its isoelectric point of 10.5.[28] These opposing charges favour a LBL process that occurs through electrostatic interactions, with each layer providing an effective surface charge reversal. The films presented here were created through alternating depositions of Ag and avidin.

The ultimate goal for these types of films is to have a degree of selectivity built into the SERS substrate. This general idea is shown in the Figure 7.14. Analytes that are biotinylated will reach the substrate, where an effective concentration enhancement will occur. In this section, concentration enhancements will be demonstrated for two types of analytes, a probe molecule which is biotinylated and another where the biotinylation is accomplished in situ.

Reproduced with permission of the copyright owner. Further reproduction prohibited without permission.

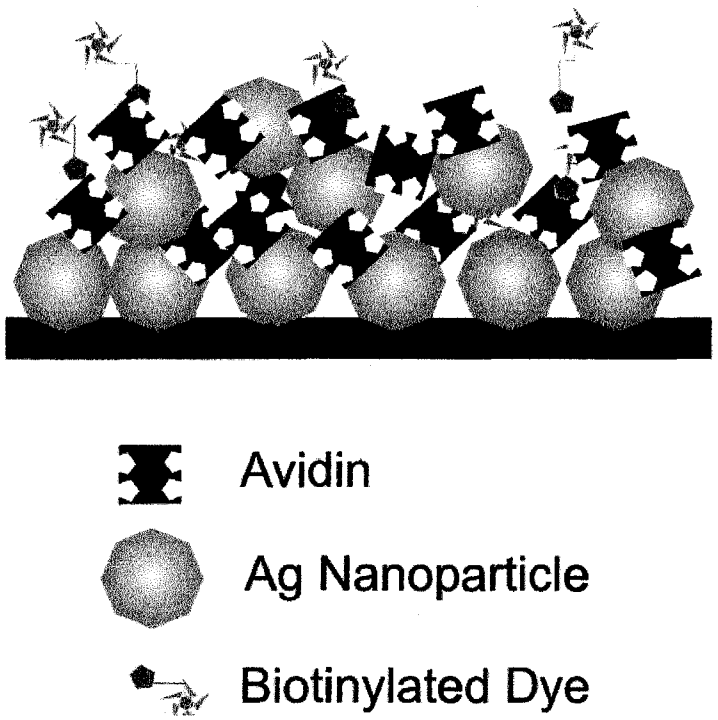

Figure 7.14: Illustration of construction of LbL avidin/Ag film showing the selective absorption of biotinylated species.

7.4.2 Experimental

Silver nitrate, sodium citrate, avidin (from egg white), fluorescein, and biotin 3-sulfo-N-hydroxysuccinimide ester were purchased from Sigma-Aldrich, while biotin-4-fluorescein (B4F) and 5-(aminomethyl)fluorescein (5-AF) were purchased from Molecular Probes. All were used without further purification. Colloidal Ag solutions were prepared by citrate reduction of $AgNO_3$ according to the well known method of Lee and Meisel,[29] and diluted by a factor of 2 before use. All avidin, fluorescein, B4F, 5-AF, and biotin solutions were prepared in 10 mM phosphate buffered saline (PBS) at pH 7.5. The in situ biotinylation of 5-AF was carried out by mixing it with biotin 3-sulfo-N-hydroxysuccinimide ester in a 1:1 molar ratio in PBS solution (pH 7.5) at room

Reproduced with permission of the copyright owner. Further reproduction prohibited without permission.

temperature, to produce a solution 10^{-4} M of each. The reaction was allowed 30 min to reach completion.

Prior to film fabrication, all glass microscope slides were cleaned and silanized. The slides were first washed in detergent and deionized water, immersed in 20% H_2SO_4, rinsed again in deionized water, and dried. Next, they were immersed into pure acetone for 5 minutes, immersed into a 2% acetone solution of 3-amino-propyltriethoxysilane for 5 minutes, and then rinsed thoroughly with water and dried. All LbL films were prepared by immersing these clean, silanized slides into colloidal Ag solution for 30 min, rinsing them with water, drying them with air, then immersing them into a 50 μg/mL avidin solution in PBS for 30 min. Upon removal, these films were again rinsed and dried, then re-immersed into colloidal Ag solution. Through these alternating deposition steps, films were built up until they were composed of 14 bilayers.

To monitor their surface plasmon absorption, UV-visible absorption spectra were obtained from LbL films after each bilayer was added. AFM measurements were performed in tapping mode with a n+-silicon tip (NSC 14 model, Ultrasharp). All images were collected at a scan rate of 0.5 Hz 512 lines per image. Topographical, amplitude, and phase images were all used for analysis of the surface morphology of these films, Raman scattering experiments were conducted with the InVia system with 514.5 nm laser excitation and a 50x objective.

All SERRS spectra were recorded from 14 bilayer films immersed for 30 min into fluorescein, 5-AF, B4F, and biotinylated 5-AF solutions with concentrations ranging from 10^{-4} to 10^{-7} M. After removal from these solutions, films were thoroughly rinsed with deionized water and dried before measurement.

Reproduced with permission of the copyright owner. Further reproduction prohibited without permission.

7.4.3 Results and Discussion

In Figure 7.15, the sequential building of these films is shown through the growth of the surface plasmon absorption from 2 to 10 bilayers. It can be seen that the extinction of these films grows with increasing number of bilayers, confirming effective film building and the advantage of adsorption over desorption under these conditions. These spectra reveal two well-resolved high energy bands at ca. 377 nm and 410 nm that redshift slightly with increasing number of bilayers. These bands can be assigned to quadrupolar and dipolar particle plasmon resonances, respectively, with the quadrupolar mode being due to the presence of larger spherical particles with diameters up to 70 nm. The slight redshifting of these bands can be attributed to changes in the dielectric function of the medium surrounding the particles with film growth. Also observed in these spectra is a very broad feature with a maximum at about 700 nm that increases in relative intensity as the number of bilayers deposited is increased. This band can be assigned to particle aggregates that are known to increase in number as film growth proceeds.

Reproduced with permission of the copyright owner. Further reproduction prohibited without permission.

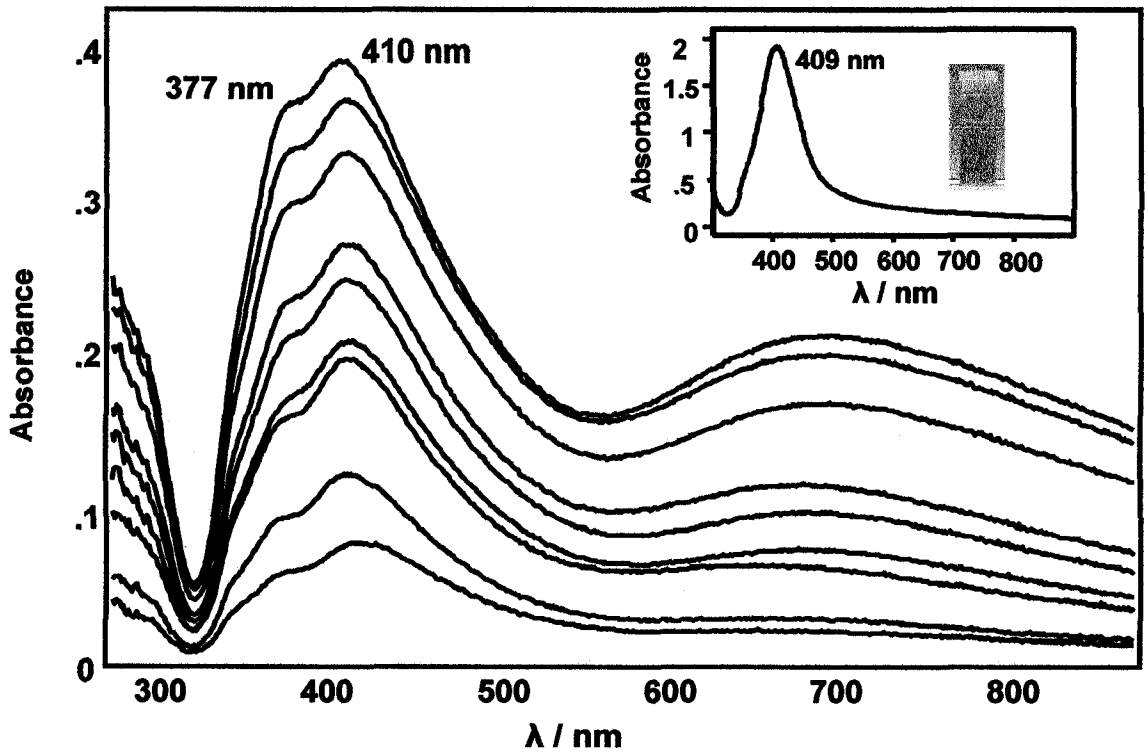

Figure 7.15: Surface plasmon absorption from films with 2 to 10 bilayers. The plasmon absorption of the Ag colloid is shown in inset.

The images shown in Figure 7.16, are the optical images of the films with 2, 8 and 14 bilayers. From these, it can be seen that at 14 bilayers the film is relatively homogeneous on the macro scale.

Reproduced with permission of the copyright owner. Further reproduction prohibited without permission.

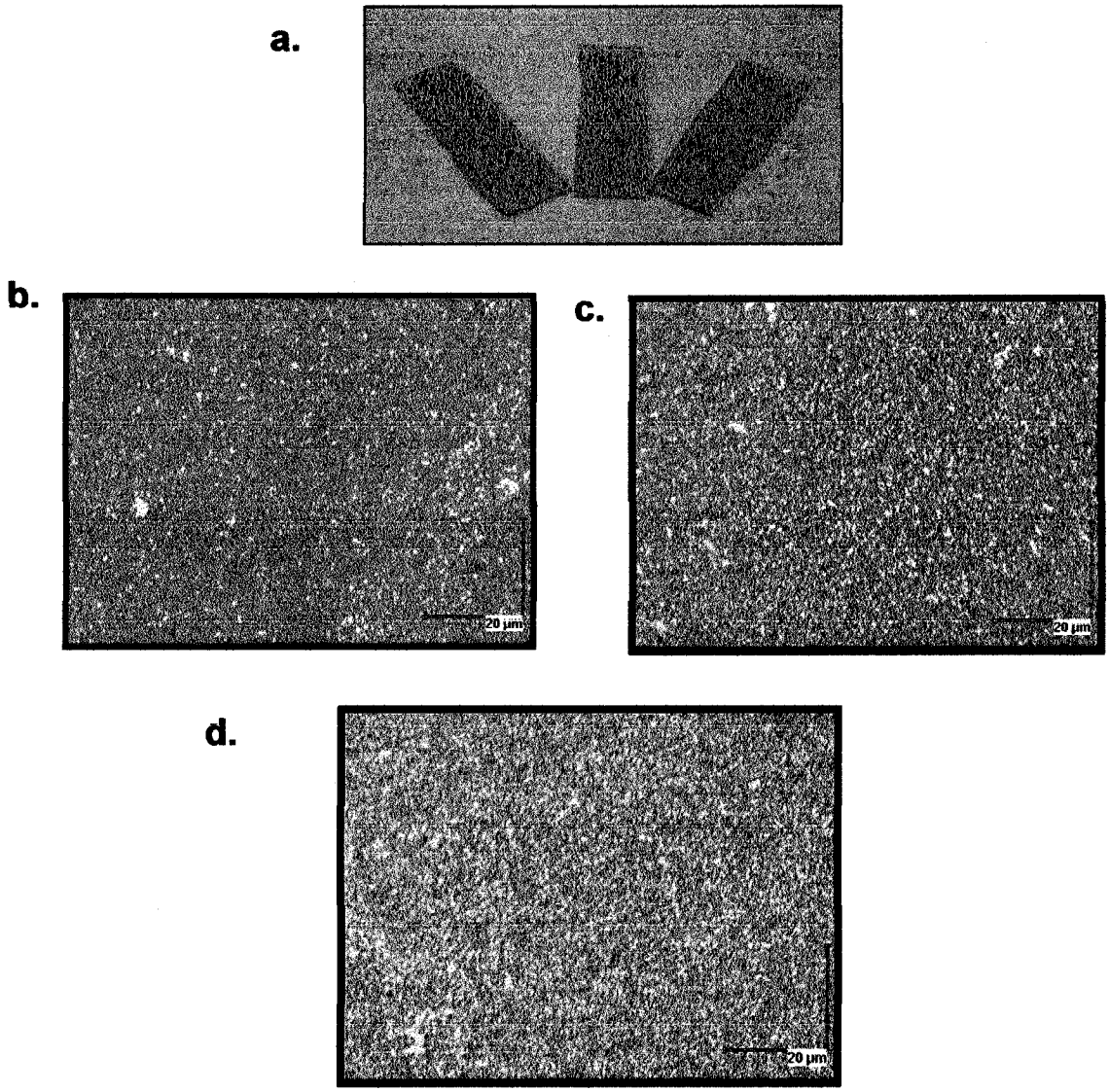

Figure 7.16: Optical images of the avidin/Ag nanoparticle LbL films. Images b-d are the films for 2, 8,14 bilayers as seen with a 50X.

To understand the relationship between the optical and physical properties of the avidin/Ag nanoparticle LbL films produced in this work, their surface morphologies were analyzed by AFM imaging.

Reproduced with permission of the copyright owner. Further reproduction prohibited without permission.

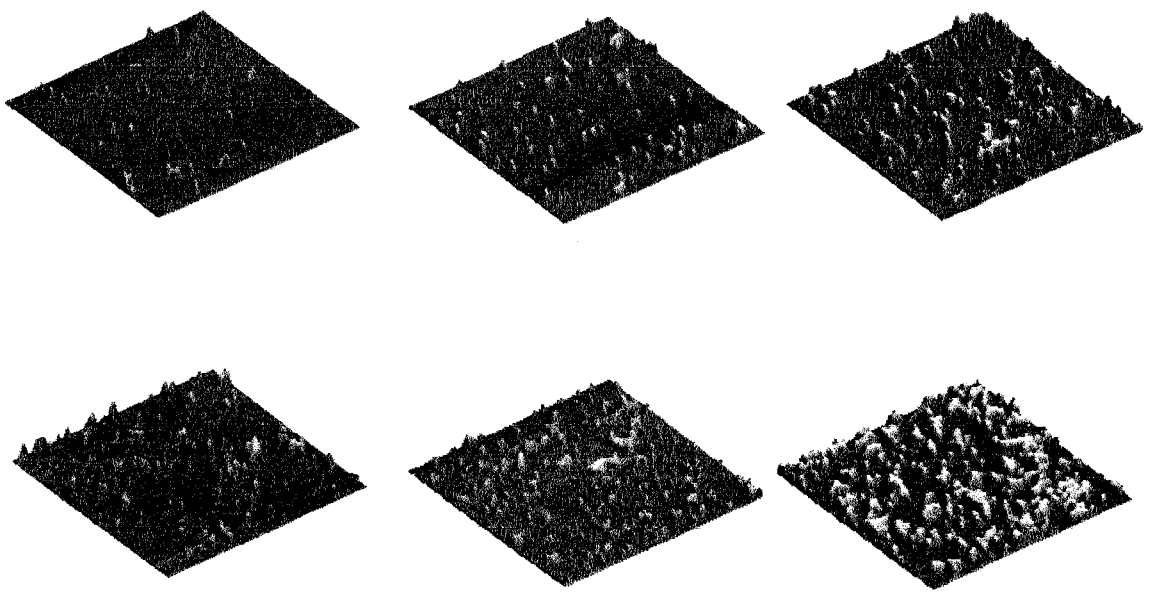

Figure 7.17: AFM topography images showing the progression from 2,4,6,8,12,14 bilayers. Each image is a 5 X 5 μm height image shown in 3D profile.

Selected representative topographical, or height, images are presented in Figure 7.17 for substrates consisting of 2, 4, 6, 8, 12, and 14 bilayers. It can be seen that as the number of bilayers deposited is increased, there is a general trend toward greater surface coverage, increased particle-particle interaction, and cluster/aggregate formation, as is expected. This trend is supported by increasing RMS roughness values with film growth, from 7.2 nm for 2 bilayers to 32.6 nm for 14 bilayers.

Reproduced with permission of the copyright owner. Further reproduction prohibited without permission.

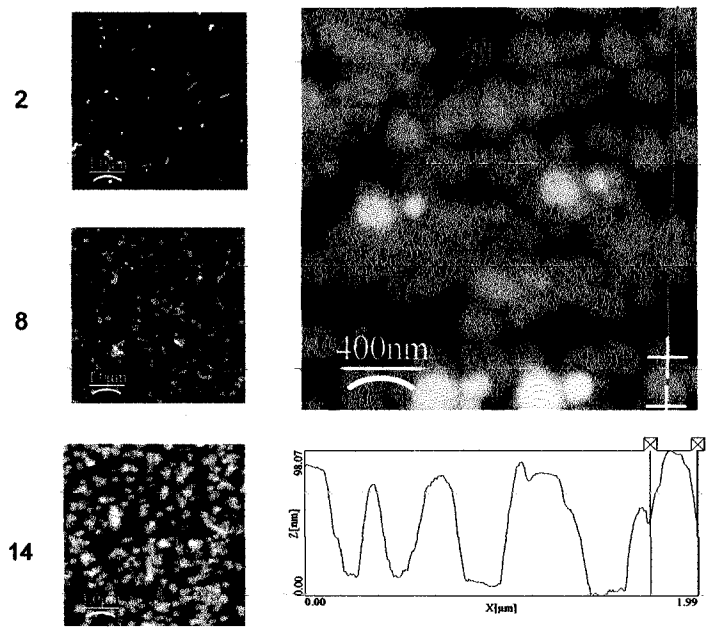

Figure 7.18: AFM for 14 bilayers. 5 x 5 μm height images for 2, 8, 14 bilayers (left). 2 x 2 μm height image of a 14 bilayer film with the line scan indicating a typical clusters size of 260 nm (right)

Also, from the analysis of these images, the diameter of single isolated particles was found to be between ca. 30 and 70 nm, while clusters were generally found to range between ca. 150 and 300 nm as can be seen in Figure 7.18. These results are consistent with what is expected on the basis of the surface plasmon results presented for these films.

SERRS test were conducted with these films using the common SERS test molecules R6G. It was found that the measured SERRS intensity levelled off after 14 bilayers.[23] Therefore, based on these results, it was decided that 14 bilayer films would be used for this application.

The ability of avidin/Ag nanoparticle LbL films to act as 'smart' SERS/SERRS substrates was then tested. The target analyte chosen was the common dye fluorescein.

Reproduced with permission of the copyright owner. Further reproduction prohibited without permission.

This molecule can be purchased with the biotin moiety attached. Fluorescein is resonant at 514.5 nm, as shown by the solution absorption spectrum given in Figure 7.19.

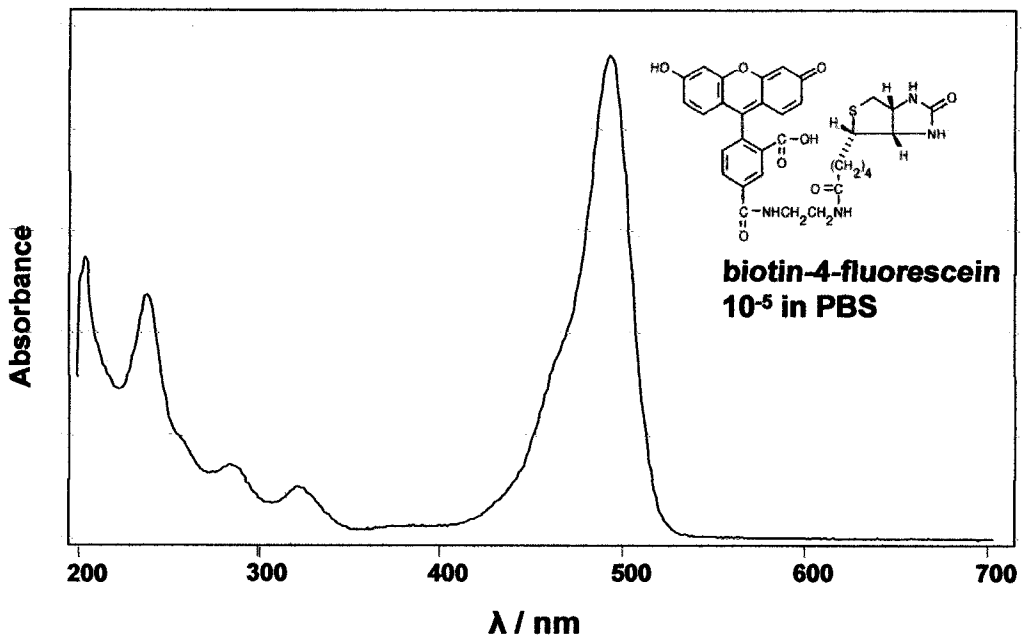

Figure 7.19: UV-Visible absorption spectrum of a B4F Solution.

A film composed of 14 bilayers of avidin and Ag nanoparticles was immersed into a 10^{-4} M solution of biotinylated fluorescein (B4F) for 30 min, while another was immersed into a solution with an equal concentration of neat fluorescein (without biotin), for an equal period of time. Upon removal, both were thoroughly rinsed with water, dried, and their SERRS spectra were recorded using 514.5 nm excitation. It was found that the spectra recorded from the two samples were essentially the same in terms of vibrational band frequencies, widths, and relative intensities. However, the biotinylated sample was found to exhibit absolute intensities that were on average 10^2 greater than its non-tagged counterpart. It was also found that fluorescein could not be observed at all spots and was near its detection limit, while B4F could be readily observed at all spots (homogeneous

Reproduced with permission of the copyright owner. Further reproduction prohibited without permission.

enhancement) with strong intensity. Further experimentation revealed B4F to be detectable from substrates dipped, using identical procedures, into solutions with concentrations as low as 10^{-7} M as shown in Figure 7.20. The neat fluorescein in contrast was undetectable from these substrates when extracted from solutions with concentrations below 10^{-5} M. Since SERRS bands for each sample arise from the same central chromophore, which is, of course, expected to have the same cross section, the 100 fold increase in intensity, and related 100 fold increase in detection sensitivity, associated with biotinylation can be attributed to a 'concentration enhancement' that arises specifically as a result of the strong, bio-specific interaction between the avidin in the LbL film and the biotin tag of B4F.

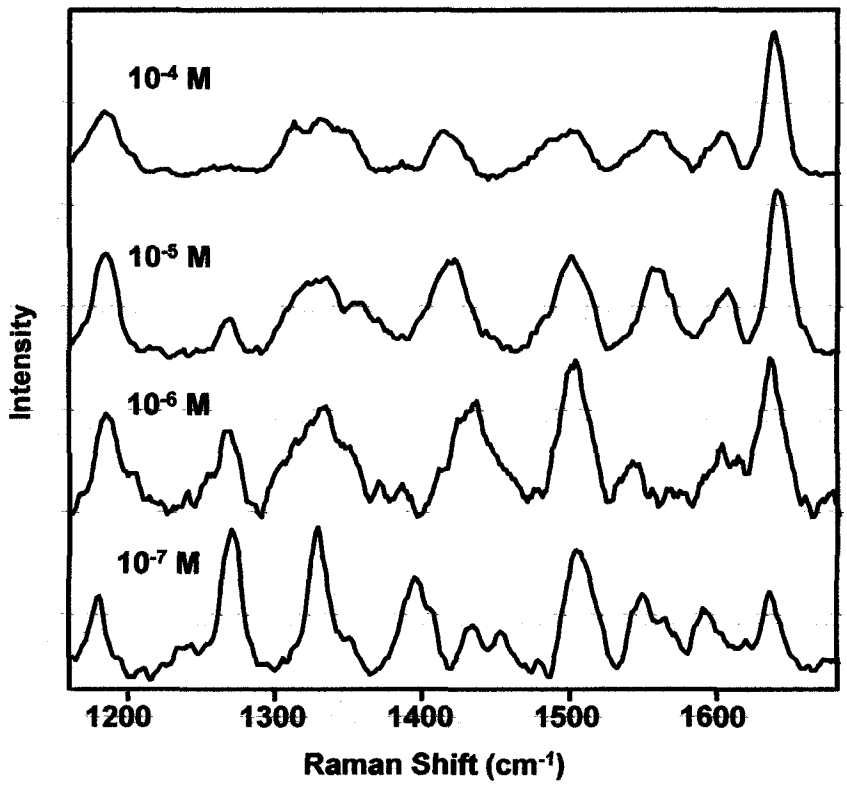

Figure 7.20: SERRS signal of B4F from 14 bilayer avidin/Ag films with decreasing concentration.

Reproduced with permission of the copyright owner. Further reproduction prohibited without permission.

To ensure that this was indeed an effect of the presence of the biotinylation, films were prepared and first exposed to a concentrated solution of biotin before that of the biotinylated analyte. In this case, the concentration enhancement is not observed, confirming the role of avidin binding sites. In addition, these films demonstrate an impressive uniformity of response over the surface of the substrate. In Figure 7.21, the intensity map for a characteristic band of fluorescein (1640 cm^{-1}) is plotted for a 10 x 10 μm map. The signal was relatively the same from each spot measured.

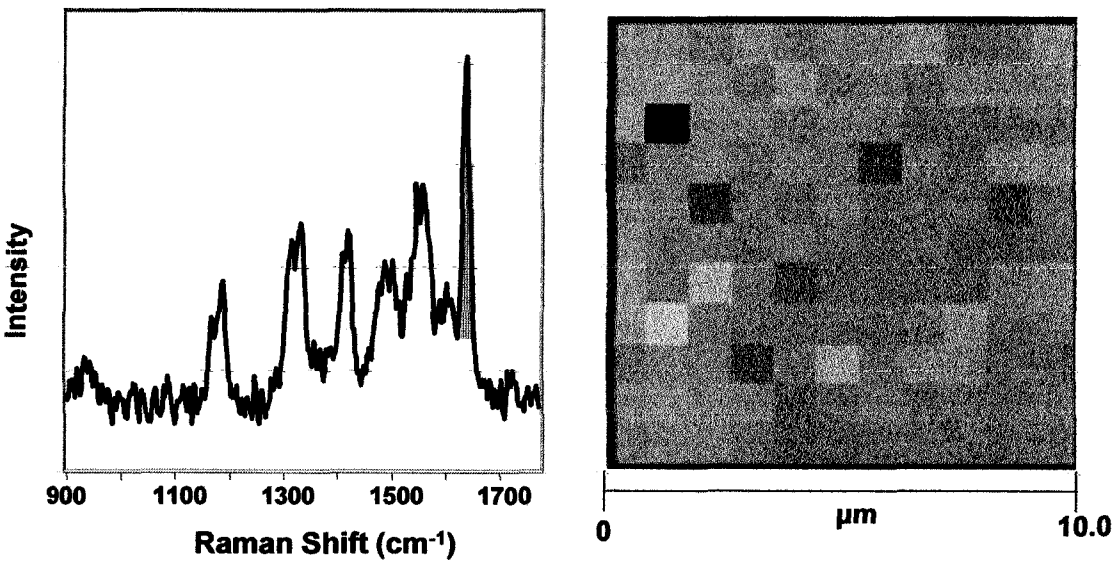

Figure 7.21: 10 x 10 μm SERRS Intensity map for the B4F for the indicated band at 1640 cm^{-1}

It is hoped that these sensors can be used for directed selectivity. There is an entire field of work using the biotinylation of different chemical species, and a substrate such a as the one described here, could be used for selective extraction and enhancement of specific targets.

Reproduced with permission of the copyright owner. Further reproduction prohibited without permission.

As a proof of concept, the same chromophore of fluorescein without prior biotinylation was probed in solution, but now with a primary amine present (5-AF). There are many biotin precursors that readily react with the primary amine. Here the water soluble biotinylation reagent, biotin 3-sulfo-N-hydroxysuccinimide ester which couples to the primary amine in the biological relevant pH range 6.5-8.5, was used. The fluorescein and the biotinylation reagent were combined in a 1:1 molar ratio in phosphate buffer at desired concentrations. The reaction was given ample time to complete before the substrate (a 14 bilayer avidin/Ag film) was submerged. Quality SERRS spectra were again recorded for concentrations down to 10^{-7} levels as shown in Figure 7.21. This demonstrates that in situ biotinylation is possible for these substrates.

Reproduced with permission of the copyright owner. Further reproduction prohibited without permission.

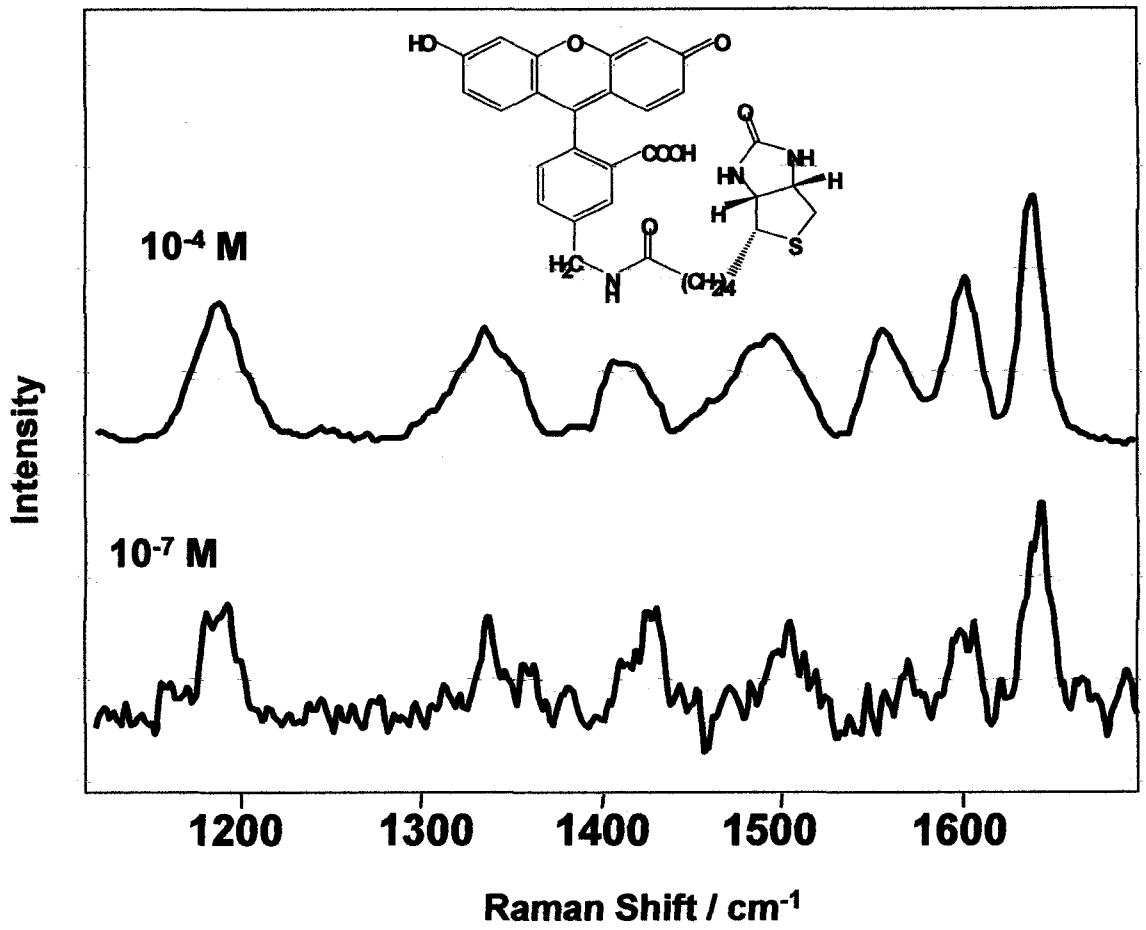

Figure 7.22: SERRS signal of 5-AF after in situ biotinylation from 14 bilayer avidin/Ag films

7.4.4 Conclusions

In conclusion, a versatile way to incorporate silver nanoparticle with the avidin/biotin system has been demonstrated. The fabrication, characterization, and application of avidin/Ag nanoparticle LbL to SERRS studies have been shown for two cases of analyte and preferential adsorption yielded an additional concentration enhancement of ca. 10^2. Therefore, detection limits were improved by at least 2 orders of magnitude. This is the first step towards the development of systems incorporating

Reproduced with permission of the copyright owner. Further reproduction prohibited without permission.

metallic nanoparticles in bio-recognition systems using the powerful LbL technique and it is anticipated that the approach can be successfully applied to many similar systems.

References

(1) Aroca, R. *Surface - Enhanced Vibrational Spectroscopy*; John Wiley & Sons, 2006.

(2) Li, X.; Xu, W.; Zhang, J.; Jia, H.; Yang, B.; Zhao, B.; Li, B.; Ozaki, Y. *Langmuir* **2004**, *20*, 1298-1304.

(3) Lesuffleur, A.; Kumar, L. K. S.; Brolo, A. G.; Kavanagh, K. L.; Gordon, R. *Journal of Physical Chemistry C* **2007**, *111*, 2347-2350.

(4) Cui, Y.; Ren, B.; Yao, J. L.; Gu, R. A.; Tian, Z. Q. *Journal of Physical Chemistry B* **2006**, *110*, 4002-4006.

(5) Addison, C. J.; Brolo, A. G. *Langmuir* **2006**, *22*, 8696-8702.

(6) Zhang, J.; Malicka, J.; Gryczynski, I.; Lakowicz, J. R. *Journal of Physical Chemistry B* **2005**, *109*, 7643-7648.

(7) Aroca, R. F.; Goulet, P. J. G.; Dos Santos, D. S., Jr.; Alvarez-Puebla, R. A.; Oliveira, O. N., Jr. *Analytical Chemistry* **2005**, *77*, 378-382.

(8) Liu, F.-M.; Green, M. *Journal of Materials Chemistry* **2004**, *14*, 1526-1532.

(9) Pieczonka, N. P. W.; Aroca, R. F. *ChemPhysChem* **2005**, *6*, 2473-2484.

(10) Tan, S. C.; Khor, E.; Tan, T. K.; Wong, S. M. *Talanta* **1998**, *45*, 713–719.

(11) Sandford, P. A. In *Chitin and Chitosan: Sources, Chemistry, Biochemistry, Physical Properties and Applications*; Skjak, G., Anthonsen, T., Sandford, P., Eds.; Elsevier: New York, 1988.

Reproduced with permission of the copyright owner. Further reproduction prohibited without permission.

(12) Esumi, K.; Takei, N.; Yoshimura, T. *Colloids and Surfaces B: Biointerfaces* **2003**, *32*, 117-123.

(13) Rabea, E. I.; Badawy, E.-T.; Stevens, C. V.; Smagghe, G.; Steurbaut, W. *Biomacromolecules* **2003**, *4*, 1457-1465.

(14) Ligler, F. S.; Schauer, C. L.; Chen, M.-S.; Chatterley, M.; Eisemann, K.; Welsh, E. R.; Price, R. R.; Schoen, P. E. *Thin Solid Films* **2003**, *434*, 250-257.

(15) dos Santos, D. S., Jr.; Riul, A., Jr.; Malmegrim, R. R.; Fonseca, F. J.; Oliveira, O. N., Jr.; Mattoso, L. H. C. *Macromolecular Bioscience* **2003**, *3*, 591-595.

(16) Stuart, D. A.; Yuen, J. M.; Lyandres, N. S. O.; Yonzon, C. R.; Glucksberg, M. R.; Walsh, J. T.; Van Duyne, R. P. *Analytical Chemistry* **2006**, *78*, 7211-7215.

(17) Dos Santos, D. S., Jr.; Goulet, P. J. G.; Pieczonka, N. P. W.; Oliveira, O. N., Jr.; Aroca, R. F. *Langmuir* **2004**, *20*, 10273-10277.

(18) Jiang, H.; Su, W.; Caracci, S.; Bunning, T. J.; Cooper, T.; Adams, W. *Journal of Applied Polymer Science* **1996**, *61*, 1163-1171.

(19) Adamczyk, M.; Mattingly, P. G.; Shreder, K.; Yu, Z. *Bioconjugate Chemistry* **1999**, *10*, 1032-1037.

(20) Bao, P.; Frutos, A. G.; Greef, C.; Lahiri, J.; Muller, U.; Peterson, T. C.; Warden, L.; Xie, X. *Analytical Chemistry* **2002**, *74*, 1792-1797.

(21) Decher, G. *Science* **1997**, *277*, 1232-1237.

(22) Penn, S. G.; He, L.; Natan, M. J. *Current Opinion in Chemical Biology* **2003**, *7*, 609-615.

(23) Goulet, P. J. G.; Pieczonka, N. P. W.; Aroca, R. F. In *New Approaches in Biomedical Spectroscopy*; Kneipp, K., Ed.; American Chemical Society, 2006.

Reproduced with permission of the copyright owner. Further reproduction prohibited without permission.

(24) Anderson, G. P.; Merrick, E. C.; Trammell, S. A.; Chinowsky, T. M.; Shenoy, D. K. *Sensor Letters* **2005**, *3*, 151-156.

(25) Maliwal, B. P.; Malicka, J.; Gryczynski, I.; Gryczynski, Z.; Lakowicz, J. R. *Biopolymers* **2003**, *70*, 585-594.

(26) Korpela, J. *Medical Biology* **1984**, *62*, 5-26.

(27) Alvarez-Puebla, R. A.; Arceo, E.; Goulet, P. J. G.; Garrido, J. J.; Aroca, R. F. *Journal of Physical Chemistry B* **2005**, *109*, 3787-3792.

(28) Green, N. M. *Methods of Enzymology* **1970**, *18*, 418-424.

(29) Lee, P. C.; Meisel, D. *Journal of Physical Chemistry* **1982**, *86*, 3391-5.

Reproduced with permission of the copyright owner. Further reproduction prohibited without permission.

CHAPTER 8

CONCLUSIONS

Reproduced with permission of the copyright owner. Further reproduction prohibited without permission.

8.1 Conclusions

In the work presented in this thesis, the potential, as well as the peculiar properties of trace chemical detection by SERS and SERRS were explored through investigations in several areas. New insights into these phenomena were uncovered. Questions put forth in the introduction were addressed and new areas of research have been suggested.

In Chapter 4 the successful observation of overtones and combinations in the single-molecule spectra of three PTCD dyes was demonstrated for the first time. The validity of the LB method to SM studies was supported and the many challenges to SM-SERRS were detailed. In particular, the role of contaminants and the need for low ED's to avoid photodegradation of the analyte. The key differences in the behavior of the SERRS signal arising from a few molecules to that that of the ensemble is described. In addition the unique spectral features of SM molecule spectra were highlighted. Finally, the rarity of the SM event was rationalized within the context of present understanding of the plasmonics of disordered systems, such as silver island films.

In an attempt to fully rationalize the SERS profiles collected from 1,8-naphthalimide and Ag colloids, the impact on the measured SERS spectra of several dispersive dependencies were examined in Chapter 5. It was shown how the SERS profile measured at different wavelength of excitation can be satisfactorily simulated with careful consideration of molecular symmetry and the appropriate application of the surface selection rules. This demonstration of the selection rules to SERS for 1,8-naphthalimide is one of the strongest and most unambiguous examples to date. In addition, the effects of non-uniform enhancement factors were discussed. Finally, possible experiments based on these results were suggested for future avenues of study.

Reproduced with permission of the copyright owner. Further reproduction prohibited without permission.

In Chapter 6, the experimental evidence for the photobleaching of three different dyes, and for two types of samples was presented. The biexponential behaviour was associated with the possible inhomogeneity in the distribution of the electromagnetic enhancement found is a disordered systems such as silver island films. It was suggested that the measured SERRS signal is composed from molecules in "hotspots" and those in areas of more common enhancement, or "average enhancement". Experiments with varying energy density, support the idea of increased scattering lifetime for a molecule under low intensity conditions. These results are important for future work of SM-SERRS, and SERRS in general, to fully understand the full impact of enhanced fields.

The fabrication, characterization, and application of three substrates were presented in Chapter 7. Work on mixed Ag/Au metal island film showed the possibilities and the benefits of combining the large enhancement of silver with the less reactive gold. When these two metals are mixed as described here, a highly effective substrate for single molecules detection, and SERRS studies in general, can be made.

Work involving the embedding of gold nanoparticles in the matrix of the biopolymer chitosan was also presented. This created self-sustained, biocompatible, biodegradeable, and non-toxic thin films. When the proper conditions of synthesis were followed, effective SERS substrates could be generated. The importance of disorder for achieving high SERS enhancements was shown. This type of film will be important for future applications of SERS for in situ detection of trace quantities in living systems.

Finally, a versatile way to incorporate silver nanoparticles into biorecognition systems was demonstrated. Using the avidin/biotin system as a basis, LbL films of avidin/Ag nanoparticle where shown to be excellent SERRS substrates. Studies with two classes of analyte, demonstrated that preferential adsorption yielded an additional

Reproduced with permission of the copyright owner. Further reproduction prohibited without permission.

concentration enhancement of ca. 10^2. This is the first step towards the development of a relatively easy way to build functionality into SERS substrates. The method for incorporating metallic nanoparticles into the biorecognition pair presented here can be successfully applied to many similar systems.

8.2 Future Work

I believe that the research presented here lays the groundwork for new paths of investigation. In the area of single molecule studies, the LB approach SM-SERS is ready to move beyond static measurements. Experiments with the inspiration taken from behaviour uncovered in Chapters 5 and 6 would be the next step. These types of studies should give important insight to the mechanism of hotspot enhancement.

Further work on the photodynamics of SERRS and also SERS is essential to SM studies. SM-SERS is at a similar point to where SM-Fluorescence was in its first 10 years, where the limitations to SM studies by photobleaching were just starting to be examined. The work presented here has raised several questions that will need to be addressed in future experiments. In particular, what is the mechanism for signal decay and can it be suppressed? All the work presented here was conducted under ambient conditions. A logical progression would be to conduct experiments under conditions of environmental control, including atmosphere and temperature.

The substrates developed here represent a small fraction of what is possible with the approaches discussed. Recent work on SERS substrates embedded in rats to monitor glucose levels suggest that bio-friendly substrates such as these made with chitosan, may soon find real applications as sensors. Work demonstrated with LbL for the incorporation

Reproduced with permission of the copyright owner. Further reproduction prohibited without permission.

of nanoparticles into biorecognition materials is only the beginning of the types of substrates that can be made with this method.

Reproduced with permission of the copyright owner. Further reproduction prohibited without permission.

VITA AUCTORIS

Nicholas Paul William Pieczonka was born in Windsor, Ontario, Canada on the 4th of March 1977. As a child he attended St. Francis Elementary School. At the age of 13 he attended Assumption Collage high school where he completed OAC.

In 1996, he enrolled in the Physics program at the University of Windsor, Windsor, Ontario, Canada and graduated with a Bachelor's of Science in 2000. Upon graduation, he completed the Howard James studentship for Medical Physics at the Windsor Regional Cancer Center. Upon completion of this program he stayed on as an Assistant to Medical Physics, through the summer of 2001. In fall 2001, he returned to academia as a Ph.D. graduate student in the Chemistry & Biochemistry department at the University of Windsor. He has since been conducting research in a very dark room in the basement of Essex hall under the supervision of Dr. Ricardo Aroca.

Reproduced with permission of the copyright owner. Further reproduction prohibited without permission.

PUBLICATIONS

Articles:

[10] **Pieczonka, N. P. W.,** Goulet, P. J. G. and Aroca, R. F. (2006). "Chemically Selective Sensing Through Layer-by-Layer Incorporation of Biorecognition into Thin Film Substrates for Surface-Enhanced Resonance Raman Scattering." Journal of the American Chemical Society. 128: 12626-12627.

[9] **Pieczonka, N. P. W.** and Aroca, R. F. (2005). "Inherent Complexities of Trace Detection by Surface-Enhanced Raman Scattering." ChemPhysChem 6(12): 2473-2484

.

[8] Aroca, R. F., Alvarez-Puebla, R. A., **Pieczonka, N. P. W.**, Sanchez-Cortez, S. and Garcia-Ramos, J. V. (2005). "Surface-Enhanced Raman Scattering on Colloidal Nanostructures." Advances in Colloid and Interface Science 116 (1-3): 45-61.

[7] Goulet, P. J. G., **Pieczonka, N. P. W.** and Aroca, R. F. (2005). "Mapping Single Molecule SERRS From Langmuir--Blodgett Monolayers on Nanostructured Silver Island Films." Journal of Raman Spectroscopy 36: 574-580.

[5] Del Caño, T., Goulet, P. J. G., **Pieczonka, N. P. W.**, Aroca, R. F. and De Saja, J. A. (2005). "Nano-structured Langmuir-Blodgett mixed films of titanyl (IV) phthalocyanine and bis(neopentylimido)perylene. Unique degree of miscibility." Synthetic Metals 148: 31-35.

Reproduced with permission of the copyright owner. Further reproduction prohibited without permission.

[4] dos Santos Jr., D. S., Goulet, P. J. G., **Pieczonka, N. P. W.**, Oliveira Jr., O. N. and Aroca, R. F. (2004). "Gold Nanoparticle Embedded, Self-Sustained Chitosan Films as Substrates for Surface-Enhanced Raman Scattering." Langmuir 20: 10273-10277.

[3] Goulet, P., **Pieczonka, N.** and Aroca, R. (2003). "Single Molecule SERRS of Mixed Perylene Langmuir-Blodgett Monolayers on Novel Metal Island Substrates." Canadian Journal of Analytical Sciences and Spectroscopy 48(2): 146-152.

[2] Goulet, P. J. G., **Pieczonka, N. P. W.** and Aroca, R. F. (2003). "Overtones and Combinations in Single-Molecule Surface-Enhanced Resonance Raman Scattering Spectra." Analytical Chemistry 75: 1918-1923.

[1] Aroca, R., **Pieczonka, N.** and Kam, A. (2001). "Surface-enhanced Raman scattering and SERRS imaging of phthalocyanine mixed films." Journal of Porphyrins and Phthalocyanines 5(1): 25-32.

Other refereed contributions:

[3] Goulet, P. J. G., **Pieczonka, N. P. W.** and Aroca, R. F. (2006). "Protein/Nanoparticle Layer-by-Layer Films as Substrates" for Surface-Enhanced Resonance Raman Scattering. New Approaches in Biomedical Spectroscopy. K. Kneipp, American Chemical Society.

[2] **Pieczonka, N. P. W.**, Goulet, P. and Aroca, R. (2006). "Applications of the enhancement of Resonance Raman Scattering and Fluorescence by Strongly Coupled

Reproduced with permission of the copyright owner. Further reproduction prohibited without permission.

Metallic Nanostructures". Surface Enhanced Raman Scattering: Physics and Applications. K. Kneipp, M. Moskovits and H. Kneipp. Berlin, Springer-Verlag. 103: 197-216.

[1] Aroca, R. F., **Pieczonka, N. P. W.** and Nazri, M. (2006). "Vibrational spectroscopy and surface-enhanced vibrational spectroscopy of carbonaceous materials: from nanotubes to graphite. S. S. Cortes, C. D. Maroto, O. Francioso and J. V. G. Ramos. Universidad de Zargoza, JACA: 111-124.

CONFERENCES

[11] **Pieczonka, N. P. W.** and Aroca, R. (2006). "The Critical Challenges Facing Surface-Enhanced Raman Spectroscopy for Trace Chemical Detection" FACSS Orlando, Florida, USA.

[10] Goulet, P., **Pieczonka, N. P. W.** and Aroca, R. F. (2005). Protein/nanoparticle layer-by-layer films as chemically selective SERS substrates. Pacifichem, Honolulu, Hawaii, USA.

[9] Aroca, R., **Pieczonka, N. P. W.**, Santos, D. and Goulet, P. (2004). Surface enhanced Raman Scattering Single particle spectroscopy and single molecule detection. 87th Conference of the Canadian Society for Chemistry, London, ON.

[8] **Pieczonka, N.**, Santos, D., Goulet, P., Osvaldo, O. and Aroca, R. (2004). The application of self sustained nanoparticle embedded biopolymer films for surface enhanced Raman scattering. European Conference of Thin Films, Valladollid, Spain.

Reproduced with permission of the copyright owner. Further reproduction prohibited without permission.

[7] Aroca, R., **Pieczonka, N. P. W.**, Santos, D. and Goulet, P. (2004). Surface enhanced Raman Scattering Single particle spectroscopy and single molecule detection. 87th Conference of the Canadian Society for Chemistry, London, ON.

[6] **Pieczonka, N. P. W.** and Aroca, R. (2004). The effect of energy density on the rate of signal degradation of dye molecules probed by Surface Enhanced (Resonance) Raman Scattering (SERRS). 87th Conference of the Canadian Society for Chemistry, London, ON.

[5] Goulet, P, **Pieczonka, N.**, and Aroca, R. (2003). Raman Microscopy and Imaging. Applications to Monolayers and Single Molecule Detection. Microscopy and Microanalysis, San Antonio, Texas, USA, Cambridge University Press, Cambridge, England.

[4] **Pieczonka, N.**, Goulet, P. and Aroca, R. (2003). Single Molecule SERRS: Fundamentals, Overtones, and Combinations. 39th IUPAC Congress and 86th Conference of the Canadian Society for Chemistry, Ottawa, Canada.

[3] **Pieczonka, N.**, Goulet, P. and Aroca, R. (2002). Single Molecule Detection on Ag/Au Substrates. Proceedings of the Fourth Biennial International Conference on Monitoring and Measurement of the Environment, Toronto, Canada.

Reproduced with permission of the copyright owner. Further reproduction prohibited without permission.

[2] **Pieczonka, N.**, Goulet, P. and Aroca, R. (2002). Single Molecule SERRS of Mixed Perylene Langmuir-Blodgett Monolayers on Novel Metal Island Substrates. XVIIIth International Conference on Raman Spectroscopy, Budapest, Hungary, John Wiley and Sons, Ltd.

[1] **Pieczonka, N.**, Goulet, P., Lemma, T. and Aroca, R. (2002). Surface Enhanced Resonance Raman Scattering: Properties and Applications. XVIIIth International Conference on Raman Spectroscopy, Budapest, Hungary, John Wiley & Sons. Ltd.

Reproduced with permission of the copyright owner. Further reproduction prohibited without permission.